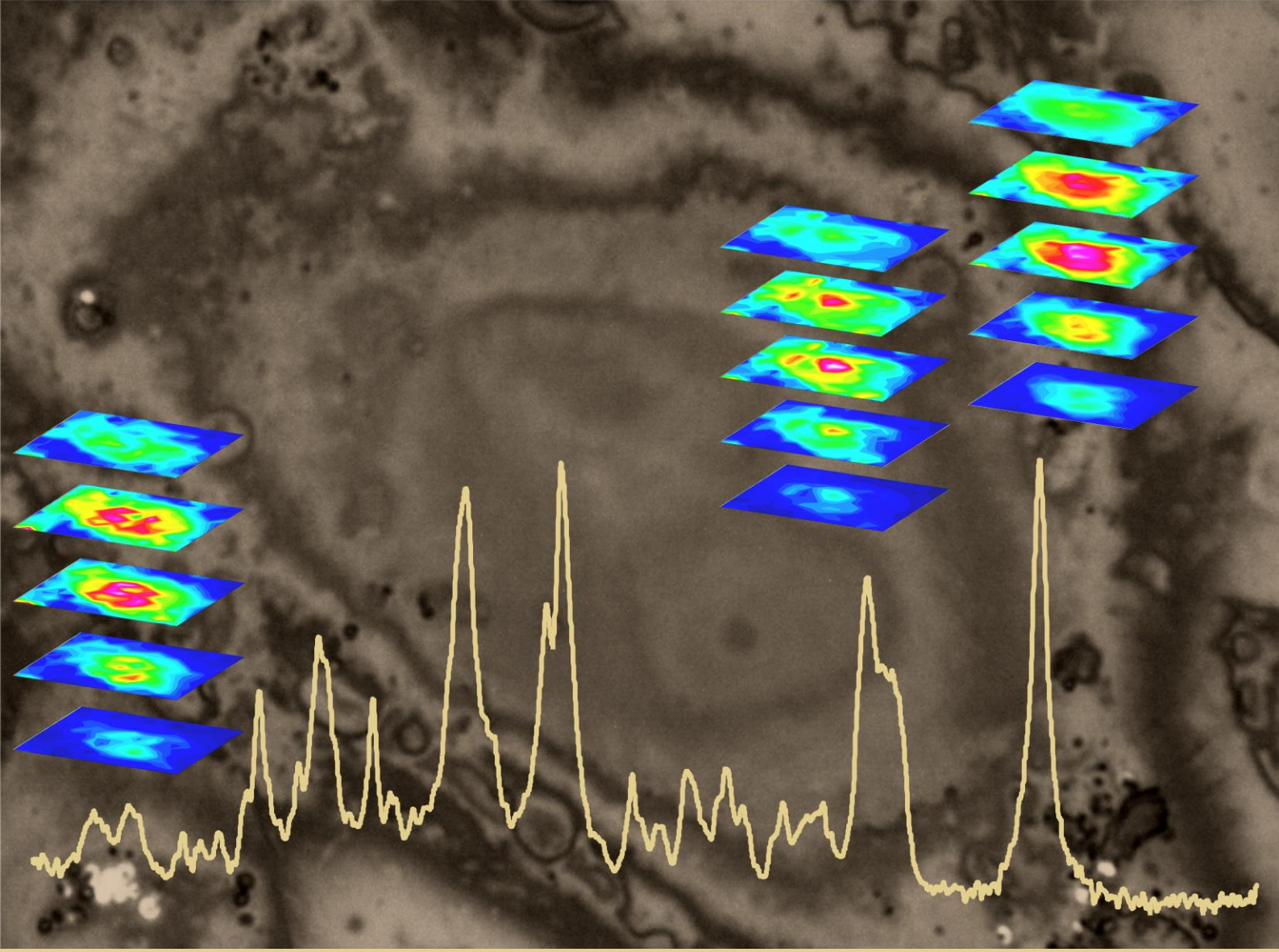

Ana Lúcia Marques Batista de Carvalho

CISPLATIN-LIKE COMPOUNDS AS POTENTIAL CHEMOTHERAPEUTICS: FROM THE BENCH TO THE CELL

Tese de Doutoramento em Biociências no ramo de especialização em Bioquímica, orientada pela Professora Doutora Maria Paula Matos Marques e apresentada à Faculdade de Ciências e Tecnologia da Universidade de Coimbra.

Agosto de 2016

· U C ·

UNIVERSIDADE DE COIMBRA

• U  C •

Cisplatin-like Compounds as Potential Chemotherapeutics: from the Bench to the Cell

by

Ana Lúcia Marques Batista de Carvalho

Tese de Doutoramento em Biociências no ramo de especialização em Bioquímica, orientada pela Professora Doutora Maria Paula Matos Marques do Departamento de Ciências da Vida da Faculdade de Ciências e Tecnologia da Universidade de Coimbra.

Doctoral thesis in Biosciences in the field of Biochemistry, supervised by Professor Maria Paula Matos Marques from the Department of Life Sciences of the Faculty of Sciences and Technology of the University of Coimbra.

Departamento de Ciências da Vida – Faculdade de Ciências e Tecnologia

Universidade de Coimbra

Coimbra, 2016

The study presented in this dissertation was supported by a PhD grant from the Portuguese Foundation for Science and Technology, FCT (SFRH/BD/72851/2010).

This dissertation is the result of my original work developed at the Unidade de I&D Química-Física Molecular from the Department of Chemistry of the University of Coimbra, Portugal which is funded by the Fundação para Ciência e Tecnologia, Portugal.

The anti-angiogenic experiments were carried at the Laboratory of Pharmacology from the Department of Drug Science of the Faculty of Pharmacy and LAQV – Requimte both from University of Porto, Portugal with is funded by the European Union (FEDER funds through COMPETE) and by the Fundação para a Ciência e Tecnologia, Portugal.

The synchrotron radiation based experiments were performed at Diamond Light Source and neutrons experiments were accomplished at the ISIS pulsed neutron and muon source both from the Rutherford Appleton Laboratory, Harwell Science and Innovation Campus – Science and Technology Facilities Council, United Kingdom. (Neutrons work supported by the European Commission – 7th Framework Programme/Key Action *Strengthening the European Research Area, Research Infrastructures* (CP-CSA_INFRA-2008-1.1.1 N° 226507-NMI3). Diamond Light Source (UK), for time on B22/MIRIAM (SM10065), under the European programme Calypso FP7.)

Aos meus Pais
Aos avós

Acknowledgments / Agradecimentos

Este trabalho não teria sido possível sem o apoio de um conjunto de pessoas a quem aqui expresso a minha mais sincera gratidão.

Gostaria de agradecer ao Professor Doutor Amorim da Costa e ao Professor Doutor Luís Batista de Carvalho coordenadores da Unidade de I&D Química-Física Molecular. Ao primeiro por me ter aceite neste grupo de investigação nos idos de 2007 e a ambos por sempre terem proporcionado as condições necessárias ao desenvolvimento dos trabalhos de investigação a que me propus.

Um agradecimento especial à Professora Doutora Maria Paula Marques, minha "chefe", mas principalmente minha amiga, por toda a disponibilidade, ensinamentos e oportunidades de poder fazer mais e melhor quer a nível científico, quer a nível pessoal.

À Professora Doutora Carmen Diniz, a minha segunda "chefe", pela amizade, apoio incondicional e por tão bem me receber ao longo destes anos.

I would like to thank Svemir, Louise and Mike for all their incredible help and availability. Moreover, I am grateful to Vicky for being more than an instrument scientist and having granted me the opportunity to learn with her.

Aos meus alunos ao longo destes anos porque com todos aprendi sempre algo.

A todos os meus colegas, perto e longe, agradeço o companheirismo e as horas de boa disposição. Nelson, um grande obrigada pela preocupação. Paula Pequena um bem-haja pela tua preciosa ajuda.

À Joana C., Mafalda, Sofia, Marguerita, Joana B., Elisa e a todos os amigos que de um modo ou de outro estiveram sempre presentes. Parafraseando Voltaire: "Todas as riquezas do mundo não valem um bom amigo".

À Susana, ao Alvier e ao Timmy o meu muito obrigada pela amizade e por me fazerem sempre sentir, mesmo longe, como se estivesse em casa.

Não poderia deixar de agradecer à minha Família, especiamente à tia Cândida, à tia Nani, ao tio Carlos, ao Vasco e ao Francisco, pelos valiosos ensinamentos que sempre me transmitiram, assim como por toda a disponibilidade demonstrada ao longo deste percurso.

Ao avô Norberto e à avó Zé – "Aqueles que passam por nós, não vão sós, não nos deixam sós. Deixam um pouco de si, levam um pouco de nós" (Antoine de Saint-Exupéry).

Ao avô Zé, à avó Pina, ao avô Tim e à avó Luísa um enorme obrigada pelos valores que me fizeram chegar através dos meus Pais. Tenho a certeza que têm muito orgulho em mim.

À Ana Isabel e à Inês por serem as melhores irmãs sem o serem.

Ao meu irmão Diogo por não fazer nada sem mim e me mandar sempre à frente! Crescer sozinha não teria tido graça nenhuma. Ao Dunga pela companhia sonolenta!

Aos meus Pais o meu mais sincero agradecimento pela sua presença, exemplos e valores que me fizeram tornar uma menina "Grande" no empenho, no saber fazer e no saber estar. Foi graças à educação que, de várias formas, me deram que hoje concluo este trabalho que vos dedico com o meu maior obrigada.

Finalmente, ao André o meu obrigada pelo carinho e paciência mesmo em momentos de desânimo. Obrigada por nunca reclamar das ausências mais longas. Sem ele nunca teria conseguido.

Abstract

Despite all efforts, cancer is still a growing health problem worldwide, metastatic breast carcinoma being the second most lethal cancer among women. So, improvement of chemotherapeutic approaches to metastatic breast carcinoma is a goal of the utmost importance in the public health area. Since Rosenberg´s serendipitous discovery of cisplatin, a widely used antineoplastic agent, other metal-based antitumour compounds have been pursued with a view to overcome cisplatin´s severe nephrotoxicity and acquired resistance. One of the research lines along this subject concerns polynuclear chelates comprising cisplatin-like moieties linked by biogenic polyamine chains. The present study focuses on two dinuclear Pt(II) and Pd(II) chelates with spermine (Pt_2Spm and Pd_2Spm), probing their cellular impact (alone or in combination).

The first aim of this work was to evaluate the antineoplastic properties of these complexes towards triple negative human breast carcinoma cells (MDA-MB-231), in sole administration and combined with the anti-mitotic agent Docetaxel (Taxotere®), regarding anti-proliferative, anti-invasive and anti-angiogenic capacities, in search for a synergistic interaction. Improved therapeutic schemes were sought, capable of increasing the survival rates for this poor prognosis cancer, hopefully circumventing chemoresistance to cisplatin-like agents. Promising anti-proliferative, anti-invasive and anti-angiogenic abilities were found for Pd_2Spm/Docetaxel combinations.

In addition, studies of drug–cell interactions in cancer model systems were pursued, since they are essential in the pre-clinical stage of rational drug design, which relies on a thorough understanding of the mechanisms underlying cytotoxic activity and biological effects, at a molecular level. With the use of complementary vibrational spectroscopy methods, the cellular impact of Pt_2Spm and Pd_2Spm was assessed, using cisplatin as a reference compound. The effects on cellular metabolism were monitored in MDA-MB-231 cells, by Raman and synchrotron-radiation infrared microspectroscopies, for different drug concentrations (2 – 8 μM) at a 48 h drug exposure. Multivariate data analysis was applied, unveiling drug- and concentration-dependent effects: apart from discrimination between control and drug-treated cells, a clear separation was obtained for the different agents studied – Pt(II) *vs* Pd(II), and

mononuclear (cisplatin) *vs* polynuclear (Pt_2Spm and Pd_2Spm). Spectral biomarkers of drug action were identified, as well as the cellular response to the chemotherapeutic insult. The main effect of the tested compounds was found to be on DNA, lipids and proteins, the Pd(II) agent having a more significant impact on proteins while its Pt(II) homologue affected the cellular lipid content at lower concentrations. These results suggest the occurrence of distinct and unconventional pathways of cytotoxicity for these dinuclear polyamine complexes. Raman and FTIR microspectroscopies were confirmed as powerful non-invasive techniques to obtain unique spectral signatures of the biochemical impact and physiological reaction of cells to anticancer agents.

Finally, the first neutron scattering study on human cells is reported, for addressing the subject of solvent slaving to a drug by probing intracellular water, with a view to ascertain variations upon drug exposure. Inelastic and quasi-elastic neutron scattering spectroscopy experiments with isotope labelling were performed, for monitoring this interfacial water response to cisplatin treatment (at 8 and 20 μM) in the same cell line (MDA-MB-231). Optical vibrational data were also obtained, for lyophilised cells. The intracellular water behaviour in the presence of cisplatin was found to be different from bulk water as well as from cytoplasmic water in drug-free cells. Concentration-dependent dynamical changes evidencing a progressive mobility reduction were unveiled between untreated and cisplatin-exposed samples, concurrent with variations in the native organisation of water molecules within the intracellular medium as a consequence of drug action. The results thus obtained yielded a clear picture of the intracellular water response to cisplatin and constitute the first reported experimental proof of a drug impact on the cytomatrix by neutron techniques. This is an innovative way of tackling a drug´s pharmacodynamics, searching for alternative targets of drug action (secondary drug targets).

Resumo

Apesar de todos os esforços, o cancro continua a ser um problema de saúde mundial sendo o cancro de mama metastático o segundo mais letal em mulheres. Assim, melhorar as abordagens quimioterapêuticas no caso do cancro de mama metastático é de extrema importância para a saúde pública. Desde a descoberta da cisplatina por Rosenberg que esta passou a ser amplamente utilizada em oncologia. No entanto, devido à sua elevada nefrotoxicidade e resistência adquirida a procura de outros compostos inorgânicos com vista a ultrapassar estes problemas é de extrema importância. Uma das linhas de investigação na área é a inclusão de unidades semelhantes à cisplatina em quelatos polinucleares utilizando poliaminas biogénicas como ligandos. Este trabalho visa explorar o impacto celular de dois quelatos dinucleares de Pt(II) e de Pd(II) com espermina (Pt_2Spm e Pd_2Spm), tanto em administração isolada como em combinação com outros fármacos.

O primeiro objetivo deste estudo foi avaliar as propriedades antineoplásicas destes complexos quando administrados isoladamente ou em combinação com o Docetaxel (Taxotere®), um agente anti-mitótico, numa linha celular humana de cancro de mama triplo negativo (MDA-MB231), avaliando a sua capacidade anti-proliferativa, anti-invasiva e anti-angiogénica, com vista à obtenção de sinergismo. O desenvolvimento de melhores esquemas terapêuticos poderá levar a um aumento da percentagem de sobrevivência para este tipo de cancro (de fraco prognóstico), contornando a resistência à quimioterapia para complexos semelhantes à cisplatina. Para a combinação Pd_2Spm/Docetaxel foram obtidos efeitos anti-proliferativo, anti-invasivo e anti-angiogénico muito promissores. Foram ainda realizados estudos de interação fármaco-célula em modelos de cancro humano, sendo estes essenciais ao desenvolvimento racional de fármacos numa fase pré-clínica.

A utilização de métodos complementares de espectroscopia vibracional permitiu determinar o impacto celular dos complexos Pt_2Spm e Pd_2Spm, usando a cisplatina como composto referência. O impacto sobre o metabolismo celular foi monitorizado para a linha MDA-MB231, por microespectroscopias de Raman e Infravermelho (com radiação de sincrotrão) utilizando diferentes concentrações de composto (2 – 8 μM) para um tempo de exposição de 48 h. O uso de análise multivariada dos dados obtidos permitiu identificar um

nítido efeito dependente da concentração, tal como discriminar entre células controlo e células tratadas, assim como o impacto dos diferentes agentes testados – Pt(II) *vs* Pd(II) e mononuclear (cisplatina) *vs* polinuclear (Pt_2Spm and Pd_2Spm). Foram identificados biomarcadores espectrais da ação destes compostos, assim como a resposta celular devida à perturbação quimioterapêutica. O efeito principal dos complexos estudados verificou-se ao nível do DNA, dos lípidos e das proteínas, tendo o agente de Pd(II) um impacto mais significativo nas proteínas enquanto que o seu homólogo de Pt(II) afetou mais os lípidos (mesmo a baixas concentrações). Os resultados obtidos sugerem a ocorrência de vias distintas e não convencionais de citotoxicidade para estes complexos dinucleares com poliaminas. As microespectroscopias de Raman e FTIR foram confirmadas como sendo técnicas potentes e não-invasivas para obtenção de assinaturas espectrais do impacto bioquímico e reação fisiológica das células a agentes anticancerígenos.

Finalmente, é reportado o primeiro estudo por difração de neutrões em células humanas, que visa abordar o condicionamento do solvente a um fármaco através da análise da água intracelular com o intuito de verificar as variações provocadas pela exposição ao agente quimioterapêutico. As experiências de espectroscopia de difração de neutrões, inelástica e quase-elástica, com marcação isotópica foram realizadas de modo a monotorizar a resposta da água interfacial ao tratamento com cisplatina (8 e 20 μM) na mesma linha celular (MDA-MB231) previamente investigada. Foram também obtidos dados de espectroscopia vibracional ótica para as células liofilizadas. Verificou-se que o comportamento da água intracelular na presença da cisplatina foi diferente do da água livre de constrangimentos, assim como da água citoplasmática em células não tratadas. As alterações dinâmicas dependentes da concentração evidenciaram uma redução de mobilidade progressiva (e dependente da concentração) entre as amostras não tratadas e as expostas à cisplatina, observadas em simultâneo às variações na estrutura nativa das moléculas de água no meio intracelular, como consequência da ação do fármaco. Os resultados obtidos permitiram obter uma imagem clara da resposta à cisplatina por parte da água intracelular, sendo esta a primeira prova experimental, mediante o uso de técnicas espectroscópicas com neutrões, do impacto de um fármaco na matriz celular. Este é um modo inovador de abordar a farmacodinâmica de um agente quimioterapêutico, na busca de recetores alternativos (alvos terapêuticos secundários).

List of Publications

The majority of the work performed during this PhD research, which constitutes the present dissertation, is already published (or submitted) in international peer-reviewed journals of the field.

1. "*Pt(II) Complexes with Linear Diamines. I – Vibrational Study of Pt-Diaminopropane Dichloride*"
   A.L.M. Batista de Carvalho, S.M. Fiuza, J. Tomkinson, L.A.E. Batista de Carvalho and M.P.M. Marques (2012), *Spectrosc-Int J*, **27**(5-6), 403. DOI: 10.1155/2012/206297

2. *"Chemotherapeutic Response to Cisplatin-like Drugs in Human Breast Cancer Cells Probed by Vibrational Microspectroscopy"*
   A.L.M. Batista de Carvalho, M. Pilling, P. Gardner, J. Doherty, G. Cinque, K. Wehbe, C. Kelley, L.A.E. Batista de Carvalho and M.P.M. Marques (2016). *Farad Discuss*, **187**, 273. DOI: 10.1039/C5FD00148J

3. *"Synergism Between Docetaxel and a Pd-Spermine Complex in Metastatic Breast Cancer"*
   A.L.M. Batista de Carvalho, P.S.C. Medeiros, F.M. Costa, V.P. Ribeiro, J.B. Sousa, C. Diniz, M.P.M. Marques (2016) *Biomed Pharmacother* (submitted).

4. *"Intracellular Water – an Overlooked Drug Target? Cisplatin Impact in Cancer Cells Probed by Neutrons"*
   M.P.M. Marques, A.L.M. Batista de Carvalho, V. Garcia Sakai, L. Hatter and L.A.E. Batista de Carvalho (2016) *Phys Chem Chem Phys* (submitted).

Introduction

1.1. The Systems

1.1.1. Breast Cancer

Breast cancer is the second most common type of cancer worldwide and the most frequent among women [1], being the fifth cause of death from neoplastic disease. Particularly regarding invasive breast cancer, although the 5-year survival rates have increased from 75% to 90% since the mid-1970s, the prognosis is still poor due to its high metastatic capacity [2-4]. In Portugal, it is estimated that there are 10600 deaths among women *per year* due to neoplasia, from which 16.9% are due to breast cancer, this being the most frequent cancer type with around 6000 new cases every year [5].

The female breast is mostly made up of a collection of fat cells that constitute the adipose tissue. This tissue extends from the collarbone down to the underarm and across to the middle of the ribcage. The normal architecture of a healthy female breast is show in Figure 1. It is made up of 12–20 sections called lobes arranged like the petals of a daisy. Each lobe arises from multiple smaller lobules which is the gland that produces milk in nursing women. These connect to a common terminal interlobular duct, the so called milk ducts, which continue to their outlet at the nipple. These breast structures are generally where cancer begins to form. Histologically, lobules and ducts are lined by a single layer of luminal epithelial cells, surrounded by transversely oriented myoepithelial cells. These structures are separated from the surrounding tissue, or stroma, by a basement membrane, the breach of which distinguishes invasive carcinoma from *in situ* carcinoma [6]. The surrounding stroma comprises the

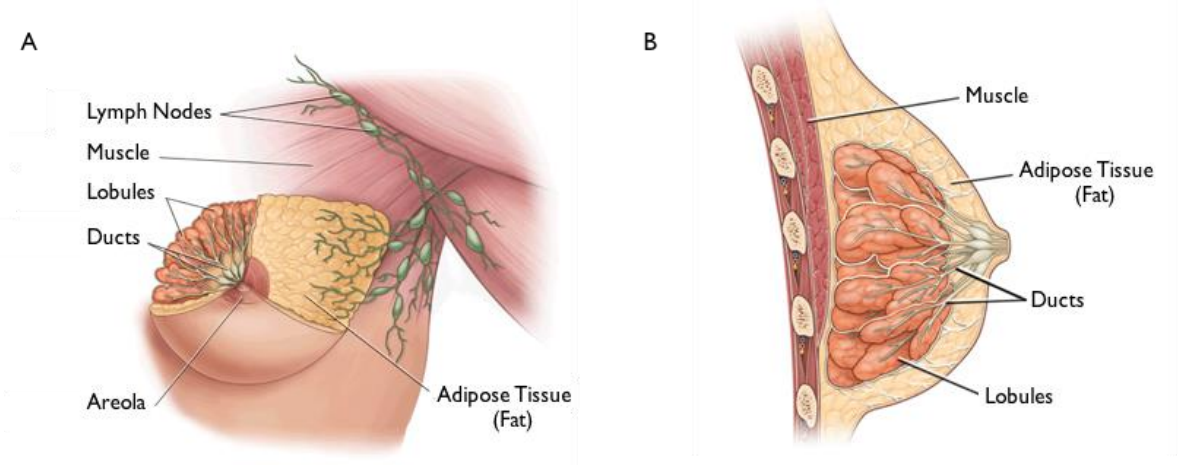

Figure 1 – Schematic representation of normal breast [7]. (A) – Front view; (B) – Side view.

extracellular matrix, discrete cells (*e.g.*, fibroblasts, immune cells and adipocytes), and organised structures (*e.g.*, blood vessels), each of which contributes to the overall configuration of the local microenvironment.

Histopathologists have long recognised, through morphological observations, the high heterogeneity of breast cancer. Actually, breast cancer is a heterogeneous neoplasm originating from the epithelial cells lining the milk ducts. Accordingly, based on their overall morphology and structural organisation, breast tumours have been classified into multiple categories. Within these, two major groups were identified: invasive ductal and invasive lobular carcinomas, respectively accounting for about 75% and 10% of the total cases [8]. These two categories and their combinations cover the vast majority (*ca.* 90%) of the breast cancers. The remaining 10% can be found under medullary, neuroendocrine, tubular, apocrine, metaplastic, mucinous (A and B), inflammatory, comedo, adenoid cystic and micropapillary types [9].

Although the histopathological classification has been progressively refined and replaced by a molecular characterisation which allow a better understanding of disease mechanisms and prediction of clinical outcome. This molecular classification is based on the presence of specific markers which can define cancer subtypes with different prognosis as well as identify their susceptibility to targeted chemotherapy [10]. The most common biomarkers detected by immunohistochemistry (IHC) methods are the oestrogen receptor (ER), the progesterone receptor (PR) and the human epidermal growth factor 2 (HER2) [11]. Assessment of the expression of these three receptors, coupled to traditional clinicopathological variables (*e.g.* tumour size, tumour grade and nodal involvement) leads not only to patient prognosis but also to the prediction of the tumours' response to specifically directed treatments. A combined assessment of the three markers (ER/PR/HER2) allows an accurate assignment to specific categories, namely ER^+ ($ER^+/HER2^-$), $HER2^+$ ($ER^-/HER2^+$), triple negative ($ER^-/PR^-/HER2^-$) and triple positive ($ER^+/PR^+/HER2^+$). From the prognostic point of view, the ER^+ tumours are those with a best overall outcome, while the triple negative breast cancer (TNBC) is the one with the worst prognosis among all subtypes [12].

The breast cancer associated (BRCA) genes – BRCA1 and BRCA2 - are very relevant in this type of neoplasia, since individuals who carry mutations in these genes are predisposed to an early-onset of breast and/or ovarian cancers, as well as of other malignancies. Many of these

genetic-related breast tumours, especially the ones with the BRCA1 mutation, are classified as TNBC (over 80%) [13,14]. Although sporadic TNBC can also arise in women without the BRCA genes mutation, they still present a downregulated expression of gene promoters through methylation and other epigenetic mechanisms [15]. As BRCA genes are involved in homologous recombination processes, mutation carriers have a higher sensitivity to drugs that induce DNA double-strand breaks [16].

TNBC accounts for at least 10-20% of all breast cancer subtypes (being more prevalent in young women [17]) and due to its aggressiveness it has a higher risk of recurrence and mortality in the first 5 years after diagnosis [17-19]. The overall survival (OS) for women with metastatic TNBC is 13 months, and less than 30% of the cases survive longer than 5 years [12]. In fact, this type of cancer can yield metastasis within 3 to 10 years after diagnosis of the primary tumour, despite its surgical removal, due to neoplastic cell dissemination that leads to minimal residual disease (MRD) – presence of metastasis-initiating malignant cells in distant organs, usually undetectable [20,21]. In order to spread and form metastasis, the initial tumour needs to mobilise blood vessels to form a vascular support. Without this, tumours have a very limited capacity to grow, as they need nutrients to be delivered to meet the metabolic requirements of the growing tumour. For this type of neovascularisation to start, the tumour must switch to an angiogenic phenotype [22]. There are several mechanisms through which a tumour can establish a blood supply, angiogenesis being one of them [23]. It consists in the generation of new blood vessels from the existing vasculature. In order to accomplish this, the angiogenic pathway requires, at an early stage, the degradation of the basement membrane followed by endothelial cell migration and invasion of the extracellular matrix and capillary lumen [24]. On a posterior phase, new vasculature is formed upon inhibition of further endothelial proliferation, reconstitution of the basement membrane and junctional complex formation, and organisation of endothelial cells into a new luminal space [25]. In order to establish a tumour blood supply *via* this mechanism, particular angiogenic promoters and inhibitors are required. An important family of angiogenic factors is the vascular endothelial growth factor (VEGF), which occurs throughout tumour stages and constitutes the foremost controller of physiological and pathological angiogenesis [26,27].

Accordingly, development of new anticancer agents and chemotherapeutic strategies against TNBC is of paramount importance, specifically aiming at a higher efficiency regarding cell growth inhibition and decreased invasiveness and angiogenesis, coupled to lower acquired resistance and deleterious side effects.

1.1.2. Biological Models

1.1.2.1. Cell lines

Cell lines are widely used as low maintenance *in vitro* models in cancer research since they are cost effective and avoid ethical concerns associated with the use of animals.

The first cell line – HeLa – was established over 60 years ago by George Gey [28]. It was named after Henriquetta Lacks, the lady who had a cervical carcinoma and from whom the cell line was derived. Shortly after, in 1958, the first breast cancer cell line – BT-20 – was established, although only 20 years afterwards have breast cancer cell lines become more recurrent, with the University of Texas MD Anderson series [29] (*e.g.* MDA-MB-231) and MCF-7. This is a particularly good model to study cancer hormone response, due to its sensitivity to oestrogen through ER expression [30]. From then on, only a few successes have been achieved, such as the SUM series comprising 10 cell lines derived from either breast primary tumours, pleural effusions or distinct metastatic sites in individual patients [31].

The breast cancer sub-classification were initially defined through a 50-gene quantitative protein chain reaction (qPCR) assay (PAM50), that was developed to identify the intrinsic biological subtypes using RNA isolated from breast tissue [32]. This assay is based on gene expression analysis and segregates breast cancer tumours into four groups: basal-like (BL), luminal, normal-like and HER2 (Table 1). When analysed through the PAM50, most of the TNBC´s fall into the BL set, the remaining being distributed among luminal and HER2. Finally, the claudin-low fifth subtype was identified, having been initially clustered with the BL group due to the lack of ER, PR and HER2 expression. This type of TNBC´s are less proliferative than the BL tumours, but display an enhanced expression of mesenchymal genes [33].

Identification of claudin-low type breast cancer was the first step for understanding that not all TNBC cases fall exactly into the intrinsic subtypes provided by PAM50. Lehmann *et al.* used the ER, PR and HER2 molecular analysis coupled to mRNA expression to identify triple-

Table 1 – Molecular classification of human breast cancer.

Classification	IHC status	Other characteristics	Example cell lines
Luminal A	ER^+, $PR^{+/-}$, $HER2^-$	Ki67 low, endocrine responsive, often chemotherapy responsive	MCF-7, T47D, SUM185
Lumina B	ER^+, $PR^{+/-}$, $HER2^+$	Ki67 high, usually endocrine responsive, variable to chemotherapy. HER2+ are trastusumab responsive	BT474, ZR-75
Basal-like	ER^-, PR^-, $HER2^-$	EGFR+ and/or cytokeratin 5/6+, Ki67 high, endocrine nonresponsive, often chemotherapy responsive	MDA-MB-468, SUM190
Claudin-low	ER^-, PR^-, $HER2^-$	Ki67, E-cadherin, claudin-3, claudinin-4 and claudinin-7 low. Intermediate response to chemotherapy	**MDA-MB-231**, BT549, Hs578T, SUM1315
HER2	ER^-, PR^-, $HER2^+$	Ki67 high, trastusumab responsive, chemotherapy responsive	SKBR3, MDA-MB-453

EGFR, epidermal growth factor receptor; ER, oestrogen receptor; HER2, human epidermal growth factor receptor 2; PR, progesterone receptor. Ki67, proliferation marker; $^+$ and $^-$, represents a positive or negative response to a specific receptor respectively. The cell line studied along this work is in blue, bold face case.

negative status through gene set enrichment analysis [34]. This led to a re-classification of TNBC into seven distinct molecular subtypes: BL1, BL2, mesenchymal (M), mesenchymal-stem cell-like (MSL), immunomodulary (IM), luminal androgen receptor/luminal-like (LAR) and unclassified subtype (UNC) (Figure 2, Table 2) [34].

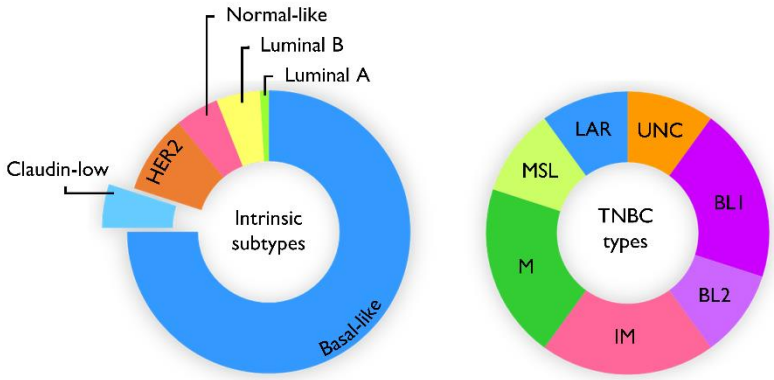

Figure 2 – Breast cancer intrinsic subtypes and TNBC types.

Based on the identification of breast cancer cell lines according to each one of these seven defined subtypes, it was possible to access the primary signaling pathways through which they may be responsive to different therapies.

Immortalised human breast cancer cell lines still remain a powerful experimental tool and information obtained from biological screenings using this *in vitro* model can often be translated into clinical benefit, preceding *ex vivo* and *in vivo* trials. Cell lines are particularly used as an *in vitro* model in cancer research as they have a number of advantages such as being easy to handle and represent an unlimited self-replicating source that can be grown in almost infinite quantities. Moreover, they display a relatively high degree of homogeneity and are easily

Table 2 – Targeting signaling pathways identified in gene set enrichment analysis of TNBC subtypes.

Subtypes	Pathways	Example cell lines
BL1	Cell cycle, DNA damage response	HCC2157, HCC1599, HCC1937, HCC1143, HCC3153, MDA-MB-468, HCC38
BL2	Cell cycle, DNA damage response, growth factor signaling	SUM149PT, CAL-851, HCC70, HCC1806, HDQ-P1
IM	Immune signaling, cytokine signaling, antigen presentation	HCC1187, DU4475
M	Cell motility, ECM receptor interactions, cell differentiation	BT-549, CAL-51, CAL-120
MSL	Cell motility, cell differentiation, growth factor signaling	Hs578T, MDA-MB-157, SUM159PT, MDA-MB-436, **MDA-MB-231**
LAR	Steroid synthesis and metabolism	MDA-MB-453, SUM185PE, CAL-148, MFM-223

BL, basal-like; M, mesenchymal; MSL, mesenchymal-stem cell-like; IM, immunomodulary; LAR, luminal androgen receptor/luminal-like. The cell line studied along this work is in blue, bold face case.

replaced from frozen stocks if lost through contamination. However, cell lines are also susceptible to genotype and phenotype drift during their continual culture, which is a disadvantage. Nevertheless, they will continue to be used, although two-dimensional culture is being gradually combined with three-dimensional (3D) studies (including co-cultures) in order to better represent the cancer microenvironment and understand the molecular basis of breast cancer behaviour [35].

1.1.2.2. Chick Embryo Chorioallantoic Membrane

The chick embryo chorioallantoic membrane (CAM) is an extraembryonic membrane which serves as a gas exchange surface, its function being supported by a dense capillary network [36,37]. As an *in vivo* model, the CAM has been broadly used to study the angiogenesis process and to investigate the efficacy and mechanism of action of proangiogenic and anti-angiogenic molecules, due to its extensive vascularisation and easy accessibility. The chick embryo is also known for the lack of a fully developed immunocompetent system, rendering the CAM a very good host tissue for tumour grafting. In fact, this is a suitable model to study the metastatic potential that characterises human malignancies [38], some of its advantages being: (a) high reproducibility and reliability; (b) easy methodology and cost effectiveness; (c) high embryo survival rate; (d) no need for sterility. The CAM contains extracellular matrix (ECM) proteins such as fibronectin, laminin, collagen type I and integrin $\alpha_v\beta_3$ [39]. These proteins allow some analogy with the physiological cancer cell environment.

Figure 3 depicts the anatomic features of an embryonated chicken egg, the chick embryo development lasting up to 21 days. Histologically, the CAM consists of three layers, the chorionic epithelium, which is the somatic mesoderm attached to the shell membrane, the allantoic epithelium that is the mesoderm facing the allantoic cavity, and the intermediate mesodermal layer, which can be found between the chorionic and allantoic epithelium and is enriched in blood vessels and stromal components [37,38,40,41]. At about 3.5 days of incubation as an evagination from the ventral wall of the endoderm, the allantois of the chick embryo appears. During the fourth day, the allantois pushes out the body of the embryo into the extraembryonic coelom. Its proximal portion is found to be parallel and caudal to the yolk sac. The narrow proximal portion is the allantoic stalk, which is wrapped around the umbilical artery and vein. The distal portion, the allantoic vesicle (full of allantoic fluid), gradually separates from the embryo and is characterised by rapidly enlarging from day 4 to day 10. Fluid accumulation distends the allantois, making the terminal portion look like a balloon in entire embryos [37,40,41]. An extensive morphometric investigation has shown a marked extension of the CAM surface area from 6 cm^2 at day six to 65 cm^2 at day 14 [42]. The CAM blood vessels appear at day 4 as a network of immature, undifferentiated capillaries. Their walls consist of a single layer of endothelial cells with large luminal diameters, scattered in the mesoderm between two epithelium layers [43]. In this process, the mesodermal stratum of the allantois fuses with the adjacent mesodermal layer of the chorion to form the CAM, that displays blood vessels growing rapidly until day 8, giving rise to a capillary plexus [37,38,40,41].

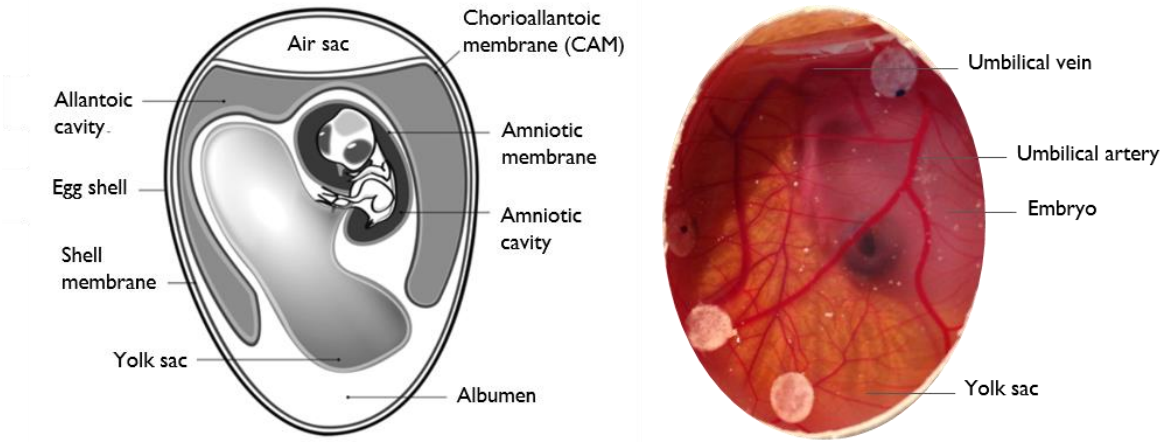

Figure 3 – Anatomical features of an embryonated chicken egg at approximately 11 days of incubation. (Adapted from [44]).

At this stage, the CAM shows small thin-walled capillaries with a small luminal diameter (10-15 lm) beneath the chorionic epithelium and other vessels with a larger diameter (10-115 lm) in the mesodermal layer, with walls containing a layer of mesenchymal cells surrounding the endothelium, completely wrapped by a basal lamina together with the endothelial cells. This capillary plexus is located between the chorionic and allantoic epithelia, and the larger umbilical artery and vein within the allantoic vesicle [45]. The umbilical artery emerges from the embryonic abdominal wall, branches into two primary chorioallantoic arteries and the CAM is drained by a single chorioallantoic vein [46]. The primary chorioallantoic arteries are reported to extend into six or seven generations [46]. The earlier fifth and sixth generations of blood vessels are located parallel to the CAM surface and deep into the vein, which has an alike distribution. The later generations change direction abruptly, passing almost vertically in the two-dimensional capillary plexus.

Capillary proliferation continues rapidly until day 10 and is now near the surface of the chorionic epithelium. The mesodermal vessels become distinct arterioles and venules. In addition to the endothelium, the walls of the arterioles contain one or two layers of mesenchymal cells and the amount of connective tissue surrounding them has increased. Venules are surrounded by an incomplete investment of mesenchymal cells, while the connective tissue has accumulated within their walls. Until day 13 the mesenchymal cells are presumed to be developing smooth muscle cells (SMC) and connective tissue, as the arterial endothelial junctions become more extensive [47]. Capillaries show no changes in the periendothelial space, the veins accumulating less SMC´s and connective tissue than arteries. At this stage, the endothelial cell mitotic index declines rapidly, arteries develop a distinct muscular layer and a more complete basement membrane, and the vascular system attains its final arrangement on day 18, just before hatching [48].

Although characterised as a very simple vascularised structure, the CAM serves multiple functions during embryo development, namely allowing for a respiratory function alongside with the capillary plexus located immediately adjacent to the porous shell [37,49]. In addition to this respiratory interchange (of oxygen and carbon dioxide), the CAM is involved in the calcium transport from the eggshell to the capillary plexus [50,51], the embryo´s acid-base homeostasis [40], and the ion and water reabsorption from the allantoic fluid [52,53]. The

allantois also serves as a reservoir for the waste products excreted by the embryo [37,45]. The CAM model can be used to study not only angiogenesis but also to follow tumour growth [54], cell invasion [55,56] and metastasis [36,38].

1.1.3. Platinum and Palladium Complexes

In order to win the battle against cancer, the discovery of new pathways, targets and antineoplastic agents is crucial. Recently, there has been a renewed interest in a class of "old-fashioned" chemotherapeutic agents, the platinum complexes.

Particularly regarding breast cancer, its most aggressive type, TNBC, has some similarities to tumours originating in BRCA1 mutation carriers. Apart from being negative for ER, PR and HER2, it frequently presents mutations at the tumour suppressor gene p53 level [57]. p53, as well as p63 and p73, form a family of related transcription factors that play an important role in tumour suppression, response to DNA damage and differentiation [58]. For these tumour proteins, a TNBC survival pathway dependent on p63-mediated cisplatin (*cis*-dichlorodiammine platinum(II); *cis*-$Pt(NH_3)_2Cl_2$) sensitivity has been reported [59], as well as a cisplatin-induced p73 phosphorylation and transcriptional activity [60]. More recently, this platinum-drug has been considered a potent inhibitor of p63 expression, capable of p73 activity regulation either directly (through post-translational modification) or indirectly (*via* reduction of p63) [61].

In addition, BRCA1 is known to be involved in DNA double-strand break repair. When in the presence of BRCA-mutated cells, the DNA cross-link strand breaks induced by platinum agents are more difficult to repair due to a deficiency in the homologous recombination repair mechanisms [62] (Figure 4). As previously stated, TNBC tends to have a mutated BRCA1 gene, which justifies the higher sensitivity of this type of tumours to DNA-damaging chemotherapeutic agents (*e.g.* platinum compounds) – triggering intrastrand and/or interstrand DNA cross-links, stalled replication forks and DNA double strand breaks [63].

Since Rosenberg's serendipitous discovery of cisplatin [64-66] and in spite of the high number of studies in this field [66-69], only three platinum-based compounds are currently

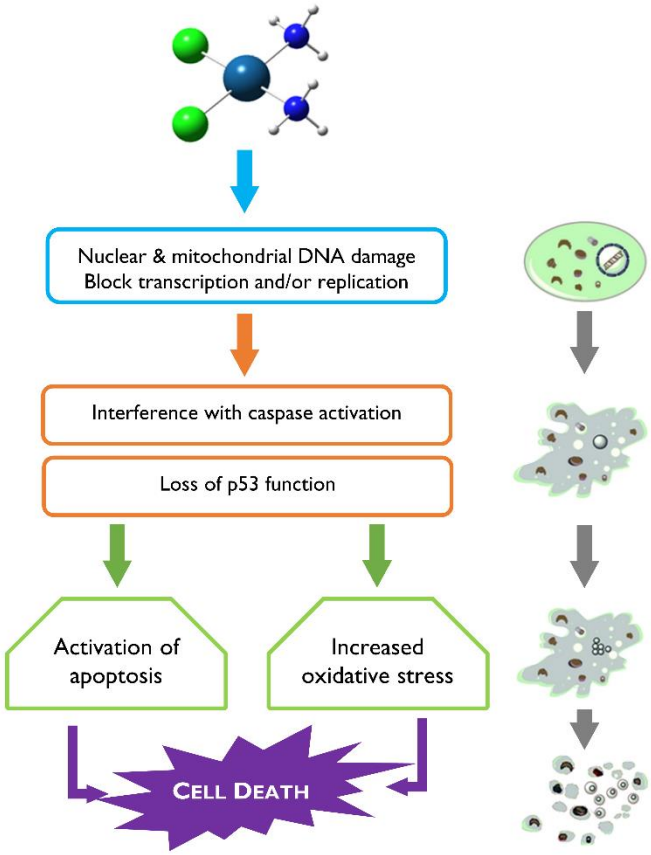

Figure 4 – Main cisplatin induced cellular effects.

approved worldwide as anticancer drugs for clinical use: cisplatin, carboplatin (second-generation) and oxaliplatin (third-generation) (Figure 5). Recent studies have shown that the use of single-agent treatment with cisplatin or carboplatin in TNBC patients as first- or second-line chemotherapy retrieved a 32% and 19% overall response rate (ORR), respectively. BRCA mutation carriers had a better outcome with an ORR of 55%. However, the median progression-free survival (PFS) and OS did not improve much. In turn, as neoadjuvant drugs against TNBC, cisplatin and carboplatin have shown sufficient antineoplastic activity. However,

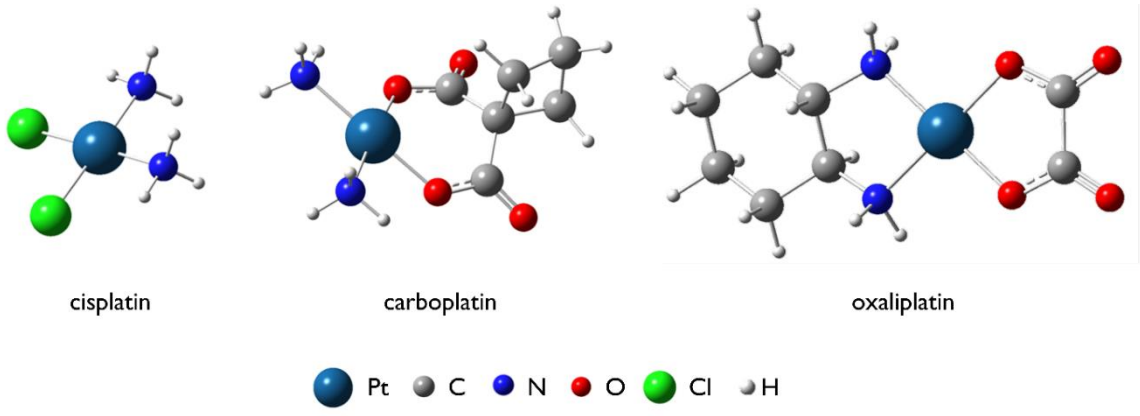

Figure 5 – Structural representation of platinum-based compounds used in the clinic as anticancer drugs.

some clinical trials are underway aiming at determining which platinum agent, treatment schedule and dosage should be used, and whether they are best administered in combination therapies or in sole administration substituting for standard treatments.

Cisplatin´s mechanism of action is schematically displayed in Figure 6, according to the current state of knowledge. Once transported into the low chloride concentration intracellular media, through either passive diffusion or active transport (*e.g.* copper transporter

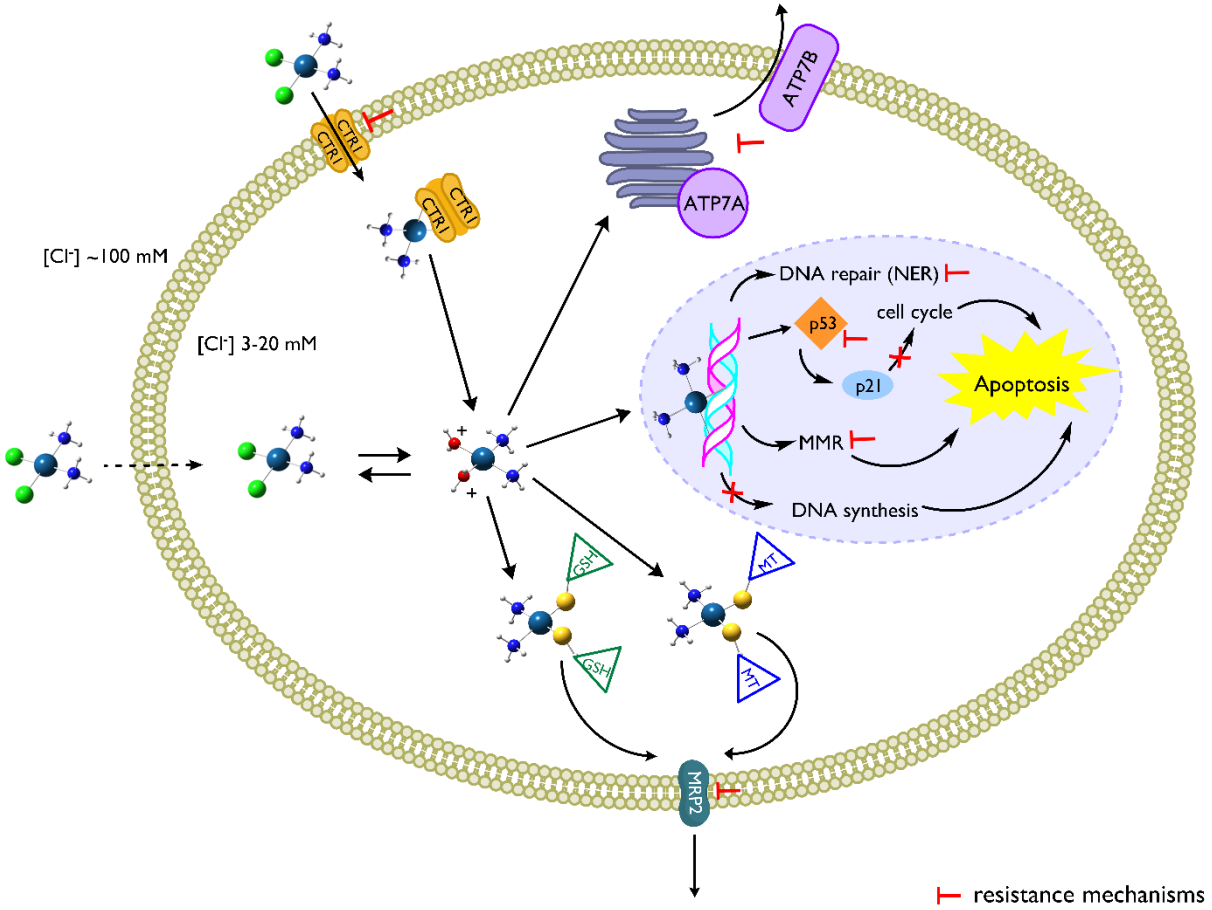

Figure 6 – Schematic representation of cisplatin mechanism of action and resistance to the drug. Cisplatin might enter the cells by passive diffusion or through transporters such as the CTR1. Once in the nucleus, cisplatin covalently binds to the N7 position of purine bases forming mainly intrastrand cross-links leading to severe DNA damage and inducing apoptotic cell death. Downregulation of CTR1 results in less drug entering the cell and, therefore, to drug resistance. The intracellular low chloride concentration is propitious to cisplatin activation, since this is dependent on chloride hydrolysis. In the cytoplasm, the activated aqua species preferentially reacts with sulphur-containing species (*e.g.* cysteine or methionine amino acids) such as glutathione (GSH) or metallothioneins (MT). If GSH and MT levels are high, cisplatin can be inactivated before DNA binding can occur, thereby causing resistance. Finally, active export of cisplatin from the cells may occur through the copper-transporting P-type adenosine triphosphate (ATP7A and ATP7B) or the multidrug resistance-associated protein 2 (MRP2), which also contributes to drug resistance. Drug effects may also be overcome by post-target resistance mechanisms such as the nucleotide excision repair (NER), mismatch repair (MMR) or p53 inactivation.

1, CTR1 [70]), its hydrolysable Cl^- ligands are displaced by water molecules, yielding a positively charged unstable and therefore highly reactive species. The resulting monoaqua $[Pt(NH_3)_2Cl(H_2O)]^+$ and diaqua $[Pt(NH_3)_2(H_2O)_2]^{2+}$ complexes will then bind covalently to nucleophilic sites on DNA, especially to the N-7 atom of purine bases (mainly guanine) [71], forming predominantly intrastrand 1,2- and 1,3-crosslinks and, less frequently, interstrand adducts, which trigger cell cycle arrest and apoptotic death. These platinum-DNA adducts interfere with DNA transcription and replication, which can lead to miscoding and single or double-strand breaks. After this damage is recognised by p53 and other checkpoint regulators (such as mismatch repair (MMR) proteins), cells are directed to apoptosis. As discussed previously, upregulation of p63 and p73-mediated apoptotic pathways may enhance the sensitivity of TNBC cells to Pt-based agents.

However, platinated DNA may undergo repair, rendering the cells resistant to therapy. The mechanisms underlying resistance to Pt-based compounds have been classified into pre-target (interference with cisplatin transport prior to DNA binding), on-target (repair of drug-DNA adducts), post-target (after Pt-DNA adduct formation) and off-target (associated to changes in signalling pathways) [72]. Apart from being administered only intravenously and developing acquired resistance, cisplatin presents severe side effects (*e.g.* nephrotoxicity, hepatotoxicity, myelosupression). Hence, numerous Pt(II) complexes have been synthesised with a view to overcome these drawbacks [73,74]. However, carboplatin and oxaliplatin are the only ones currently approved for clinical use worldwide.

Carboplatin comprises a bidentate dicarboxylate ligand as a leaving group, instead of the more labile cisplatin's chlorides [75] (Figure 5). This renders its kinetics of hydrolysis much slower when compared to cisplatin´s, leading to a significantly lower toxicity arising from parallel reactions with other molecules/receptors apart from the pharmacological target following drug activation (upon hydrolysis). Therefore, while yielding the same type of DNA adducts [76], carboplatin allows more time for the drug to be activated and reach the target [77]. Although being responsible for reduced side-effects (particularly regarding nephrotoxicity, which is negligible), it still retains a limiting myellosupressive activity. Carboplatin was tested in combination with Docetaxel (Taxotere®, DTX, Figure 7) against metastatic TNBC and showed contradictory results concerning the improvement on

pathologic complete response values (absence of residual invasive disease) [78,79]. DTX is an established taxane-type antineoplastic drug, used in the clinic against several types of cancer (namely metastatic breast adenocarcinoma [80], hormone-refractory prostate cancer and lung cancer), but it is generally administered in combination regimes in order to avoid chemoresistance [81]. As opposed to the DNA-damaging metal-based agents, DTX is an anti-mitotic compound (acting *via* an effect on the centrosome of the mitotic spindle).

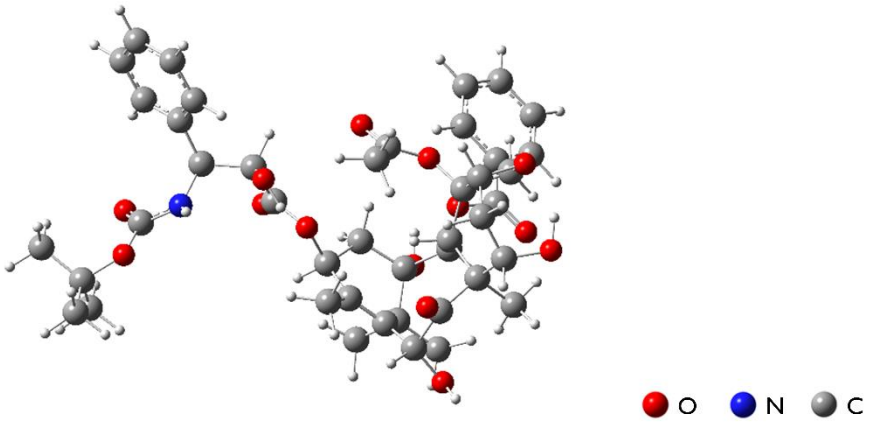

Figure 7 – Structural representation of Docetaxel.

Oxaloplatin, on the other hand, contains an oxalate as the leaving group and a quite bulky bidentate ligand (1,2-diaminocyclohexane, Figure 5) that confers an extra stability [82,83] and partially hinders the formation of adducts with GSH and other sulphur-containing biomolecules (*e.g.* MT), leading to a lower ototoxicity and nephrotoxicity as well as to a higher tolerability profile, especially in older patients [84-86]. Additionally, it was found to have a higher cytotoxicity when compared to cisplatin and carboplatin, as well as a lower acquired resistance, particularly for colorectal cancer (where it is administered in combination regimens, *e.g.* with 5-fluorouracil and folinic acid [87]), but also for gastric [88] and prostate cancers [89]. Nevertheless, it has a high grade of neurotoxicity, which can result in an acute and chronic neuropathy [90,91].

In order to develop new metal-based compounds with a higher efficiency and less side effects, coupled to a lower acquired resistance, particular attention has been paid to polynuclear Pt(II) chelates (comprising 2 or 3 metal centres), namely with linear alkyl polyamine ligands (*e.g.* biogenic polyamines (PAs)), aiming at an increased antitumour activity and a higher selectivity [92]. Biogenic polyamines - putrescine ($H_2N(CH_2)_4NH_2$, Put), spermine

($H_2N(CH_2)_3HN(CH_2)_4NH(CH_3)_3NH_2$, Spm) and spermidine ($H_2N(CH_2)_3NH(CH_2)_4NH_2$, Spd) (Figure 8) - are ubiquitous in almost all living cells and are essential for their normal growth and differentiation [93,94]. They are obtained exogenously, from the diet, and are biosynthesised in the presence of intestinal bacteria [95]. Biogenic PAs are polycations at physiological conditions due to protonation of the corresponding amino groups [96], the positive charge being distributed along the entire aliphatic carbon chain. These molecules are known to interact, both electrostatically and covalently, with DNA, RNA, proteins, phospholipids and nucleotide triphosphates, interfering in their synthesis and normal biological function [97,98]. They are also involved in the repair of the extracellular matrix, in cell adhesion and in certain signalling processes [99].

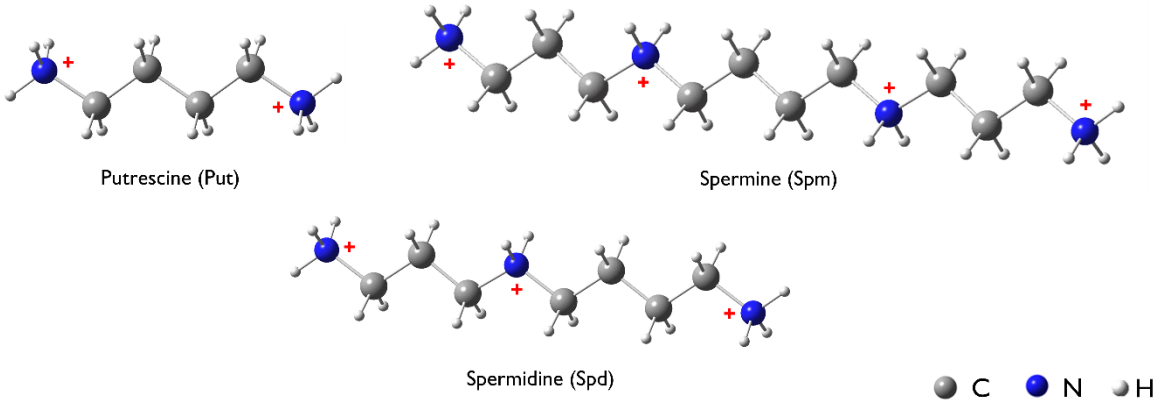

Figure 8 – Representation of the biogenic polyamines (putrescine, spermine and spermidine) under physiological conditions.

Polynuclear Pt-PA complexes were found to display a higher cytotoxicity towards several types of cancers, including TNBC, as compared to the clinically used Pt(II) agents, due to a more severe and less repairable DNA damage upon formation of long-range interstrand adducts with DNA, not available to the conventional mononuclear Pt-drugs [100,101]. However, their mechanism of action is not yet fully understood at the molecular level. Furthermore, their Pd(II) analogues have recently arisen as innovative and promising alternatives to the Pt(II) agents [68,69,92,102,103], particularly towards metastatic breast cancer [104]. Palladium complexes are among the most widely investigated metal-based prospective anticancer agents (fifth after platinum, copper, gold and ruthenium compounds) [105]. Since Pd(II) is a d^8 cation similar to Pt(II), it was expected to yield a comparable antitumour activity. However, this was not found to be the case already for the first Pd(II)

agents tested [106], due to their higher kinetic lability relative to the Pt(II) compounds (*e.g.* faster intracellular hydrolysis) [106]. Actually, palladium complexes were shown to cause a greater DNA distortion than their Pt(II) analogues in several cancer cell lines [104,105,107,108]. In addition, the presence of strongly coordinating polydentate ligands such as polyamines is expected to reduce Pd(II) reactivity as well as to minimise metal displacement by sulphydryl groups from GSH and other cellular thiols (responsible for drug inactivation and deleterious side effects), thus minimising toxicity (*e.g.* nephrotoxicity [109,110]). Furthermore, these complexes have a slightly higher water solubility as compared to the Pt(II) homologues.

Numerous platinum agents have been developed in recent years, aiming at an improved administration (*e.g.* oral pharmacological formulations), transport and targeting. Pt(IV) complexes, with two additional axial ligands, and inert to substitution, are especially stable in the blood circulation due to negligible interaction with plasma proteins. As a result of their high stability, these complexes can be administered orally and they are less prone to react with proteins leading to diminished side effects [111]. In addition, the axial ligands can be tailored to improve the pharmacological properties, namely for targeting the drug to the tumour [112]. Lipoplatin, a cisplatin liposomal formulation currently in phase III clinical trials [113], has a substantially reduced renal toxicity, peripheral neuropathy, ototoxicity, myelotoxicity relative to cisplatin, causing less nausea and asthenia [114,115].

In sum, going from mononuclear metal complexes to polynuclear ones is highly advantageous for achieving an improved antineoplastic activity, since it allows a non-conventional interplay with the main pharmacological target (DNA) yielding bifunctional adducts *via* long-range, interstrand cross-links. Additionally, they may act as multimodal agents [116], impacting on more than one target, since their bioactive ligands can interact with distinct receptors apart from DNA. Finally, distinct drug formulations, such as nano-encapsulation and targeting, have been found to lead to an optimised cytotoxicity coupled to minimal deleterious side-effects.

In the present work, Pt(II) and Pd(II) chelates with the polyamine ligand spermine were synthesised (Figure 9), fully characterised and screened as to their potential anticancer properties. In order to better assign the conformational behaviour of these polynuclear chelates, the Pt(II) compound with the diamine 1,3-diaminopropane ($H_2N(CH_2)_3NH_2$, Dap)

was also synthesised (Figure 9) and analysed by vibrational spectroscopy coupled to theoretical calculations.

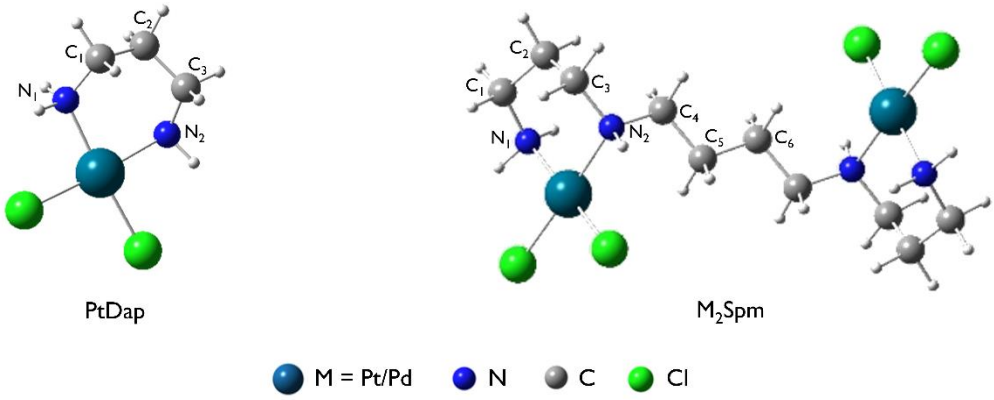

Figure 9 – Structural representation of the polyamine Pt(II) and Pd(II) complexes presently studied.

1.2. The Methods

1.2.1. Optical Vibrational Spectroscopy

Spectroscopy (from the latin word *spectare*, meaning to look or to observe) can be defined as the analysis of the interaction between radiation and matter [117]. One of the most powerful of these techniques is vibrational spectroscopy, which has a key role in chemistry, allowing the determination of molecular structure and conformation. Nowadays it can also be used to accurately identify functional groups and compounds, as well as to assess inter- and intramolecular forces, the degree of association in condensed matter, the strength of chemical bonds and several thermodynamic properties. Furthermore, vibrational spectroscopy had become very important in life sciences, since it is a cutting-edge technique to characterise biomolecules, either alone or within cells and tissues. Coupled to optical microscopy, it allows to probe even heterogeneous biological samples, both *in vitro* and *in vivo* (*in situ*) with an extremely high spatial resolution, having a wide range of applications from drug monitoring to clinical diagnosis.

In order to understand the many uses of vibrational spectroscopy, it is important to know that the vibrational energy of molecules which are spatially confined can only assume certain discrete levels (they are quantified). A molecule can accept or release energy discontinuously. If this exchanged quanta of radiation can be determined, then the separation

between the two energy levels involved in the transition may be found [117]. Radiation is allowed to interact with matter through three distinct processes: absorption, emission or scattering, all of them yielding information about the system´s energetics and structural behaviour. Absorption is the result of photon annihilation, in the process of exciting the atom or molecule to a higher energy excited sate. Emission is the reverse phenomenon, characterised by the release of a photon by a molecule while relaxing from an excited state to a less energetic one. Finally, scattering is a combination between the absorption and emission processes, the incident beam creating a virtual excited state (different from any excited stationary state) that immediately relaxes originating the dispersed radiation [117].

With the aim of describing molecular vibrations, a simple physical model may be used where atomic nuclei are treated as masses separated by a weightless elastic spring (Figure 10). In such a model the electrons are totally disregarded and each vibrational mode has a different energy value (matching the transition between two specific vibrational levels), *i.e.* a distinct wavenumber in the vibrational spectrum. For the simplest case, a diatomic molecule, the model is based in Hooke's law: the two nuclei with mass (m) are separated by a spring characterised by the elastic constant force, k. This system is mathematically represented by a sinusoidal function, since it is defined by a harmonic oscillator (Figure 10). The k value is related with the electronic characteristics of the system, that define the spring restoring force, F, for an Δr shift from its equilibrium position. The Newton's second law for the system is given by:

$$F = ma = \mu \frac{d^2r}{dt^2} = -k\Delta r \qquad (1)$$

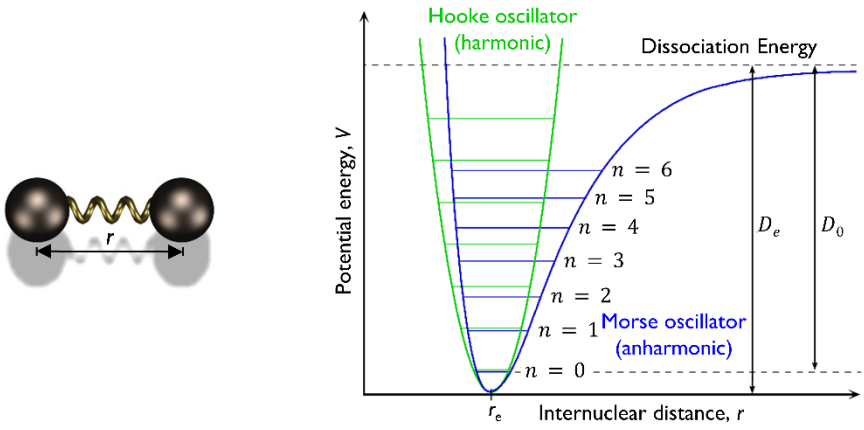

Figure 10 – Potential energy curve and energy levels corresponding to the Hooke model (harmonic oscillator) for a diatomic molecule *vs* the Morse model (anharmonic oscillator). (Adapted from [118])

This second order differential equation has a time dependent solution given by $r(t) = r_{max}\cos(2\pi\nu t)$ and the frequency of vibration is calculated to be:

$$\nu = \frac{1}{2\pi}\sqrt{\frac{k}{\mu}} \tag{2}$$

where μ is the system reduced mass,

$$\mu = \frac{m_1 m_2}{m_1 + m_2} \tag{3}$$

For a diatomic molecule there is only one mode of vibration: the stretching (ν) of the bond. However, for a polyatomic molecule with N atoms the vibrations are described along the corresponding $3N$ coordinates (x, y and z, for each atom). Three of these are needed to define the position of the centre of mass and three more to specify the rotational motion. If the molecule is linear, only two coordinates are required to specify its rotation. Thus, there are $3N - 6$ possible vibrational modes for a non-linear molecule with N atoms and $3N - 5$ if the molecule is linear.

The harmonic oscillator model is a simplistic approximation when applied to a real molecular system, since it does not consider dissociation at long distances or different spacing between vibrational levels. A diatomic molecule is thus better defined by an anharmonic oscillator (Morse model, Figure 10), its vibrational states being defined by,

$$V(r) = D_e[1 - \exp(-\beta\Delta r)]^2 \tag{4}$$

where Δr is the difference between the maximum distance, r, between the two atoms and their equilibrium internuclear distance, r_e. D_e is the dissociation energy of the molecule and β is a constant parameter. The energy for a vibrational level, n, of the oscillator is given by the expression [119]:

$$E_n = h\nu\left(n + \frac{1}{2}\right) - h\nu k_{an}\left(n + \frac{1}{2}\right)^2 \tag{5}$$

In equation (5) the first component is familiar: it refers to the energy levels of the harmonic oscillator, ν, representing the fundamental frequency of the oscillator. The second part reflects the anharmonicity of the oscillator, k_{an} being the anharmonicity constant. When $n = 0$, the potential energy reaches its lowest value, although this is not the energy of the potential minimum. Actually the energy of the $n = 0$ level is always higher than this minimum by ½ $h\upsilon$, and is called zero point vibrational energy (ZPVE). ZPVE is therefore the vibrational energy of

a system in its ground state and is always an intrinsic and constant value, even at the absolute zero [117]. Experimentally, the dissociation energy, D_e, can be measured only relative to the ZPVE level and is symbolised by D_0 (Figure 10).

Anharmonicity leads to combinations between the fundamental modes, yielding non-fundamental transitions with lower intensities than the fundamental ones, at frequencies that are the sum of the wavenumbers corresponding to the two fundamental vibrations involved. Other spectroscopic features liable to be identified under the anharmonic model, but not foreseen by the harmonic theory, are the overtones, due to transitions between more than two consecutive vibrational levels (*e.g.* from $n = 0$ to $n = 2$), leading to low intensity spectral bands centred at approximately a multiple of the frequency corresponding to the fundamental mode. Another possibility is a process called Fermi Resonance (FR), responsible for combinations between fundamental vibrations and either an overtone or a combination mode (of the same symmetry) which have a similar energy. Such a process leads to an intensity enhancement of the overtone and to an intensity decrease of the fundamental mode, originating two signals with similar intensities which are often frequency shifted in opposite directions (the lower frequency band is red-shifted while the higher wavenumber one is blue shifted) [117,119].

The intensity of the bands in a vibrational spectrum is also an important property (apart from the frequency). Since each signal in the spectra corresponds to a transition between vibrational states, its intensity is proportional to the probability of transition from the initial vibrational energy level to the final one (vibrational ground and excited states, respectively). Spectral intensities can be predicted for each vibrational mode and each vibrational spectroscopic technique.

1.2.1.1. Infrared Spectroscopy

In 1800 Sir William Herschel discovered the infrared (IR) light, when measuring the heating effect of the sunlight. However, it was only more than 80 years later (between 1882 and 1900) that Abney and Festing used this radiation to register the IR spectra of 52 compounds [120]. From then on IR spectroscopy was undergone major developments, presently being one of the most widely used vibrational spectroscopy techniques.

The infrared region of the electromagnetic spectrum corresponds to longer wavelengths (lower energies) than the visible range (Figure 11) and is normally divided into near-, mid- and far- infrared (named after their proximity to the visible window): near-infrared between 14000 and 4000 cm^{-1} (containing most of the overtones); mid-infrared from 4000 to 400 cm^{-1} (associated to fundamental vibrations of the system, comprising their fingerprint profile); far-infrared from 400 to 10 cm^{-1}, adjacent to the microwave zone (may also be used for rotational spectroscopy) [117]. The present work is centred on the features comprised in the mid-infrared region.

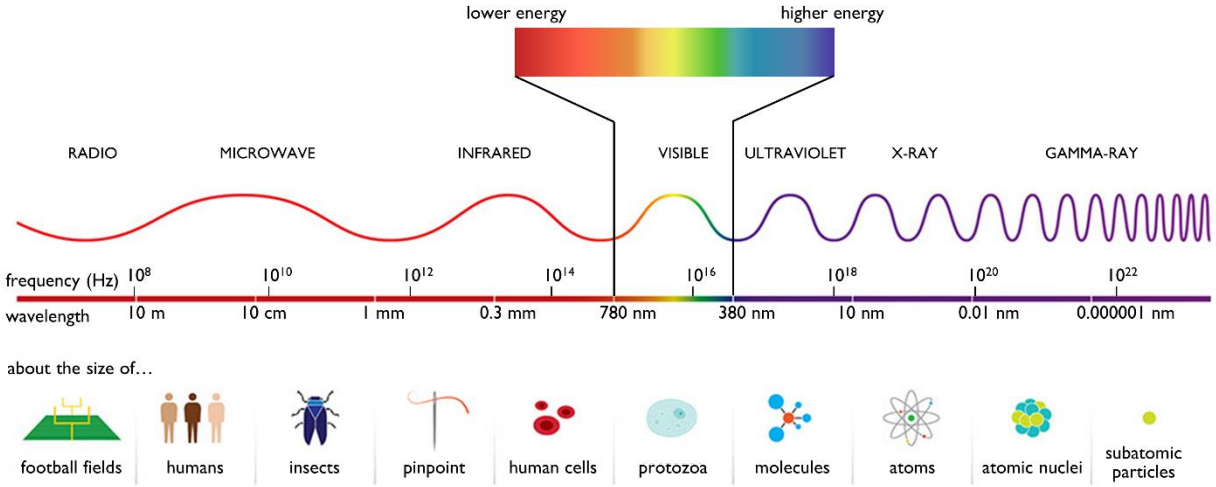

Figure 11 – Schematic representation of the electromagnetic spectrum.

In a conventional infrared experiment, the IR radiation is absorbed whenever the frequency of this incident beam matches the energy gap between adjacent vibrational levels of the sample. It can only interact with a vibrating molecule if the electric vector of the radiation field oscillates with the same frequency as the molecular dipole moment [117]. So, not all molecular vibrations absorb IR radiation being active in infrared. For a molecular vibration to be active it has to be able to modulate the molecular dipole moment, μ. The derivative of this dipole moment along the coordinate of the motion, r, should then be different from zero [118],

$$\left(\frac{\partial \mu}{\partial r}\right)_0 \neq 0 \qquad (6)$$

r describing the motion of the atoms during a normal vibration.

The molecular dipole moment can be described as the sum of all the charges present in a molecule relative to its centre of mass. The distance between each charge, q_i, and the centre

of mass, r_i, may vary with time due to the molecular vibrations. These variations lead to instantaneous changes in the molecular dipole moment, μ,

$$\mu = \sum_i q_i r_i \tag{7}$$

In fact, a sample can only absorb IR radiation when its frequency matches the energy of each fundamental vibrational mode and there is a net change in dipole moment. If, for instance, an atom is symmetrically substituted ($\mu = 0$) the corresponding symmetric stretching mode will not be detected in the IR spectrum. Hence, in general antisymmetric molecules are therefore more active in IR spectroscopy than symmetric ones.

1.2.1.1.1 Fourier Transform Infrared

Fourier-Transform Infrared (FTIR) is the widely used technique nowadays, for which a coherent light source is applied to the sample [121], being guided through an interferometer (Michelson interferometer) before interfering with the sample. This interferometer comprises five basic components: a source, three optical elements and a detector. The registered signal reflects the interference between two different beams from the same source, each one being reflected into a mirror, a fixed and a movable one. The beams´ interference allows the temporal coherence of the light to be measured at each different time delay setting. Both beams are then directed to the same pathway, the resulting final beam going through the sample and finally to the detector. The data thus obtained is called an interferogram [121] and represents the radiation output as a function of time and dependent on mirror position. In order to use this raw data, a Fourier transformation is undertaken. It converts the interferogram (intensity as a function of time) into a spectrum (intensity as a function of energy). This is the most widely used approach in IR experiments nowadays, mainly because all information is collected simultaneously for all frequencies, improving both speed and signal-to-noise (S/N) ratio [117] and ultimately enhancing sensitivity.

As compared to the conventional thermal incandescent bulbs (globar sources), recently developed tunable quantum cascade lasers (QCL) have been shown to constitute an ideal light source for discrete frequency IR microscopy [122-124]. Moreover, due to the huge increase in the possible applications of FTIR, mainly in the life sciences field, the use of synchrotron

radiation (SR) as a photon source has been implemented [125-127], leading to a dramatically improved spatial resolution. The first attempts to couple SR sources to IR acquisition go back to the 1970s [128,129], but only in the early 1980s did this technology become available to researchers at the SR source ring at Daresbury, UK [130]. SR is generated at a synchrotron, which is a circular particle accelerator where both magnetic and electric fields are synchronised with bunches of charged particles travelling in a closed orbit. This type of sources have a highly enhanced brightness relative to the standard bench-top globar ones, since the photon beam (with a very low divergence) is contained within a narrow transverse area.

Regarding detectors, L-alanine doped triglycine sulphate (DLaTGS) or deuterated triglycine sulphate (DTGS) thermal detectors, that already allow high throughput experiments with good resolution, have been progressively replaced by highly sensitive liquid nitrogen (LN_2) cooled elements, namely mercury cadmium telluride (MCT) detectors (in both single-element and multi-element configurations). Hence, the infrared technique came into its own when FTIR spectrometers started to be equipped with this type of detection, that leads to a particularly high sensitivity even for low-flux exciting radiation levels (coupled to a rather constant signal *vs* data-collection speed). Furthermore, it soon became noticeable that FTIR could be used to analyse very small or localised areas of larger (and even heterogeneous) samples when interfaced to an optical microscope. Thus FTIR microspectroscopy was born, allowing to monitor a wide array of systems, from materials [131] to proteins [132], cells [133,134] or tissues [135-137], with extremely high spatial resolution (down to the sub-cellular level), sensitivity and specificity. In addition, the use of focal plane array (FPA) detection is presently the cutting-edge approach for high-throughput IR chemical imaging of biological samples such as tissue microarrays.

These technical improvements currently allow bio-spectroscopists to probe the infrared signatures of individual cells with enhanced spatial resolution and sensitivity, using small apertures (*ca.* 5 μm x 5 μm), whilst maintaining a relatively good S/N ratio [138,139]. Accordingly, landmark studies have been performed, namely: IR imaging to identify small molecules-metabolites in human lung cancer cells [140]; direct observation of a reversible B- to A-DNA conformational transition in live bacterial cells [141]; discrimination between two

grades of human glioma based in blood vessel imaging [142]; identification of green pigments in 15th century paintings [143].

The SR-FTIR experiments within this work were carried out in the Multimode InfraRed Imaging and Microspectroscopy beamline (MIRIAM B22, Figure 12) at the Diamond Light Source (DLS) of the Harwell Science and Innovation Campus, (Science and Technology Facilities Council (STFC), UK [144]).

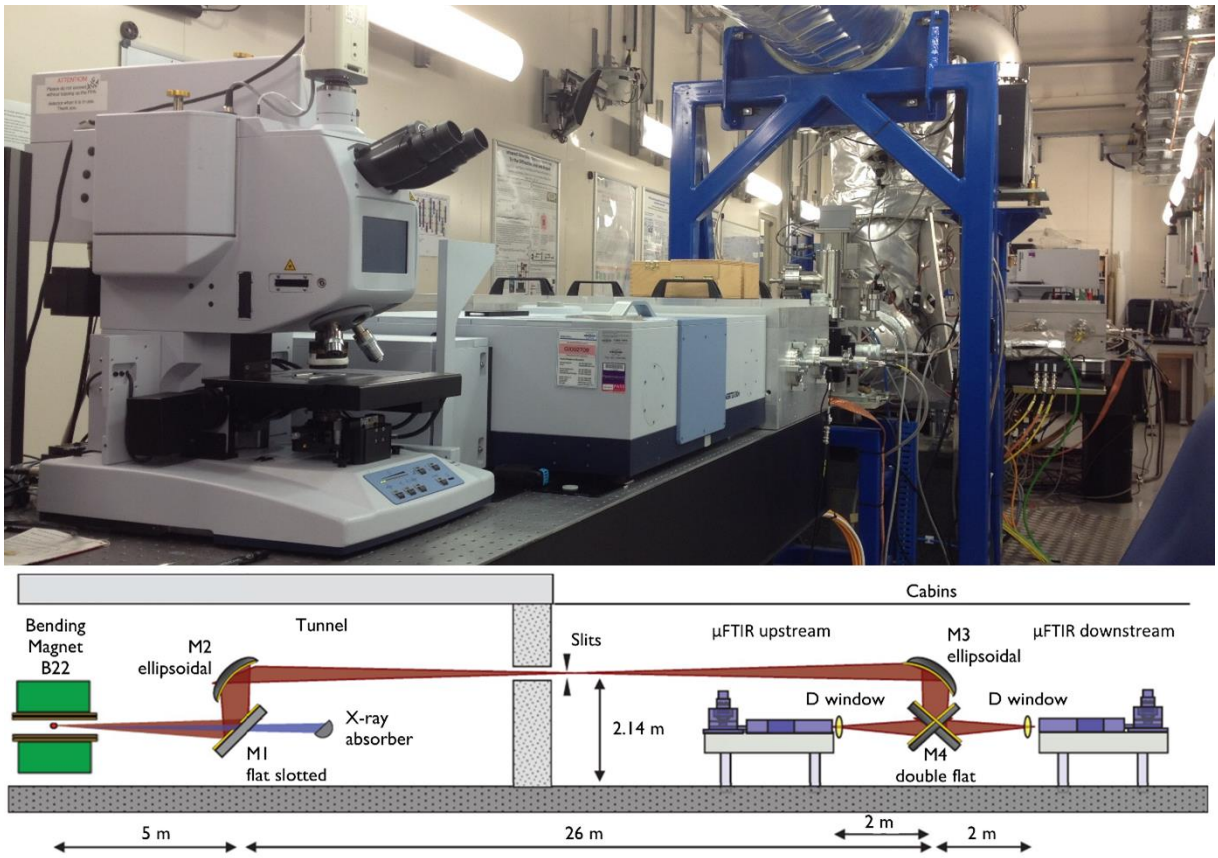

Figure 12 – IR microspectroscopy MIRIAM beamline at the Diamond Light Source and schematic diagram of the spectrometer configuration. The side view (not to scale) shows the front end area and bending magnet source in the synchrotron tunnel (left), together with the cabin area and experimental stations (right). Adapted from [145], with permission from STFC (UK).

1.2.1.2. Raman Spectroscopy

The fascination with the deep blue colour of the Mediterranean Sea was responsible for a landmark discovery in physics and physical-chemistry: the discovery of the inelastic scattering of light by liquids by the Indian physicist Chandrasekhara Venkata Raman – the so-called the Raman effect, first published on the 28th February of 1928 [146,147]. The first excitation source used to obtain a Raman spectrum was simply filtered sunlight. The beam of light entering a

liquid sample emerged with a different colour due to the Raman scattering process, that was found to be dependent on the type of sample. Nevertheless, due to the extremely low intensity of the phenomenon, detection of the bands proved to be quite difficult. In later experiments, Raman substituted the sunlight for a mercury arc lamp, which delivered a more intense and monochromatic (435.83 nm) radiation. The scattered light was then projected through a quartz spectrograph onto a photographic plate (the detector used in those days), which was developed in order to yield the spectrum [148].

By the end of 1928, seventy Raman studies could already be found in the literature and by the late 1930s the Raman spectroscopy technique had become the main method of non-destructive chemical analysis for both organic and inorganic compounds. However, the lack of a light source providing a radiation that was both monochromatic and intense was still the major drawback of the method, that was only overcome by the development of the Light Amplification by Stimulated Emission of Radiation (laser) technology, in the 1960´s.

An incident radiation can be scattered in two different ways upon interaction with a molecule: it can maintain its original frequency (elastic process) – Rayleigh scattering [149]; or it may exchange energy with the sample – Raman scattering. Raman spectroscopy is based on this inelastic scattering of a monochromatic beam of photons and detection of the energy difference due to light scattering by the sample. There are two types of Raman scattering, depending on the direction of the energy exchange between the photon and the molecule [150] (Figure 13): if the final vibrational state is more energetic than the initial one, the emitted photon transfers energy to the sample and is red-shifted relatively to the excitation radiation – Stokes scattering; if the final vibrational state is less energetic than the initial one, the scattered light is blue-shifted relative to the incident beam – anti-Stokes scattering The intensity of the anti-Stokes bands is significantly weaker than the Stokes signals, as a consequence of the Boltzmann distribution within the vibrational states of the sample, the population of the excited states being much lower than that of the ground state low [151]. Hence, the Stokes region is the one usually registered when Raman spectroscopy is used for characterisation/identification purposes.

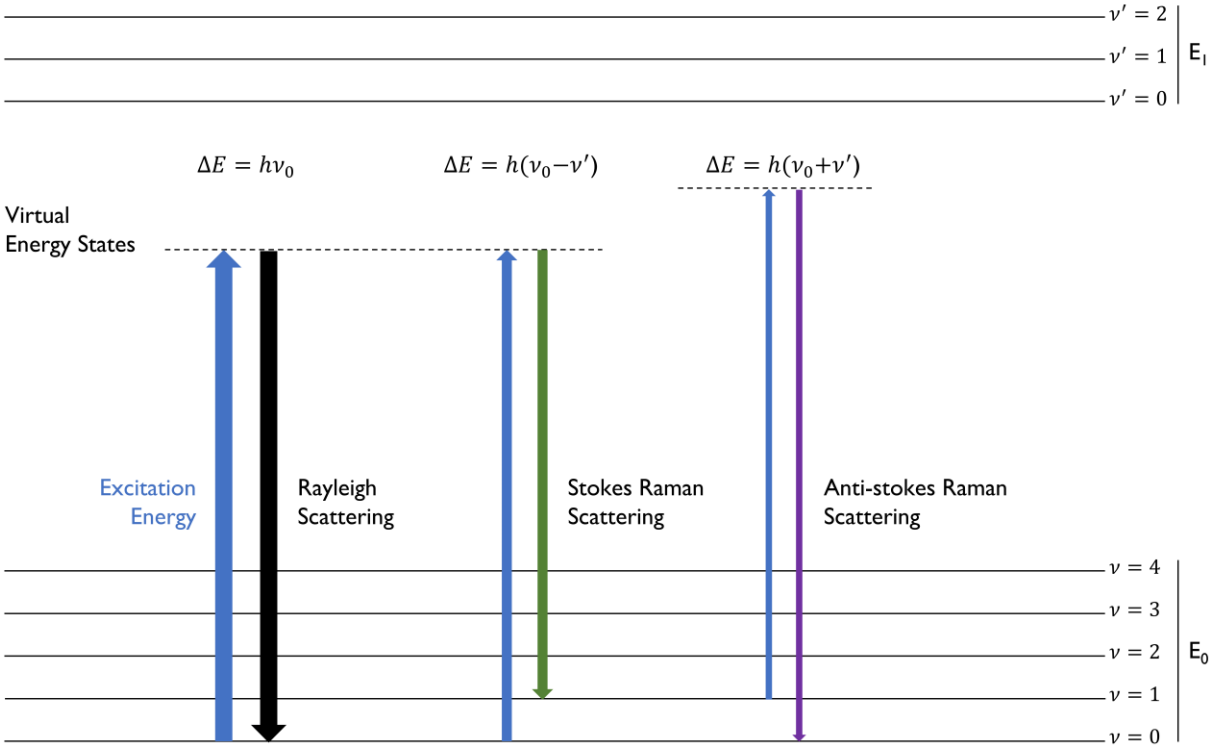

Figure 13 – Schematic representation of the light scattering phenomena. The thickness of the arrows represents the probability of each phenomenon to occur. (Adapted from [152])

While absorption and emission processes involve a single photon, either absorbed or emitted, scattering always involves two photons, the incident one and the emitted. Additionally, while in absorption and emission there are only two states involved, in inelastic light scattering three different energy states should be considered – the initial, the final and a third one, non-stationary, physically non-observable and hence designated as *virtual state*.

In order for a molecular vibration to be active in Raman it must affect the molecular polarisability, α, [117] (*i.e.* induce a deformation of the molecule´s electronic cloud). This perturbation can be represented by the derivative of α, which is related to the displacement coordinate r of the vibrational mode:

$$\left(\frac{\partial \alpha}{\partial r}\right)_0 \neq 0 \tag{8}$$

When this derivative is different from zero, a vibration is Raman active. The classical theory of Raman scattering allows to describe the corresponding selection rules, in order to explain the intensity of the bands in terms of polarisability change: the electric field (due to the incident radiation) imposed on the molecule induces a dipole moment, which is proportional to the

electric field strength and the molecular polarisability. This induced dipole moment, $\vec{\mu}$, is the results of the electric field vector, ***E*****,** multiplied by the polarisability, α:

$$\vec{\mu} = \alpha\vec{E} \quad (9)$$

Soon after its discovery, the Raman effect was recognised as a precious tool for structural elucidation, since it is a universal phenomenon and the basis for a non-destructive and hardly invasive spectroscopic technique, that requires no specific sample preparation. At present, spectral resolutions as small as 0.3 μm x 0.3 μm x 0.5 μm can be achieved by Raman microspectroscopy (combining optical microscopy to the conventional method), allowing it to explore cells (at the subcellular level) [153], tissues [154] and even living organisms (including patients [155]) unveiling biochemically and clinically relevant spectral changes. Furthermore, the lack of limitations due to the presence of water (in biological and clinical samples) renders this spectroscopic technique a most promising tool for biological imaging, both *in vitro* in the laboratory setting and *in vivo*/*in situ* for non-invasive, accurate and rapid clinic diagnosis (*e.g.* cancer [155]).

Therefore, Raman spectroscopy is one of the most widely used and versatile spectroscopic techniques, with an impressive range of applications from industry to arqueometry and biosciences. Regarding the latter, some impacting accomplishments have been achieved, such as the quick and reliable identification of bacteria (and bacteria strains) in a wide range of samples [156] as well as in hospital environments [157,158], and the single cells imaging unveiling the subcellular localisation of drugs and their interaction with biomolecules [159-164]. In addition, Raman spectroscopy is being more and more applied to medical diagnosis, as an additional tool, apart from the conventional histopathological analysis. It ensures a rapid and extremely accurate discrimination between healthy and diseased tissue, and a precise cancer staging, as well as a very reliable *in situ* identification of surgical margins during surgical tumour removal [154,165-167]. More recently, Raman fibre optic probes have been developed in order to make it possible to carry out non-invasive optical biopsies [155,168] (as opposed to the regular surgical biopsies) leading to the *in loco* identification and characterisation of pathological cells and tissues (*e.g.* early oesophageal cancer detection [169]).

1.2.2. Spectroscopy with Neutrons

In the 1910's-1920's it was believed that the atom was constituted by positively charged particles, the protons discovered by Sir Rutherford [170], and negatively charged particles, the electrons identified by Thomson [171] spinning around as it was idealised by Bohr [172-174]. Nevertheless, there were some clues that led scientists to think that there should be something more within an atom. For instance, something should prevent the protons to repel from each other (having the same charge). Another important clue was that the mass of the helium atom, which should be twice that of hydrogen, was in fact about four times higher. It soon became clear that there was something else in the nucleus that had a mass and the ability to stabilise the protons. It was only in 1932, however, that Sir James Chadwick discovered a new subatomic particle with mass but no charge, the neutron, for which he was awarded the Nobel Prize in Physics (in 1935). He performed an experiment that would radically change the picture of the atom and urge milestone discoveries in atomic physics. He showed that when beryllium atoms were hit with α-particles (helium nuclei), rays were released from the atoms of beryllium (Figure 14). The composition of these rays was still not clear, but they were known to comprise noncharged particles (as previously speculated). In order to understand what this new entity was, Chadwick performed another experiment during which a proton-rich surface (paraffin wax) was irradiated with an α beam, which caused a discharge of some of the sample´s protons that were then detected by a Geiger counter (Figure 14). The new particle thus discovered was called neutron:

$$^{9}_{4}Be + ^{4}_{2}He \rightarrow ^{12}_{6}C + ^{1}_{0}n \qquad (10)$$

The neutron is thus a subatomic particle with no net electric charge and a mass slightly larger than that of the proton. While neutrons are stable inside the atomic nuclei, they are unstable when they become free and undergo beta decay (yielding a proton, an electron and an antineutrino) with a lifetime of 881.5±1.5 s [175].

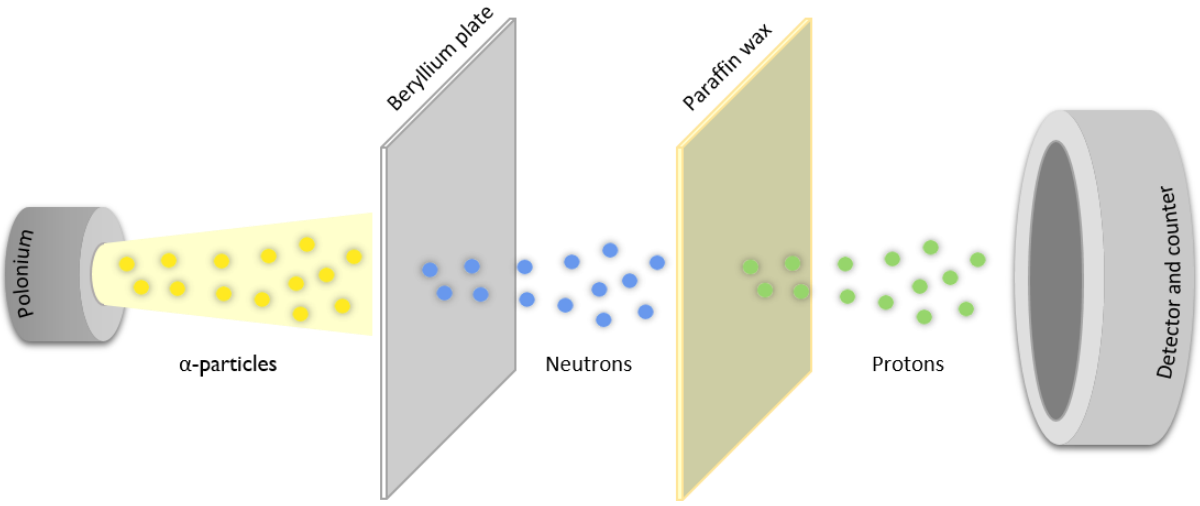

Figure 14 – Schematic representation of Sir James Chadwick´s experiment, that led to the discovery of neutrons.

In the 1970´s, Colella and co-workers performed a series of experiments that enabled to conclude that neutrons have properties of both a particle and a wave [176]. This duality was soon recognised to allow their use in a wide range of studies, coupled to the fact that neutrons are ideal "bullets" for bombarding other nuclei. Unlike charged particles, they are not repelled by similarly-charged bodies and have a high penetration power when traveling through a sample.

Nowadays, neutrons are used in a wide range of techniques, from diffraction to spectroscopy, and can be generated through fission processes in nuclear reactors (continuous sources) or by accelerator-based pulsed sources, either *via* photofission or spallation. Although nuclear reactors have been employed in research to produce neutrons since the 1950´s, neutron beams from spallation sources were only available twenty years later [278]. The number of neutron facilities has increased in the last decade, the ISIS spallation source of the Rutherford Appleton Laboratory, at the Harwell Science and Innovation Campus (United Kingdom) [177] being still the leading pulsed neutron and muon source with the brightest neutron beam worldwide (800 MeV with a current of *ca.* 200 *m*A).

Neutrons are scattered by nuclei while photons and electrons, are scattered by the atomic electron cloud. Figure 15 depicts a typical neutron scattering experiment, where the monochromatic beam of neutrons is scattered after striking a sample, through a θ angle (defined with respect to the unscattered beam), into a detector of area dA at a x distance from the sample position. The scattering process takes place in an elementary cone of solid

angle $d\Omega$. Measurement of the scattered neutrons allows the determination of the neutron scattering cross-section of an element, σ_{tot}, defined by,

$$\sigma_{tot} = \frac{num_{tot}}{I_0} \tag{11}$$

where num_{tot} stands for the total number of neutrons scattered *per* second in all directions, and I_0 represents the incident neutron flux. Hydrogen atoms have a particularly high scattering cross section (about 80 barns), much larger than for most other elements (at most *ca.* 5 barns) and similar to that of the incident neutrons, which ensures an efficient momentum transfer upon interaction with the incident neutron beam.

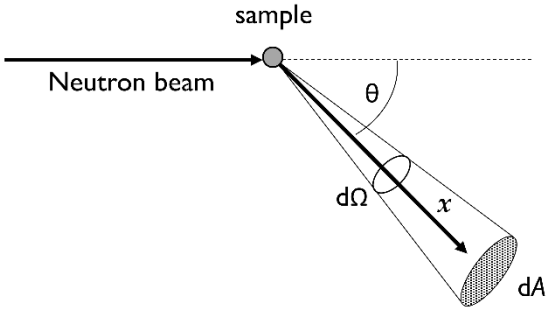

Figure 15 – Schematic representation of a simple neutron scattering measurement. (Adapted from [178])

Neutron scattering spectroscopy encompass inelastic as well as quasielastic processes. In the latter, the spectrum appears as a broadening of the elastic line (at zero energy) rather than a discrete set of peaks associated with inelastic scattering (Figure 16). The elastic component is due to scattering from atoms that move too slowly to be resolved (within the resolution limit of the instrument). The inelastic peaks arise from scattering from atoms that vibrate in a periodic manner and with a fixed frequency. The inelastically scattered neutrons can either loose or gain energy (respectively Stokes or anti-Stokes scattering).

A neutron scattering experiment measures, for each amount of energy transferred, the number of neutrons scattered. These experience both an energy and a momentum transfer, according to,

$$\hbar\omega = \left(E_i - E_j\right) = \frac{\hbar}{2m}\left(k_i^2 - k_j^2\right) \tag{12}$$

$$Q = k_i - k_j \tag{13}$$

E and ω stand for the energy and frequency, respectively; k_i and k_j are the neutron momentum corresponding to the initial and final energy states i and j, respectively.

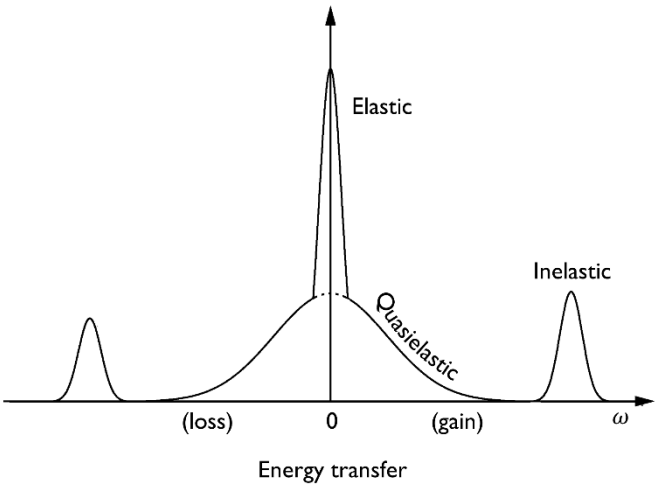

Figure 16 – Schematic representation of a neutron scattering experiment, containing elastic, inelastic, and quasielastic components. The inelastic scattering has contributions from Stokes (neutron energy loss) and anti-Stokes (neutron energy gain) processes, respectively. (Adapted from [179])

The representation of this process as a function of Q (the neutron momentum transfer vector) and ω, $(S(Q,\omega))$, depicts the scattered neutron intensity as a function of the energy transfer between the incident neutron and the scattering nucleus,

$$S(Q,\omega)_l = \frac{4\pi}{\sigma_l}.\frac{k_i}{k_j}\left(\frac{d^2\sigma}{dE_j d\Omega}\right)_l \tag{14}$$

$$d\Omega = \frac{da}{X^2} \tag{15}$$

where da is the detector area. Equation (14) is the scattering law that describes the atom scattering, l, for which σ_l is its atomic cross-section, k_i/k_f the ratio between the initial and the final neutron momentum, and $(d^2\sigma/dE_j d\Omega)_l$ the double differential cross-section [178,180]. The strength of the sample's response is a function of energy, E, and of the solid angle $d\Omega$. The cross-section σ is the total number of neutrons with energy E scattered into the angle $d\Omega$, divided by the incident neutron flux [178].

In most neutron spectroscopic techniques, experimental data is reduced to the scattering law as this allows it to be straightforwardly related to the common model of molecular vibrations. Additionally, this law can be directly associated to the observed neutron scattering intensities.

Biological samples can be thought of as "multi-scale" materials, because their relevant dynamics take place over extended lengths and time scales [181]. With a view to address this multi-scale behaviour experimentally, different techniques must be applied. Figure 17 shows the length and time scales accessible by distinct methodologies, some of them used in the present work. The relevant length scale for neutron scattering goes from < 1Å to more than 100 nm, with a time scale from the picoseconds to almost one microsecond. While inelastic neutron scattering (INS) yields molecular structure information, quasielastic neutron scattering (QENS) leads to molecular dynamic information.

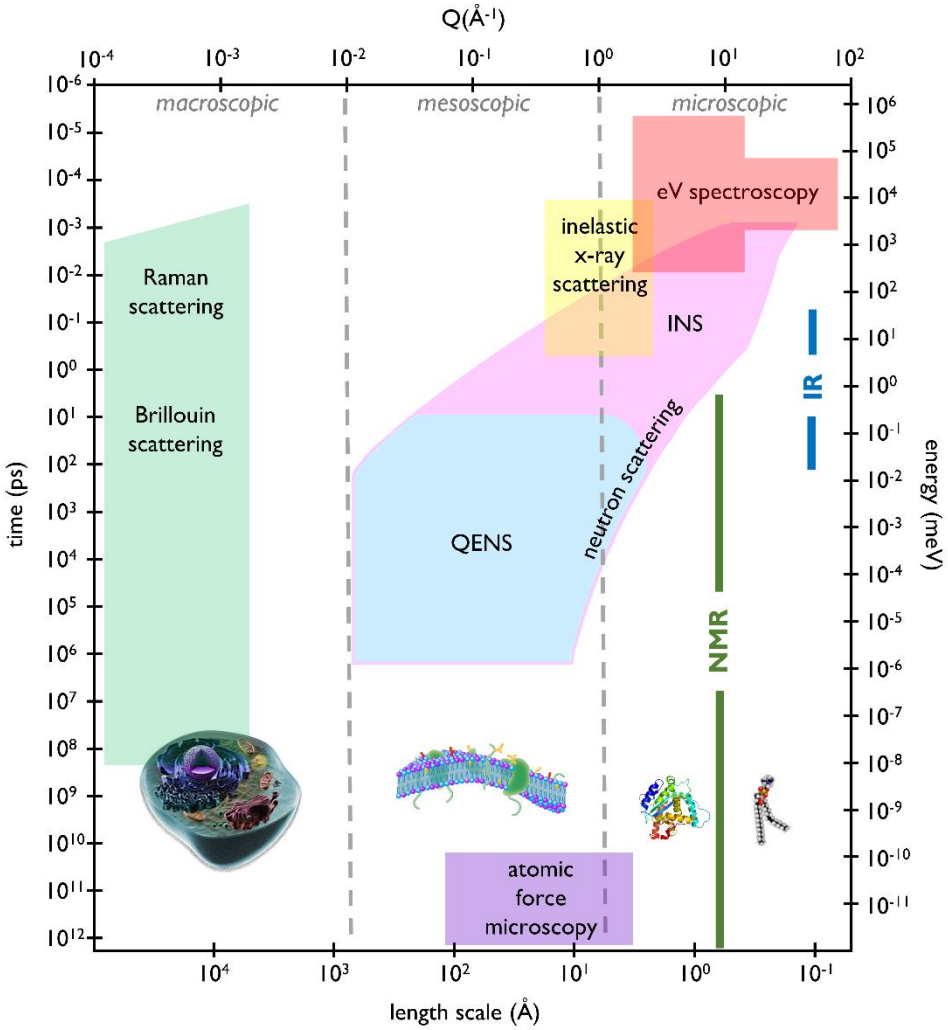

Figure 17 – Schematic representation of length and time scale, as well as energy and momentum transfer, for some spectroscopic techniques encompassing microscopic to macroscopic samples.

In this work, neutron scattering was used to tackle water within a biological matrix – human cancer cells. The cell interior may be pictured as a gel-like structure, in which intracellular water is mostly confined and interacting with surfaces and biomolecules –

interfacial water – thus displaying properties that are significantly different to those of pure (extracellular) water.

Nuclear magnetic resonance (NMR) has long been applied to investigate the intracellular hydrodynamics as a response to either external agents or abnormal physiological conditions [182-190], as well as nonlinear optical spectroscopy techniques [191-193]. However, the NMR spatial and time scales (typically a few milliseconds) limits the results to average properties, and does not allow to discriminate the different dynamical contributions. Up to this date, a microscopic picture of cellular water has only been achieved by neutron scattering techniques that have the ability to "see" proton positions, probing the space domain down to a few Angstroms at the picosecond time scale, thus yielding results not obtainable by other methods. So far, these techniques have been applied to biological systems such as proteins [194-197], enzymes [198], DNA [199,200], Artemia shrimp cysts [201], yeast cells [202], human red blood cells [189,203], extreme halophiles [189,204], *Escherichia coli* bacterium [189,205] or stratum corneum [206]. In addition, molecular dynamics simulations of water-biomolecules interactions have been performed [207-209] in order to assist interpretation of the experimental data gathered for these complex biological systems (which is directly comparable to the theoretical results). Nevertheless, the major emphasis of these studies has been on the biomolecules rather than the water properties.

Apart from water, all biomolecules present within a cell are suitable to analysis by neutron spectroscopy. Although optical vibrational spectroscopy techniques may yield much information on this kind of systems, only the combination with neutron spectroscopy will allow to probe the whole set of vibrations of interest (including the acoustic modes), with high sensitivity to both the intra- and intermolecular modes within the cellular aqueous matrix.

1.2.2.1. Inelastic Neutron Scattering

Incoherent INS vibrational spectroscopy is a particularly appropriate technique to tackle biological molecules, since it is optimal for studying materials containing hydrogen atoms, due to their high scattering cross section. The neutron scattering cross-section of an element (σ) is a characteristic of each isotope, independent of the chemical environment, and determines the effectiveness of the energy transfer during the scattering event, which is directly related

to the band intensities. Thus, the vibrational modes with the largest hydrogen displacements will dominate the INS spectrum. Therefore, INS will be particularly informative for samples with a high hydrogen content, and/or displaying hydrogen close contacts. These are particularly well probed by this technique, especially in the low frequency range,

The INS intensity of each vibrational transition is normally expressed in terms of the so-called dynamic structure factor $S_i^*(Q, \nu_k)$, which obeys to the simplified expression, for a given atom,

$$S_i^*(Q, \nu_k) = \frac{(Q^2 u_i^2)\sigma}{3} exp\left(-\frac{Q^2 \alpha_i^2}{3}\right) \quad (16)$$

where Q (Å^{-1}) is the momentum transferred to the sample at a given scattering angle, ν_k is the energy of a vibrational mode, $u_i(\text{Å})$ is the displacement vector of atom *i* in mode *k*, σ is the neutron scattering cross section of the atom, and $\alpha_i(\text{Å})$ is related to a mass-weighted sum of the displacements of the atom in all the vibrational modes. The exponential term, $(exp[(-Q^2\alpha_i^2)/3])$ is the Debye-Waller factor, that describes the attenuation of the neutron scattering process due to thermal motion. The harmonic frequencies (energies) of the vibrational modes correspond to eigenvalues, and the displacements to eigenvectors, of the dynamical matrix, and can be calculated by theoretical methods.

As opposed to the optical vibrational techniques, inelastic neutron scattering spectroscopy is not limited by selection rules and all vibrational modes are active, their intensity depending solely on the atoms involved. This renders INS even more useful, since it allows to detect modes unavailable to Raman or IR.

The INS experiments performed in the present work were carried out in the TOSCA spectrometer (Figure 18) [210], one of the instruments available at the ISIS Facility of the Rutherford Appleton Laboratory, at the Harwell Science and Innovation Campus (United Kingdom).

1.2.2.2. Quasielastic Neutron Scattering

High-resolution QENS, in turn, analyses the incoherent (hydrogen-dominated) scattering signal within a meV energy transfer range, on a nanometre length scale (*ca.* 0.1-3 nm,

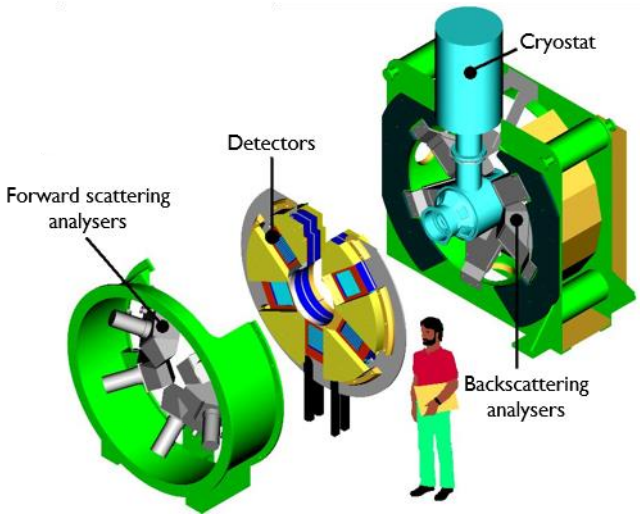

Figure 18 – Schematic view of the TOSCA spectrometer (at the ISIS Facility (UK)). (Adapted from [210], with permission from STFC (UK)).

corresponding to inter- and intramolecular distances) and a nano- to picosecond time scale (*ca.* 10^{-9} – 10^{-13} s). Hence, QENS is a method of choice for directly accessing different spatially resolved dynamical processes, from fast localised modes including vibrations and rotations to slower global translational motions. It is particularly suited for hydrogen-containing molecules, allowing to accurately probe water dynamics under different conditions in multi-component systems such as biological samples, thus helping to determine a relationship between dynamics and function [194,211,212].

The QENS signal is detected as a broadening around the elastic line and is due to a variety of motions (which fall in the spectrometer's time window). In a neutron scattering experiment, information on the molecular dynamics is obtained by measuring the dynamic structure factor, $S(Q,\omega)$, which represents the probability of an incident neutron to undergo a scattering event by transferring a momentum Q and an energy ω. The corresponding experimental scattering function can be represented by,

$$S_{measured}(Q,\omega)=\exp\left(-\frac{\hbar\omega}{2kT}\right)R(Q,\omega)\otimes S(Q,\omega) \quad (17)$$

where $exp(-\hbar\omega/2kT)$ is a detailed balance factor, and $R(Q,\omega)$ is a resolution function (experimentally obtained) which is convoluted with the scattering model ($S(Q,\omega)$) that describes the dynamical behaviour of the sample (accounting for all the dynamical components of the system). In an hydrogenous sample, $S(Q,\omega)$ is dominated by incoherent scattering, as the incoherent scattering cross section of an H atom is much greater than the coherent or

incoherent scattering cross section of any other atom. $S_{inc}(Q,\omega)$ corresponds to the self-correlation function (incoherent dynamic structure factor) and is approximated as the convolution of vibrational, rotational and translational components, which are assumed as independent motions:

$$S_{inc}(Q,\omega)=S_{vib}(Q,\omega)\otimes S_{rot}(Q,\omega)\otimes S_{trans}(Q,\omega) \quad (18)$$

Strictly in the elastic and quasielastic regions,

$$S_{inc}(Q,\omega) = exp(-Q^2\langle u^2\rangle)\left[A_0(Q)\delta(\omega) + \left(1 - A_0(Q)\right)L(Q,\omega)\right] \quad (19)$$

where the exponential term is the Debye-Waller factor, $A_0(Q)\delta(\omega)$ represents the elastic contribution due to motions slower than the longest observable time as defined by the energy resolution of the spectrometer, and the second term in the equation corresponds to the quasielastic component(s).

$S_{inc}(Q,\omega)$ directly provides time/space information on the system investigated: on the time scale of the dynamical processes (through the neutron energy transfer, ω), and on the spatial extent of these processes (from the momentum scattering transfer, Q). Since the QENS data in the time-domain is represented by an exponential, it can be approximated in the energy domain by Lorentzian functions of different widths, Γ (full width at half-maximum, $FWHM = 2 \times HWHM$ (half-width at half-maximum)), describing motions on different time scales:

$$L(x) = \frac{1}{\pi}\frac{\Gamma}{\Gamma^2 + \omega^2} \quad (20)$$

The behaviour of each Γ value with Q may subsequently be analysed to yield detailed information on each dynamical component contributing to the overall experimental QENS profile.

The QENS experiments along this work were performed in the OSIRIS instrument [213] at the ISIS Facility of the Rutherford Appleton Laboratory, at the Harwell Science and Innovation Campus (United Kingdom). This is a spectrometer that is optimised for studies at very low energy and long wavelength diffraction, and can be used as either a high-resolution, long-wavelength diffractometer or for high-resolution quasielastic neutron scattering spectroscopy (Figure 19) [213], which was the case in the present study. In this high-flux time-of-flight inverted geometry instrument neutrons scattered by the sample are energy analysed

by means of Bragg scattering from a large-area pyrolytic graphite crystal-analyser array. The analyser is associated with 42-element ^{3}He detectors.

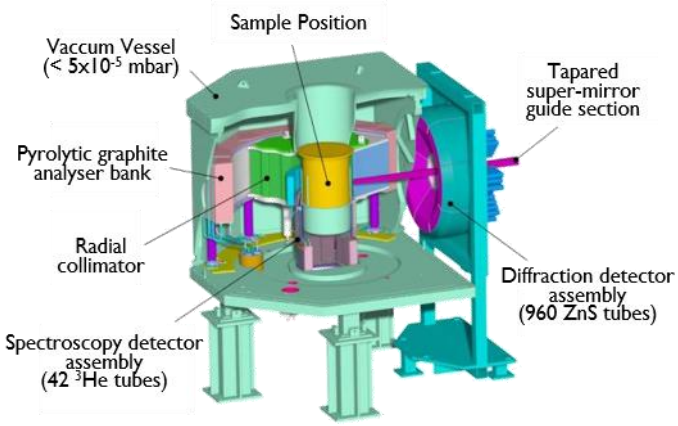

Figure 19 – Schematic view of the OSIRIS spectrometer (at the ISIS Facility (UK)). (Adapted from [213], with permission from STFC (UK)).

The IR, Raman, INS and QENS vibrational techniques used along this work are totally complementary and its combination is ideal to fully characterise the structural/conformational behaviour of the metal complexes under study and to elucidate their mechanism of action, through their impact on cellular components.

1.2.3. Biological Assays

1.2.3.1. Anti-proliferative activity

The Suforhodamine B (SRB, Figure 20) colorimetric assay has been used throughout this work to evaluate cell integrity and density. The SRB test was first described by Skehan, in 1990 [214], and remains one of the most widely used method for *in vitro* screening of cell proliferation. The SRB assay proved to be adequate for the systems under study [215-217], as the dye binding mechanism is independent of any metabolic processes - it is based on the capacity of SRB to bind to basic amino-acid residues of the proteins within the cells, which were fixed under mild acid conditions and can be dissociated by weak bases before optical reading of the coloured product at 540 nm.

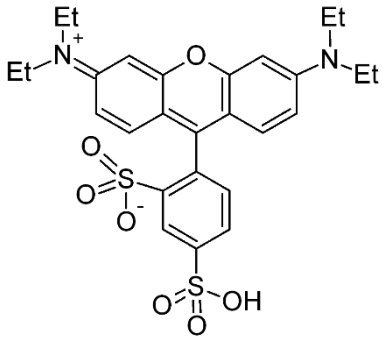

Figure 20 – Chemical structure of the Suforhodamine B dye.

This is a standard method to evaluate the growth-inhibiting effect of a tested agent, since the amount of SRB extracted from stained cells is directly proportional to the cell mass. The IC_{50} - the drug concentration inducing a 50% cell reduction - is a quantitative measure of this anti-proliferative ability. However, it is not possible to determine if proliferation reduction is due to cell death (cytotoxic effect) or to cell cycle arrest (cytostatic effect).

1.2.3.2. Anti-angiogenic capacity

Angiogenesis is a multistep physiological process that leads to the generation of new blood vessels from pre-existing vasculature. In order for cancer to be able to spread to adjacent or distant organs relative to the primary tumour, with consequent metastasis formation, cells have to penetrate blood vessels, circulate through the intravascular stream, and then proliferate at a new site forming secondary tumours [218]. As it was previously stated this metastatic spread of cancer needs a nutrients supply, oxygen and immune cells which can be attain through angiogenesis [219]. Therefore, the angiogenic process is stimulated when tumour tissues require a more adequate blood supply, and it is regulated by both activator and inhibitor molecules. More than a dozen different proteins have been identified as angiogenic activators, including the VEGF [220] that plays an important part in the growth and spread of tumours (Figure 21) as it is a powerful angiogenic agent, in both neoplastic tissues as well as in normal tissues [221]. When present, VEGF can bind to the vascular endothelial growth factor receptors (VEGFR) found in the blood vascular endothelial cells, with its consequent activation that will induce tumour growth and metastasis [222]. This growth factor is found in about half of the human cancers investigated so far [223]. A significant

correlation between VEGF expression and prognosis has been described, namely regarding breast cancer [224-228].

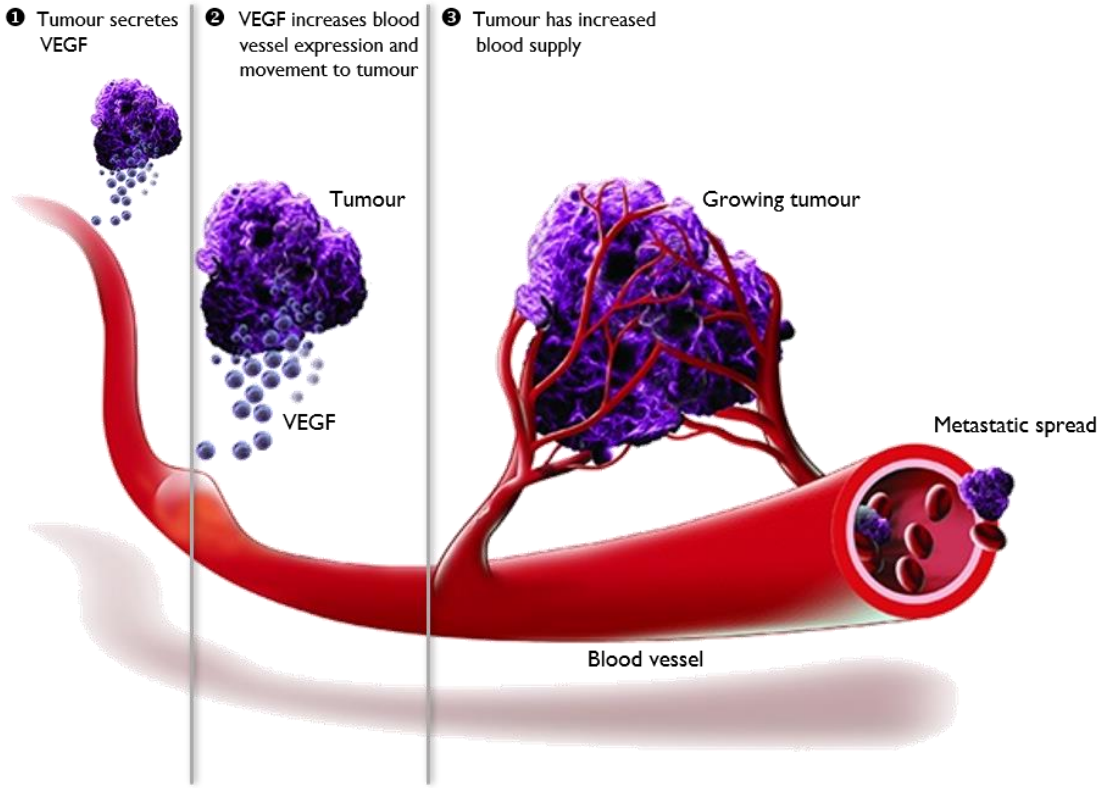

Figure 21 – Angiogenesis process in the presence of VEGF secreted by a tumour. Adapted from [229].

In the present study, the CAM assay was used to evaluate angiogenesis in the presence of the tested compounds.

1.2.3.3. Anti-invasive ability

Cells, particularly cancer cells, have the ability to migrate and invade tissues and organs that can be quite distant from the original tumour. The transwell migration assay provides an *in vitro* system to assess this invasive capability.

This method is suited for numerous applications including: (1) assessment of the metastatic potential of tumour cells [230]; (2) inhibition of metastasis by antineoplastic drugs [231]; (3) altered expression of cell surface proteins [232], or matrix metalloproteinases in metastatic cells [233]; (4) invasion of normal cells such as fibroblasts [234]. It is based on two medium-containing cavities separated by a microporous membrane coated with a BD Matrigel™ matrix, which is used as an *in vitro* reconstituted basement membrane (Figure 22) [235,236]. It blocks the pores of the membrane and prevents non-invasive cells from migrating

through it (Figure 22). However, invasive cells (both malignant and non-malignant) are able to cross the membrane pores, due to their ability to secrete proteases that enzymatically degrade the Matrigel.

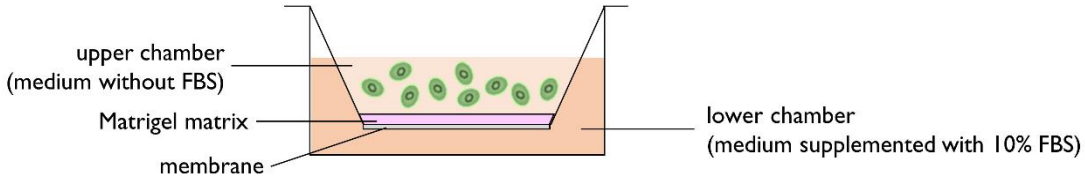

Figure 22 – Schematic representation of an invasion assay insert.

This assay was currently used to evaluate cells´ migration in the presence of the tested prospective anticancer agents. The different fetal bovine serum (FBS) gradient used between the upper (apical) chamber, containing FBS-free medium, and the lower (basolateral) chamber (medium supplemented with 10% FBS) acts as a chemoattractant for the invasive cells located in the apical chamber, which are allowed to migrate vertically through the membrane to the lower compartment (Figure 22) [235,236].

1.3. Aim of the work

Following previous biological studies carried out at the Molecular Physical Chemistry R&D Unit (QFM-UC) regarding the effect of Pt(II) and Pd(II) spermine complexes on the growth and viability of several types of human cancer cells [102-104,237-243], including the hormone-unresponsive breast carcinoma currently investigated, a cellular response at the biochemical level is presently sought. This multidisciplinary approach aims to link biological response to changes in cellular biochemistry and water dynamics, thus identifying spectral markers of drug activity and its impact on intracellular water. This will pave the way for a thorough understanding of the drugs´ mechanism of action at the molecular level, hopefully contributing to the development of improved chemotherapeutic agents and helping to predict their efficacy under specific conditions.

This is an innovative study, that applied cutting-edge spectroscopic techniques to the investigation of new anticancer drugs, and a pioneer one since, to the best of the author´s knowledge, it is the first of its kind.

2 Experimental

2.1. Reagents and Material

Table 3 – List of reagents, material, equipment and software used along this work.

Reagents	
Acetic acid glacial (99.7%)	Sigma-Aldrich S.A., Sintra, Portugal
Acetone (≥ 95%)	Sigma-Aldrich S.A., Sintra, Portugal
Cloridric acid (37%)	Sigma-Aldrich S.A., Sintra, Portugal
Crystal Violet (≥ 90.0%)	Sigma-Aldrich S.A., Sintra, Portugal
Deuterium oxide	Sigma-Aldrich S.A., Sintra, Portugal
1,3-diaminopropane (Dap) (≥ 99%)	Sigma-Aldrich S.A., Sintra, Portugal
cis-dichlorodiammine platinum(II) (cisplatin) (99.9%)	Sigma-Aldrich S.A., Sintra, Portugal
Dimethyl sulfoxide (DMSO) (≥ 99%)	Sigma-Aldrich S.A., Sintra, Portugal
Docetaxel (DTX) ≥ 97.0%	Sigma-Aldrich S.A., Sintra, Portugal
Dulbeco's Modified Eagle Medium – High Glucose (DMEM-HG) (with 4500 mg/L glucose and L-glutamine, without sodium bicarbonate)	Sigma-Aldrich S.A., Sintra, Portugal
Ethanol (99.8%)	Sigma-Aldrich S.A., Sintra, Portugal
Ethylenediaminetetraacetic acid (EDTA) (≥ 98.5%)	Sigma-Aldrich S.A., Sintra, Portugal
Fetal Bovine Serum (FBS) (EU Approved (South American))	Gibco-Life Technologies, Porto, Portugal
Formalin solution, neutral-buffered, 10%	Sigma-Aldrich S.A., Sintra, Portugal
Matrigel™	BD Falcon, Enzifarma, Portugal
Methanol (≥ 99.8%)	Sigma-Aldrich S.A., Sintra, Portugal
Penicillin-Streptomycin solution (Pen/Strep) (10,000 units penicillin and 10 mg streptomycin/mL)	Sigma-Aldrich S.A., Sintra, Portugal
Potassium bromide, (FTIR grade, ≥ 99%)	Sigma-Aldrich S.A., Sintra, Portugal
Potassium chloride	Sigma-Aldrich S.A., Sintra, Portugal
Potassium phosphate monobasic (≥ 99.0%)	Sigma-Aldrich S.A., Sintra, Portugal
Potassium tetrachloropalladate(II) (98%)	Sigma-Aldrich S.A., Sintra, Portugal
Potassium tetrachloroplatinate(II) (98%)	Sigma-Aldrich S.A., Sintra, Portugal
Quercetin (≥ 95%)	Sigma-Aldrich S.A., Sintra, Portugal
Sodium bicarbonate (≥ 99.7%)	Sigma-Aldrich S.A., Sintra, Portugal
Sodium chloride (99.0%)	Sigma-Aldrich S.A., Sintra, Portugal
Sodium hydroxide	Sigma-Aldrich S.A., Sintra, Portugal

Sodium phosphate dibasic (≥ 99.0%)	Sigma-Aldrich S.A., Sintra, Portugal
Spermine (97%)	Sigma-Aldrich S.A., Sintra, Portugal
Sulforhodamine B (SRB) (75%)	Sigma-Aldrich S.A., Sintra, Portugal
Tris(hydroxymethyl)aminomethane (Tris)	Absolve, Odivelas, Portugal
Trypan Blue (0.4% (*w*/*v*) solution)	Sigma-Aldrich S.A., Sintra, Portugal
Trypsin (10x solution, 25 g porcine trypsin *per* liter in 0.9% sodium chloride)	Sigma-Aldrich S.A., Sintra, Portugal
Vascular Endothelial Growth Factor (VEGF)	Sigma-Aldrich S.A., Sintra, Portugal
1,3-Dihydro-3-[(3,5-dimethyl-1H-pyrrol-2-yl)methylene]-2H-indol-2-one (SU 5416)	Sigma-Aldrich S.A., Sintra, Portugal
Hydrocortisone	Sigma-Aldrich S.A., Sintra, Portugal
Material	
12 wells plates	OrangeScientific, Frilabo, Portugal
24 wells plates	OrangeScientific, Frilabo, Portugal
96 wells plates	OrangeScientific, Frilabo, Portugal
24 wells plates for inserts	BD Falcon, Enzifarma, Portugal
T 75 cm^2 culture flasks	OrangeScientific, Frilabo, Portugal
15 and 50 mL conic tubes	OrangeScientific, Frilabo, Portugal
1.5 and 2 mL micro-tubes	OrangeScientific, Frilabo, Portugal
5 mL syringes	BD Falcon, Enzifarma, Portugal
23G needles	BD Falcon, Enzifarma, Portugal
Individual polyethylene terephthalate (PET) inserts (8.0 µm pore)	BD Falcon, Enzifarma, Portugal
MgF_2 (2x20 mm) windows	Crystran, United Kingdom
$CaFl_2$ (IR-grade, 1x13 mm) windows	Crystran, United Kingdom
Main Equipment	
Analytical balance (Toledo AB54)	Mettler, Rotoquímica, Portugal
pH-meter (Basic 20 +)	Crison, Rotoquímica, Portugal
Shaker "Vortex" (MS2 Minishaker)	IKA® Works, Frilabo, Portugal
Water purification apparatus Milli –Q (Gen Pure)	TKA, Frilabo, Portugal
Centrifuge with cooling (MPW-350R)	MPW, Frilabo, Portugal
Incubator MCO-19AIC (UV)	Sanyo, Frilabo, Portugal
Laminar flow hood (BW 100) (flow rate : 1050m^3/h)	BioWizard, Frilabo, Portugal

Microplate reader μQuant MQX200	BioTek, Portugal
Microscope CRX41 coupled to a DP20 camera	Olympus®, Portugal
Orbital incubator	GFL, Certilab, Portugal
Moticam 5 digital camera coupled to a Motic® AE200 inverted microscope	Spectra Services VWR, Portugal
Jobin-Yvon T64000 Raman spectrometer coupled to a Olympus® BH2 microscope	Horiba Jobin-Yvon, Bióptica, Portugal
RFS-100 Fourier transform Raman spectrometer	Bruker, Portugal
Senterra dispersive Raman microspectrometer with a charge-coupled device (CCD) detector	Bruker, UK
Infrared beamline B22 (MIRIAM – Multimode InfraRed Imaging And Microspectroscopy) – Vertex 80v FTIR spectrometer, Hyperion 3000 microscope	Diamond Light Source, UK [244]
Vertex 70 FTIR spectrometer	Bruker, Portugal
TOSCA indirect geometry time-of-flight neutron spectrometer	ISIS Facility, UK [210]
OSIRIS indirect geometry time-of-flight neutron spectrometer	ISIS Facility, UK [213]
Software	
aCLIMAX version 4.0.1 [245]	ISIS Facility, Rutherford Appleton Laboratory, United Kingdom
Angiogenesis Analyser package [246]	Paris, France
DAVE version 2.3 [247]	NIST, Gaithersburg, USA
Extended Multiplicative Signal Correction (EMSC) toolbox [248]	Copenhagen, Denmark
Fiji [249]	
Gaussian 03	Gaussian Inc., Wallingford, USA
GaussView 4	Gaussian Inc., Wallingford, USA
GraphPad Prism 6 Software	La Jolla, CA, USA
LabSpec 5.0	Horiba, Villeneuve d'Ascq, France
MANTID version 3.4.0 [250]	
Matlab 2012a	The MathWorks Inc., Natick, MA
OPUS 7.2	Bruker Optik, Germany
Origin Pro 8.0	OriginLab, USA
ProSpect Toolbox	London Spectroscopy Ltd., London, UK
Unscrambler® X software version 10.2	CAMO, Norway

2.2. Experimental Methods

2.2.1. Synthesis of Metal Complexes with Polyamines

2.2.1.1 PtDap

PtDap was synthesised according to an optimised procedure based on a previously reported method for PtEn ($Pt(en)Cl_2$, en=$NH_2CH_2CH_2NH_2$) [251].

Briefly, 2 mmol of K_2PtCl_4 were dissolved in 12.5 mL of HCl-0.1 M, and a solution containing 2 mmol of Dap in 75 mL of HCl-0.05 M was added dropwise, under continuous stirring, at 60°C, for *ca.* 2 h. Upon standing overnight, a dark yellow powder of the complex was formed, which was filtered and washed repeatedly with acetone.

PtDap (yield: 29.7%) – Elemental analysis found (for $Pt(C_3N_2H_{10})Cl_2$): C: 9.6 %; H: 3.0%; N: 8.3%; Calculated – C: 10.6%; H: 3.0%; N: 8.2%.

2.2.1.2. Pt_2Spm and Pd_2Spm

Synthesis of the Pt_2Spm and Pd_2Spm complexes was carried out based on published procedures [252], previously optimised for the Pd(II) compound [104,238,253] and currently modified for the Pt(II) analogue. Briefly, 2 mmol of K_2PtCl_4 or K_2PdCl_4, were dissolved in a minimal amount of water, and an aqueous solution containing 1 mmol of spermine was added dropwise under continuous stirring. The reaction was allowed to occur for 24 h, after which the resulting yellow powder was filtered off and washed with acetone. Recrystallization of this product from water afforded needle-shaped crystals (yellow-orange for the Pt(II) complex and yellow for the Pd(II) analogue)

Pt_2Spm (yield 60%) – Elemental analysis found (for $Pt_2(C_{10}N_4H_{26})Cl_4$): C: 16.2%; H: 3.5%; N: 7.6%, Cl: 19.1%; Calculated – C: 16.4%; H: 3.6%; N: 7.5%, Cl: 19.3% [238].

Pd_2Spm (yield 68%) – Elemental analysis found (for $Pd_2(C_{10}N_4H_{26})Cl_4$): C: 21.2%; H: 4.7%; N: 9.6%, Cl: 25.9%; Calculated – C: 21.6%; H: 4.7%; N: 10.1%, Cl: 25.5% [104]

2.2.2. Preparation of Solutions

Table 4 – Solutions used along the experimental work.

Solution	Components	pH	Storage
Cell culture			
Phosphate Buffered Saline (PBS) 10x	2.0 g KH_2PO_4 (15 mM) 6.1 g Na_2HPO_4 (43 mM) 2.0 g KCl (27 mM) 87.7 g NaCl (1.5 M) 1000.0 mL ultrapure water	7.4	Room temperature
PBS 1x	100.0 mL PBS 10x 900.0 mL ultrapure water	7.4	Room temperature
DMEM-HG	13.4 g DMEM-HG 1.5 g $NaHCO_3$ 1000.0 mL (final volume) ultrapure water	7.4	4°C
DMEM-HG 10% (*v*/*v*) FBS / 1% Pen/Strep	890.0 mL DMEM-HG 100.0 mL FBS 10.0 mL Pen/Strep	7.4	4°C
Trypsin-EDTA 1x	90.0 mL PBS 1x 10.0 mL Trypsin 10 x 20.0 mg EDTA	7.4	4°C
Tested agents			
cisplatin 1mM	3.0 mg cisplatin 10.0 mL PBS 1x		-20°C
Pd_2Spm 500 µM	2.8 mg Pd_2Spm 10.0 mL PBS 1x		-20°C
Pt_2Spm 250 µM	1.9 mg Pt_2Spm 10.0 mL PBS 1x		-20°C
DTX 1 mM	5.0 mg DTX 6.2 mL PBS 1x		-20°C
SRB colorimetric assay			
Methanol 1% (*v*/*v*) in Acetic acid	495.0 mL Methanol 5.0 mL Acetic acid		-20°C
1% Acetic acid	990.0 mL deionised water 10.0 mL Acetic acid		Room temperature
SRB 0.5%	2.5 g Sulforhodamine B 500.0 mL 1% Acetic acid solution		Room temperature
Tris 10 mM	1.2 g Tris base 1000.0 mL ultrapure water	10	Room temperature

Matrigel assay			
Matrigel 250 µg/ml	252 µL Matrigel 2248 µL Tris 10 mM, 0.7% NaCl		-20°C
Tris 10 mM, 0.7% NaCl	1.2 g Tris base 7.0 g NaCl 1000.0 mL ultrapure water	8	4°C
DMEM-HG / 1% Pen/Strep	990.0 mL DMEM-HG 10.0 mL Pen/Strep	7.4	4°C
DMEM-HG 10% (*v*/*v*) FBS / 1% Pen/Strep	890.0 mL DMEM-HG 100.0 mL FBS 10.0 mL Pen/Strep	7.4	4°C
Formalin 4%, 0.9% NaCl	40.0 mL 60.0 mL NaCl 0.9%		4°C
Crystal violet 0.1%	50.0 mg crystal violet 2.5 ml 100% methanol 7.5 ml ultrapure water		4°C
Spectroscopic experiments			
Sodium chloride 0.9%	9.0 g Sodium chloride 1000 mL ultrapure water	7.4	Room temperature
Formalin 4%	40.0 mL 60.0 mL NaCl 0.9%		4°C

All stock solutions for the tested compounds used in the cell culture experiments were sterile-filtered and stored at -20 °C. Further dilutions to the final desired concentrations were made in PBS 1x immediately before addition to the cells.

2.2.3. In vitro Assays

2.2.3.1. Cell Culture

The epithelial human breast cancer cell line MDA-MB-231 (human Caucasian triple-negative, claudin-low, MSL, breast carcinoma) [254] was purchased from the European Collection of Cell Cultures (ECACC, UK). The cells were cultured as monolayers, at 37 °C, in a humidified atmosphere of 5% CO_2. The cultures were maintained in DMEM-HG 10% (*v*/*v*) FBS / 1% Pen/Strep. Cells were subcultured at 80% confluence, using a trypsin-EDTA 1x solution. Under these conditions, the duplication time was 26 h [104]. The cells were always in the logarithmic phase of growth when the tested agents were added. Whenever needed cells where counted using the Trypan Blue 0.4% (*w*/*v*) assay which allows the quantification of

morphologically intact cells by exclusion of the dye [255]. Particularly, for the anti-invasive assay the Crystal Violet 0.1% (*w*/*v*) dye was used.

2.2.3.2. Evaluation of Antitumour Activity

2.2.3.2.1. Cell Proliferation Assays

Sole Administration

For the determination of the anti-proliferative activity of Pd_2Spm, Pt_2Spm and DTX against the MDA-MB-231 cells, cultures were established in 24-well plates (1 mL/well) at a density of $3x10^4$ cells/cm^2, and were allowed to attach for about 24 h. Triplicates were treated for different incubation periods with several concentrations of the tested compounds (Pd_2Spm and Pt_2Spm from 1 to 16 μM and DTX from $1x10^{-2}$ to $8x10^{-2}$ μM). DTX was solubilised in DMSO and diluted in PBS prior to addition to the cell cultures, the DMSO concentration never exceeding 0.1% (*v*/*v*). According to the population doubling time for MDA-MB-231 cells (26 h [104]) the 48 and 72 h time-points after Pd_2Spm, Pt_2Spm or DTX addition were chosen. At each of these, the growth media was aspirated, the cells were washed and fixed with ice-cold methanol (1% (*v*/*v*) in acetic acid) and stored at -20 °C. After this fixation process, cell proliferation was evaluated through staining with SRB (1 hour) to obtain the cellular protein content, considered as directly proportional to the cell density [215,256,257]. A 0.01% *(w/v)* DMSO solution was always considered as a control.

Combined Administration

Cells were seeded in 24-well plates (1 mL/well) at a density of $3x10^4$ cells/cm^2 and were allowed to attach for about 24 h. Two different drug administration schemes were used: (i) The cells were simultaneously exposed to $1x10^{-2}$ μM DTX and 2 or 4 μM Pd_2Spm; (ii) the cells were initially pre-treated with DTX ($1x10^{-2}$ μM) for 24 h, after which the media was removed, the cells were washed with PBS, fresh DMEM-HG was added and Pd_2Spm was administered, the end-points being counted from this time forward (Figure 23).

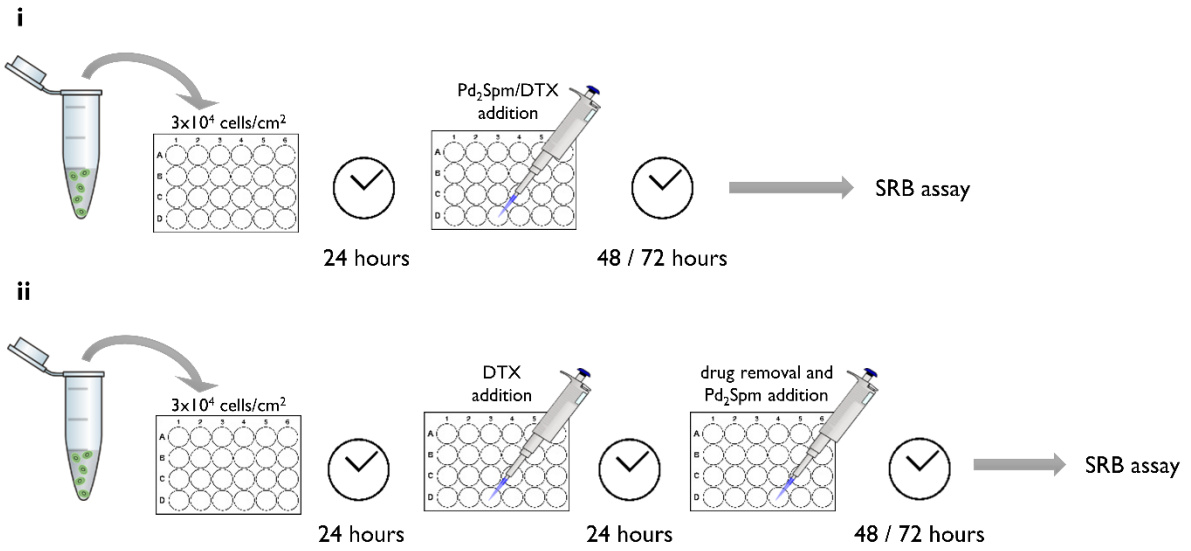

Figure 23 – Schematic representation of combined administration according to schemes i and ii.

2.2.3.2.2. Cell Invasion Assays

Migration of MDA-MB-231 cells was measured using the Matrigel™ cell invasion assay [235,236,258]. Briefly, the inserts were coated with 250 μg.mL^{-1} Matrigel™ and placed in a cell incubator for 2 h. The top chambers were then seeded with 5×10^4 cells in FBS-free DMEM-HG medium along with 4 μM–Pd_2Spm and 1×10^{-2} μM–DTX, either alone or in combination. The bottom chambers contained DMEM-HG supplemented with 10% (*v*/*v*) FBS. After 72 h, the cells on the top surface of the membrane (non migrating cells) were gently rubbed with a cotton swab moistened with PBS (Figure 24). The cells spreading to the bottom surface of the membrane (invasive cells) were washed with PBS and fixed with cold 4% formalin for 20 min, after which they were stained with Crystal Violet 0.1% (*w*/*v*) for 1 hour. Images were taken using a camera coupled to an inverted microscope (Olympus, Portugal) equipped with a 10x objective, and invasive cells were quantified by manual counting.

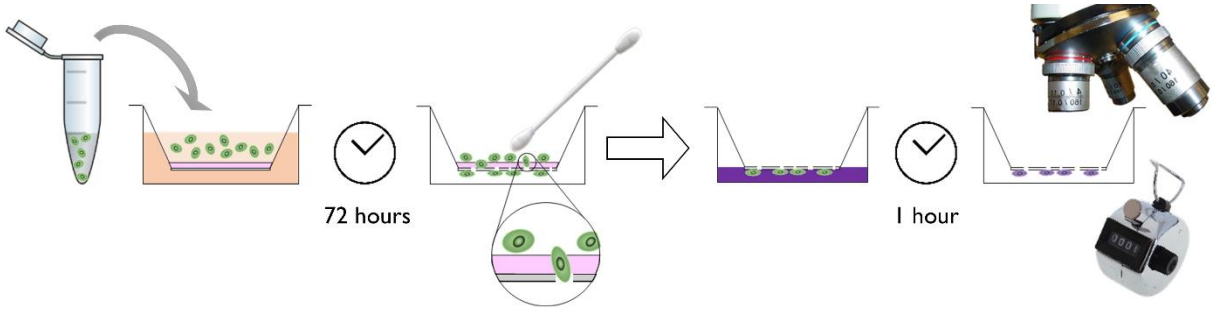

Figure 24 – Schematic representation of cell invasion assay.

2.2.3.3. In vivo CAM Assays

The chicken embryo CAM assay is a suitable and cost-effective model for monitoring neovascularisation [36,38,42,45,47,56,259], and was presently used as an *in vivo* model for angiogenesis, as described elsewhere [41]. Figure 25 schematically represents the experiments carried out. Briefly, the fertilised chicken eggs were incubated, with shaking, at 37.5 °C in a humidified atmosphere. After 3 days of incubation, *ca.* 2.5 mL of albumen were removed, in order to detach the shell from the developing CAM, and a window was opened in the eggshell to expose the embryo. At this stage, the fertilised eggs were sealed with paraffin and incubation continued until day 9, when the windows were unsealed. Three PBS-soaked and one VEGF-soaked (10 ng/mL) coverslips were then placed in each egg, in direct contact with the CAM, and the openings were sealed again with paraffin. The coverslips were previously sterilised and pre-treated with hydrocortisone (a cyclooxygenase inhibitor), with the purpose of avoiding inflammatory responses. At day 11, the windows were unsealed and two of the PBS-soaked coverslips were treated with Pd_2Spm (1 to 4 μM), DTX ($1x10^{-2}$ to $4x10^{-2}$ μM) and Pd_2Spm/DTX combinations (1 to 8 μM/$1x10^{-2}$ to $8x10^{-2}$ μM). The untreated coverslips were then used as controls (respectively PBS and VEGF). The windows were sealed once more and the eggs incubated until day 13, when angiogenesis was assessed. At this time-point, the eggs were opened and the coverslips (bound to the CAM) were removed and placed in PBS. Contrast-phase images were obtained using a Moticam 5 digital camera coupled to a Motic® AE200 inverted microscope (with a 4x magnification). The digital images were analysed using the software package Angiogenesis Analyser package [246] for Fiji program [249].

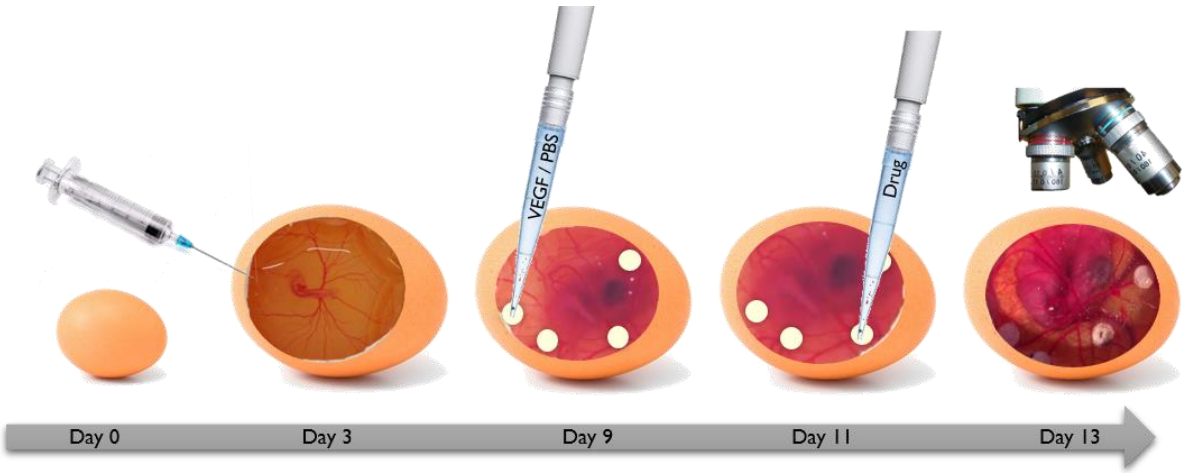

Figure 25 – Schematic representation of the CAM assay.

2.2.3.4. Assessment of the in Vitro Tyrosine Kinase Activity

In vitro VEGFR2 tyrosine kinase activity was analysed by using an enzyme-linked immunosorbent assay kit as previously described [260]. Briefly, this assay (performed in 96-well plates) employs an affinity tag labelled capture antibody and a reporter conjugated detector antibody which immunocaptures the sample analyte in solution. The complex (captured antibody/analyte/detector antibody) is, in turn, immobilised *via* immunoaffinity of an anti-tag antibody coating the well.

Pd_2Spm and DTX were tested separately (at their IC_{50} concentrations, respectively 2.9 and $1.5x10^{-2}$ μM), or in combination (at $6x10^{-1}/6x10^{-3}$ μM for Pd_2Spm/DTX), by incubation with the antibody mixture. Subsequent substrate phosphorylation was monitored by the colour development, measured at 450 nm in an automated microplate reader.

2.2.3.5. Quantification of Intracellular vs Extracellular Water in the Cell Pellets

The intracellular:extracellular water ratio was determined in the cell pellets, by comparing the weight of differently prepared samples: cell pellet immediately after harvesting and centrifugation (195 x g, for 10 min), containing both inter- and intracellular water (w_P); cell pellet after drying in a dry atmosphere at 37 °C for *ca.* 3 hours, allowing for extracellular water to evaporate completely (w_D); lyophilised cell pellet, comprising only the dehydrated cellular components (w_L). Hence, (w_P-w_L), (w_D-w_L) and (w_P-[w_D-w_L]) yielded the total water (inter+intracellular), the intracellular, and the extracellular water, respectively.

2.2.4. Computational Methods

Quantum mechanical calculations were performed for PtDap and Pt_2Spm, using the Gaussian 03 program [261] – both geometry optimisation and calculation of the harmonic vibrational frequencies – within the Density Functional Theory (DFT) approach, at a level which was previously shown by the authors to be the best choice for describing this type of Pt(II)-amine complexes, since it presents the finest compromise between accuracy and computational demands [262,263]. The mPW1PW method, which comprises a modified version of the exchange term of Perdew-Wang and the Perdew-Wang 91 correlation functional [264,265] was used, along with the split valence basis set 6-31G* [266], for all atoms

except for the metal. Pt(II) was represented by the relativistic Effective Core Potentials of Hay and Wadt [267] (G03W keyword LANL2DZ), n=5 and n=6 being considered as valence electron shells.

Molecular geometries were fully optimised by the Berny algorithm, using redundant internal coordinates [268]: the bond lengths to within *ca.* 0.1 pm and the bond angles to within *ca.* 0.1°. The final root-mean-square (rms) gradients were always less than $3x10^{-4}$ hartree.bohr^{-1} or hartree.radian^{-1}. No geometrical constraints were imposed on the molecules under study. The harmonic vibrational wavenumbers, as well as Raman activities and infrared intensities, were obtained at the same theory level as the geometry optimisation procedure.

Simulation of the INS spectra (both the theoretical transition intensities and wavenumbers) was carried out with the dedicated aCLIMAX program [245].

2.2.5. Sample Preparation for Spectroscopic Analysis

Upon harvesting by trypsinisation, cells were centrifuged and the pellet was resuspended in culture medium and seeded, at a concentration of 3×10^4 cells/cm^2, on the optical substrates suitable for either Raman [269] or FTIR data collection [270]: respectively MgF_2 (2x20 mm) and $CaCl_2$ (UV-grade, 1x13 mm) disks, previously cleaned with ethanol-70%. Upon incubation for 24 h (allowing the cells to attach), cells were treated for different concentrations of each tested compound (2, 4 and 8 μM) and left to culture for a further 48 h. The growth medium was then removed, cells were washed twice with NaCl-0.9%, fixed in 4% formalin (diluted in NaCl-0.9% from the commercial 10% neutral-buffered formalin solution) for 10 min [270] and washed several times with ultrapure water (to remove any residual salt). The disks were allowed to air-dry prior to spectroscopic analysis.

All samples were prepared in triplicate, in a single experiment.

2.2.6. Optical Vibrational Spectroscopy

2.2.6.1. Raman Spectroscopy

Raman spectra of the newly synthesised compounds was recorded (at room temperature) at the University of Aveiro, in a Bruker RFS-100 FT-Raman spectrometer, equipped with an InGaAs detector, with near-infrared excitation (in order to overcome

fluorescence) provided by the 1064 nm line of a Nd:YAG laser (Coherent, model Compass-1064/500N) yielding *ca.* 150 mW at the sample position. A 180° geometry was employed, and each spectrum was the average of three repeated measurements of 50 scans each, resolution being set to 2 cm^{-1}.

Raman spectra of MDA-MB-231 fixed cells on $MgCl_2$ disks, both untreated and drug-treated, were recorded (at room temperature) at the VIBIMA laboratory of the QFM-UC (Portugal) [271] and at the peripheral laboratories of the B22 beamline from DLS (UK) [144,145]. Spectral collection was performed both for the dry samples (at B22/Diamond) and within NaCl-0.9% *(w/v)* solution (at VIBIMA/QFM-UC). In all cases, samples of untreated cells were used as control.

At VIBIMA/QFM-UC, the spectra were obtained in the 600-1800 cm^{-1} range, in a Horiba Jobin-Yvon T64000 spectrometer in direct configuration mode (focal distance 0.640 m, aperture *f*/7.5), equipped with a holographic grating of 1800 grooves.mm^{-1}. The entrance slit was set to 200 μm. Rayleigh elastic scattering was rejected by a Notch filter, which reduces its intensity by a factor of 10^6. The detection system was a LN_2 cooled non-intensified 1024×256 pixels (1") CCD. The 514.5 nm line of an Ar^+ laser (Coherent, model Innova 300-05) was used as the excitation radiation, yielding *ca.* 10 mW at the sample position. All the spectra were recorded using an Olympus 60x water immersion objective (Olympus LUMPLFLN 60XW, NA 1.0, wd 2 mm). A 200 μm confocal pinhole rejected signals from out-of-focus regions of the sample. Apart from the control (untreated cells), samples containing 2, 4 and 8 μM of the tested drugs (48 h exposure) were analysed. 30 to 40 spectra were collected *per* sample (in different cells), with 4 accumulations and 60 s of exposure, at a <1 cm^{-1} spectral resolution.

At DLS, Raman data for samples of fixed cells exposed to drugs at 2, 4 and 8 μM and the controls were acquired in the 600-1800 cm^{-1} and 2600-3600 cm^{-1} regions, in a Bruker Senterra dispersive Raman microspectrometer with a CCD detector (1024x265 pixels), using a 100x objective (Olympus BX, NA 0.9, Japan), a 50 μm diameter confocal aperture and a 532 nm laser line providing *ca.* 25 mW at the sample position. 150 to 200 spectra were collected *per* sample (from cytoplasm and nucleus for each cell), with 5 s of exposure and 6 co-added

scans *per* chosen point, sampling approximately 75 to 100 cells *per* sample, at a 9-18 cm^{-1} spectral resolution.

2.2.6.2. FTIR Spectroscopy

Globar FTIR spectra of the solid complexes were obtained at VIBIMA/QFM-UC (at room temperature, in KBr disks *ca.* 0.5% *(w/w)*) in a Bruker Optics Vertex 70 FTIR spectrometer, with a KBr beamsplitter and a LN_2 cooled MCT detector. Each spectrum was the sum of 128 scans, at a 1 cm^{-1} resolution. The error in wavenumbers was estimated to be less than 1 cm^{-1}.

Synchrotron-radiation infrared microspectroscopy (SR-IRMS) data of MDA-MB-231 fixed cells on CaF_2 optical substrates, both untreated and drug-treated, were acquired (at room temperature) at the infrared beamline B22 (MIRIAM) from DLS (UK) [144,145].

Acquisition in the mid-IR region 650-3900 cm^{-1} (Ge filter cut off) was carried out in transmission mode, under a Hyperion 3000 microscope coupled to a Bruker Vertex 80v FTIR spectrometer, equipped with a LN_2 cooled MCT high sensitivity detector (50x50 μm^2 area) and a synchrotron radiation IR source yielding 300 mA at the sample position (microbeam FWHM *ca.* 15x15 μm^2 and detected area between 5x5 to 15x15 μm^2 selected *via* slits). An area of 10x10 μm^2 at the sample (NA 0.5) matched with a 36x cassegrain condenser for transmission measurement.

Samples containing drug at 4 and 8 μM concentrations were analysed, as well as the controls (drug-free). 150 to 200 spectra were collected *per* sample (from at least 2 points *per* cell sampling, 75 to 100 cells *per* sample), with 256 co-added interferograms *per* chosen point (as well as background every 10 spectra), *i.e. ca.* 40 s *per* spectrum in order to obtain a high enough S/N ratio for further data analysis. Three replicates were acquired for each sample.

2.2.7. Spectroscopy with Neutrons

The neutron spectroscopy measurements were carried out at the ISIS Pulsed Neutron Source (United Kingdom [177]). The newly synthesised complexes, as well as the cellular samples containing *ca.* 100 mg/1 cm^3 of cell pellet (*ca.* $5x10^8$ cells), were wrapped in aluminium foil sachets (which filled the beam) and loaded into flat thin walled aluminium cans.

2.2.7.1. Inelastic Neutron Scattering

INS spectra were obtained on the TOSCA spectrometer [210,272], an indirect geometry time-of-flight, high resolution ($(\Delta E/E)$ *ca.* 1.25 %), broad range spectrometer. To reduce the impact of the Debye-Waller factor (the exponential term in equation (16)) on the observed spectral intensity, the samples (in 0.2 mm-thick (4×4 cm) flat Al cans) were cooled to cryogenic temperature (*ca.* 10 K). Data were recorded in the energy range -24 to 4000 cm^{-1}.

For the studies in cells, apart from the drug-containing samples untreated cellular controls were measured (for comparison when ascribing the cisplatin-induced changes), as well as cisplatin solutions (at all concentrations) in PBS and PBS buffer (to assess the drug effect on the saline medium in the absence of the biological matrix). Lyophilised cells with and without drug (8 μM) were also measured, with a view to identify the vibrational components due to biomolecules (mainly from proteins and DNA).

The cellular samples were plunged into liquid nitrogen for rapid freezing, in order to avoid slow ice crystal growth during freezing that could extract water from cells leading to dehydration (an eventually to membrane disruption).

2.2.7.2. Quasielastic Neutron Scattering

QENS spectra of MDA-MB-231 cells were acquired on the low-energy OSIRIS high-flux indirect-geometry time-of-flight spectrometer [213,273], equipped with a newly installed beryllium filter [274], and using the 002 reflection of the cooled pyrolytic graphite analyser bank (PG002 25Hz configuration) with a 25.4 μeV energy resolution (FWHM). The data was recorded in the Q range 0.18 to 1.81 $Å^{-1}$ (covering a 11° to 155° angular interval, for a total of 41 detectors), within the energy transfer window -0.8 to 2.0 meV.

Drug-treated cells and untreated cellular controls were measured, as well as PBS and cisplatin solutions in PBS. Both non-washed and PBS_{deut}-washed samples were used, to accurately identify the contribution from bulk water.

In all cases 0.1 mm-thick (4×4 cm) flat Al cans were used, except for the PBS_{deut}-washed samples and for PBS which were placed in 0.4 mm-thick (4×5 cm) Al containers (to allow for

a higher amount of scatterer in the beam, still keeping to a 10% scatterer to reduce the possibility of multiple scattering). Spectra were run at 298 K, for *ca.* 20 h each.

A vanadium sample (a purely incoherent elastic scatterer) was measured to define the instrument resolution and correct for detector efficiency.

2.2.8. Data Pre-processing, Fitting Procedures and Statistical Analysis

Cell proliferation data were obtained from experiments in which both controls and cell cultures exposed to the tested compounds were established and processed in parallel. IC_{50} values (relative inhibitory concentration inducing 50 % of cell growth) were calculated from dose-response studies for DTX (0 to $8x10^{-2}$ μM) and Pd_2Spm (0 to 16 μM) according to previous procedures [275]. The results were expressed as a percentage of the control and were an average of at least three independent experiments. The standard error of the mean (SEM) was calculated in all cases, and the statistical significance of the differences was assessed using Dunnett's post-test for the control. All data analysis was performed with the GraphPad Prism 6 Software.

The synergetic effect of Pd_2Spm when in combination with DTX was evaluated according to the method of isoboles [276]. An isobologram was plotted for both drugs in order to determine if the combined administration of Pd_2Spm and DTX produces a response different than an additive one. A line (isobole) was drawn, connecting the points of 50% maximum response for each agent in the absence of the other one, allowing to interpolate the Pd_2Spm/DTX combinations producing a 50% response.

Raman spectra collection was carried out using the LabSpec 5.0 and OPUS 7.2 programs, respectively at VIBIMA/QFM-UC and DLS. Data pre-processing was performed with The Unscramber® X software. Spurious peaks caused by cosmic rays were removed and the spectra were selected for data treatment by discarding those with very poor S/N ratio. The spectra were baseline corrected (second order polynomial in the 600-1800 cm^{-1} region and linear baseline correction in the 2650-3450 cm^{-1} interval), smoothed by the Savitsky-Golay filter (order 1, 9 points) which enabled reduction of noise without band distortion, and vector normalised (minimising the effects of variable thickness within and among the cell samples).

FTIR data acquisition was performed using OPUS 7.2, which compensated for atmospheric and water vapour interferences, and corrected for background intensity changes within the chosen wavenumber interval. Infrared absorbance spectra were obtained by rationing to a background measured from a clean area of the sample where no cells were present. Since for spectral acquisition of the cells in transmission mode the sample is illuminated through the substrate, reflection losses related to the relative refractive indices at the substrate–sample interface must be considered in the data treatment, as well as optical contributions from sample–air and air–substrate boundaries. This was achieved by RMieS correction (with the EMSC algorithm [277,278], 20 iterations) of the single cell spectra, vector normalised and mean centred. The spectra were corrected independently before computing the average spectrum *per* cell, as each spectrum may have experienced a different spectral distortion due to the heterogeneous nature of the cells distributed along the two-dimensional arrangement of pixels over which the sample was illuminated. Data were quality checked to remove any spectra which still exhibited high levels of scattering. Quality checking was based on the amide I band intensity, spectra with absorbance between 0.1 and 1 being retained. Initial pre-processing was based on a principal component (PC)-based noise reduction algorithm: noise reduction was achieved by retaining a selected number of principal components and then recombine the dataset. Careful selection of the retained components enabled random noise to be removed while still preserving the chemical information in the spectra. Utilising PC-based noise reduction of the data with 40 PC´s allowed good improvements to be observed in the S/N ratio.

For both FTIR and Raman, the spectra were plotted using Origin 8.0. Multivariate analysis of the results – unsupervised principal components analysis (PCA) – was carried out in The Unscramber X 10.2 and using Matlab 2012a and the ProSpect Toolbox. The order of the PCs denotes their importance to the dataset, PC1 corresponding to the highest amount of variation. Analysis was carried out separately for each spectral region probed. For the Raman data, PCA was performed using the cross validation method, while for the IR results the nonlinear iterative partial least squares algorithm and the leverage correction validation method were applied. The use of chemometric techniques is essential when analysing complex systems such as cells, due to the complexity of the biochemical processes taking place within

them. It provides further insight into the source of the observed spectral variability, enabling discrimination between spectral patterns obtained for distinct levels of drug exposure. From the loading plots corresponding to each principal component it was possible to derive biochemical information based on the differentiation between the tested conditions, and to evidence inter-group variance. Additionally, loading plots could be matched with the corresponding experimental spectra, and the positive and negative peaks in the loadings were assigned to the different groups observed in the score plots. Once discrimination was attained according to PC´s dominated by spectral features characteristic of the cellular components (and not the drugs), it could be concluded that the detected spectral variances were not due to the presence of the external agents but instead to their distinct effects on the cell´s biochemical profile coupled to specific physiological reactions – the impact of the drugs was therefore monitored, as initially proposed.

The neutron data was reduced from raw time-of-flight signals into energy transfer spectra using the MANTID program [250]. QENS spectra were corrected for detector efficiency. Resolution functions were determined independently from calibration runs for vanadium (used for non-cell containing samples), as well as for untreated non-washed and PBS_{deut}-washed cells (applied for the corresponding cell-containing samples).

Fitting of the QENS spectra was performed for the energy transfer range -0.8 to 2.0 meV, with the DAVE program [247]. One Delta function (elastic component) and three Lorentzians (quasielastic contributions), plus an energy independent instrumental background, were necessary for an accurate representation of the system. FWHM values were extracted from each of the Lorentzian functions representing the distinct dynamical components assigned to the system, yielding the translational diffusion coefficients (D_T) and jump times (τ_T), as well as the correlation times for the localised motions of the cellular macromolecules (τ_L). For the translational Lorentzians, either a continuous diffusion (Fickian model, $\Gamma = DQ^2$) or a jump-reorientation mechanism were considered, the latter following the equation [279-282],

$$\Gamma_T(Q) = \frac{D_T Q^2}{1 + D_T Q^2 \tau_T^{jump}} \tag{21}$$

where D_T represents the translational coefficient at temperature T and τ_T^{jump} is the translational jump time (*i.e.* the mean residence time of a water molecule in each possible location).

3 Results and Discussion

3.1. Characterisation of the Complexes

3.1.1. PtDap

Figure 9 comprises the most stable geometry calculated for the newly synthesised PtDap chelate. This conformation belongs to the C_s point group, and displays 48 vibrational modes – 26 with A´ symmetry and 22 with A´´ symmetry – all Raman and infrared active.

The vibrational spectra obtained for PtDap are comprised in Figure 26 and Figure 27. The use of all vibrational techniques – FTIR, Raman and INS – allowed to observe virtually all the modes of the molecule and to achieve a complete assignment of its vibrational pattern (Table 5). Special attention was paid to spectral regions comprising particular vibrations which can be considered as a fingerprint of this kind of complexes: (i) the Cl–Pt–Cl and N–Pt–N deformations and stretchings; and (ii) the vibrations associated to the diamine ligand, especially $\delta(NH_2)$ and $\nu(NH_2)$, which reflect the chelating ability of this particular bidentate moiety.

Table 5 – Experimental and calculated vibrational wavenumbers (cm^{-1}) for PtDap.

Experimental			[a]Calculated	Sym. species	[b]Approximate description
Raman	FTIR	INS			
3265	3262		3260	(A")	$\nu_{as}(NH_2)$
3249	3242		3261	(A')	$\nu_{as}(NH_2)$
3198	3198		3174	(A'; A")	$\nu_s(NH_2)$
3130	3130				$2x\delta_s(NH_2)$ FR $\nu_s(NH_2)$
2967	2967sh		2972	A'	$\nu_{as}(CH_2)$
2956	2953		2928	(A'; A")	$\nu_s(CH_2)$
2944					
2933					
2920	2924				
2890	2890		2910	A'	$\nu_s(CH_2)$
	2852				
2799					
2777					
1589	1586	1588	1588	A'	$\delta(NH_2)$ in-phase
1581		1573	1583	A"	$\delta(NH_2)$ out-of-phase
1465	1469				$\delta(CH_2)$
1458	1462	1458	1456	A'	$\delta(CH_2)$
1453	1451		1445	A"	$\delta(CH_2)$
1436	1436		1430	A'	$\delta(CH_2)$
1405	1403	1406	1380	A'	ω (CH_2)
1398	1395		1377	A"	$\omega(CH_2)$
1353	1352				
1334	1330	1331	1339	A"	$\omega(CH_2)$
1321			1303	A'	t (CH_2)

1288	1290	1287	1289	A”	t (CH_2)
1254	1254	1254	1265	A”	t(CH_2) + ω(NH_2)
1207	1206		1213	A’	t(CH_2) + t(NH_2)
1198	1193		1195	A’	ω(NH_2)
	1173				
1165	1162	1172	1161	A”	ω(NH_2)
1126	1127	1134			
1087	1085		1089	A”	ν(CN) + ν(CC)
1074	1073	1069	1056	A”	ν(CN) + ν(CC) + t(NH_2)
1060	1055				
1040	1037	1042	1048	A’	ν(CN)
943	949 943sh	945	931	A”	ν(CN) + ν(CC)
	901	900	909	A’	ρ(CH_2)
817	815	813	783	A’	ν(CC)
774	772				ρ(CH_2)
763	758sh	757	761	A’	ρ(NH_2)
		744	752	A”	ρ(NH_2)
532 ([c]508)	527	535 ([c]505)	510	A”	ν_{as}(N-Pt-N)
488 ([c]524)	486sh		508	A’	ν_s(N-Pt-N) + δ(CCC)
481sh	477	477 ([c]521)	470	A’	δ(CCC) + ν_s(N-Pt-N)
384		378	381	A”	δ(NCC)
359		358	349	A’	δ(CCC) + ν_s(Cl-Pt-Cl)
[d]325 [d]314			336	A”	ν_{as}(Cl-Pt-Cl)
246		249	232	A'	δ_s(N-Pt-N)
		[d]224 [d]212	211	A”	γ(CN-Pt-NC) out-of-phase
			174	A’	γ(CN-Pt-NC) in-phase
159		160	153	A”	δ(N-Pt-Cl)
151sh		142	143	A’	δ(Cl-Pt-Cl)
		123			external libration
		102			external libration
		96	95	A”	[e]global “torsion” mode
66		73	63	A’	[e]global “butterfly” mode

[a]At the mPW1 level. Scaled according to: 0.9499 for the bands in the 700-3150 cm^{-1} range [283]; 0.920 for ν(NH_2) [262]; 0.933 for δ(NH_2); 0.986 for ω(NH_2) and ρ(NH_2); [b]Symbols for vibrational modes: δ – in-plane deformation, t – twisting, ρ – rocking, ω – wagging, γ – out-of-plane deformation, *s*, *as*, and *a* refer to symmetric, antisymmetric and asymmetric modes, respectively, sh refers to a shoulder; [c]For cisplatin [263,284]; [d]Davydov splitting; [e][284].

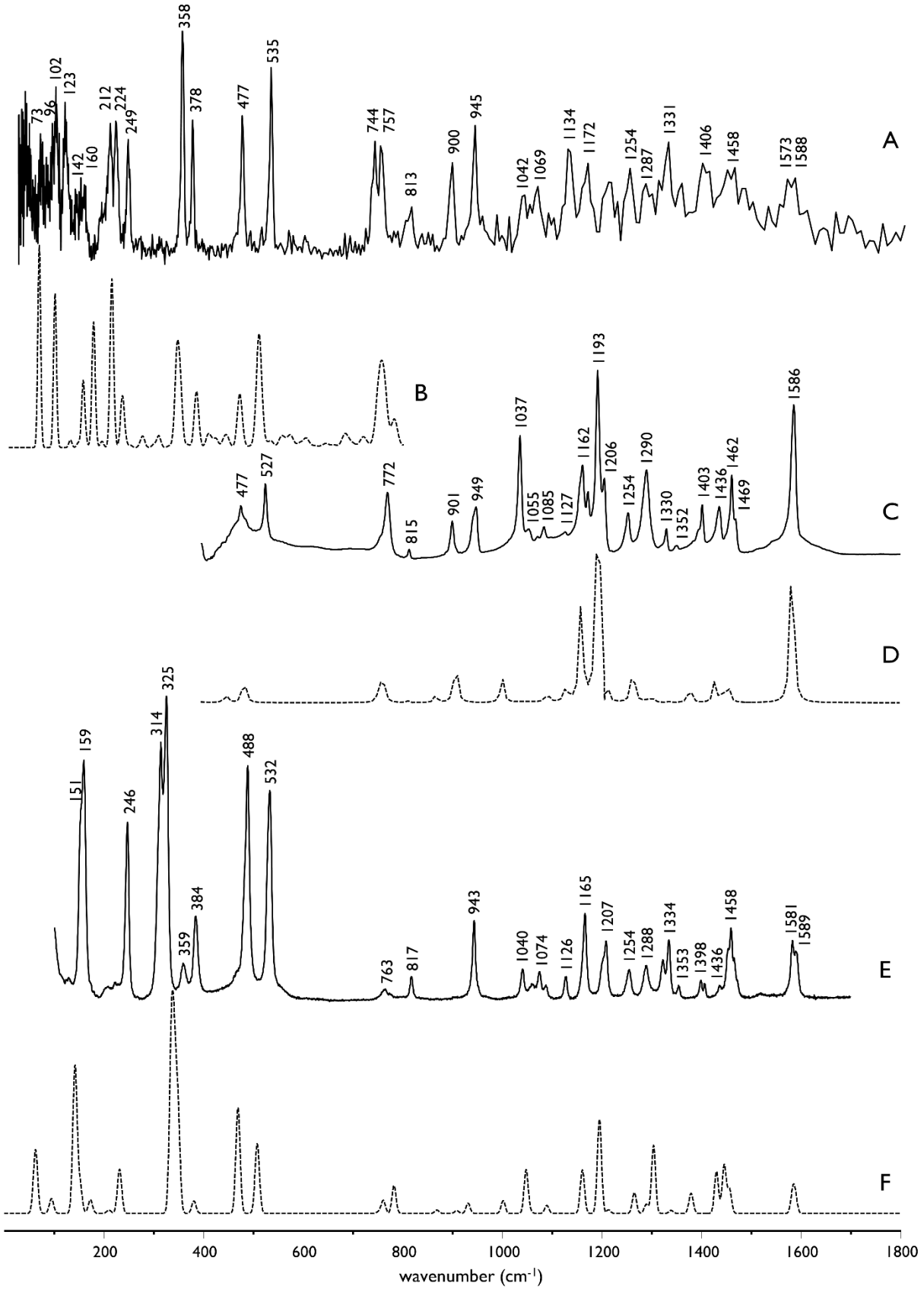

Figure 26 – Vibrational spectra (0-1800 cm^{-1}) for PtDap: experimental (A) and calculated (B) INS; experimental (C) and calculated (D) FTIR; experimental (E) and calculated (F) Raman.

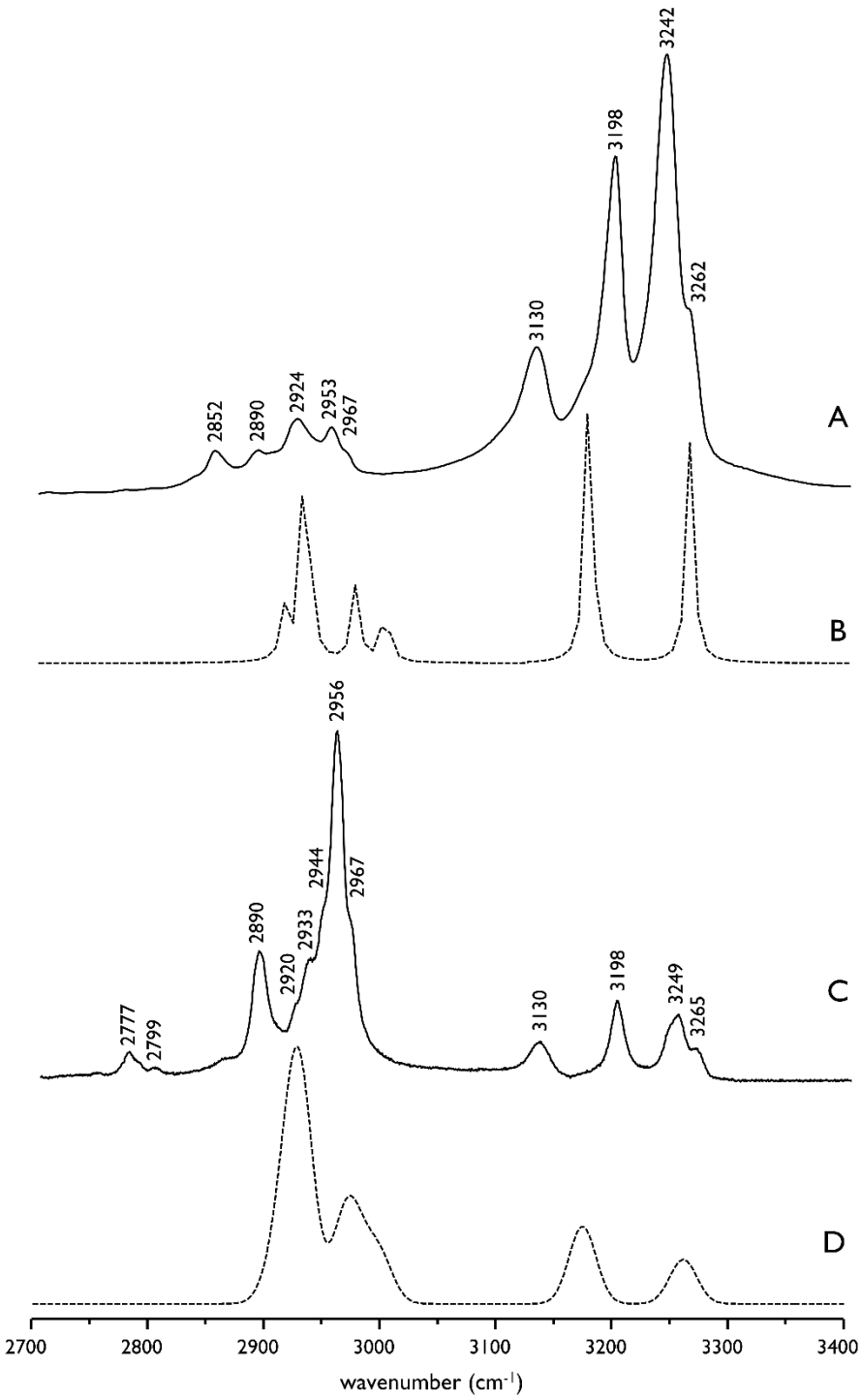

Figure 27 – Optical vibrational spectra (2700-3400 cm^{-1}) for PtDap: experimental (A) and calculated (B) FTIR; experimental (C) and calculated (D) Raman.

Interpretation of the experimental data was assisted by the predicted spectra obtained from the quantum mechanical calculations, as well as by comparison with the results previously obtained for cisplatin and analogous complexes [262,284], as well as the free diamine ligand [285]. A quite good agreement was found between the experimental and calculated vibrational data (Figure 26 and Figure 27), namely in the low wavenumber region. Scaling of the calculated

values was carried out, in order to correct for the known overestimation of the calculated harmonic vibrational frequencies relative to the experimental ones, mainly above 700 cm^{-1}, due to the neglect of anharmonicity effects in the theoretical treatment. As there are no reported scaling methodologies for this type of inorganic Pt-containing systems, and since the widely used scaling factors developed by Merrick *et al.* [283] are recommended for organic compounds only, a four-factor scaling scheme (considering different frequency sets) was applied for PtDap (Table 5): Merrick´s factor of 0.9499 (for the theory level presently used) for the frequencies between 700 and 3150 cm^{-1} (assigned to the ligand); the value previously determined for cisplatin [262] for the amine stretching modes (above 3000 cm^{-1}) – 0.920; two factors presently optimised for the deformations of the amine bound to the metal – 0.933 for $\delta(NH_2)$; and 0.986 for $\omega(NH_2)$ and $\rho(NH_2)$.

A red shift was detected for the amine scissoring modes, occurring at 1589/1581 cm^{-1} (Raman), 1586 cm^{-1} (FTIR) and 1588/1573 cm^{-1} (INS), relative to the free diaminopropane ligand and similar linear alkylamines which display a typical NH_2 scissoring vibration centred at 1619 cm^{-1} [285]. This is anticipated by the metal chelate effect, that leads to an anchoring of the otherwise conformationally free amine groups. Furthermore, there is a significant narrowing of the signals associated to the amine groups upon Pt(II)-coordination.

A well-defined and intense INS band appears at 378 cm^{-1} (Figure 26) ascribed to the (NCC) deformation (Table 5). This can be compared to the δ(NCC) longitudinal mode (LAM1) of the free ligand, occurring at 409 cm^{-1} [286], the shift to lower frequency in the chelate being due to metal coordination. The two signals assigned to the (N–Pt–N) symmetric and anti-symmetric stretching modes of the diaminopropane complex display a considerably larger separation than for cisplatin (45-60 *vs* 16-20 cm^{-1}, Table 5), most probably due to the significantly lower flexibility of the diamino1propane bidentate chelate as compared to the two free rotating NH_3 moieties in cisplatin. Furthermore, an inversion is detected between the symmetric and anti-symmetric ν(N–Pt–N) wavenumbers, the latter being observed at higher values for PtDap as opposed to $Pt(NH_3)_2Cl_2$, while the former is mixed with the δ(CCC) mode. Also, cisplatin´s typical $\rho(NH_3)$ feature (centred at *ca.* 790 cm^{-1}) is substituted in the Dap chelate by the amine rocking modes, clearly detected by INS at 757 and 744 cm^{-1} (Table 5).

A clear splitting of the INS band ascribed to the out-of-plane out-of-phase (CN–Pt–NC) deformation (212 and 224 cm^{-1}, Figure 26), theoretically predicted as a single feature at 211 cm^{-1} (Table 5), may be attributed to a Davydov splitting, reflecting the presence of more than one molecular entity in the crystalline unit cell for this sample. In fact, this may lead to a doubling of the spectral features due to the occurrence of crystallographically inequivalent conformations. This was previously detected by INS in *n*-alkanes [287] and linear alkyl-polyamines [288]. A similar splitting was verified for the ν(Cl-Pt-Cl) vibration in PtDap, calculated at 336 cm^{-1} and yielding the 325 and 314 cm^{-1} experimental bands. These are only detected by Raman, which is a good example of the clear advantage of applying several vibrational techniques to the study of the same system.

3.1.2. Pt_2Spm

The most stable geometry calculated for the Pt_2Spm chelate (Figure 9) corresponds to a C_i symmetry, displaying 132 vibrational modes – 66 Raman active (with A_g symmetry) and 66 infrared active (with A_u symmetry).

The vibrational spectra obtained for Pt_2Spm (FTIR, Raman and INS) are comprised in Figure 28 and Figure 29, allowing to access all the vibrational modes of the molecule and a thorough assignment of its vibrational profile. Once more, special attention was paid to the features that evidenced more significant changes upon complexation: metal coordination was clearly verified by comparing the spectra of the free ligand (Spm) and its dinuclear Pt(II) complex (Figure 28), mainly through the characteristic Cl–Pt–Cl and N–Pt–N deformation and stretching bands.

Table 6 comprises the vibrational wavenumbers for Pt_2Spm, as well as a comparison with the corresponding features for cisplatin and the model complex PtDap. N-Pt-N deformation is observed at 244 cm^{-1} for the Spm complex and at *ca.* 246 cm^{-1} for PtDap. Regarding the Pt-Cl stretching mode, it occurs in Raman at 327 cm^{-1} for Pt_2Spm and at 323 cm^{-1} for cisplatin (for which it is also detected by INS at ~330 cm^{-1} [284]). The Pt-N stretching at 531 (Raman) and 526 (INS) cm^{-1} was also identified for cisplatin (at 524/521 cm^{-1}) and PtDap (at 532/535

cm^{-1}). This band also contains contributions from skeletal deformations (Table 6), being slightly blue shifted relative to the free ligand. In the complex, these modes are degenerated.

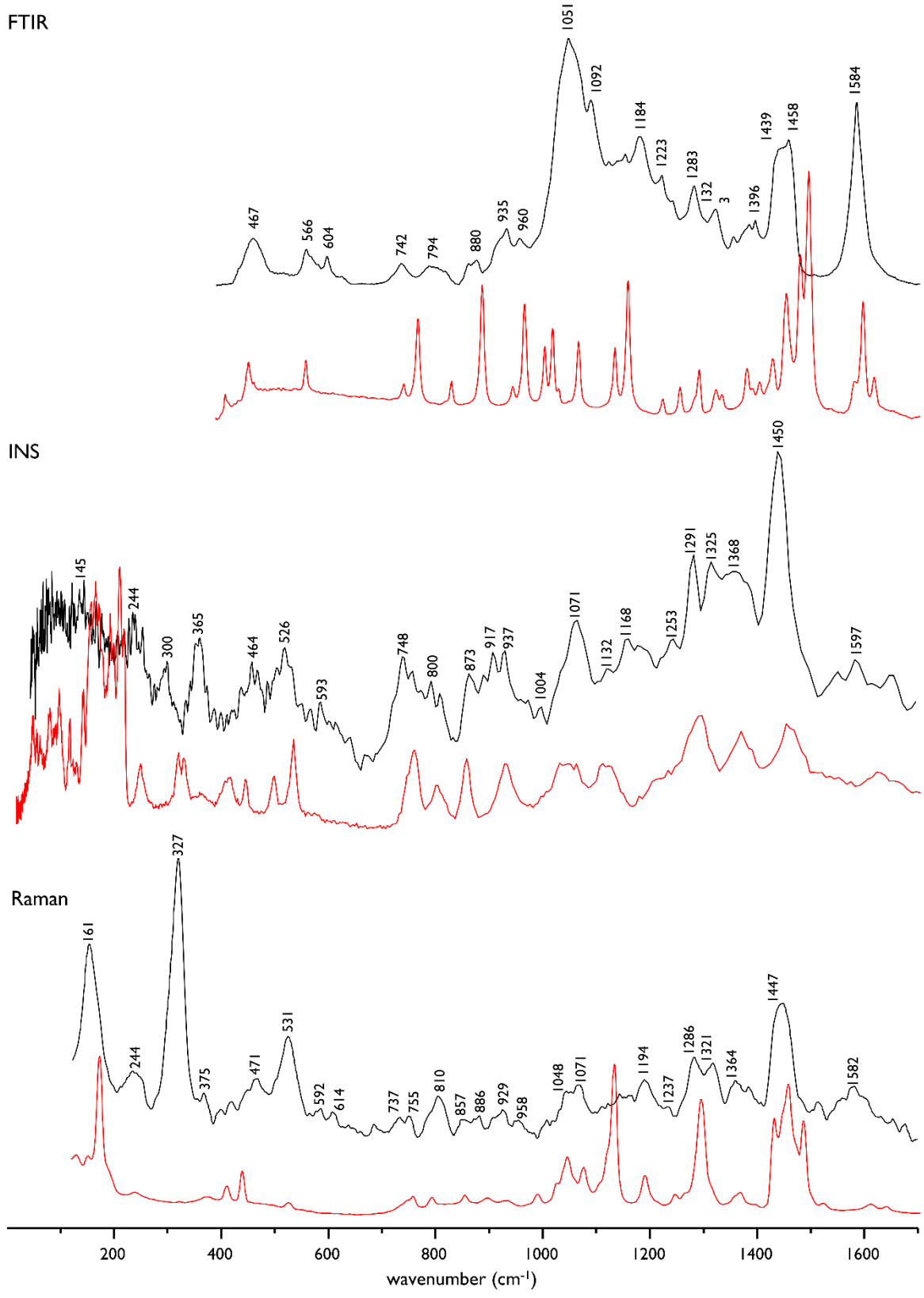

Figure 28 – Experimental Raman, FTIR and INS spectra (0-1700 cm^{-1}) for Pt_2Spm (black) and Spm (red).

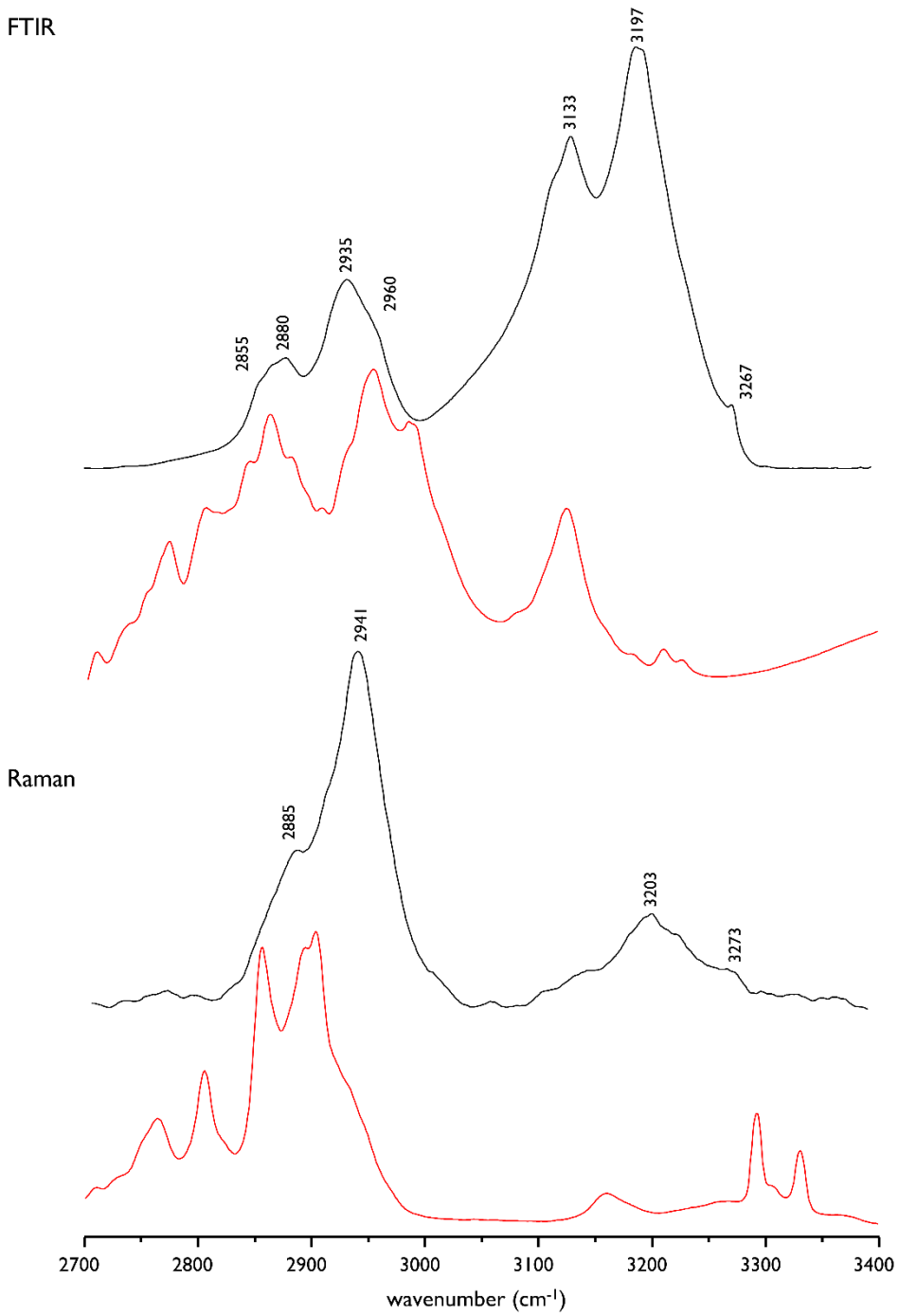

Figure 29 – Optical vibrational spectra (2700-3400 cm^{-1}) for Pt_2Spm (black) and Spm (red).

The CH_2 stretching modes of the intramolecular ring moiety within the Pt_2Spm chelate (Figure 9), at 2885 and 2941 cm^{-1} in the Raman spectrum, were blue shifted relative to free spermine, which is a clear proof of metal coordination. A similar behaviour was observed for PtDap.

The INS spectrum allowed an unequivocal identification of both CH_2 and NH_2 rocking modes (not clearly detected by the optical techniques), as well as of the torsion bands from

the intramolecular ring structures formed upon complexation. These were also recognised in PtDap, that accurately represents this moiety (Figure 9).

Table 6 – Experimental (INS, Raman, FTIR) vibrational wavenumbers (cm^{-1}) for Pt_2Spm, and comparison with the main features for cisplatin and PtDap.

(The most representative wavenumbers for the complex are in bold face).

Pt_2Spm			[a]Calc.	Sym. species	[b]cisplatin			PtDap			[c]Approximate description
Experimental					Experimental			Experimental			
Raman	FTIR	INS			Raman	FTIR	INS	Raman	FTIR	INS	
3273			3261	A_g				3265			$\nu_{as}NH_2$
	3267		3261	A_u					3242		$\nu_{as}NH_2$
3203			3166	A_g				3198			ν_sNH_2
			3164	A_g							νNH
	3197		3166	A_u							ν_sNH_2
			3164	A_u							νNH
	3133										$2x\delta_s(NH_2)$ FR $\nu_s(NH_2)$
			3001	A_u							$\nu_{as}CH_{2\ (ring)}$
			3001	A_g							$\nu_{as}CH_{2\ (ring)}$
	~2960		2992	A_u							$\nu_{as}CH_{2\ (chain)}$
			2990	A_u							$\nu_{as}CH_{2\ (ring)}$
			2990	A_g							$\nu_{as}CH_{2\ (ring)}$
			2982	A_g							$\nu_{as}CH_{2\ (chain)}$
2941		**2940**	2971	A_g				**2956**	**2953**		$\nu_{as}CH_{2\ (ring)}$
	2935		2969	A_u							$\nu_{as}CH_{2\ (ring)}$
			2974	A_u							$\nu_{as}CH_2$
			2963	A_g							$\nu_{as}CH_{2\ (chain)}$
	2880		2931	A_u							$\nu_sCH_{2\ (chain)}$
			2930	A_u							$\nu_sCH_{2\ (ring)}$
2885			2930	A_g				**2890**	**2890**		$\nu_sCH_{2\ (ring)}$
			2925	A_g							$\nu_sCH_{2\ (ring)}$
	~2867		2925	A_u							$\nu_sCH_{2\ (ring)}$
			2921	A_g							$\nu_sCH_{2\ (chain)}$
	~2855		2913	A_u							$\nu_sCH_{2\ (ring)}$
			2913	A_g							$\nu_sCH_{2\ (ring)}$
			2903	A_g							$\nu_sCH_{2\ (chain)}$
			2903	A_u							$\nu_sCH_{2\ (chain)}$
	1584	1597	1580	A_u	1601		~1595		1586	1588	δNH_2 (δNH_3)
1582			1580	A_g							δNH_2
			1463	A_u							$\delta CH_{2\ (chain)}$
			1457	A_g							$\delta CH_{2\ (chain)}$
	1458		1454	A_u							$\delta CH_{2\ (ring)}$
			1454	A_g							$\delta CH_{2\ (ring)}$
	1446	1450	1441	A_u				1458	1462	1458	δCH_2
1447			1439	A_g							$\delta CH_{2\ (ring)} + \beta N^2H$
	1439		1438	A_u							$\delta CH_2 + \beta N^2H$
			1436	A_g							$\delta CH_2 + \beta N^2H$
	~1433		1436	A_u							$\delta CH_{2\ (ring)}$
			1435	A_u							$\beta N^2H + \delta CH_2$

			1435	A_g							$\beta N^2H + \delta CH_2$
			1435	A_g							δCH_2
	1396		1380	A_u				1398	1395		$\omega CH_{2\ (ring)}$
		1390	1383	A_g							ωCH_2
1387			1376	A_g							ωCH_2
	1385		1369	A_u							ωCH_2
1364		1368	1367	A_g							$\omega CH_2 + \delta C^4N^2H$
	1355		1354	A_u							$\omega CH_2 + \delta C^4N^2H$
			1337	A_g							$\omega CH_{2\ (ring)}$
	1323	1325	1336	A_u					1330	1331	$\omega CH_{2\ (ring)}$
1321			1311	A_g							$tCH_{2\ (ring)} + \omega CH_{2\ (chain)}$
			1301	A_u							tCH_2
1286		1291	1295	A_g				1288	1290	1287	$tCH_{2\ (ring)} + \omega CH_{2\ (chain)}$
	1283		1292	A_u							$tCH_{2\ (chain)}$
			1285	A_g							$tCH_{2\ (chain)}$
			1265	A_g							tCH_2
			1265	A_u							tCH_2
	1243	1253	1259	A_u				1254	1254	1254	$tCH_{2\ (ring)}$
			1258	A_g							$tCH_{2\ (ring)} + tNH_2$
1237			1234	A_g							$tCH_{2\ (chain)}$
	1223	1231	1223	A_u							$\omega CH_{2\ (chain)}$
1194		1188	1188	A_g							ωNH_2
	1184		1186	A_u							ωNH_2
			1190	A_u							$tCH_{2\ (chain)} + tNH_2$
1166		1167	1168	A_g							$tNH_2 + \rho CH_{2\ (chain)}$
	1125	1132	1128	A_u				1126	1127	1134	$\delta PtN^1\text{-}H^1$
1125			1121	A_g							$\delta PtN^1\text{-}H^1 + \delta PtN^2\text{-}H$
1114			1107	A_g							$\nu_aN^2\text{-}C^3\text{-}C^2 + \omega NH_2$
	1092		1104	A_u							$\delta PtN^2\text{-}H + \nu_aN^2\text{-}C^3\text{-}C^2$
1071	~1065	1071	1068	A_u							$\delta PtN^2\text{-}H + tCH_{2\ (chain)}$
			1056	A_g							$\nu_aN^1\text{-}C^1\text{-}C^2 + \delta PtN^2\text{-}H$
	1051	~1050	1054	A_u				1040	1037	1042	$\nu_aN^1\text{-}C^1\text{-}C^2 + \delta PtN^2\text{-}H$
1048			1051	A_g							$\nu N^1\text{-}C^1 + \nu N^2\text{-}C^3 + \nu C^4\text{-}C^5$
			1049	A_g							$\delta PtN^2\text{-}H$
			1042	A_g							$\nu C^5\text{-}C^6 + \nu N^2\text{-}C^4$
			1034	A_u							$\delta PtN^1\text{-}H^2$
1012			1023	A_g							$\delta PtN^1\text{-}H^2$
		1004	1021	A_u							$\nu C^4\text{-}C^5 + tNH_2$
958			964	A_g							$\nu N^2\text{-}C^3 + \nu C^4\text{-}C^5 + tNH_2$
	960		949	A_u							$\nu N^2\text{-}C^3 + tNH_2$
	935	937	928	A_u				943	949 943sh	945	$\nu N^1\text{-}C^1 + \nu N^2\text{-}C^3 + \rho CH_2$
929			920	A_g							$\nu N^1\text{-}C^1 + \nu N^2\text{-}C^3 + \rho CH_2$
	~920	917	912	A_u							$\rho CH_2 + tCH_2\ \delta PtNH$
886		873	901	A_g					901	900	$\rho CH_{2\ (ring)} + \delta PtNH$
	880		892	A_u							$\rho CH_2 + tCH_2$
857			857	A_g							$\rho CH_{2\ (ring)}$
	866		853	A_u							$\rho CH_{2\ (ring)}$

	794	800	789	A_u							$\nu_s C^1\text{-}C^2\text{-}C^3$
810		818	787	A_g				817	815	813	$\nu_s C^1\text{-}C^2\text{-}C^3$
755		765	775	A_g							$\rho CH_{2\ (chain)}$
	742	748	756	A_u				763	758sh	757	ρNH_2
737			755	A_g							ρNH_2
			710	A_u							$\rho CH_{2\ (chain)}$
	604 566		595	A_u							$\delta N^2C^3C^2$
614 592		593	587	A_g							$\delta N^2C^3C^2$
531		**526**	530	A_g	**524**		**521**	**532**	**527**	**535**	$\delta C^3N^2C^4 + \delta C^4C^5C^6 + \nu PtN^2$
			509	A_u							$\delta N^1C^1C^2 + \nu PtN^1$
			508	A_g							$\delta N^1C^1C^2 + \nu PtN^1$
		464	496	A_u							$\nu_a NPtN + \delta C^3N^2C^4C^5$
471	467		482	A_u				488			$\nu_s NPtN + \delta C^1C^2C^3$
			464	A_g				481sh		477	$\nu_s NPtN + \delta C^1C^2C^3$
			437	A_u							$\delta C^1C^2C^3 + \delta C^4C^5C^6$
375	-		379	A_g							$\delta C^4C^5C^6 + \gamma$ ring
	-	365	360	A_u							γ' ring
	-		354	A_g							γ ring
	-		341	A_u							ν_s Cl-Pt-Cl
327	-		340	A_g	**323**		**~330**				ν_s Cl-Pt-Cl
			332	A_g							ν_{as} Cl-Pt-Cl
	-		332	A_u							ν_{as} Cl-Pt-Cl
	-	300	312	A_g							$\delta N^2C^4C^5$
	-		293	A_u							γ' ring
244	-	**244**	247	A_g				**246**		**249**	δNPtN
	-		231	A_u							δNPtN
	-		226	A_g							γ ring
	-		218	A_u							γ (N-Pt-N)
	-		191	A_u							γ (Pt-N^1)
161	-		162	A_g							γ (Pt-N^1)
	-		155	A_g							γ C-C-C_{chain}
	-		154	A_u							γ C-C-C_{chain}
	-		147	A_g							γ C-C-C_{chain}
	-	~145	145	A_u							γ C-C-C_{chain}
	-		144	A_u							δ'Cl-Pt-Cl
	-		142	A_g							δCl-Pt-Cl

[a]Calculated at the LANL2DZ/6-31G* level, for the isolated molecule. Values scaled according to: 0.9499 for the bands above 700 cm^{-1} [283]; 0.920 for $\nu(NH_2)$; 0.933 for $\delta(NH_2)$; 0.986 for $\omega(NH_2)$ and $\rho(NH_2)$ [289]; [b]according to reference [284]. [c]ν – stretching; δ – in-plane deformation; β – parallel bending; ρ – rocking; t – twisting; γ and γ' – in phase and out of phase out-of-plane deformation; *s*, *as*, and *a* refer to symmetric, antisymmetric and asymmetric modes, respectively. Numbering according Figure 9.

Previous studies carried out by QFM-UC elements on biogenic polyamines [286,288] demonstrated that INS is a particularly suited technique to detect low frequency vibrational modes in these highly hydrogenated compounds, namely their characteristic transverse and longitudinal acoustic modes (TAMs and LAMs, respectively). In the Pt_2Spm chelate, however, since the two metal centres are linked by the tetraamine ligand (Figure 9), the low frequency

vibrations of the chain are not real TAM and LAM modes, the polyamine being anchored by coordination to the two Pt(II) ions.

Interestingly enough, the Raman data allowed to discriminate the distinct Pt-N stretching frequencies due to the different environments in Pt-N^2 and Pt-N^1 (Figure 9). As a consequence, these modes are non-degenerate and it was possible to identify more than the two bands assigned to the symmetric and antisymmetric stretching modes, which would be the only ones detected if the complex had identical symmetry regarding both metal-nitrogen bonds (for each coordination site).

The full conformational characterisation of this type of Pt(II)-amine compounds, will help to clarify their mechanism of action within a biological matrix (*e.g.* a cell) and expose the molecular basis of their cytotoxicity, thus contributing for a tailored design of new and more efficient cisplatin-like anticancer agents.

3.2. Antitumour Activity

3.2.1. Anti-proliferative

Since combination schemes of the Pt(II) agent will be assessed along this work, confirmation of the high anti-proliferative profile of DTX against the MDA-MB-231 cell line was carried out. Although DTX was not found (through the SRB assay [214]) to be very effective at the lowest concentration tested ($1.0x10^{-2}$ μM), for the two highest dosages ($4x10^{-2}$ and $8x10^{-2}$ μM) it showed a dramatic effect within 24 h of exposure (Figure 30(A)).

Concerning the Pt_2Spm compound, the IC_{50} was found to be 9.5 μM at 48 h, much higher than the value obtained for Pd_2Spm (2.9 μM at 48 h, Table 7). The latter is in good accordance with previously reported results for the same cell line, at a different incubation time (24 h, [11]). In fact, this Pd(II) complex had previously been shown to exert a higher cytotoxic effect than the well-established cisplatin drug (for the same concentration range), not only against the oestrogen-unresponsive MDA-MB-231 cells but also towards the oestrogen-responsive MCF-7 cell line [104]. In the present study, comparison of the effects of Docetaxel and Pd_2Spm against the triple-negative breast cancer cells (MDA-MB-231) clearly evidenced that while the Pd-agent induced an increasing anti-proliferative activity at all the dosages tested, for DTX a

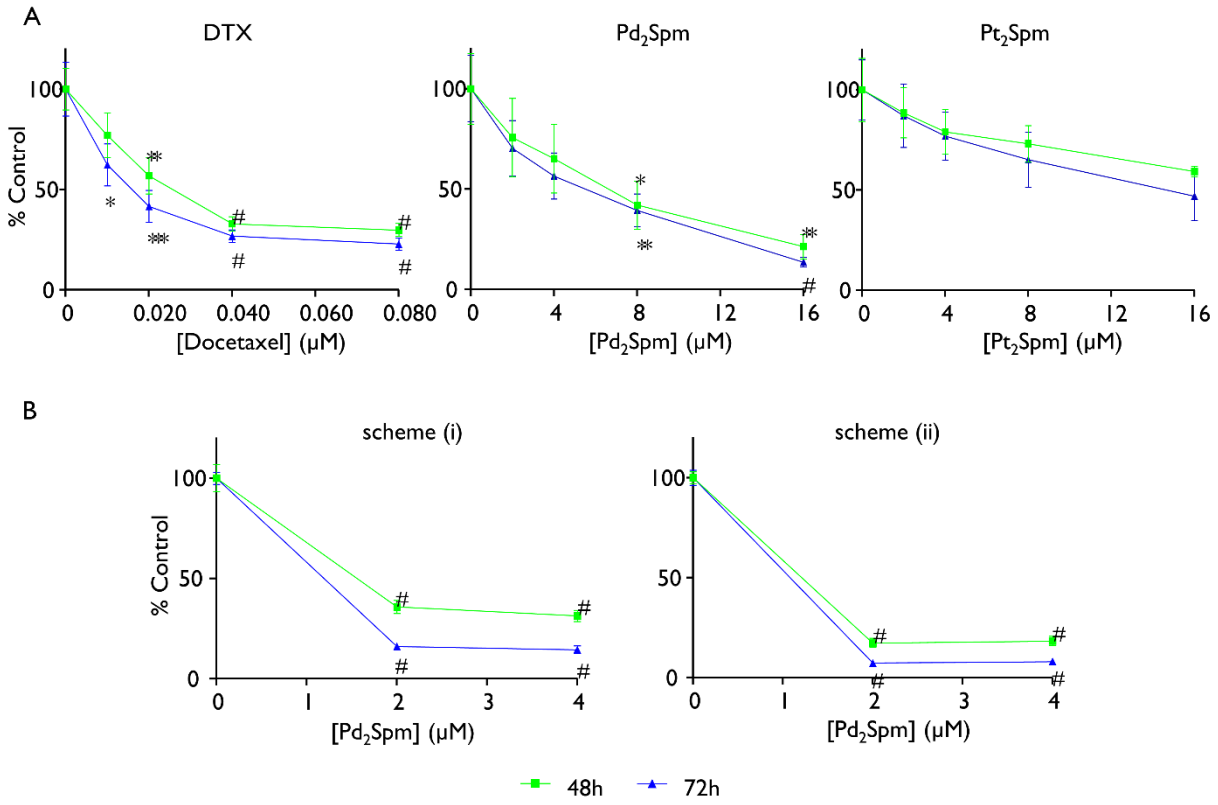

Figure 30 – Anti-proliferative assays for the MDA-MB-231 cell line upon exposure to Pt_2Spm, Pd_2Spm, DTX or Pd_2Spm/DTX. Simple proliferation of MDA-MB-231 cells: (A) – treated with either DTX (1 to $8x10^{-2}$ μM), Pt_2Spm or Pd_2Spm (1 to 16 μM), in sole administration; (B) – simultaneously exposed to $1x10^{-2}$ μM DTX, and to 2 or 4 μM Pd_2Spm (scheme(i)) or initially exposed to DTX ($1x10^{-2}$ μM) for 24 hours, and then to Pd_2Spm (2 or 4 μM) (scheme (ii)).

The results are expressed as a percentage of the control ± SEM. The one-way ANOVA statistical analysis was used, and the Dunnett's post-test was carried out to verify the significance of the obtained results (*$p<0.05$, **$p<0.01$, ***$p<0.001$, #$p<0.0001$ *vs* the control, for the same time-points).

Table 7 – IC_{50} values for Pd_2Spm, DTX and Pd_2Spm/DTX combination against the MDA-MB-231 cell line.

Therapeutic scheme	IC_{50} (μM)	
	48 hours	72 hours
Sole administration		
DTX	$1.5x10^{-2}$	$1.0x10^{-2}$
Pd_2Spm	2.9	2.9
Pt_2Spm	9.5	8.5
Pd_2Spm/DTX combination (scheme i)	$3.0x10^{-1}$	1.2
Pd_2Spm/DTX combination (scheme ii)	$2.5x10^{-2}$	$2.4 x10^{-2}$

IC_{50} values calculated according to [275].

plateau was attained, the highest effect being measured for a $4x10^{-2}$ μM concentration and remaining unaltered at $8x10^{-2}$ μM (Figure 30(A)). The effect of the platinum analogue against the TNBC cells, in turn, although still concentration-dependent, was much lower when compared to the Pd-agent. Therefore, the subsequent studies were performed only for Pd_2Spm (Figure 30(A)).

In turn, a high antitumour activity was verified for the Pd_2Spm/DTX combination schemes, their growth-inhibiting effect towards the MDA-MB-231 cells having been evaluated through two distinct procedures: (i) the cells were exposed to both drugs at the same time (DTX – $1x10^{-2}$ μM / Pd_2Spm – 2 to 4 μM); (ii) the cells were previously sensitised with DTX – $1x10^{-2}$ μM and then exposed to two different concentrations of Pd_2Spm. Figure 30(B) shows that both schemes led to a higher cytotoxicity when compared to each drug in sole administration, which was confirmed by the evaluation of synergism (Table 8) through the analyse of the correspondent isobologram. An obvious synergetic activity was observed, leading to much lower IC_{50} values relative to those ascribed to either the Pd(II) complex or DTX alone. Additionally, pre-sensitisation with DTX (for 24 h) prompted a more pronounced effect than the simple co-administration of both drugs, although the molecular basis for this sensitisation still remains to be elucidated. Overall, combination between the metal-based agent and the taxane prompted a striking enhancement in cell growth inhibiting efficiency for this type of invasive breast cancer.

Table 8 – Pd_2Spm/DTX synergetic effect towards the MDA-MB-231 cell line, evaluated by the SRB method (scheme (i)).

Drugs	Effect
$1x10^{-2}$ μM DTX / 2 μM Pd_2Spm	Synergism
$1x10^{-2}$ μM DTX / 4 μM Pd_2Spm	Synergism

3.2.2. Anti-invasive

The anti-invasive ability of the tested antineoplastic agents against MDA-MB-231 cells was measured using the transwell migration technique [236]. The cells were treated for 72 h with either DTX ($1x10^{-2}$ μM) or Pd_2Spm (4 μM), in sole administration, as well as with

Pd_2Spm/DTX combinations (1 μM/1x10^{-2} μM). Matrigel™ coated inserts were used to assess whether these treatment schemes affected cancer cell migration and adhesion.

Histological images revealed that in the presence of DTX, both *per se* (1x10^{-2} μM) or combined with Pd_2Spm, a sparse number of cells spread through the membrane, up to 7.2%, whereas for Pd_2Spm alone a significantly smaller amount of cells were counted in the lower chamber (43.8%) relative to the control (Figure 31(A)). Nevertheless, even at 4 μM, the Pd(II) complex was able to prevent cell migration and adhesion (Figure 31(B)). In turn, combined Pd_2Spm/DTX (1 μM/1x10^{-2} μM) administration effectively inhibited cell invasion, as compared to the control (Figure 31(B)).

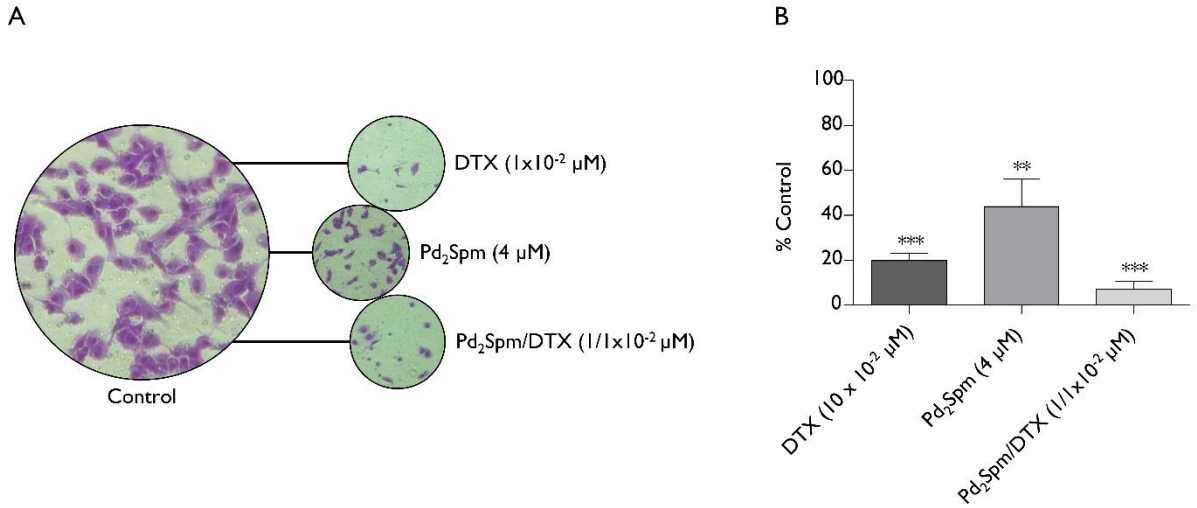

Figure 31 – Anti-invasive assays on Matrigel™ for the MDA-MB-231 cell line, upon exposure to DTX (1x10^{-2} μM), Pd_2Spm (4 μM) or Pd_2Spm/DTX (1 μM/1x10^{-2} μM). Microscopic image (x10) of crystal violet stained MDA-MB-231 cells treated with the therapeutic schemes under study (A); cell quantification by simple counting (B). The results are expressed as a percentage of the control ± SEM. The one-way ANOVA statistical analysis was used, and the Dunnett's post-test was carried out to verify the significance of the obtained results (**p<0.01, ***p<0.001 *vs* the control, for the same time-points).

These results clearly evidenced that the Pd_2Spm/DTX combination is efficient as an anti-invasive strategy, and more effective than either Docetaxel and Pd_2Spm in sole administration, although both displayed a considerable anti-invasive capacity *per se*. This synergetic effect, coupled with that already detected for anti-proliferative capacity, is of paramount relevance for a potential application of these compounds as effective antitumour agents, since their combination schemes (at the dosages and incubation times presently assessed) appear to exert both growth inhibiting and anti-invasive activities against low prognostic TNBC.

3.2.3. Anti-angiogenic

The impact of Pd_2Spm and DTX, either *per se* or in combination, on angiogenesis modulation was assessed by the CAM assay. Several parameters were evaluated: (i) number of extremities, branches and junctions – in order to determine if the vessels were multiplying; (ii) total length, total branching length and total branches length – to assess spreading of the vessels. Both multiplication and spreading were found to decrease in a concentration-dependent manner, in comparison to values obtained for both the control (PBS, where normal development of egg neovascularisation occurred) and VEGF conditions (for which neovascularisation was stimulated). The effect elicited by increasing concentrations of Pd_2Spm is depicted in Figure 32.

The angiogenesis inhibition caused by DTX [290-292], also measured by the CAM assay, was greatly enhanced by the presence of the Pd(II) agent. Actually, although increasing concentrations were tested for DTX in sole administration ($1x10^{-2}$ to $4x10^{-2}$ μM, corresponding to those commonly used in the clinical practice [293,294]), a significant anti-angiogenic effect was only observed at the highest concentration, for all parameters tested (Figure 32). In turn, in sole administration, Pd_2Spm-prompted inhibition of angiogenesis was very effective: 81.8±4.4% for total length values, at 4 μM, when compared to the 26.4±14.4% DTX-triggered at the clinically used dosage of $4x10^{-2}$ μM (n=4 to 11).

Furthermore, Pd_2Spm/DTX combinations were assessed, in search for an additive or synergistic interaction between both drugs (Figure 33). This association prompted an increase of the anti-angiogenic effect when compared to that due to each individual compound: 77.7±11.2% for total branching length values *vs* 42.5±14.9% and 49.5±11.5% for DTX and Pd_2Spm alone, respectively. At lower concentrations, Pd_2Spm – 1 μM/DTX – $1x10^{-2}$ μM, a statistically significant reduction in blood vessels development was observed when compared to the control: above 50% in the number of extremities (51.6±12.3%), nodes (60.1±9.5%) and branches (58.0±12.6%). Similar results were obtained with total branching length (64.6±11.2%), total branches length (67.0±9.8%) and total length (58.7±9.7%) (n = 4 to 11).

A synergetic effect between Pd_2Spm and DTX was thus identified from the CAM assays (Table 9). An isobologram for the two drugs (Pd_2Spm and DTX) was analysed, for each parameter (Table 9), unveiling a clear synergism between both drugs.

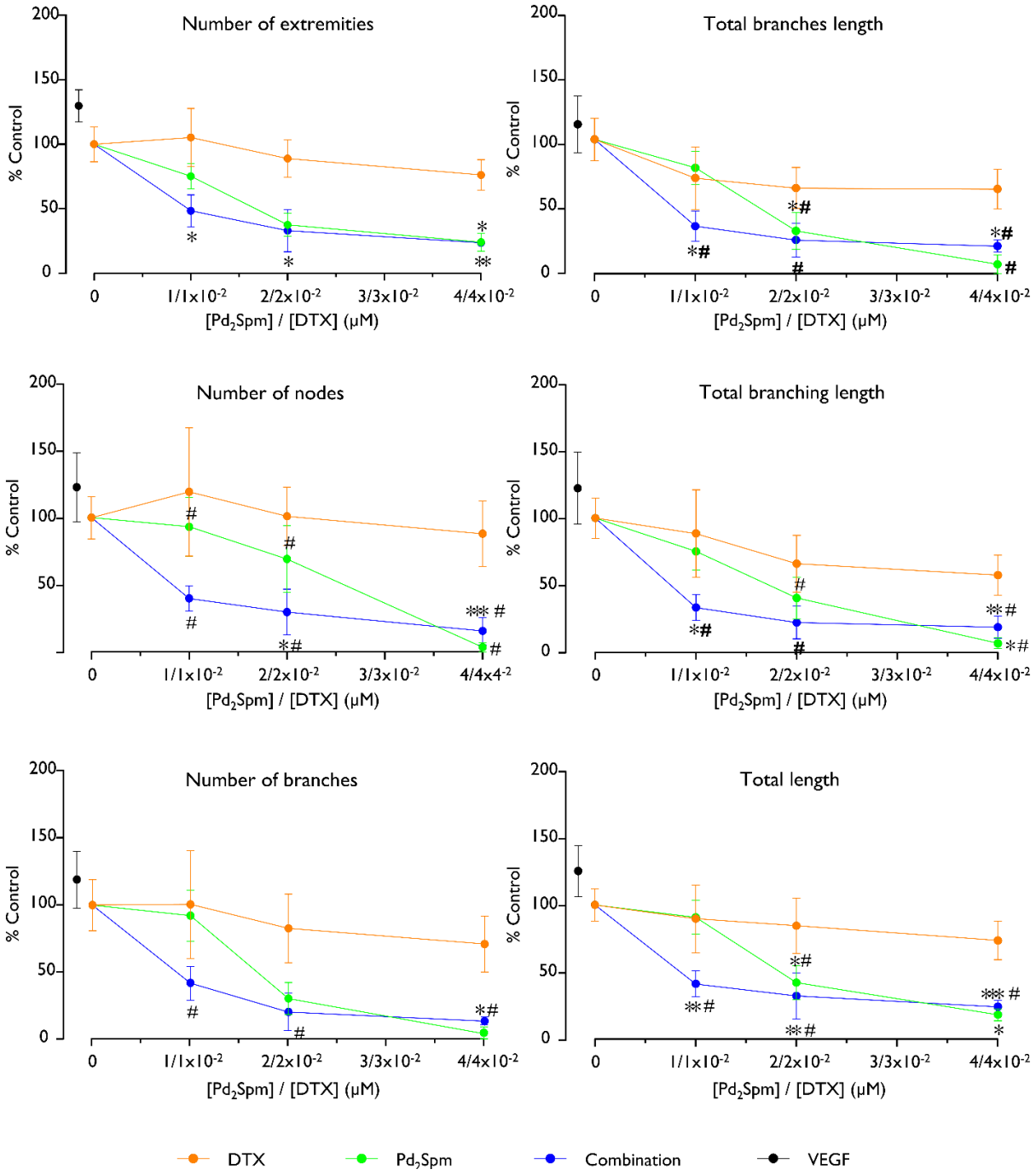

Figure 32 – Quantitative CAM angiogenesis results in the presence of increasing concentrations of DTX, Pd_2Spm and Pd_2Spm/DTX (according to 2.2.3.3., Experimental section). The results are expressed as a percentage of the control ± SEM. The one-way ANOVA statistical analysis was used, and the Dunnett's *post*-test was carried out to verify the significance of the obtained results (*p<0.05, **p<0.01, ***p<0.001 *vs* the control and #p<0.05 *vs* the VEGF).

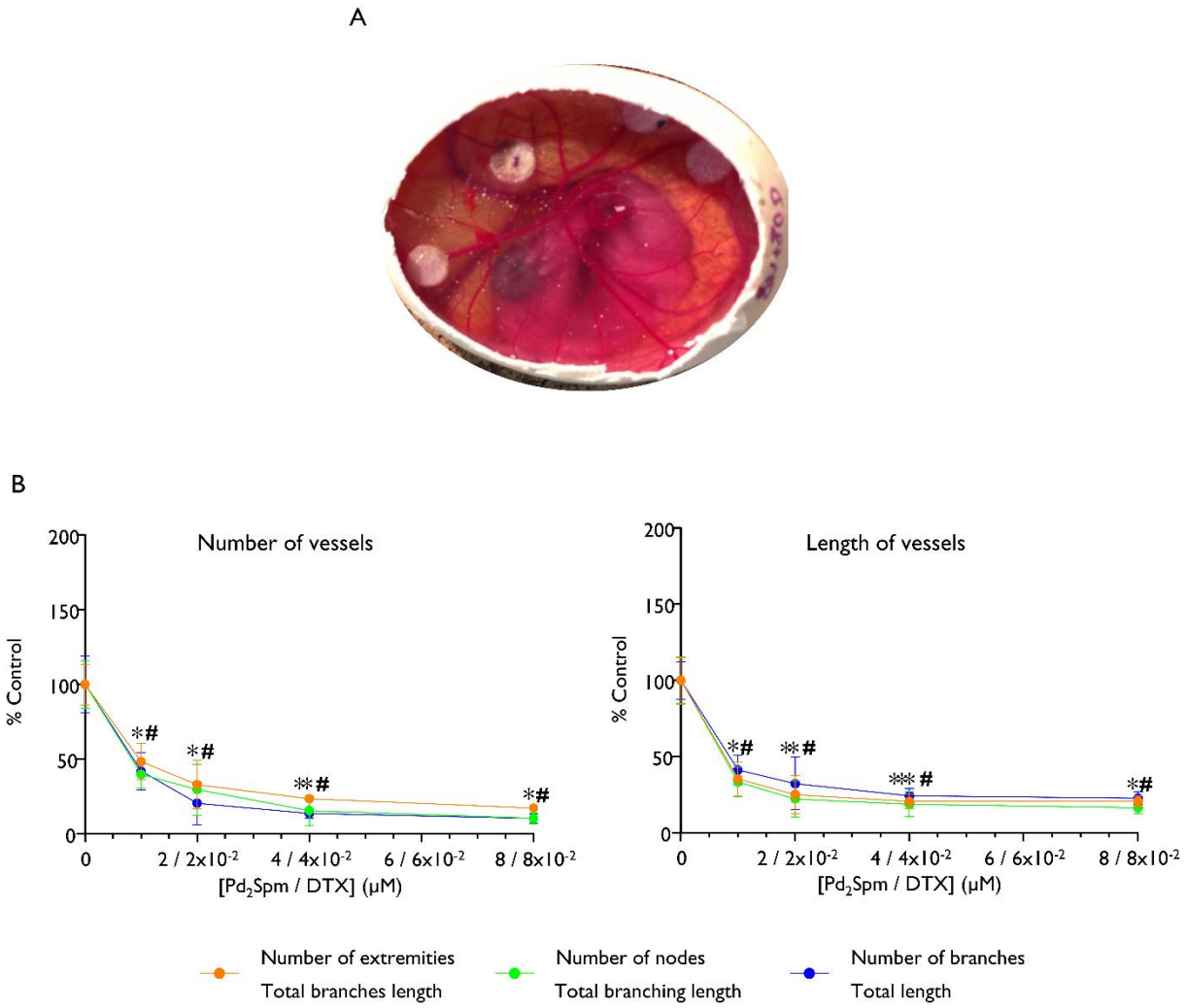

Figure 33 – Combination effect of DTX and Pd_2Spm on CAM angiogenesis (according to 2.2.3.3., Experimental section). (A) – representative digital CAM image; (B) –anti-angiogenic effect in the presence of increasing concentrations of Pd_2Spm/DTX. The results are expressed as a percentage of the control ± SEM. The one-way ANOVA statistical analysis was used, and the Dunnett's post-test was carried out to verify the significance of the obtained results (*p<0.05, **p<0.01, ***p<0.001 *vs* the control and #p<0.05 *vs* the VEGF).

The currently measured anti-angiogenic effect was distinct for the Pd_2Spm and DTX compounds. The latter was unable to supress proliferation of endothelial cells (a required condition to hinder formation of new vessels), which was evidenced by its inability to alter the number of vessel extremities, nodes or branches. Therefore, the rather low DTX anti-angiogenic effect presently determined can only be assigned to its capacity to inhibit formation of tubular-like structures, reflected in the slight detected reduction of the total branches length, total branching length and total length. By opposition, Pd_2Spm revealed a high efficacy in supressing both endothelial cell proliferation and tubules development. A synergetic effect

Table 9 – Pd_2Spm/DTX synergetic effect evaluated by the CAM assay.

Parameter Analysed	IC_{50}			Synergism
	DTX ($x10^{-2}$ µM)	Pd_2Spm (µM)	Pd_2Spm (µM)/DTX ($x10^{-2}$ µM)	
Number of Extremities	1.9	1.3	0.7	Yes
Number of Nodes	1.9	2.3	0.6	Yes
Number of Branches	1.9	1.6	0.7	Yes
Total Branches Length	0.6	1.5	0.5	Yes
Total Branching Length	1.5	1.5	0.4	Yes
Total Length	1.7	1.6	0.5	Yes

was observed for Pd_2Spm and DTX combined administration, leading to an effective anti-angiogenic role regarding endothelial cell invasion and migration, as well as tubules formation.

Furthermore, the effect of Pd_2Spm and DTX, *per se* or in association, on the activation of the vascular endothelial growth factor receptor 2 (VEGFR2) was assessed, since tyrosine kinase activation by VEGFR2 is one of the main pathways required for angiogenesis (proliferation, migration and vascular permeability). SU 5416 (IC_{50}=1 µM [295]), a known VEGFR2 inhibitor, was used as a positive control (inhibiting kinase activity) (Figure 34).

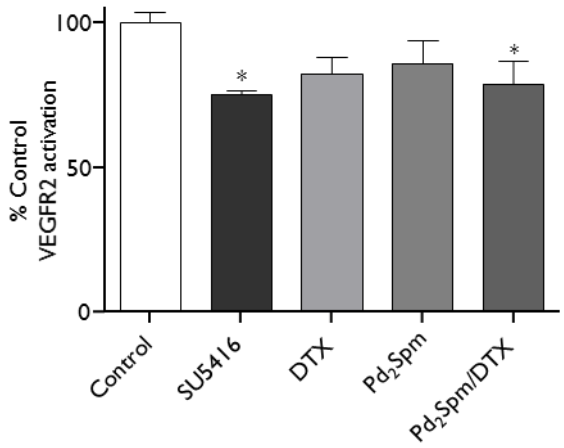

Figure 34 – Inhibition of VEGFR2 activity (determined by the CAM assay) in the presence of DTX, Pd_2Spm or Pd_2Spm/DTX (at IC_{50} concentrations) and SU 5416. The results are expressed as a percentage of the control ± SEM. The one-way ANOVA statistical analysis was used, and the Dunnett's post-test was carried out to verify the significance of the obtained results (*$p<0.05$ *vs* the control).

It was verified that only the concurrent administration of both drugs triggered a significant inhibitory effect: while Pd_2Spm and DTX in sole administration were able to slightly reduce VEGFR2 activation, the Pd_2Spm/DTX combination was shown to be much more effective (Figure 34). However, angiogenesis inhibition induced by Pd_2Spm/DTX combinations observed in the CAM assay was only partially endorsed to VEGFR2 tyrosine kinase activation.

Since the Pd_2Spm/DTX IC_{50} dosage caused only a 25% inhibition of the VEGFR2 pathway, it is suggested that additional mechanisms may be involved in angiogenesis promotion which are not targeted by the compounds under study, namely activation of the NRP1 (neuropilin 1) or the TIE 2/ANG (tyrosine kinase endothelial-2 /angiopoietin) 1/2 receptors [296,297].

The reported data confirms previous results that describe DTX´s anti-angiogenic effect in combination with other drugs (*e.g.* monoclonal antibodies such as the VEGF blocker bevacizumab). In fact, anti-angiogenic agents have been essentially used in joined administration with established cytotoxic chemotherapies. This is due to the fact that by normalising the vasculature around the tumour, the concentration of the chemotherapeutic agent in the diseased tissue is increased. In addition, anti-angiogenic drugs *per se* were shown to have limited survival benefits.

From all the analysed DTX concentrations, in sole administration, $4x10^{-2}$ μM was found to be the most effective dosage in supressing angiogenesis. The anti-angiogenic capacity elicited by the Pd(II) complex, in turn, was surprisingly high, even for the lowest dosage investigated (1 μM). This polynuclear Pd(II) complex was therefore shown to be a very promising antitumour agent, corroborating previous studies at QFM-UC reporting a high impact on proteins and DNA backbone [298] as compared to its Pt(II) homologue and cisplatin, as well as a significant effect on cell morphology particularly targeting the cytoskeleton (mostly the microtubules [104]). This effect is closely related to the prevention of formation of the tubular network needed for new vessel development [299] and may explain the anti-angiogenic effect presently observed (associated to the inhibition of tubular-like structure formation). Additionally, this marked synergetic effect between Pd_2Spm and Docetaxel may be justified through the cell sensitisation triggered by the metal-based agent, known to induce a severe DNA damage *via* direct coordination to the purine bases [71,104]. However, the exact mechanism of synergism between these two agents is still to clarify at the molecular level, and will be the goal of future studies.

Recently, a significant anti-angiogenic activity was reported for organoplatinum(II) complexes in human ovarian carcinoma [300], but no synergetic interactions with conventional drugs were searched for. The present synergetic effect regarding angiogenesis inhibition for Pd_2Spm/DTX combinations is a major conclusion aiming at the application of these combined

strategies against metastatic breast cancer, justifying further studies that include pre-clinical trials. In fact, although cisplatin/DTX combinations have been reported to display synergetic anti-proliferative and anti-angiogenic activities against human TNBC [301,302], no reports to combination therapies involving improved new-generation metal-containing drugs (namely Pd-based) and yielding synergism towards this type of cancer are to be found.

Following the studies on combination schemes of Paclitaxel with the monoclonal antibody bevacizumab, commonly used as a first-line therapy against metastatic breast cancer [303], the present study evidences the potential of combined administration of another taxane drug (Docetaxel) with a Pd(II)-spermine cisplatin-like agent that has previously shown to display promising cytotoxic properties against human invasive breast cancer, combined with less severe deleterious side effects [104]. Actually, this strategy couples the high cytotoxicity of the DNA-damaging polynuclear metal complex with the anti-angiogenic capacity of both the taxane derivative and the Pd-drug, turning Pd_2Spm into a dual cytotoxic and anti-angiogenic agent. Moreover, DTX is suggested to overcome the recognised VEGF-mediated protective role against Pt-drugs´ anti-proliferative activity (firstly reported for cisplatin-treated human ovarian carcinoma [304]), therefore enhancing Pd_2Spm-induced cell death.

3.3. Metabolic Impact on Cells

3.3.1. Raman Microspectroscopy

According to a former evaluation of the antitumour effect of Pt_2Spm and Pd_2Spm towards MDA-MB-231 cells, at different time-points and doses, carried out at QFM-UC [104] a 2 to 8 μM concentration range was chosen for the current spectroscopic study, for a drug-exposure period of 48 h, once these conditions correspond to an optimal drug effect. Hence, since IC_{50} will induce cell growth inhibition in half the population of the probed cells, higher concentrations (*ca.* twice the IC_{50} value) were also tested in order to better identify the drug-induced biochemical changes.

Spectral biochemical signatures of the cell, at each condition tested (type of drug and concentration), were generated by averaging the spectra acquired from different cellular locations. The data (both FTIR and Raman) were captured as single point spectra (Figure 35), across a cell population comprising randomly distributed cells displaying a high spectral

heterogeneity (also due to cells being in different points of the cell cycle). Therefore, a large number of data points was required, for the mean resulting spectrum to be representative of the sample. This procedure, as opposed to single cell spectral acquisition, minimises the effect of the cell cycle profile (predominantly G_1 under normal conditions).

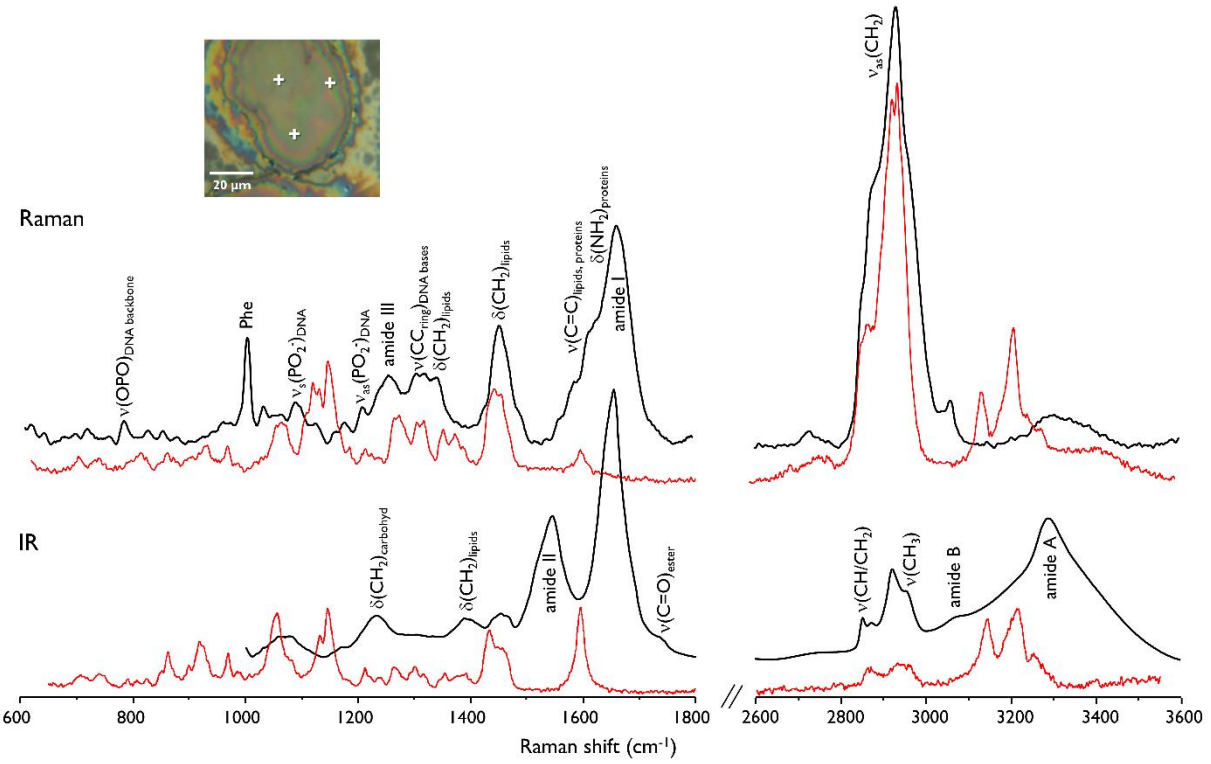

Figure 35 – Mean Raman (saline-dipped fixed cells, Horiba Jobin-Yvon T64000/514.5 nm) and infrared spectra (fixed cells, MIRIAM) for untreated MDA-MB-231 cells, and microscopic image of a cell (x100 magnification) showing some of the points at which data were captured. The spectra for Pd_2Spm are shown in red.

Cisplatin, a DNA major groove binder with a well characterised mechanism of action [305] (Figure 6) was used as a reliable control, its effect on the MDA-MB-231 cells being compared and correlated to that of the cisplatin-like dinuclear Pt(II) and Pd(II) chelates. Similarly, to cisplatin, these are expected to be cell-cycle non-specific agents, allowing their cellular impact to be accurately retrieved from analysis of the mean spectra currently recorded, which average out the possibly different chemical fingerprints from cells at different cell cycle stages within the probed population. The MDA-MB-231 cell line showed to be sensitive to both spermine complexes, which induced clear spectral changes (complementary Raman and infrared) in the wide range presently analysed (600-3600 cm^{-1}), enabling to identify specific features (biomarkers) associated with the biochemical effect of each investigated agent and the subsequent physiological response from the cell – spectral signature of drug action.

The cells were analysed upon chemical fixation with a 4% formalin solution. This type of biocompatible preservation method is intended to retain biochemical conditions as similar as possible to the native physiological state, for prolonged time periods, whilst minimising auto-fluorescence and avoiding contamination from the fixative. The effects of chemical fixation are known to be cell line- and fixative-dependent, but are still not fully characterised in the literature. Formalin is a widespread chemical fixative that causes cross-linking between the aldehyde and the primary and secondary amine groups of cellular proteins (*via* methylene bridges), creating a gel and thus retaining cellular constituents in a close to *in vivo* relationship. While no considerable effects of this fixation procedure have been observed in the IR spectra of single cells [306], it is expected to induce some reduction in vibrational band intensity, resulting from the disruption of lipid assembly and from changes in protein conformation (mainly reflected in the amide I and II bands). Nevertheless, formalin fixation has been found to be the best method for preserving cellular integrity with a weak impact on the overall molecular content and yielding the spectral profile closest to that observed in the live state (Figure 36), while hardly affecting discrimination between cells under distinct conditions

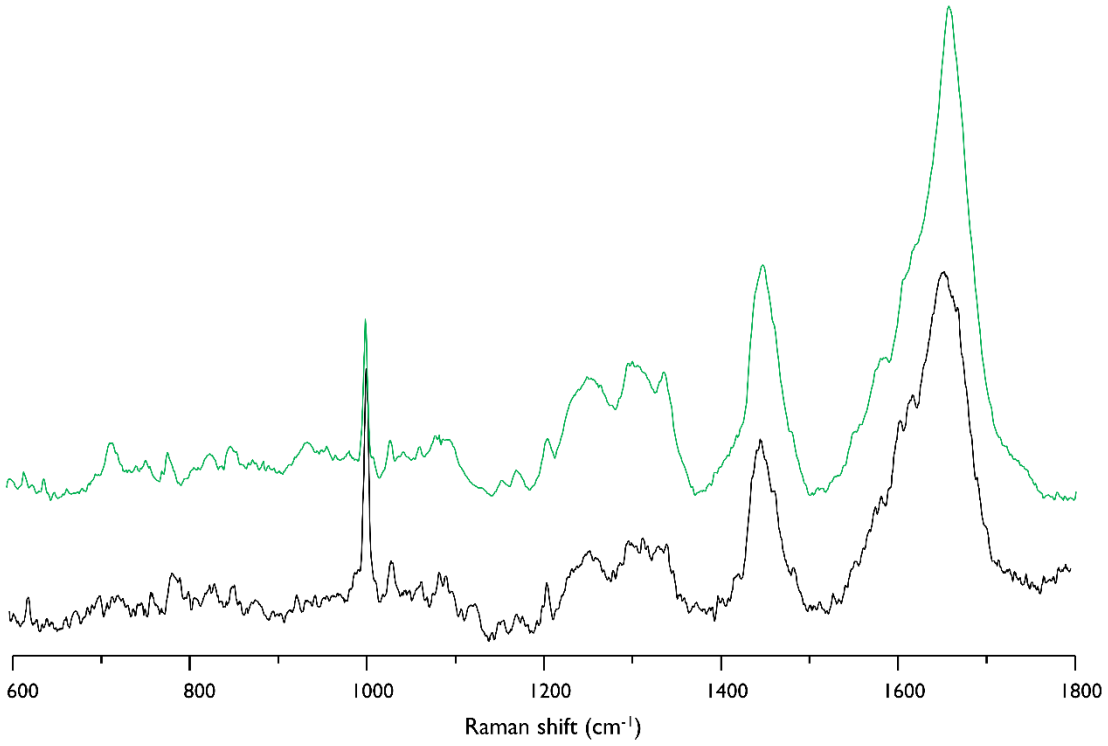

Figure 36 – Mean Raman spectra for saline-dipped fixed cells (black) and for saline-dipped live cells (green) (Horiba Jobin-Yvon T64000/514.5 nm) for untreated MDA-MB-231 cells.

(namely control and drug-exposed) [139,307-309]. No formalin contamination was verified in the measured spectral data, no signals being detected for its typical $t(CH_2)$, $\nu(CO)$ and $\delta(CH_2)$ modes at *ca.* 907, 1040 and 1490 cm^{-1}.

Despite the intense vibrational bands characteristic of the tested Pt(II) and Pd(II) agents within the currently probed spectral window (Figure 35 and Figure 37) [253,284], they were indiscernible intracellularly (either by FTIR or Raman), which can be explained by the low concentrations used (not exceeding 8 μM), coupled to intracellular chloride hydrolysis and strong interaction with their main pharmacological target (DNA) and other biomolecules [71,253,284]. Also, the vibrational modes involving the metal centre lie in the low frequency

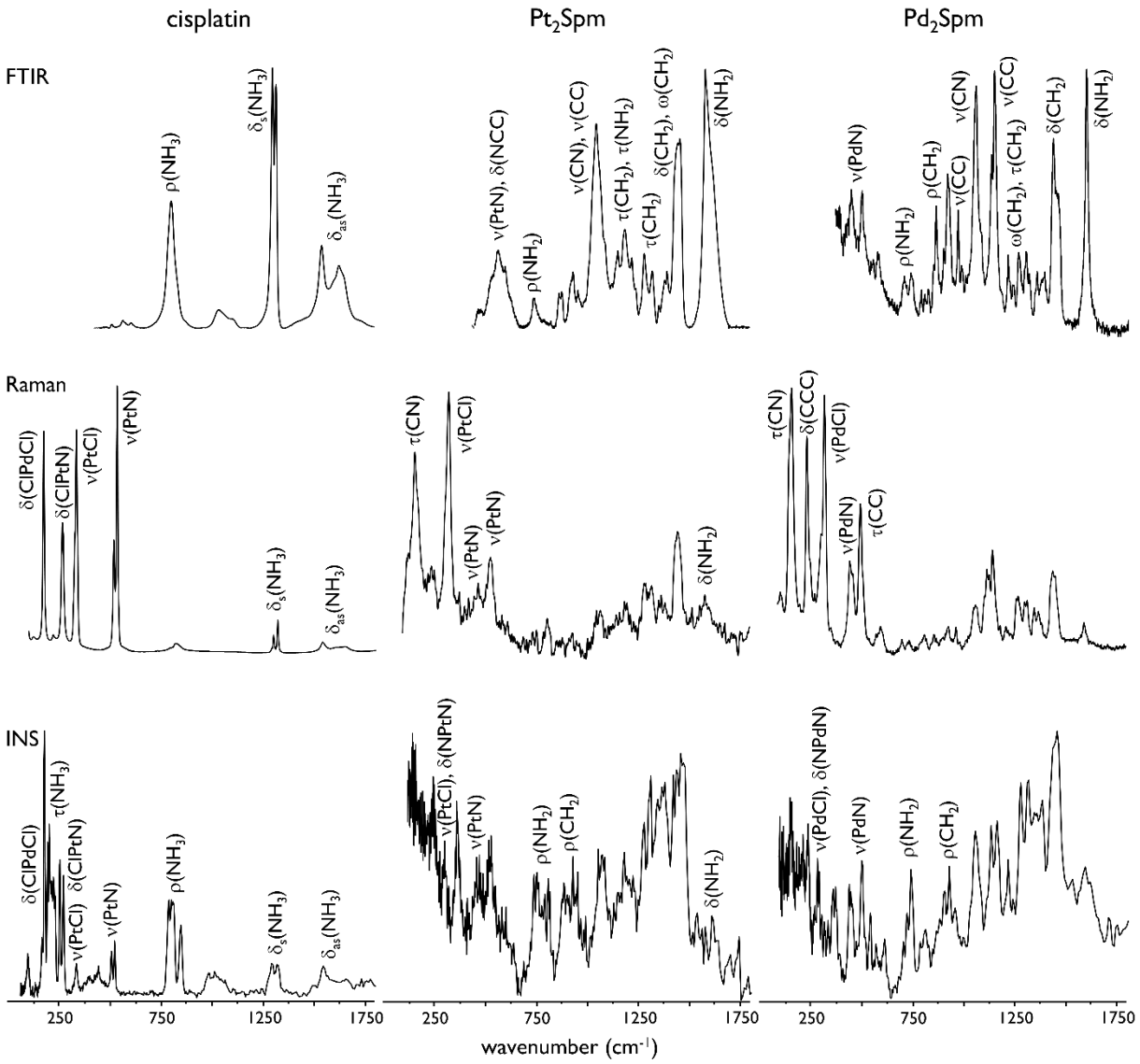

Figure 37 -Raman, FTIR and INS spectra of the complexes under study. (Data for cisplatin from [263,289]; data for Pd_2Spm from [253]).

region of the spectrum (below 550 cm^{-1}) which does not fall within the interval currently measured (>600 cm^{-1}). It should be noted, however, that the 1000-1800 cm^{-1} range may comprise features from the polyamine ligand within the dinuclear complexes [253], but these are overruled by the strong signals due to the cellular components (Table 10, Figure 35).

The Raman spectra of the MDA-MB-231 fixed cells, prior to drug administration (Figure 35), reflected a vibrational pattern consistent with a healthy state as opposed to dead cells [310,311], mainly evidenced by the DNA ν(O–P–O) backbone and ν(PO_2^-) modes (respectively at 785, and 1092/1237 cm^{-1}), the ν(O–P–O) features assigned to phosphorylated proteins (from 950 to 1250 cm^{-1}) and the protein amide I band (ν(C=O) at 1660 cm^{-1}). The DNA $\nu(O–P–O)_{backbone}$ is the most sensitive peak to recognise cell death, since this is accompanied by a breakdown of the phosphodiester bonds in the double helix, leading to a significant reduction (up to 80%) of the band´s intensity. The main Raman signals observed for untreated MDA-MB-231 cells are encompassed in Table 10. Assignment of the signals relied on reported studies on several cell lines and biomolecules [161,311,312]. Two different visible lasers were used for the acquisition of the Raman spectra, with 514 and 532 nm wavelengths (at QFM-UC and DLS, respectively). This very small energy difference in the incident radiations did not lead to significant changes in the intensity of the observed bands (the efficiency of the Raman scattering process depending on the fourth power of the excitation frequency). Moreover, data collection in either dry samples or saline-dipped cells did not elicit any significant variations in the spectral profile.

Spectra of drug-exposed cells after 48 h of incubation with cisplatin and the Pt- and Pd-spermine agents displayed marked differences relative to the non-exposed (control) cells, reflected in vibrational features associated with specific biomolecules. Additionally, a slight blue shift (*ca.* 2-3 cm^{-1}) was detected for some features assigned to proteins (ν(CN), amide I) and lipids (δ(CH_2/CH_3)), in agreement with previously reported studies [313,314]. Upon unsupervised PCA analysis, a more detailed picture of drug-impact on the cellular biochemical profile was attained. A drug-dependent response was verified, as depicted in Figure 38, which represents the mean Raman spectra measured for cells upon incubation with cisplatin, Pt_2Spm and Pd_2Spm, at 4 μM, and the difference spectra to the control, the corresponding PCA loading and score plots being shown in Figure 39.

Table 10 – Raman and infrared bands for live human breast cancer cells (MDA-MB-231).

Features from specific drug-prompted DNA and protein conformational rearrangements are presented in red. The signals exclusively detected by infrared are shaded in grey.

Band (cm^{-1})	[a]**Assignment**			
	Nucleic acids	Proteins	Lipids	Carbohydrates
622	Z-DNA/dG ($\nu(CC)_{ring}$)	Phe (t(CC))		
645		ν(CS), Tyr (t(CC))		
668	A-DNA/dG ($\nu(CC)_{ring}$)			
669	B-DNA/G,T ($\nu(CC)_{ring}$)			
678	B-DNA/A,G,T,C ($\nu(CC)_{ring}$)	Trp ($\nu(CC)_{ring}$)		
697-900			phosphate esters ($\nu_s(OPO)$)	
698	B-DNA/dG ($\nu(CC)_{ring}$)	Met (ν(CS))		
717			phosphocholine ($\nu(C–(CH_3)_3N^+)$	
728	B-DNA/A ($\nu(CC)_{ring}$)	Trp ($\nu_s(CC)_{ring}$)		
746	B-DNA/T ($\nu(CC)_{ring}$)	porphyrin ($\nu(CC)_{ring}$)		
749	Z-DNA ($\nu(OPO)_{backbone}$)			
757	B-DNA/dT ($\nu(CC)_{ring}$)	Trp ($\nu_s(CC)_{ring}$)		
782-795	C,T,U ($\nu(CC)_{ring}$)			
785	B-DNA ($\nu(OPO)_{backbone}$)			
792	Z-DNA ($\nu(OPO)_{backbone}$)			
805	A-DNA ($\nu(OPO)_{backbone}$)			
812	RNA ($\nu(OPO)_{backbone}$)	Pro, Tyr (ν(CC))		
830	B-DNA ($\nu(OPO)_{backbone}$)	Pro, Tyr (ν(CC))		
835-840	Z-DNA ($\nu(OPO)_{backbone}$)			Glu (δ(CCO))
855		Pro, Tyr, Val (ν(CC), δ(CCH))		polysaccharides (Υ(COC))
868	Z-DNA ($\nu(OPO)_{backbone}$)	Pro (ν(CC))		mono, disaccharides (ν(COC))
879	RNA (ribose, $\nu(CC)_{ring}$)	Tyr ($\nu(CC)_{ring}$), Hyp (ν(CC))	phosphocholine ($\nu_s(CCN^+)$)	ν(CC), $\nu(C\text{-}O)_{ring}$
883		$\rho(CH_2)$		
901	deoxyribose ($\nu(CC)_{ring}$)	ν(CC)	fatty acids (ν(CC), ν(CO))	ν(COC)
915	RNA (ribose, $\nu(CC)_{ring}$)			
920-940	B-DNA/deoxyribose ($\nu(CC)_{ring}$)	Pro (ν(CC))		Glu (ν(CC))
925-930	Z-DNA ($\nu(OPO)_{backbone}$)			
935-940		ν(CC) (α-helix)	glycolipids (ν(COC))	$\nu(COC)_{glycosidic}$
940	RNA/ribose ($\nu(CC)_{ring}$)			polysaccharides (skeletal modes)
950-1250		phosphorylated proteins (ν(OPO))		
951		$\nu_s(CH_3)$ (α-helix)		
965-973	DNA ($\nu(CC)/\nu(CO)_{backbone}$)			polysaccharides (δ(C=O))
974	RNA (ribose, $\nu(CC)_{ring}$)			
980		ν(CC) (β-sheet)	δ(C=CH)	
1003		Phe ($\nu_s(CC)_{ring}$)		
1032		Phe (δ(CH)), $\nu(O–CH_3)$	ν(CC), phospholipids (δ(CH))	ν(CC), ν(CO), ν(C–OH)
1050	RNA (ν(OPO))		phosphate esters ($\nu_{as}(OPO)$)	ν(C–OH)
1063	B-DNA/deoxyribose (ν(CO))	ν(CC), ν(CN)	ν(CC), ν(CO)	ν(CC), ν(CO), δ(OCH)
1082		ν(CC), ν(CN)	phospholipids ($\nu_s(PO_2^-)$)	glycogen (ν(CC), ν(CO))
1092	B-DNA ($\nu_s(PO_2^-)$)			
1095	Z-DNA ($\nu_s(PO_2^-)$)		ν(CC), ν(CN)	ν(CC), ν(CO)
1099	A-DNA ($\nu_s(PO_2^-)$)			
1127	RNA/ribose (ν(CO))	ν(CN)	$\nu(CC)_{acyl}$ (*trans* conformation)	ν(CO), ν(CC)
1157		ν(CC), ν(CN), $\delta(CH_2)$	$\delta(CH_2)$, $\nu(=C–C=)_{conjugated}$	$\delta(CH_2)$
1158		ν(CC), ν(CO), ν(CN)	phosphocholine ($\nu_s(N(CH_3)_3^+)$)	ν(CO)
1175	C,G,T ($\nu(CC)_{ring}$)	Tyr, Phe (δ(CH))		
1207		Hyp, Phe, Tyr (ν(CC))		
1220-1300		amide III (δ(NH), ν(CN))		
1229-1235		amide III/β-sheet		
1237	B-DNA ($\nu_{as}(PO_2^-)$)			
1240	RNA ($\nu(PO_2^-)$)			
1243-1259		amide III/random coil		
1242-1266	RNA/dT ($\nu(CC)_{ring}$)			
1247-1252	C ($\delta(NH_2)$)			
1252-1264	A,T ($\nu(CC)_{ring}$)	$\delta(CH_2)$, δ(C=C–H)	$\delta(CH_2)$, $\delta(C=C–H)_{phospholipids}$	$\delta(CH_2)$, $\omega(CH_2)$, $t(CH_2)$
1254	dC ($\nu(CC)_{ring}$)			
1270	RNA/C,U ($\nu(CC)_{ring}$)		phospholipds (δ(C=C))	
1272		amide III/α-helix	$\delta(CH_2)$, $\omega(CH_2)$, $t(CH_2)$	$\delta(CH_2)$, $\omega(CH_2)$, $t(CH_2)$
1300	RNA/A,C ($\nu(CC)_{ring}$)			
1318	G ($\nu(CC)_{ring}$)	$\delta(CH_2)$	$\delta(CH_2)$	$\delta(CH_2)$
1323	G ($\nu(CC)_{ring}$)			
1339	G ($\nu(CC)_{ring}$)			
1340	A,G ($\nu(CC)_{ring}$)	$\delta(CH_2)$, Trp ($\nu(CC)_{ring}$)		$\delta(CH_2)$
1375	A,G,T ($\nu(CC)_{ring}$)	glycoproteins ($\delta(CH_3)$)	lipids/acyl chains ($\delta(CH_3)$)	saccharides ($\delta(CH_2)$)
1396		$\delta(CH_2)$, $\rho(CH_2)$	membrane lipids ($\delta(CH_2)$)	$\delta(CH_2)$, $\rho(CH_2)$
1405		$\delta(NH_2)$		
1420	A-DNA ($\delta(CH_2)$)			
1420-1480		$\delta(CH_2)$, $\delta(CH_3)$	$\delta(CH_2)$, $\delta(CH_3)$, aromatic lipids	$\delta(CH_2)$
1421	A,G ($\nu(CC)_{ring}$)			
1423	B-DNA/A,G ($\delta(CH_2)$)			

1425	Z-DNA ($\delta(CH_2)$)			
1440-1450			$\delta(CH_2)$	
1483		$\delta(NH_3)$		
1487	A,G ($\nu(CC)_{ring}$)	$\delta(NH_3^+)$		
1512		Tyr ($\nu(CC)_{ring}$)		
1513	C ($\nu(CC)_{ring}$)			
1518		$\nu(C=C)_{porphyrin}$		
1550-1560		amide II ($(\delta(CN-H)/\nu(CN)$)		
1555	G ($\nu(CC)_{ring}$)	Trp ($\nu(CC)_{ring}$), $\nu(C=C)_{porphyrin}$		
1579	A,G ($\nu(CC)_{ring}$)			
1582		$\nu(C=C)$, $\nu(C=N)$	$\nu(C=C)$, $\nu(C=N)$	
1604	T ($\nu(CC)_{ring}$)	Phe ($\delta(C=CH)$)		
1604-1618	A ($\nu(CC)_{ring}$), C ($\delta(NH_2)$)	Phe, Tyr, Trp ($\nu(C=C)$), $\delta(NH_2)$		
1660	DNA ($\delta(NH)$)	Amide I ($\nu(C=O)$)/α-helix	$\nu(C=C)$	
1612-1690		amide I/β-sheet, antiparallel		
1626-1640		amide I/β-sheet, parallel		
1640-1650		amide I/random coil		
1690		$\nu(C=O)_{amino\ acid\ side\ chain}$		
1712	A-DNA ($\nu(C=O)$)			
1717	B-DNA ($\nu(C=O)$)			
1730-1742			phospholipids ($\nu(C=O)_{ester}$)	
2850-2875		$\nu_s(CH_2)$	$\nu_s(CH)$, $\nu_s(CH_2)$	$\nu_s(CH)$, $\nu_s(CH_2)$
2880		$\nu_s(CH_3)$	$\nu_s(CH_3)$	$\nu_s(CH_3)$
2900-2935		$\nu_{as}(CH_2)$	$\nu_{as}(CH_2)$	$\nu_{as}(CH_2)$
2960		$\nu_{as}(CH_3)$	$\nu_{as}(CH_3)$	$\nu_{as}(CH_3)$
3060		amide B		
3250-3290		amide A ($\nu(NH)$)		
3300-3350			$\nu(OH)$	$\nu(OH)$

[a] A – adenine; C – cytosine; dG – deoxyguanine; dT – deoxythymine; G – guanine; Glu – glucose; Hyp – hydroxyproline; Met – methionine; Phe – phenylalanine; Pro – proline; T – thymine; Trp – tryptophan; Tyr – tyrosine; U – uracil; Val – valine. δ – in-plane deformation; ϒ – out-of-plane deformation; ν – stretching; ρ – rocking; t – twisting; ω – wagging. s – symmetric; as – anti-symmetric.

The most affected DNA bands upon drug exposure were found to be those from deoxyguanine (dG, 698 cm^{-1}), thymine (746, 782, 1375, 1604 cm^{-1}), adenine (728, 1252, 1340-1487, 1579, 1604-1618 cm^{-1}), cytosine (782-795 cm^{-1}), guanine (669-678, 1175, 1318-1375, 1421-1487, 1555-1579 cm^{-1}) and deoxyribose (901-940, 1063 cm^{-1}, more perturbed by the polynuclear agents than by cisplatin) (Table 10). These variations evidence the occurrence of drug-DNA crosslinks, predominantly intrastrand 1,2 GG, 1,2 AG, 1,3 GTG [315], leading to local unwinding of the native helix. While the adenine ring breathing vibration at 728 cm^{-1} decreased in intensity and was slightly red-shifted upon treatment with Pt_2Spm and Pd_2Spm (to 723 and 725 cm^{-1}, respectively), the thymine band at 746 cm^{-1} was deviated to higher frequencies in the presence of cisplatin or Pt_2Spm (755 cm^{-1}) and Pd_2Spm (749 cm^{-1}) (Figure 38(C)). The guanine signal at 1487 cm^{-1} (detected as a shoulder of the strong $\delta(CH_2)_{lipids}$ band at 1448 cm^{-1}) is particularly sensitive to binding of electrophilic agents (such as cisplatin-like compounds) at the N_7 acceptor, having decreased in intensity (nearly disappearing) upon drug-interaction. As for the guanine band at *ca.* 1579 cm^{-1}, it was found to be slightly reduced in the presence of the polynuclear Spm agents, as opposed to the cisplatin-induced blue shift (to 1585 cm^{-1}). Additionally, the strong signal centred at 1660 cm^{-1}, encompassing contributions

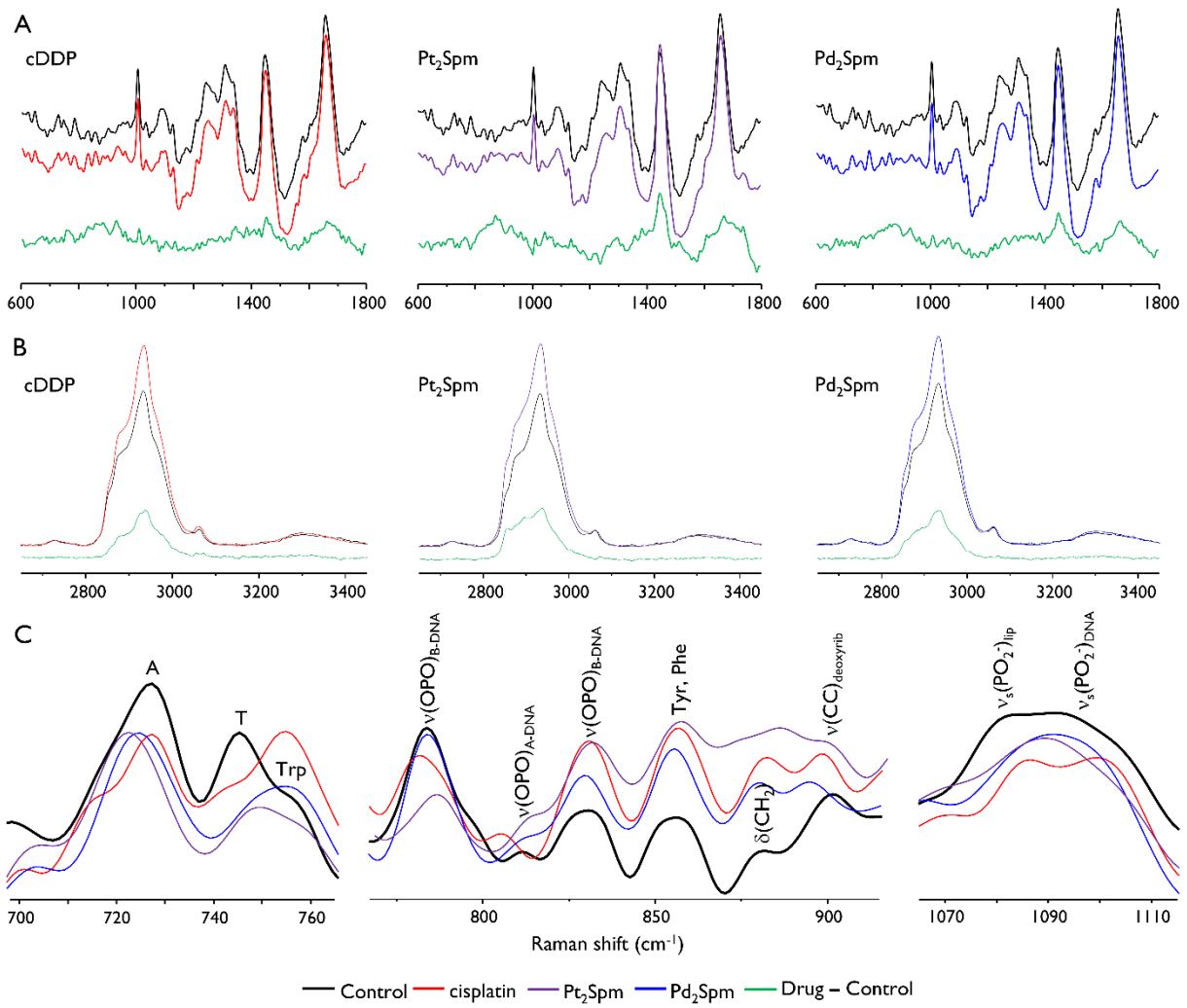

Figure 38 – Mean Raman spectra (fixed cells, Bruker Senterra/532 nm, 600 - 1800 cm^{-1} (A) and 2650 - 3450 cm^{-1} (B)), and difference spectra to the control, for drug-treated (4 μM) MDA-MB-231 cells. (C) – Particular spectral regions affected by drug exposure.

from protein ν(C=O) (amide I), lipid ν(C=C) and DNA δ(N–H) modes, (the latter being highly sensitive to breakage of Watson-Crick H-bonds), rose in intensity in the presence of all three metal complexes studied (as evidenced by the difference spectra in Figure 38(A)). This intensity increase observed for DNA Raman bands in drug-exposed cells may be explained by a hyperchromic effect upon base unstacking and unpairing. Changes in the bands associated with the DNA phosphate groups are especially informative regarding a drug-prompted distortion of the double helix, namely those at 785 cm^{-1} (ν(O–P–O) backbone characteristic of B-DNA, combined to cytosine ring breathing), 1092 cm^{-1} ($\nu_s(PO_2^-)$) and 1237 cm^{-1} ($\nu_{as}(PO_2^-)$). $\nu(O–P–O)_{backbone}$ suffered an intensity decrease, more evident in the presence of Pt_2Spm (main discrimination from the control in PC1) as compared to Pd_2Spm (mostly differentiated in PC2)

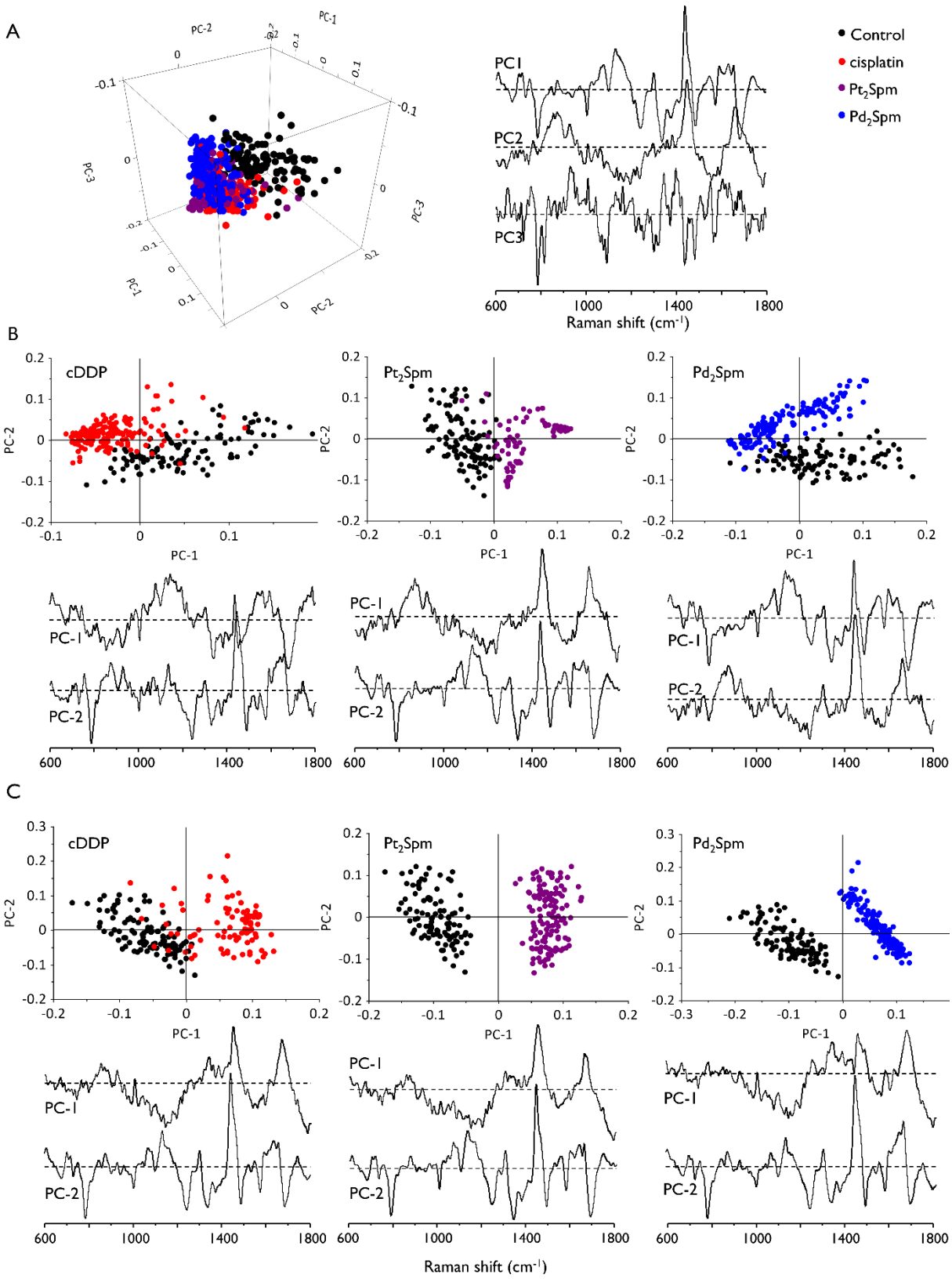

Figure 39 – PCA score and loading plots of Raman data (fixed cells, Bruker Senterra/532 nm, 600 - 1800 cm-1) for drug-treated MDA-MB-231 cells *vs* the control: all tested agents, 4 μM (A). Cisplatin, Pt2Spm and Pd2Spm – 4 μM (B) and 8 μM (C).

(For clarity the loadings are offset, the dashed horizontal lines indicating zero loading).

(Figure 38(C) and Figure 39). The symmetric stretching mode of the PO_2^- groups external to the helix backbone (at 1092 cm^{-1}, partially overlapped with the $\nu_s(PO_2^-)$ band from phospholipids at 1082 cm^{-1}) showed slight deviations for Pt_2Spm(1090 cm^{-1}) and Pd_2Spm (1091 cm^{-1}), as compared to cisplatin (1099 cm^{-1}) (Figure 38(C)). These spectral changes are in agreement with a B- to A-DNA (or ultimately Z-DNA) transition due to covalent drug-binding [71], yielding strong crosslinks responsible for disruption of the base stacking and/or base pairing. Apart from the intensity decrease upon drug exposure of the $\nu(O–P–O)_{backbone}$ bands ascribed to the native double helix structure (at 785 and 830 cm^{-1}), a red shift of the 698 cm^{-1} signal assigned to B-DNA deoxyguanine was detected, for all tested agents, to about 668 cm^{-1} (compatible with a B- to A-DNA transition) and 622 cm^{-1} (reflecting a B- to Z-form rearrangement). Moreover, apart from the B-DNA marker at 830 cm^{-1}, a typical band for A-DNA [316] was detected at 805, 809 and 810 cm^{-1} respectively for cisplatin, Pt_2Spm and Pd_2Spm-containing cells (Figure 38(C)). These are reliable spectral biomarkers of the metal-based drugs´ interaction with DNA and consequent distortion of the DNA backbone, the $\nu(PO_2^-)$ modes being particularly responsive to variations in the electrostatic environment of the phosphate group within the double helix.

Changes in the vibrational modes ascribed to cellular proteins (Table 10) were also observed, reflecting a drug effect either by direct interaction (*e.g.* binding to cytoplasmic proteins) or indirectly (namely *via* proteolysis during the apoptotic process). In addition, the recognised cytotoxic mechanism of metal-based agents involves the binding of high mobility group (HMG) proteins to DNA upon platination- (or palladation)-induced conformational rearrangement of the double helix (precluding repair mechanisms). The most relevant markers associated with protein variations were those at 728/757 cm^{-1} (tryptophan ring breathing), 855 cm^{-1} (Tyr), 935-940 cm^{-1} ($\nu(CC)_{protein}$, α-helix), 1003 cm^{-1} (phenylalanine symmetric ring stretching), 1207 cm^{-1} (ν(CC) from phenylalanine, tryptophan and hydroxyproline), 1127-1158 cm^{-1} (ν(CN)), 1220-1300 cm^{-1} (amide III, ν(CN)/(δ(CN–H)), 1448 cm^{-1} (δ(CH) overlapped with similar modes from lipids) and 1660 cm^{-1} (predominantly amide I). While the impact on the protein skeletal stretching modes (*e.g.* ν(CN) at 1127 and 1157 cm^{-1}) was found to be noteworthy for the cells incubated with cisplatin (PC1), it was much less marked for Pt_2Spm (PC1) and Pd_2Spm (PC1 and PC2), for which variance was more significant in the amide III

band (Figure 39(B)). The Trp ring breathing feature, detected at 757 cm^{-1} in the untreated cells, suffered a slight red shift (to 755 cm^{-1}) upon exposure to cisplatin and the Spm complexes (for which this signal was partially overlapped with the one from the thymine ring, Figure 38(C)). As for the $\rho(CH_2)$ signal from the peptide chains, it was shifted from 883 to 885 cm^{-1} only in the presence of Pt_2Spm. Additionally, direct binding of the drugs to membrane and cytoplasmic proteins is anticipated to cause variations in their secondary and tertiary structures, reflected in the characteristic features of β-sheet, random coil and α-helix conformations (at 1229-1235 cm^{-1}, 1243-1253 cm^{-1} and 1270-1300 cm^{-1}, respectively, Table 10). These were perceived in the amide III band, namely through changes in the signal characteristic of α-helix signal at 1272 cm^{-1}, primarily in the presence of Pt_2Spm (1260 cm^{-1}) and Pd_2Spm (1254 cm^{-1}), evidencing a partial conversion to a random coil structure. Moreover, exposure of side chains containing aromatic residues as a consequence of protein unfolding is suggested to be responsible for a very slight intensity increase of some of the bands ascribed to their ring breathing modes [314], which was currently observed only for Phe (Figure 38(A)). The drug impact on the protein´s amide I band, in turn, showed to be noticeable for cisplatin, as clearly evidenced by the respective PC1 loading (Figure 39(B)). In turn, Pt_2Spm and Pd_2Spm were found to have a higher effect on the $\delta(CH_2)$ and $\delta(NH_2)$ modes from the peptide chains (at *ca.* 1440 and 1618 cm^{-1}, Table 10), as shown in the PC2 loading plot. Analysis of the high frequency region of the spectra (Figure 38(B) and Figure 40(A)) allowed to conclude that the amide A band at 3290 cm^{-1} (exclusively due to protein ν(NH) modes), as well as the amide B signal at 3060 cm^{-1} (arising from a Fermi resonance between amide I and ν(NH) and hence strongly dependent on intramolecular H-bonds), did not undergo significant changes upon drug exposure, as opposed to the CH stretching modes of the cellular biomolecules (2850-2960 cm^{-1}).

MDA-MB-231 cells are especially rich in lipids (*e.g.* glycerophospholipids, known to be increased in cancer cells [317]). The direct drug impact on these cell constituents was reflected as an increase of the intense Raman feature centred at 1448 cm^{-1} ($\delta(CH_2)$), particularly for Pt_2Spm, as well as of the bands at 2850-2960 cm^{-1}, clearly evidenced in the difference spectra obtained for all tested drugs (Figure 38(A) and (B)). This may also be inferred by analysis of the loading plots corresponding to Pt_2Spm and Pd_2Spm (respectively in PC1 and PC2, Figure

39(B)). However, since CH_2 deformations from cellular lipids occur in the same wavenumber interval as similar modes from proteins and carbohydrates (Table 10), as well as from the spermine polyamine ligand (Figure 35), PCA differentiation should be interpreted with care in

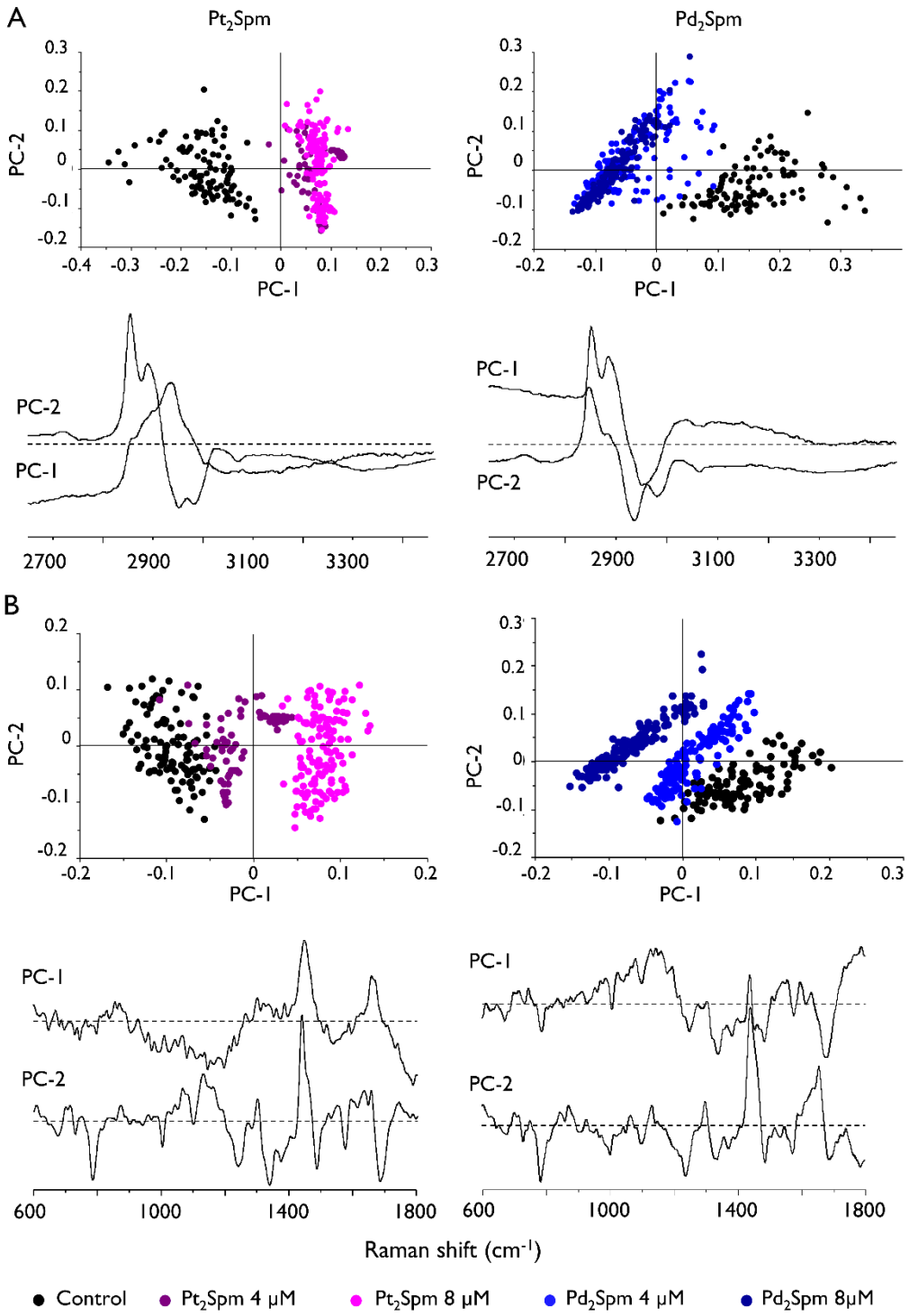

Figure 40 – PCA score and loading plots of Raman data (fixed cells, Bruker Senterra/532 nm, 2650 - 3450 cm^{-1} (A) and 600 - 1800 cm^{-1} (B)) for Pt_2Spm- and Pd_2Spm-treated (4 and 8 µM) MDA-MB-231 cells *vs* the control. (For clarity the loadings are offset, the dashed horizontal lines indicating zero loading).

this region. The PC2 loading plot for Pd_2Spm, for instance, also showed a very marked discrimination according to protein and carbohydrate CH_2 deformations (*ca.* 1430 cm^{-1}). The highest frequency spectral region is therefore more suited for this analysis, the drug-induced changes observed in the typical $\nu(CH_2)$ (2850-2935 cm^{-1}) and $\nu(CH_3)$ (2960 cm^{-1}) vibrational modes from lipids being reflected in the clear separation from the untreated cells along PC1, for all agents investigated: the loadings corresponding to the (CH) stretchings from methyl groups being positive for cisplatin and negative for both spermine complexes (Figure 40(A)). This evidences different biochemical impacts induced by these mono- and dinuclear agents on lipid terminal moieties (CH_3) *vs* $–(CH_2)_n–/–(HC=CH–CH_2)_n–$ chains, which is in accordance with the presence of the alkyl moieties within the ligand in the Pt_2Spm and Pd_2Spm complexes that are prone to interact efficiently with the hydrophobic chain of lipid molecules (as opposed to $Pt(NH_3)_2Cl_2$). Regarding membrane lipids, it was possible to identify changes in the vibrational mode ascribed to their phosphate-ester head groups, at 1732 cm^{-1}, that was shifted to 1739 cm^{-1} for Pt_2Spm but hardly detectable (at *ca.* 1742 cm^{-1}) for cisplatin- and Pd_2Spm-treated cells. The $\nu(COC)$ modes from glycosidic bonds in glycolipids, centred at 938 cm^{-1}, were found to be deviated to 934 cm^{-1} for cisplatin and Pd_2Spm, and to 931 cm^{-1} for Pt_2Spm. Moreover, the signal at 1158 cm^{-1}, characteristic of the $N(CH_3)_3^+$ choline group (*e.g.* from phosphatidylcholine and sphingomyelin, two main cell membrane constituents), experienced a shift to 1163 cm^{-1} for the cisplatin-exposed cells and an intensity decrease for the samples exposed to the dinuclear Spm chelates. This may be indicative of the formation of membrane vesicles, as a way for the cell to remove toxins (*e.g.* the administered compounds) by exocytosis. Overall, the drug effect on cellular lipids results from an interplay of several (sometimes disparate) factors, such as an increase in neutral lipids (associated with cisplatin's nephrotoxicity), an enhanced lipid peroxidation, and a reduction in the total lipid content due to membrane degradation and decreased cell viability.

Figure 39(A) displays the unsupervised PCA analysis considering all agents under study, allowing to identify discrimination according to PC2 that represents variances in protein, lipids and DNA (specifically $\delta(NH_2)$, and ring modes from bases and deoxyribose), with a slight overlap between drug-exposed and control cells (mostly for cisplatin). Apart from this distinction between control and treated cells, it was possible to separate each of the three

drugs currently tested based on their effect on the cell´s chemical profile, as compared to the control (Figure 38 and Figure 39), reflecting the previously described drug-dependent response. Differentiation was achieved in PC1 for cisplatin and Pt_2Spm, while for Pd_2Spm it was attained in PC2 for the lowest doses and in PC1 for 8 μM (Figure 39(B) and (C)). For cisplatin-treated samples a main impact on DNA and proteins was observed, an effect on lipids being detected only for 8 μM. The dinuclear Pt(II) complex, in turn, was responsible for a strong effect on lipids, already at the lowest concentration tested (2 μM), also evidenced through changes in the corresponding high energy $\nu(CH_2)$ modes. In turn, the effect on proteins (noticeable in PC1 and PC2) was only verified for concentrations equal to 4 μM or higher. At 8 μM there was a small effect on RNA (bands centred at 879 cm^{-1}). Pd_2Spm produced a noteworthy impact on proteins, for all concentrations tested. As to the Pd_2Spm-induced variance on lipids and DNA, it was significant for 4 μM and did not increase at 8 μM (Figure 39 (B) and (C)).

A dose-dependent effect was uncovered by separate analysis of the data measured for each compound, a significantly improved discrimination having been achieved for higher concentrations, as expected (Figure 39(B) and (C)). Comparing the results for Pt_2Spm- and Pd_2Spm-treated cells *vs* the control, for 4 and 8 μM (Figure 40(B)), allowed to conclude that separation from the control as well as between both Pt_2Spm concentrations occurred along PC1, the discriminant peaks corresponding predominantly to DNA and lipids. For Pd_2Spm, this distinction was not as noticeable (increasing with drug concentration), and occurred in PC1 reflecting DNA (at 785 and *ca.* 1320 cm^{-1}) and protein components (at *ca.* 1150 and 1660 cm^{-1}), with a very small variance for the lipids (at 1448 cm^{-1}). Interestingly, while in the fingerprint region discrimination was achieved between 4 and 8 μM concentrations for both Pt- and Pd-complexes (Figure 40(B)), in the highest frequency range, mainly reflecting the impact on lipids, no differentiation was observed between distinct drug doses for Pt_2Spm and a very small separation was detected for Pd_2Spm (Figure 40(A)). Hence, the effect on lipids appears to become dose-independent above 4 μM, which implies a higher sensitivity of the cellular lipid content to the administered drugs as compared to the other biomolecules, a maximum effect being attained for lower concentrations of the chemotherapeutic agent, particularly for Pt_2Spm.

Discrimination between the two dinuclear spermine complexes was also attained, through PC2 (Figure 41) that predominantly represents the cellular DNA (at 678, 728, 746, 785, 974, *ca.* 1180, 1315, 1420, 1490 and 1620-1660 cm^{-1}) and RNA (at 812 and 920-940 cm^{-1}). This reflects a distinct impact of each chelate on nucleic acids, suggesting the occurrence of different pathways for cytotoxicity according to the nature of the metal centre.

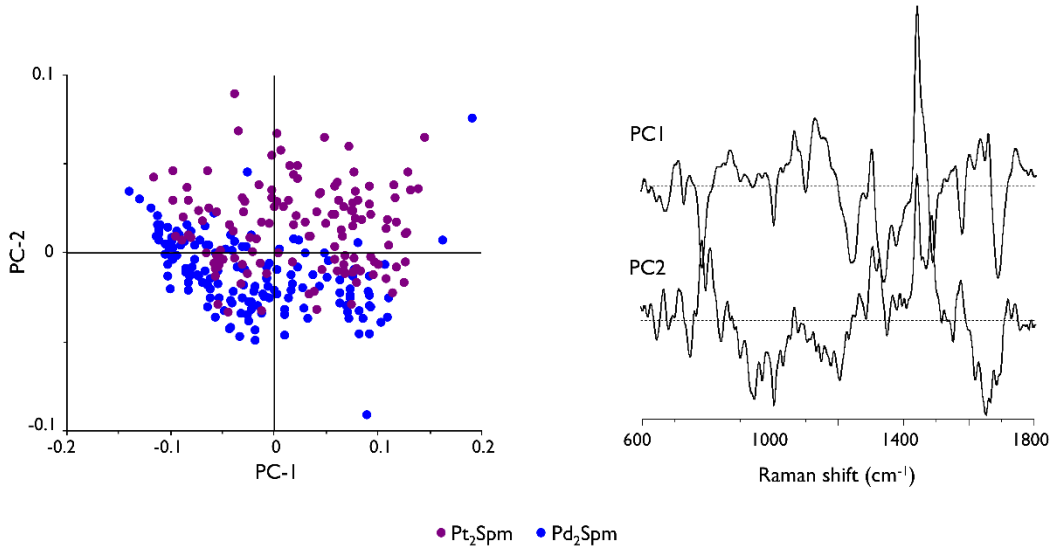

Figure 41 – PCA score and loading plots of Raman data (fixed cells, Bruker Senterra/532 nm, 600 - 1800 cm^{-1}) for drug-treated MDA-MB-231 cells: Pt_2Spm *vs* Pd_2Spm (8 μM).
(For clarity the loadings are offset, the dashed horizontal lines indicating zero loading).

In summary, the Raman spectra presently obtained for the MDA-MB-231 cells may be resolved into distinct regions of statistically significant spectral biomarkers which were found to undergo variations upon drug treatment, corresponding to different biochemical impacts. The overall effect of the tested agents on the vibrational features from the main cellular components is consistent with changes in DNA, as well as in cytoplasmic proteins and lipids, and the onset of apoptosis involving chromatin condensation, DNA fragmentation, membrane blebbing, protein proteolysis (*e.g.* in the cytoskeleton) and lipid accumulation. The distinct outcomes on the cell´s chemical content currently unveiled for Pt_2Spm and Pd_2Spm may be indicative of the occurrence of alternative pathways of cytotoxicity for the palladium complex, as opposed to a preferentially apoptotic mechanism of cell death induced by its platinum homologue (as widely accepted for the Pt-drugs in clinical use – cisplatin, carboplatin and oxaliplatin).

The results presently obtained for cisplatin are in accordance with reported Raman studies on the cisplatin effect on human lung adenocarcinoma cells [313,314], despite the longer drug exposure time considered by these authors – 96 h as compared to the 48 h incubation period used in the current work. Additionally, the chemical variations associated with the apoptotic process presently described agree with time-course Raman imaging experiments during apoptosis performed in the same TNBC cell line, maintained under physiological conditions [269].

3.3.2. Synchrotron-Radiation Infrared Microspectroscopy

The spectroscopic signature of the MDA-MB-231 cells in the presence of anticancer agents was also monitored by SR-IRMS. The main infrared bands presently observed are depicted in Figure 35, clearly showing the signals assigned to the protein´s characteristic modes amide A (ν(NH) at 3290 cm^{-1}) and amide II (δ(CN–H)/ν(CN) at *ca.* 1550 cm^{-1}), as well as to the ester groups from phospholipids (*ca.* 1730 cm^{-1}, Table 10). Infrared profiles from untreated and drug-treated cells were successfully retrieved from the data, evidencing a good PCA discrimination on the basis of the distinct biochemical profile observed for each condition. Since the main conclusions are in accordance with the Raman results previously described in detail, the following discussion will only emphasise the specific effects unveiled by IRMS analysis.

In view of the optical substrate transmission range (0.35-10 μm wavelength) it was not possible to reliably explore the data below *ca.* 1100 cm^{-1}, *i.e.* the nucleic acid region was strongly affected by the cut off of the CaF_2 substrate at 1000 cm^{-1} [270]. Spectra were therefore truncated between 1100 and 1800 cm^{-1} for baseline correction prior to PCA analysis. When applying the PCA, the spectral interval from 1100 to 1250 cm^{-1} was not found to yield significant information. PCA applied to the spectral range 1250-1800 cm^{-1} showed the largest variability in the data, allowing to distinguish the impact of each drug type effectively. Actually, the score and loading plots extracted for PC2 and PC3 (Figure 42) evidenced significant differences between cisplatin and the platinum and palladium-spermine complexes. In each case, good discrimination was observed along PC3, enabling separation between the

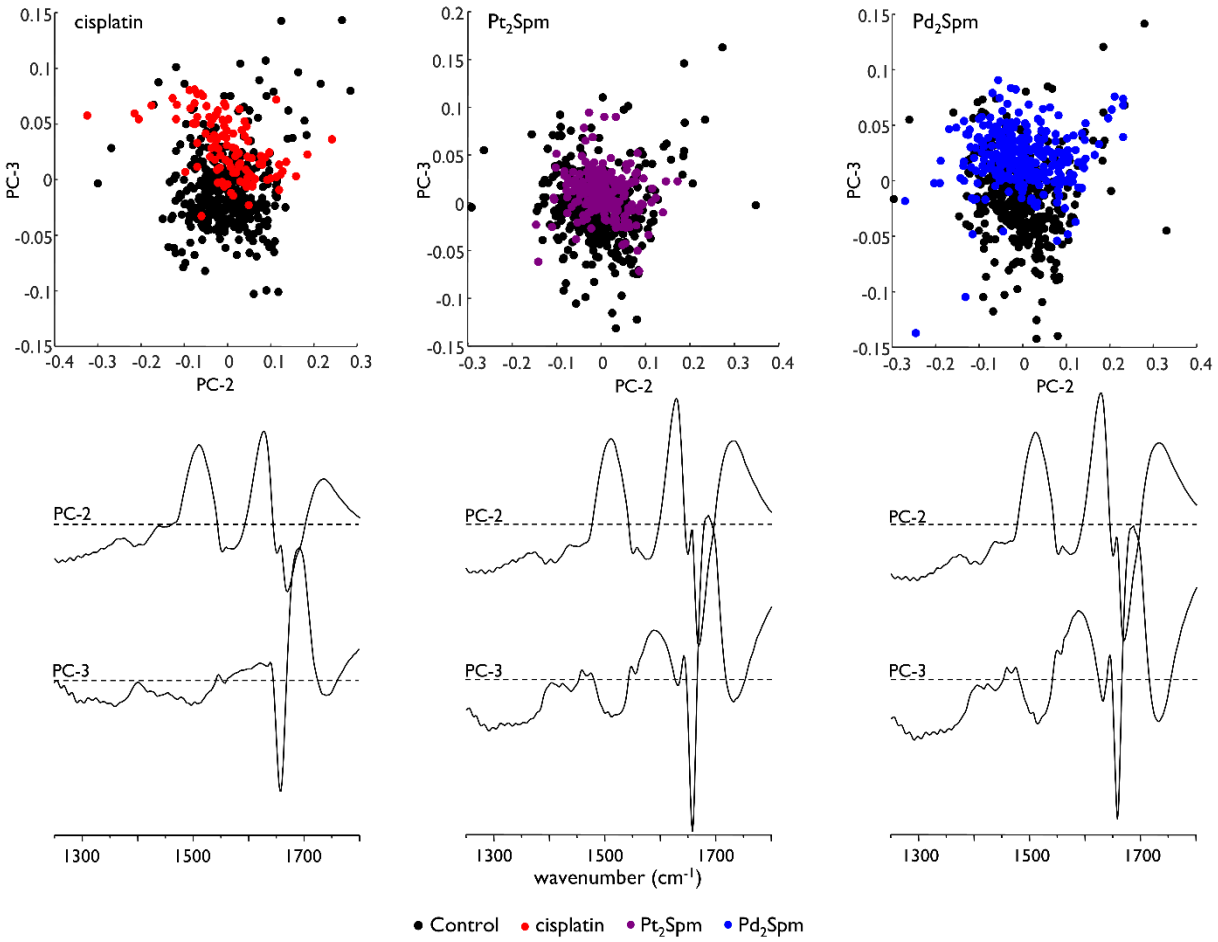

Figure 42 – PCA score and loading plots of FTIR data (fixed cells, MIRIAM, 1250 - 1800 cm^{-1}) for cisplatin-, Pt_2Spm- and Pd_2Spm-treated (4 μM) MDA-MB-231 cells *vs* the control.
(For clarity the loadings are offset, the dashed horizontal lines indicating zero loading).

untreated control and the drug-treated cells: while there was some overlap in the scatter plots, two centroids could be clearly distinguished. No other principal components were able to successfully discriminate between the control and drug-exposed cells. The loading plot along PC3 for the cisplatin-containing samples displayed an intense peak at 1659 cm^{-1} (amide I) and a relatively weak band at 1556 cm^{-1} (amide II), reflecting a clear effect on proteins. Furthermore, two distinct signals ascribed to ν(C=O) modes appeared, respectively from amino acid side chains and antiparallel β-sheet conformations (at 1690 cm^{-1}), and from phospholipid ester groups (at 1741 cm^{-1}, Table 10). In addition to these peaks observed for cisplatin-exposed samples, further bands were detected upon incubation with the spermine complexes, at 1460 and 1628 cm^{-1}, due to anti-symmetric CH_2 scissoring from lipids and to the amide I protein mode (β-sheet parallel), respectively. The band at 1741 cm^{-1} for the cisplatin-treated cells was found to be slightly shifted to 1728 cm^{-1} in the presence of Pt_2Spm

and Pd_2Spm, possibly as a consequence of drug interaction with the cell membrane (phospholipid moieties). These results indicate a significant impact of the Pt(II) and Pd(II)-polyamine agents on the cellular proteins and lipids, as verified by Raman. Strong similarities were apparent in the loading plots for PC3 for both Pt_2Spm and Pd_2Spm, which suggests an identical impact of these drugs on the MDA-MB-231 cells, differing from cisplatin mostly in the bands ascribed to the CH_2 stretching modes from lipids (*ca.* 1450 cm^{-1}). Also, the differences exposed by comparison with the cisplatin loading plot indicate that the activity of Pt_2Spm and Pd_2Spm follows a different pathway, which is to be expected since the biochemical interaction of these dinuclear highly flexible complexes to DNA and other cellular components is likely to occur *via* a somewhat distinct mechanism to that of mononuclear cisplatin.

The effect of drug exposure on the cellular lipid constituents was also assessed by applying PCA to the 2650-3450 cm^{-1} spectral region (comprising the amide A and lipid CH stretching vibrational modes). Figure 43 depicts the score and loading plots for the cells

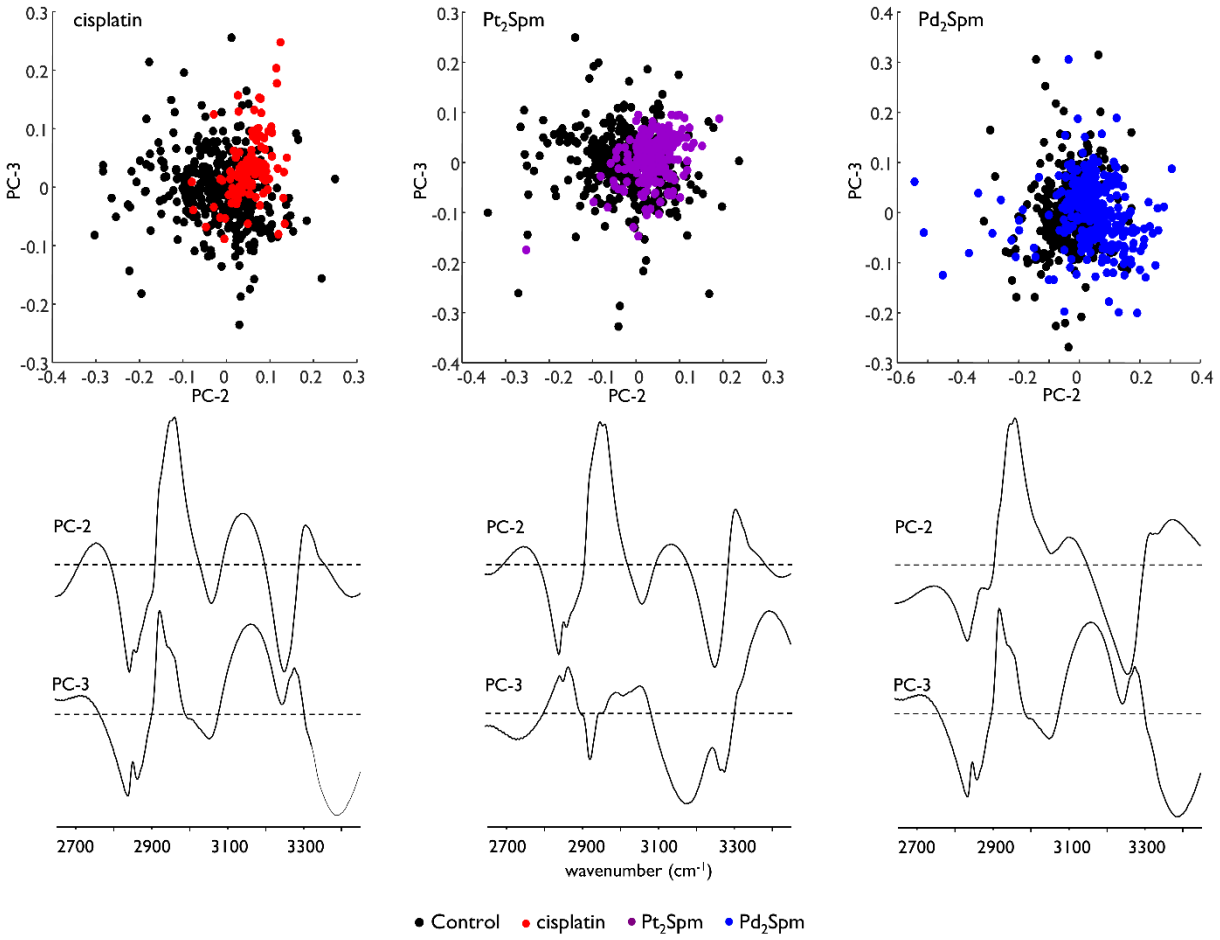

Figure 43 – PCA score and loading plots of FTIR data (fixed cells, MIRIAM, 2650 - 3450 cm^{-1}) for cisplatin-, Pt_2Spm- and Pd_2Spm-treated (4 μM) MDA-MB-231 cells *vs* the control.

(For clarity the loadings are offset, the dashed horizontal lines indicating zero loading).

exposed to each of the three tested drugs *vs* the control, showing some separation along PC2. For each compound, these plots display predominantly positive scores while the untreated controls are chiefly negative, reflecting different modes of action. Similar profiles were obtained in the PC2 loadings, the main differentiating signal from the control being the one centred at 2960 cm^{-1} ascribed to methyl group stretching (mainly from the lipids). The increase in this band´s intensity upon drug exposure is in agreement with the PCA plots obtained from the Raman spectra (Figure 40(A)). The amide A (3290 cm^{-1}) and amide B (3060 cm^{-1}) protein modes were also found to undergo drug-induced changes (namely an intensity decrease) for both Spm complexes, supporting an impact on proteins. The effect on these particular features could only be clearly evidenced by infrared, since these are weak signals in Raman (Figure 38).

The effect of changing the metal centre within the spermine chelates was also probed, in the high frequency spectral range. The biological effect on the treated cells (for a 4 μM drug concentration) was borne out on examination of the score and loading plots represented in Figure 44, a good discrimination having been achieved between Pt_2Spm and Pd_2Spm along PC2. Major variances were observed in the typical bands from lipids (2850 to 2960 cm^{-1}), as well as in a broad feature due to the amide A mode, once more evidencing an impact on proteins and lipids.

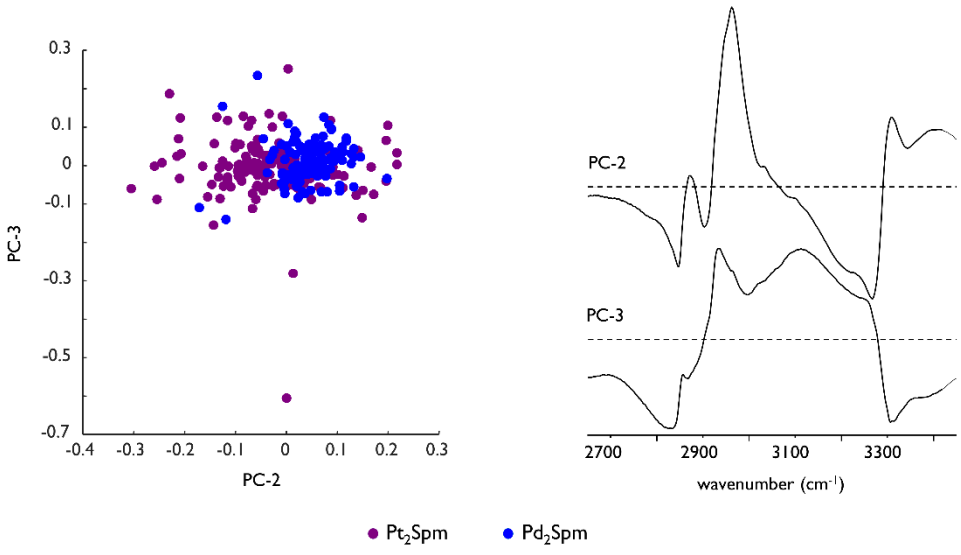

Figure 44 – PCA score and loading plots of FTIR data (fixed cells, MIRIAM, 2650 - 3450 cm^{-1}) for drug-treated MDA-MB-231 cells: Pt_2Spm *vs* Pd_2Spm (4 μM).
(For clarity the loadings are offset, the dashed horizontal lines indicating zero loading).

3.3.3. Effect of Dietary Antioxidants on Chemotherapeutic Response

About 30% of cancer mortality is attributable to an inappropriate diet, containing suspected carcinogens and an insufficient amount of beneficial components. Indeed, there seems to be an inverse relationship between a decreased risk of cancer and a regular consumption of fruits and vegetables, which is ascribed to phytochemicals with potential chemopreventive properties – phenolic acids, polyamines and flavonoids. Cancer being a multifactorial disease that involves numerous pathways, its prevention may be achieved by these pharmacologically safe compounds from natural sources that are capable of modulating multiple targets and cell signalling routes [318-320]. Additionally, this type of non-toxic agents can be used alone to prevent cancer, or in combination with chemotherapy (*e.g.* in chemosensitisation strategies or for downregulating chemoresistance processes).

The combined effect of quercetin, an abundant dietary flavonoid with a recognised antioxidant capacity [321], with cisplatin and the new generation cisplatin-like polynuclear Pd(II) chelate (Pd_2Spm) [100,104,253] was evaluated, aiming at an improved selectivity and antitumour activity. The effect of pre-sensitisation (24 h) of a human TNBC cell line (MDA-MB-231) with this bioactive agent (at 50 μM) on the pharmacodynamic behaviour of cisplatin and Pd_2Spm (at 4 μM) was assessed through Raman (Figure 45) and SR-IR (Figure 46), with a view to understand the influence of the daily diet on chemotherapeutic intervention.

The present results reflected a clear separation between the cisplatin- or Pd_2Spm-treated pre-sensitised cells and those exposed to either agent without pre-sensitisation. Upon unsupervised PCA analysis, the impact of quercetin pre-sensitisation on the cellular biochemical profile was attained.

For the Raman data, discrimination took place through PC1, revealing a main impact on the DNA O–P–O stretchings and on protein´s NH_2 deformations (Figure 45). This is in accordance with the mechanism of action of Pt-based drugs (as explained before) which exert their cytotoxic effect through covalent binding to DNA, combined to coordination to specific proteins thus altering their secondary and tertiary structure and leading to unfolding and exposure of side chains (evidenced by intensity changes in the Phe band at *ca.*1000 cm^{-1}). The Raman results also allowed to distinguish non-treated from treated cells (either pre-sensitised or not) – along PC4, mostly representing DNA and amide I.

In turn, the SR-IR loading plots for the 1200-1800 cm^{-1} region allowed to identify an intense peak recognised as the amide I, which is in agreement to what was previously discussed regarding the effect of these compounds on proteins. The SR-IR results for the 2800-3650 cm^{-1} region evidence a significant impact on the lipids CH_3 stretching, through the presence of an intense band at *ca.* 3000 cm^{-1} (Figure 46).

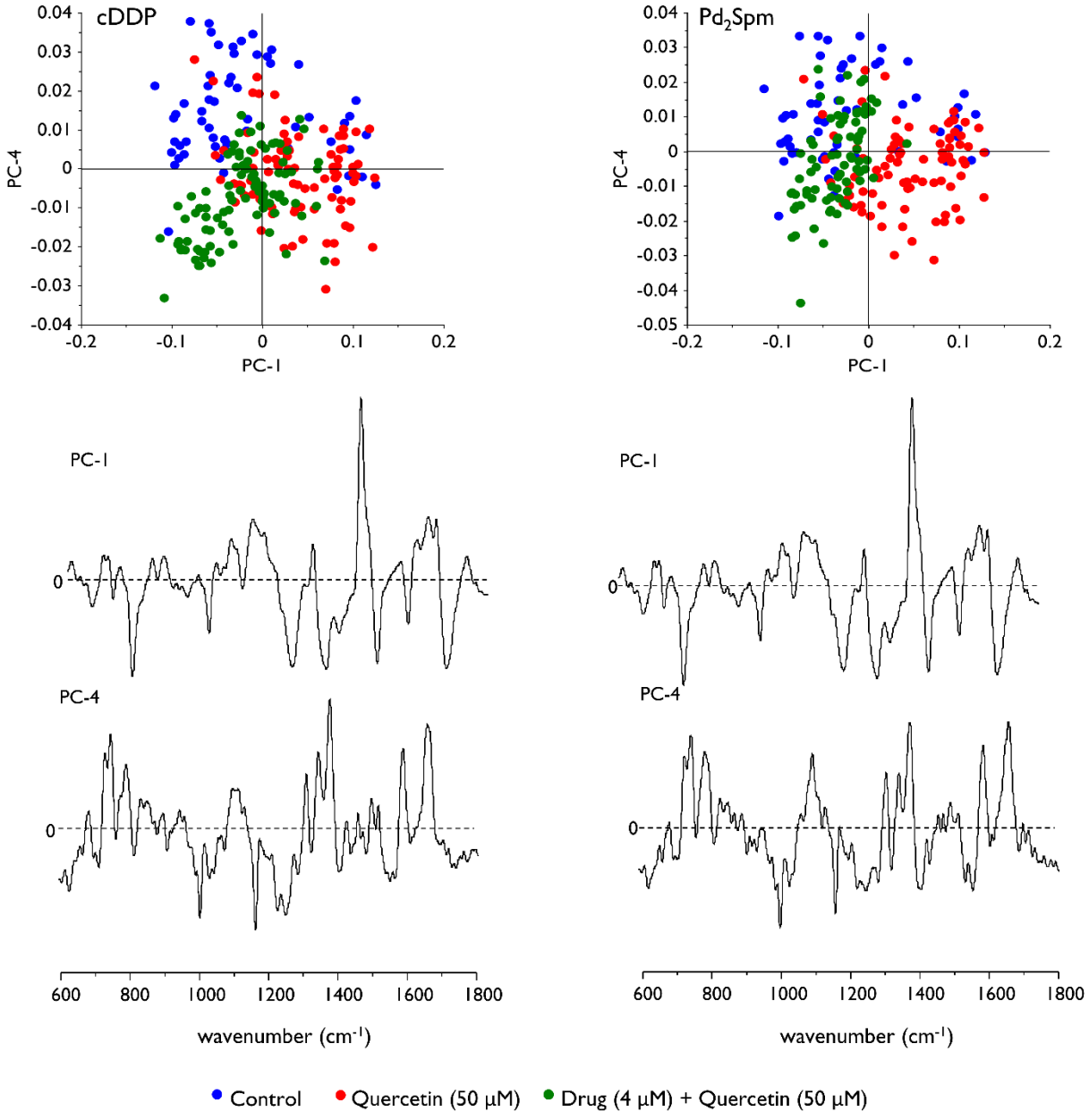

Figure 45 – PCA score and loading plots of Raman data (fixed cells, Bruker Senterra/532 nm, 600 - 1800 cm^{-1}) for quercetin (50 µM) pre-sensitised and drug-treated MDA-MB-231 cells *vs* the control: cisplatin and Pd_2Spm – 4 µM.

(For clarity the loadings are offset, the dashed horizontal lines indicating zero loading).

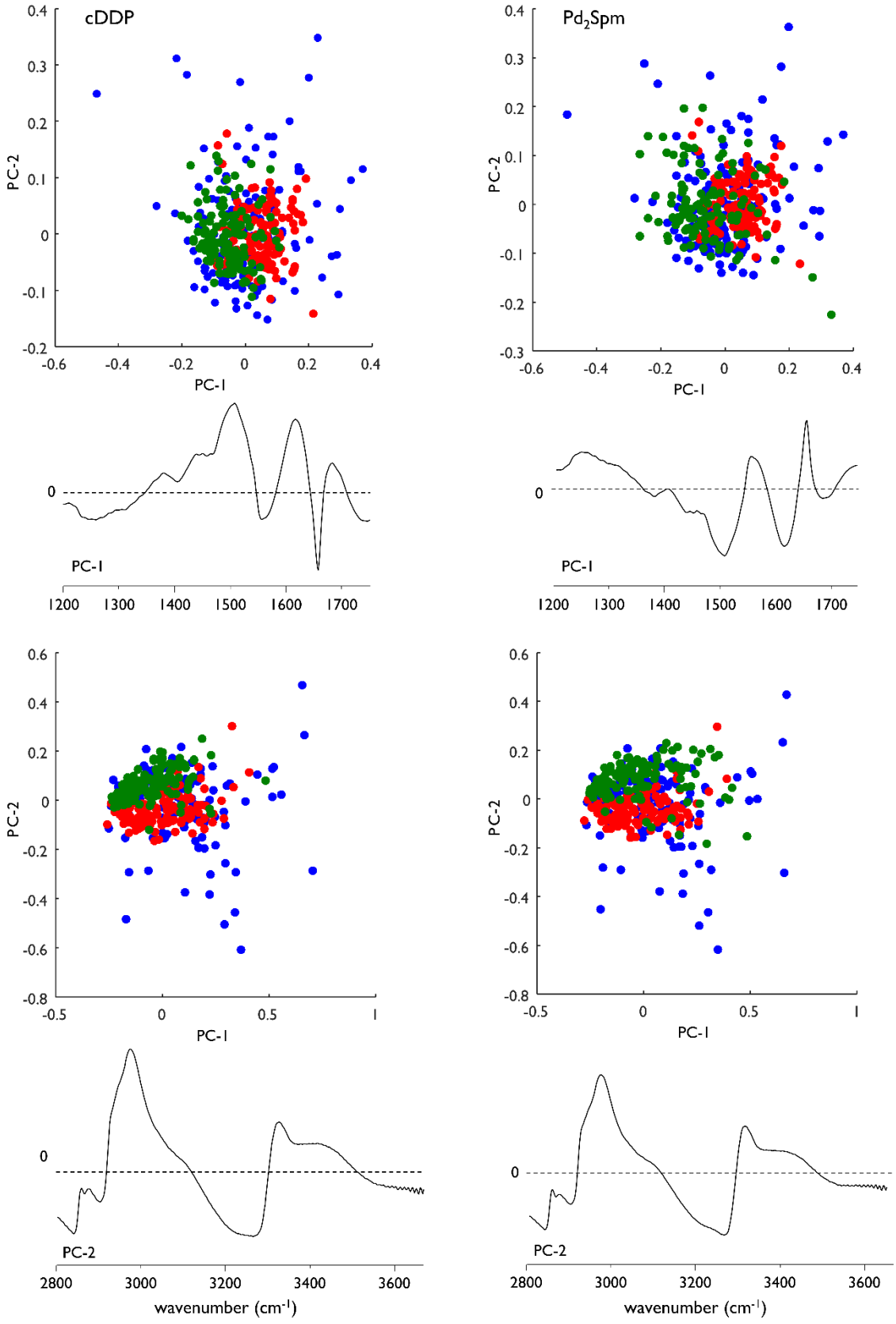

Figure 46 – PCA score and loading plots of FTIR data (fixed cells, MIRIAM, 1250 - 1800 cm^{-1}) for quercetin (50 µM) pre-sensitised and drug-treated MDA-MB-231 cells *vs* the control: cisplatin and Pd_2Spm – 4 µM.
(For clarity the loadings are offset, the dashed horizontal lines indicating zero loading).

3.4. Effect on Intracellular Water

Water supports vital biochemical processes in a living organism, influencing key cellular functions such as protein folding and stability, enzyme catalysis, DNA packaging, molecular recognition, intracellular signalling, transport processes and cellular tolerance to freezing [322-331]. Actually, hydration is required for bioactivity, since it is essential for maintaining the functional structure of biomolecules. Within a biological system such as a cell, water structure and dynamics are known to be changed by the presence of metabolites or extrinsic entities (*e.g.* drugs), while in turn water properties are prone to affect the conformational behaviour and function of biomolecules, which are slaved to the variations occurring in their hydration shell [202,205,328-330,332-336]. The aqueous cytoplasm comprises a complex array of organised macromolecular structures, including skeletal elements and organelles, and dissolved solutes of various dimensions (*e.g.* ions, amino acids, proteins) [322,337-341], water amounting for about 80% of the total cell mass. The unique properties of water in the intracellular space have long been a matter of dispute, and they have been found to determine the stiffness of the cytoplasm [342]. Dynamic labile H-bond networking, macromolecular crowding and confinement effects (by biomolecules and membranes of diverse physical-chemical nature) have been proposed to explain these distinctive molecular properties. Self-association through hydrogen bonding is a particularly important property, which is constantly changing as a consequence of the rotation of individual water molecules, as well as to accommodate the presence of solutes within the cellular milieu or to adapt to specific conditions (*e.g.* ionic strength, pH, temperature or pressure).

Because water provides the dynamical matrix in which all biochemical and biophysical processes occur, interference with its structural and dynamical characteristics is expected to have significant consequences at the functional level, and may even induce cell damage. Unravelling water behaviour within the cell, at the molecular level, is thus of key importance. Actually, even subtle changes in intracellular water may be the driving force to disrupt homeostasis and initiate a series of events leading to biomacromolecular dysfunction that can facilitate disease (*e.g.* cancer or neurological disorders) [343]. This concept is presently extended to the mechanism of action of pharmacological agents, which are likely to affect the inhomogeneous highly crowded cytoplasmic medium, with still unknown effects on cellular

function. This is an innovative approach to better interpret pharmacodynamics (drug interaction with its pharmacological target), possibly unveiling secondary therapeutic targets, and attain an improved understanding of the drug´s *in vivo* mode of action, helping to develop more effective therapies against cancer and optimise the use of presently available drugs.

In this proof-of-concept study on the effect of a drug on intracellular water, the widely recognised anticancer chemotherapeutic agent cisplatin was used. Its direct cytotoxic effect mediated by DNA conformational rearrangement [69,71,344] is well known. However, should cisplatin induce changes in the intracellular milieu, these might have a noteworthy impact on vital biomolecules and affect cellular proliferation and viability. To the best of the author´s knowledge this is the first study of the kind to be carried out, as well as the first neutron spectroscopy probing of human cells.

Water dynamics and structure were directly probed (through INS and QENS experiments, as well as by optical vibrational spectroscopy) in lyophilised and intact MDA-MB-231 cells, in the presence of cisplatin, to monitor their response as a function of drug concentration (8 to 20 μM, for an exposure time of 48 h). Water was therefore directly probed within intact human cancer cells, with a view to ascertain both structural and dynamical modifications upon drug incubation. Several samples were investigated: (1) PBS (both undeuterated and deuterated), as a good model for bulk water; (2) cell pellets, comprising biomolecules as well as extra- and intracellular water – non-washed cells; (3) cells in deuterated saline medium allowing to observe only intracellular water and biomolecules, as this PBS_{deut}-washing procedure suppresses practically all the extracellular (bulk) water dynamical component by replacing the exchangeable hydrogens with poor scatterer deuterium atoms – PBS_{deut}-washed cells; (4) cisplatin-exposed cells, including extra- and intracellular water and cellular constituents affected by the drug; (5) cisplatin-exposed cells in deuterated saline medium, containing intracellular water and cellular constituents affected by the drug – PBS_{deut}-washed cisplatin-treated cells (or simply washed cisplatin-treated cells); (6) lyophilised cells, with and without drug, containing solely cytoplasmic biomolecules. Hence, subtracting the data for lyophilised cells from that for cells in deuterated saline, either untreated or drug-treated (respectively [3 minus 6] or [5 minus 6]), corresponds to removal of the contributions from the biomass and bulk water and allows to directly probe the drug impact on the intracellular

water. The data acquired for both bulk water (H_2O and D_2O) and PBS (non-deuterated and deuterated) was subtracted from that of the cell samples (respectively non-washed and PBS_{deut}-washed), in order to better distinguish the features due to interfacial water.

3.4.1. Structure

Optical vibrational data (FTIR and Raman) obtained for lyophilised cell samples (untreated and cisplatin-treated/8 μM) is represented in Figure 47 –, showing the main bands

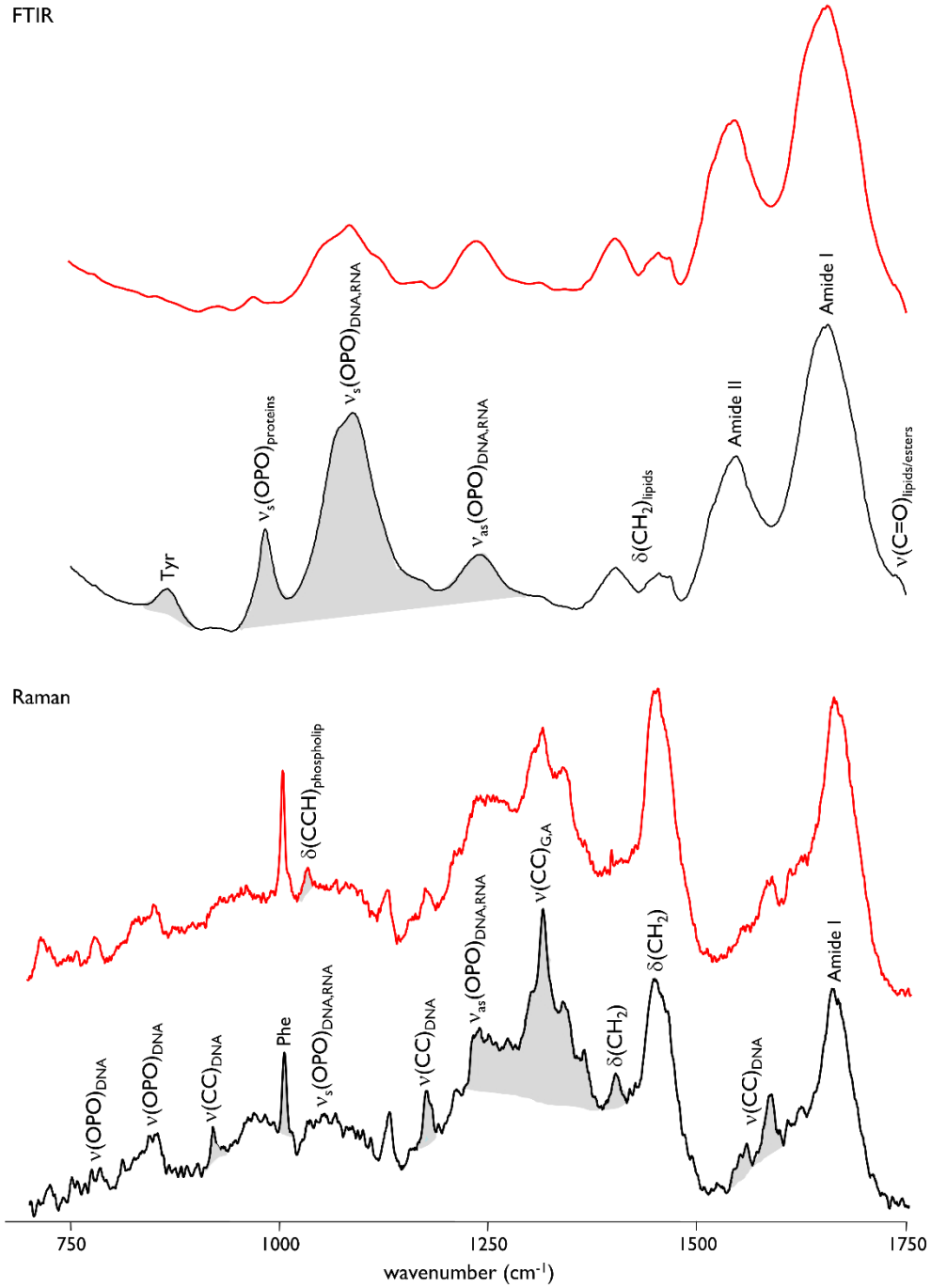

Figure 47 – Raman and FTIR spectra (at room temperature) of lyophilised MDA-MB-231 cells, untreated (black) and cisplatin-treated/8 μM (red).

(The most significant spectral changes are shaded in grey.)

from the cellular metabolites (Table 11): (i) amide bands from the peptide bonds – I ($\nu_{C=O}$, at 1660 cm^{-1}), II (60% δ_{N-H} + 40% ν_{C-N}, at 1550 cm^{-1}) and III (30% δ_{N-H} + 40% ν_{C-N}, centred at 1250 cm^{-1}); signals from the aromatic aminoacids (phenylalanine, tryptophan and tyrosine) at 1585, 1170, 1003 ($\nu_s(CC)_{ring}$) and 863 cm^{-1}, and from phosphorylated proteins (PO_3^{2-} stretchings at *ca.* 980 cm^{-1}); (ii) typical features from the main cellular components, mostly lipids – ν_{CC} (*ca.* 1130 cm^{-1}) and δ_{CH^2/CH^3} (intense bands between 1400-1470 cm^{-1}); (iii) symmetric and antisymmetric (O–P–O) stretching modes from DNA and RNA (at 1090 and 1240 cm^{-1}, respectively), and $\nu(CC)_{ring}$ from DNA´s purine bases (*e.g.* 1320 to 1370 cm^{-1}).

Comparison of the infrared data from the control and drug-containing cells clearly demonstrates a marked effect of cisplatin on DNA and the protein cellular constituents (in accordance with previously reported studies for live MDA-MB-231 cells [345] (according to 3.3., Results and Discussion section)), that is reflected by an almost complete disappearance of the peaks assigned to tyrosine (at 863 cm^{-1}) and the PO_3^{2-} symmetric stretching mode from proteins (at 980 cm^{-1}), coupled to a strong intensity decrease of the ν_s(O–P–O) signal from DNA (at *ca.* 1090 cm^{-1}), the latter being a recognised spectral biomarker of cell death [310]. The Raman spectra also expose the drug impact on the cellular chemical fingerprint: on DNA, supported by changes in the bands at *ca.* 720, 780, 920, 1170, 1314 and 1555 cm^{-1} due to $\nu(CC)_{ring}$ modes from B-DNA bases and deoxyribose, and at 830 cm^{-1} assigned to $\nu(O–P–O)_{backbone}$ (Table 11); on phospholipids (membranes), evidenced by the feature at 1033 cm^{-1} clearly seen in the drug-treated sample; and on phenylalanine, which gives rise to a characteristic signal at 1003 cm^{-1} that is enhanced in the cisplatin-containing samples, since drug binding to cellular proteins triggers conformational rearrangements and unfolding leading to an increased exposure of aromatic aminoacids.

Neutron vibrational spectroscopy allows us to define the local structures of water molecules within the cell by comparing their vibrational signatures with known geometries, namely from ice in its different phases (since the neutron scattering measurements are performed at cryogenic temperatures). Interfacial water molecules in the vicinity of membranes and biomolecules within the cellular environment were reported (both by experimental data and molecular dynamics simulations) to yield different INS profiles relative

Table 11 – Main FTIR, Raman and INS bands observed for human breast cancer cells (MDA-MB-231).

FTIR	Raman	INS	[a]Assignments
		56-80	Water – acoustic modes
		155	Water – acoustic modes
		160	Lipids (membranes) – $\tau(CH_3)$
		224	Water – H-bonded (weak)
		240	Proteins – $\tau(CH_3)$
		290	Proteins – $\tau(CH_3)$
		304	Water – H-bonded (strong)
		540-1100	Water – librational modes
		560	Water – intracellular
	720	728	B-DNA (A,T) – $\nu(CC)_{ring}$
	780-785		B-DNA (C,T,U) – $\nu(CC)_{ring}$ B-DNA – $\nu(OPO)_{backbone}$
	830-850		B-DNA – $\nu(OPO)_{backbone}$ Proteins (Pro,Trp,Tyr) – $\nu(CC)$, $\delta(CCH)$ Polysaccharides – $\gamma(COC)$
863			Tyr – $\nu(CC)_{ring}$
	920		B-DNA (deoxyribose) – $\nu(CC)_{ring}$
980			Proteins (phosphorylated) – $\nu(OPO)$
1003	1003		Proteins (Phe) – $\nu_s(CC)_{ring}$
	1033		Phospholipids – $\delta(CCH)$
1080-1090	1070-1090		B-DNA, RNA – $\nu_s(PO_2^-)$ Proteins – $\nu(CC)$, $\nu(CN)$ Phospholipids – $\nu_s(PO_2^-)$ Glycogen – $\nu(CC)$, $\nu(CO)$
1139	1128		RNA (ribose) – $\nu(CO)$ Proteins – $\nu(CN)$ Lipids – $\nu(CC)_{acyl}$ Carbohydrates – $\nu(CO)$, $\nu(CC)$
1170	1170		DNA (C,G,T) – $\nu(CC)_{ring}$ Proteins (Phe,Trp,Tyr) – $\delta(CH)$
1235-1245	1235-1245		Lipids, carbohydrates – $\delta(CH_2)$, $\omega(CH_2)$, $t(CH_2)$ B-DNA, RNA – $\nu_{as}(PO_2^-)$
	1250		Proteins – amide III (δ(CN–H)/ν(CN))
	1314	1350	DNA (A,G) – $\nu(CC)_{ring}$, $\delta(CH)$ Proteins (Trp) – $\nu(CC)_{ring}$, $\delta(CH_2)$
1400-1450	1400-1450	1430-1470	Proteins, lipids, carbohydrates – $\delta(CH_2)$; $\delta(CH_3)$ membranes
1550-1560	1555		Proteins – amide II (δ(CN–H)/ν(CN)) DNA (G) – $\nu(CC)_{ring}$
1585	1585		DNA (T) – $\nu(CC)_{ring}$ Proteins (Phe,Trp) – ν (C=C), ν (C=N)
	1622	1620	Water – $\delta(OHO)$
1650-1660	1650-1660		DNA – $\delta(NH_2)$ Proteins – amide I (ν(C=O)) Lipids – ν(C=C)
1740			Phospholipids ($\nu(C=O)_{ester}$)
2850-2875	2850		Proteins, lipids, carbohydrates – $\nu_s(CH)$, $\nu_s(CH_2)$
2880	2880-1890		Proteins, lipids, carbohydrates – $\nu_s(CH_3)$
2900-2935	2933		Proteins, lipids, carbohydrates – $\nu_{as}(CH_2)$
2960	2960		Proteins, lipids, carbohydrates – $\nu_{as}(CH_3)$
	3060		Proteins – amide B (2 x amide I FR ν(NH))
3250-3300	3300		Proteins – amide A (ν(NH))
3300-3400			Lipids, carbohydrates – ν(OH)
3450	3450		Water – ν(OH)

[a]A – adenine; C – cytosine; dG – deoxyguanine; dT – deoxythymine; G – guanine; Glu – glucose; Hyp – hydroxyproline; Met – methionine; Phe – phenylalanine; Pro – proline; T – thymine; Trp – tryptophan; Tyr – tyrosine; U – uracil; Val – valine. δ – in-plane deformation; γ – out-of-plane deformation; ν – stretching; ρ – rocking; t – twisting; ω – wagging. s – symmetric; as – anti-symmetric; FR – Fermi resonance.

to bulk water, in the translational (below *ca.* 300 cm^{-1}), librational (500 to 1000 cm^{-1}) and OH stretching (3200 to 3600 cm^{-1}) regions of the spectrum [199,202,207,325]. Figure 48 comprises the INS spectra presently measured (at 10 K) for human breast cancer cells: untreated and cisplatin-treated (8 and 20 μM) cell pellets and lyophilised cells, as well as PBS difference spectra (resulting from subtraction of the saline buffer to each of the cell pellet samples). Three distinct structural contributions could be identified, due to: 1) extracellular (bulk) water, yielding a broad and intense librational band at 540 to 1000 cm^{-1} (identical to the H-bonded tetrahedral network of ice Ih), and a translational region comprising two peaks at 224 and 304 cm^{-1}, assigned to intermolecular water-water hydrogen bonding [346], as well as acoustic modes at 56 (very intense) and 155 cm^{-1}; 2) intracellular (interfacial) water, responsible for a distinctive feature at *ca.* 560 cm^{-1}; 3) cellular components, clearly perceived in the lyophilised sample in the 1280-1500 cm^{-1} range (centred at *ca.* 1370 cm^{-1}, mainly arising from CH_2 deformation modes of proteins, lipids and carbohydrates), 240 and 290 cm^{-1} from proteins ($\tau(CH_3)$, partially overlapped with the water intramolecular H-bonding features) and 160 cm^{-1} from membrane lipids ($\tau(CH_3)$) (Table 11). Indeed, unlike the INS profile of the cell pellets, the spectrum of the lyophilised cells gave rise to INS peaks solely due to the biomolecules within the cell since these samples were devoid of both extra- and intracellular water. Comparison of this data for the lyophilised cells with and without cisplatin allowed to uncover a drug effect on DNA through the corresponding adenine and timine $\nu(CC)_{ring}$ band at 728 cm^{-1} (which was not observed in the treated sample, Figure 48). A slight blue shift (from 552 to 556 cm^{-1}) was detected in the librational band peak between the spectrum of PBS (as a model for extracellular water) and the drug-free cell pellet, which is ascribed to an enhanced rigidity in the structure of interfacial water (within the crowded cytoplasm). Upon cisplatin incubation a marked change in the spectral profile was observed, the librational band (540-1000 cm^{-1}) resembling the profile characteristic of low-density amorphous ice [346], in accordance with a noteworthy decrease in the ordering of water molecules within the drug-containing cytoplasm. The contribution from intracellular water was clearly unveiled upon subtraction of PBS from the data measured for the cells, either untreated or cisplatin-treated, evidencing striking variations relative to bulk (extracellular) water as a consequence of

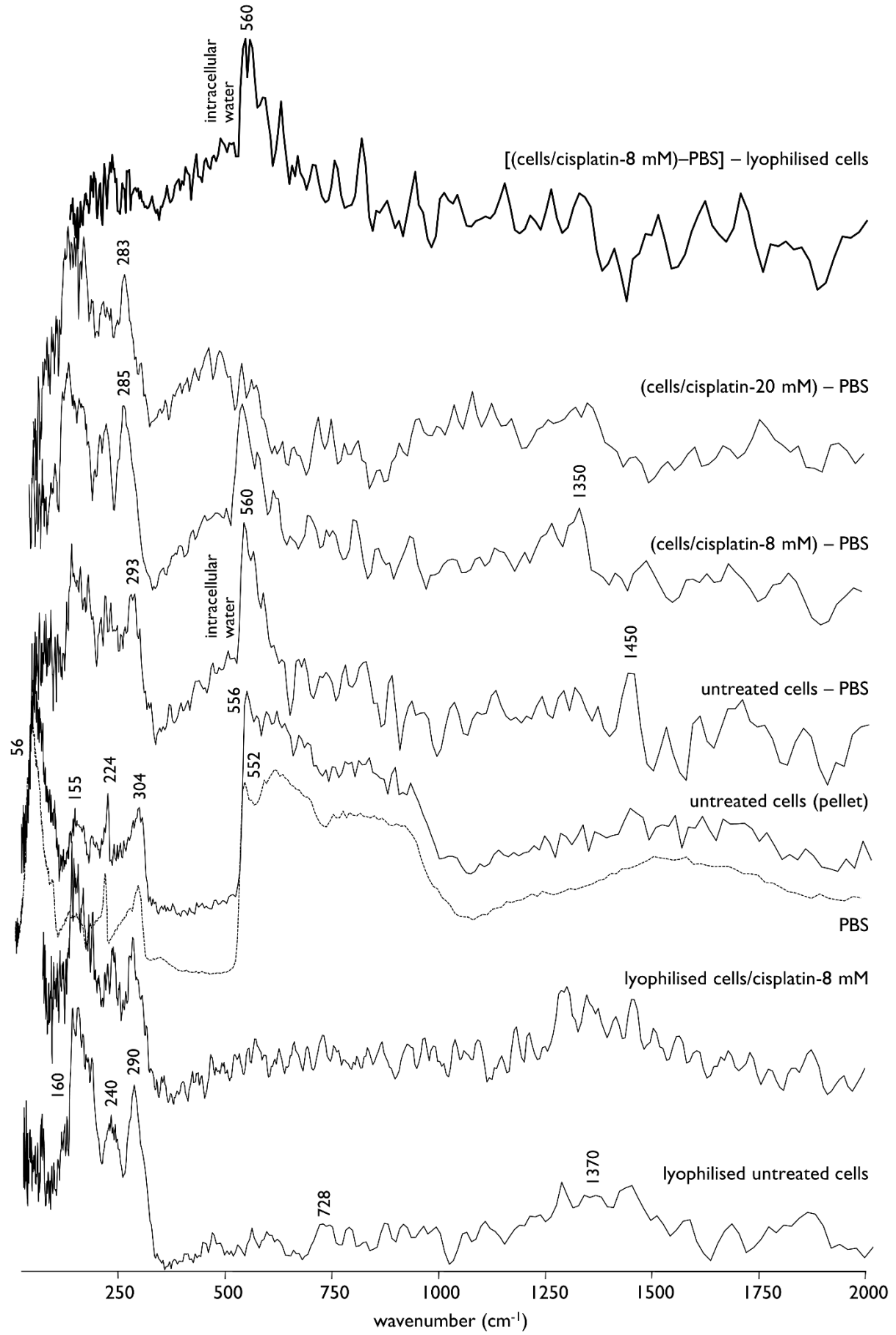

Figure 48 – INS spectra (at 10 K) of MDA-MB-231 cells (pellet and lyophilised samples), both untreated and cisplatin-treated.

modifications in the respective H-bonding network (Figure 48): 1) the broad librational 540-1000 cm^{-1} band was substituted by a much narrower signal centred at 560 cm^{-1}, ascribed to interfacial water, which was progressively reduced in intensity with increasing cisplatin concentration; 2) the features characteristic of H-bonded bulk water molecules were affected – the 224 cm^{-1} translational peak decreases, while the 304 cm^{-1} signal shifts to 293, 285 and 283 cm^{-1} (more noticeably in the drug-exposed samples, as a direct function of cisplatin concentration); 3) the $\delta(CH_2)$ signal at 1450 cm^{-1} mainly due to the cellular lipid constituents disappears, as a consequence of the recognised metabolic impact of this type of Pt(II)-based agents [345] (according to 3.3., Results and Discussion section), while a band is detected at *ca.* 1350 cm^{-1}, assigned to $\nu(CC)_{ring}$ and $\delta(CH)$ modes from DNA (adenine and guanine) and proteins (particularly tryptophan). Subtraction of the data for the lyophilised cells from the cisplatin (8 μM)-exposed cells (after PBS exclusion) yielded a double-difference spectrum which best revealed the confined (cytoplasmic) water in the presence of the drug, since the contributions from extracellular water and the cellular constituents (metabolites and biomolecules) were removed. Analysis of this spectral profile corroborates the assignment of the 560 cm^{-1} signal to intracellular water.

These results plainly show that drug exposure induces structural changes in intracellular water H-bonding network which are mainly reflected in the librational region, as expected, since this is strongly dependent on proton ordering defining the geometrical arrangement within the lattice [199,346,347]. In fact, the hydrogen bonds in confined intracellular water, known to display significantly longer lifetimes (5 to 10x than those occurring in unconstrained water, are proposed to be further changed by cisplatin, with a profound impact on the intrinsic dynamics of water molecules within the cell as to their ability to rotate, translate and interact with biomolecules (in their hydration layers). Several water structures displaying different H-bonding profiles, resembling some of the known ice phases studied so far [346], may then coexist within the cell upon increasing cisplatin exposure – e.g. hexagonal (Ih) to low-density amorphous (LDA) ice-like geometries. Indeed, the drug-induced conformational changes in DNA and proteins are expected to affect these molecule´s hydration patterns, this effect being assumed to propagate into the native hydrogen bond network of water in the highly packed

cytoplasm (the average distance between macromolecules in an eukaryotic cell being ca. 2 nm [341]).

These results evidence that the intramolecular H-bond network characteristic of intracellular water appears to be disrupted by the presence of the antitumour drug, the average interaction of each H_2O to four neighbouring molecules being changed to a distinct lattice organisation within the intracellular medium, which encompasses water–water and water–biomolecules hydrogen-type interactions. Actually, the librational profile observed in the INS spectra of cisplatin-exposed cells compares better with LDA or cubic (Ic) forms of ice than with the polycrystalline hexagonal geometry of water at cryogenic temperatures (ice Ih). This data is in accordance with previous INS and QENS studies on the structure of water associated with DNA [199,200,348,349] and yeast cells [202].

3.4.2. Dynamics

Quasielastic data was acquired in the OSIRIS spectrometer (ISIS Facility, UK [213]), that is sensitive to motions with time scales of the order of the picoseconds (*ca.* 4-200 ps, within a length interval of *ca.* 4-20 Å), optimal for the detection of intracellular water dynamics and still allowing to perceive local motions of the biological macromolecules in the cytosol. Nevertheless, discrimination between both types of motions is far from straightforward considering the diversity of entities present in the heterogeneous cellular system under observation: cellular components such as sugars, lipids, proteins and DNA (moving with similar time-scales) and intracellular milieu comprising water molecules in different local environments – cytoplasmic (less constrained) water and hydration water (in the vicinity of biomolecules, strongly adsorbed at their surface).

Intracellular water dynamics was currently investigated in the TNBC cells under different conditions, by measuring several samples (at 298 K): (i) phosphate buffered saline (PBS) and cisplatin-containing (8 μM) PBS, to assess a possible drug effect on the saline medium; (ii) cell pellets, both drug-free (control) and cisplatin-treated (8 and 20 μM); (iii) cell pellets in deuterated saline (apart from the non-washed samples), in order to minimise the bulk water component and accurately identify the contribution from intracellular water.

In these densely packed cell pellets the intracellular medium accounts for *ca.* 95% of the total water within the system (according to the quantification of intra- *vs* extracellular water in the samples, see Experimental Section – 2.2.3.5.). A good approximation to the scattering signal due to the extracellular water contribution (*ca.* 5%) may be visualised in the difference QENS profile of the non-washed cells minus the PBS_{deut}-washed ones depicted in Figure 49(A) (profile in blue), which clearly evidences the attenuation of this component upon its deuteration (σ_{inc}(D)=2.05 *vs* σ_{inc}(H)=80.26 barns) that allows an improved detection of the contribution from the intracellular water. Therefore, the henceforth discussion is mostly based on the analysis of PBS_{deut}-washed cell samples, which are dominated by intracellular water apart from cellular metabolites and biomolecules. In addition, subtraction of the PBS data from these cell pellets was carried out, with a view to completely remove the reminiscent bulk water component and plainly show the contributions from the intracellular milieu (Figure 49(B)).

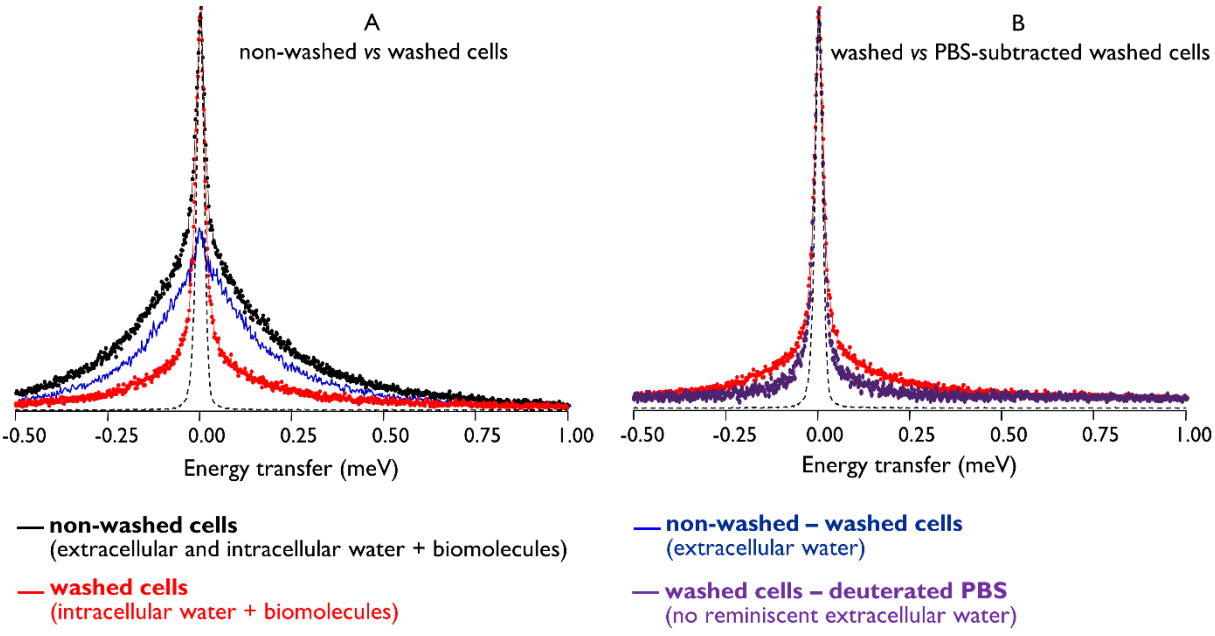

Figure 49 – QENS spectra (298 K) at Q=1.079 $Å^{-1}$, measured for untreated MDA-MB-231 cells: (A) Non-washed *vs* PBS_{deut}-washed cells. (B) Washed *vs* PBS-subtracted washed cells.
(Spectra were normalised to maximum peak intensity. The dashed line represents the instrument resolution, as measured by a standard vanadium sample).

Exposure to cisplatin was found to induce a reduced flexibility in both non-washed and washed cells, reflected in the narrowing of the corresponding QENS profiles in a concentration-dependent way (Figure 50 (A) and (B)). This drug-prompted reduced mobility of intracellular water is consistent with a glassy form as opposed to a flexible state in drug-

free cells. Hence, a dynamical transition is proposed to take place upon drug exposure, associated to the onset of translational diffusion and localised motions of the cellular macromolecules, from an intracellular water plasticity in untreated cells to a significantly higher rigidity upon drug administration. This transition from a flexible to a glassy state is suggested to involve jumping between sites of different energy within the intracellular confined space, in the time window of the spectrometer, and the onset of glassy dynamics was found to depend on drug concentration. Since the cisplatin solutions were prepared in PBS, the drug effect on the saline medium was also monitored, a slight narrowing of the QENS profile having been observed for the drug-containing deuterated PBS (Figure 50(C)).

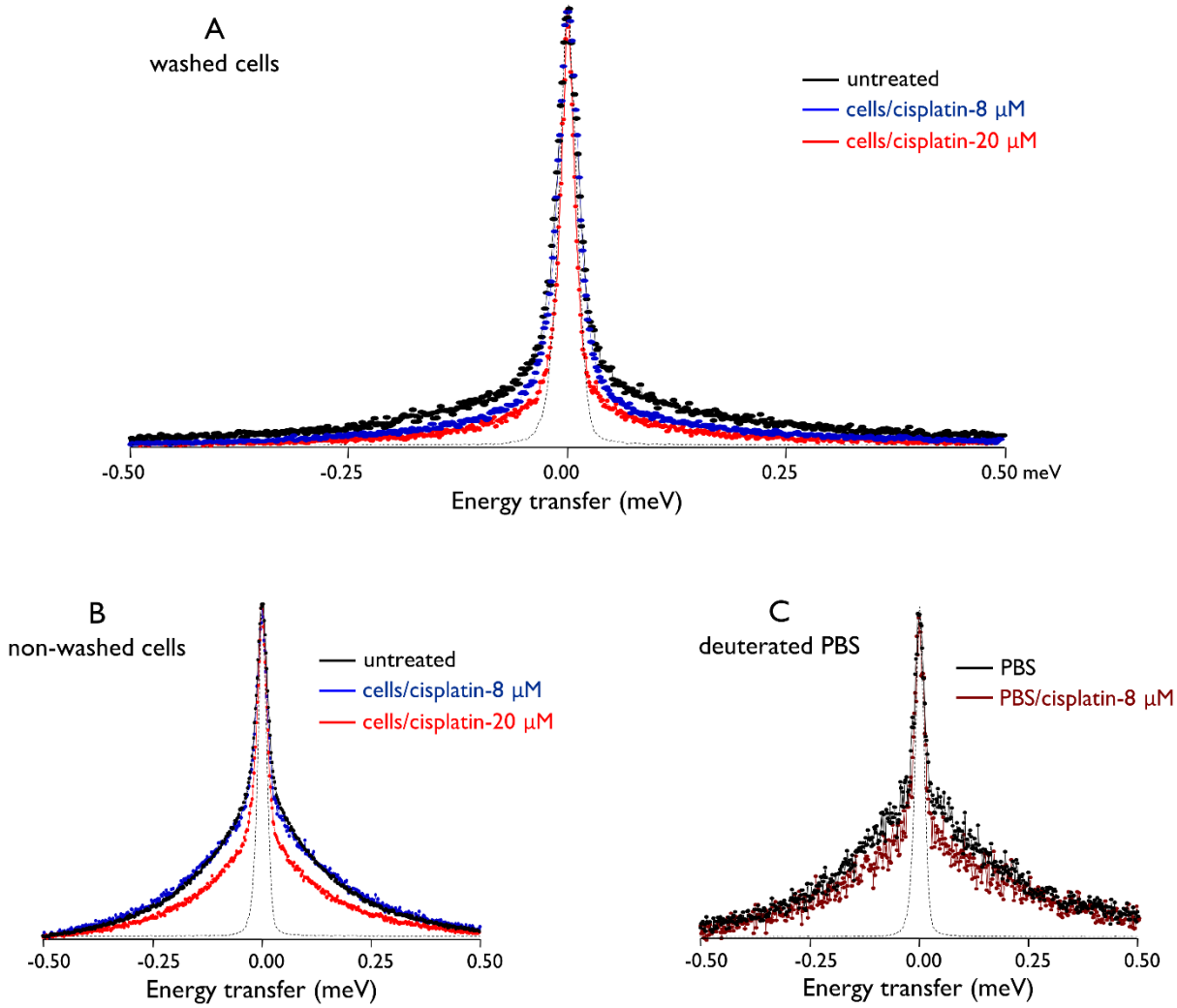

Figure 50 – QENS spectra (298 K) at Q=1.079 $Å^{-1}$, measured for MDA-MB-231 cells and PBS, with and without cisplatin: (A) Cells in deuterated saline medium (washed). (B) Non-washed cells. (C) Deuterated saline medium. (Spectra were normalised to maximum peak intensity. The dashed line represents the instrument resolution, as measured by a standard vanadium sample).

Fitting of the QENS spectra was attained using one Delta function (elastic component) and three Lorentzians (quasielastic contributions) (Figure 51). In fact, two Lorentzian functions were found not to suffice for accurately fitting the experimental data acquired for the complex system under study (Figure 52). One Delta and three Lorentzians were thus used to represent three major dynamical components which are proposed to correspond to the following three populations: 1) very slow motions of the largest organelles and cytoskeleton within the cell

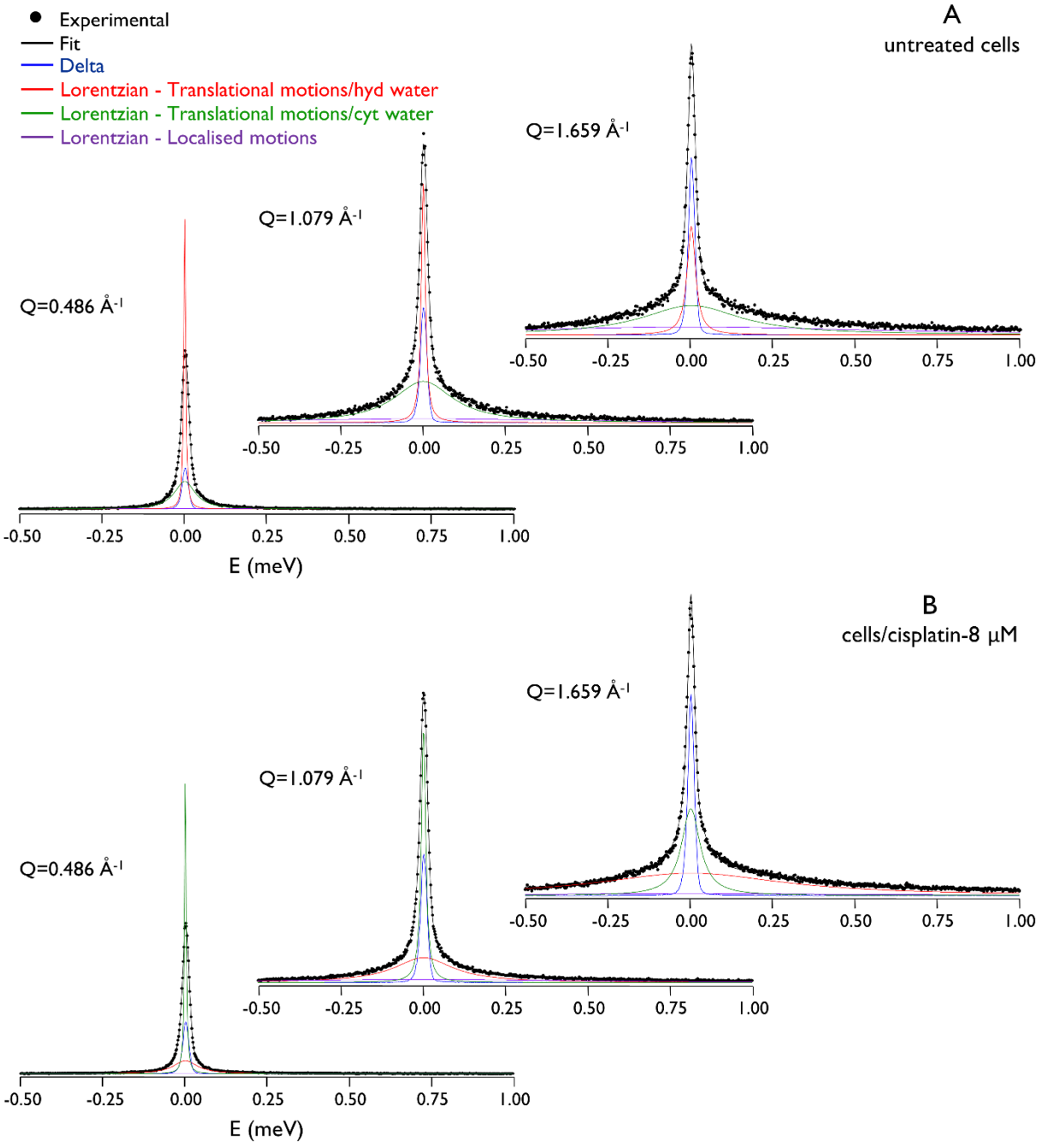

Figure 51 – QENS spectra (298 K) for untreated (A) and cisplatin-treated/8 µM (B) MDA-MB-231 cells, in deuterated saline medium (washed), fitted using three Lorentzian and one Delta functions, at some typical Q values.

(slower than the longest observable time defined by the spectrometer resolution), represented by the Delta function; 2) slow diffusion of the intracellular water molecules (Q-dependent reorientations mediated by hydrogen bonds), represented by the two narrower Lorentzians, corresponding to two different regimes that we ascribe to two types of intracellular water – water in the vicinity of the biomolecules and water from the rest of the intracellular milieu, beyond the hydration shells (hereafter called hydration and cytoplasmic water, respectively); 3) internal localised motions of the macromolecules and/or fast rotation of the water molecules within the cellular medium (Q-independent), attributed to the broader Lorentzian function.

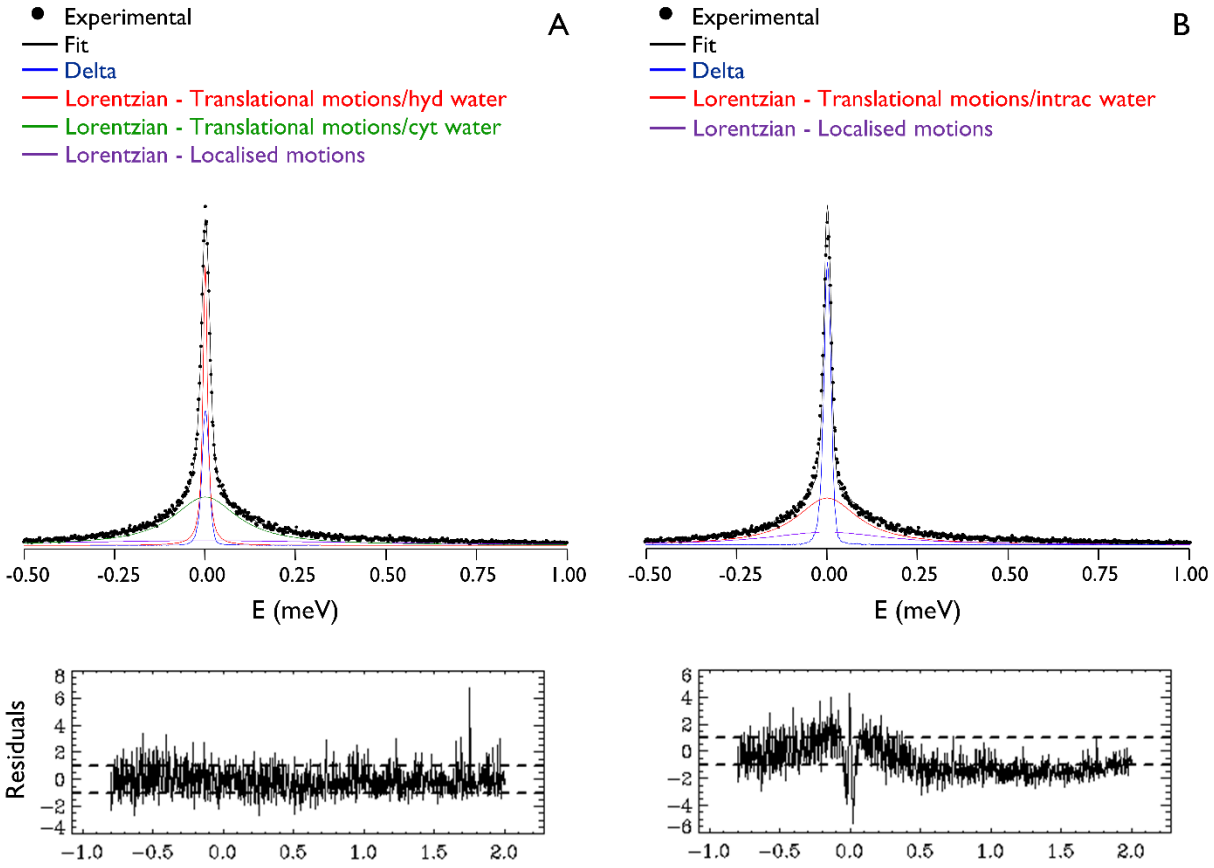

Figure 52 – QENS spectra (at 298 K) at Q=1.079 $Å^{-1}$for untreated MDA-MB-231 cells in deuterated saline medium (washed), fitted using: (A) three Lorentzian and one Delta functions. (B) two Lorentzian and one Delta functions.
(The corresponding residual plots are shown).

Fitting of the QENS profiles obtained for the PBS_{deut}-washed samples (with and without cisplatin) allowed to probe biomolecules and intracellular water exclusively. The fitting parameters were analysed as a function of the wave vector transfer (Q). The full widths at

half-maximum were extracted from the Lorentzian functions representing each of these quasielastic dynamical components, and their dependence on Q^2 provided information on the dynamical behaviour of the system, at the different conditions tested: the confined localised motions (broad Lorentzian) yielded a flat, Q-independent, profile, while the non-localised translations of intracellular water (narrower Lorentzians) gave rise to Q-dependent functions (Figure 53).

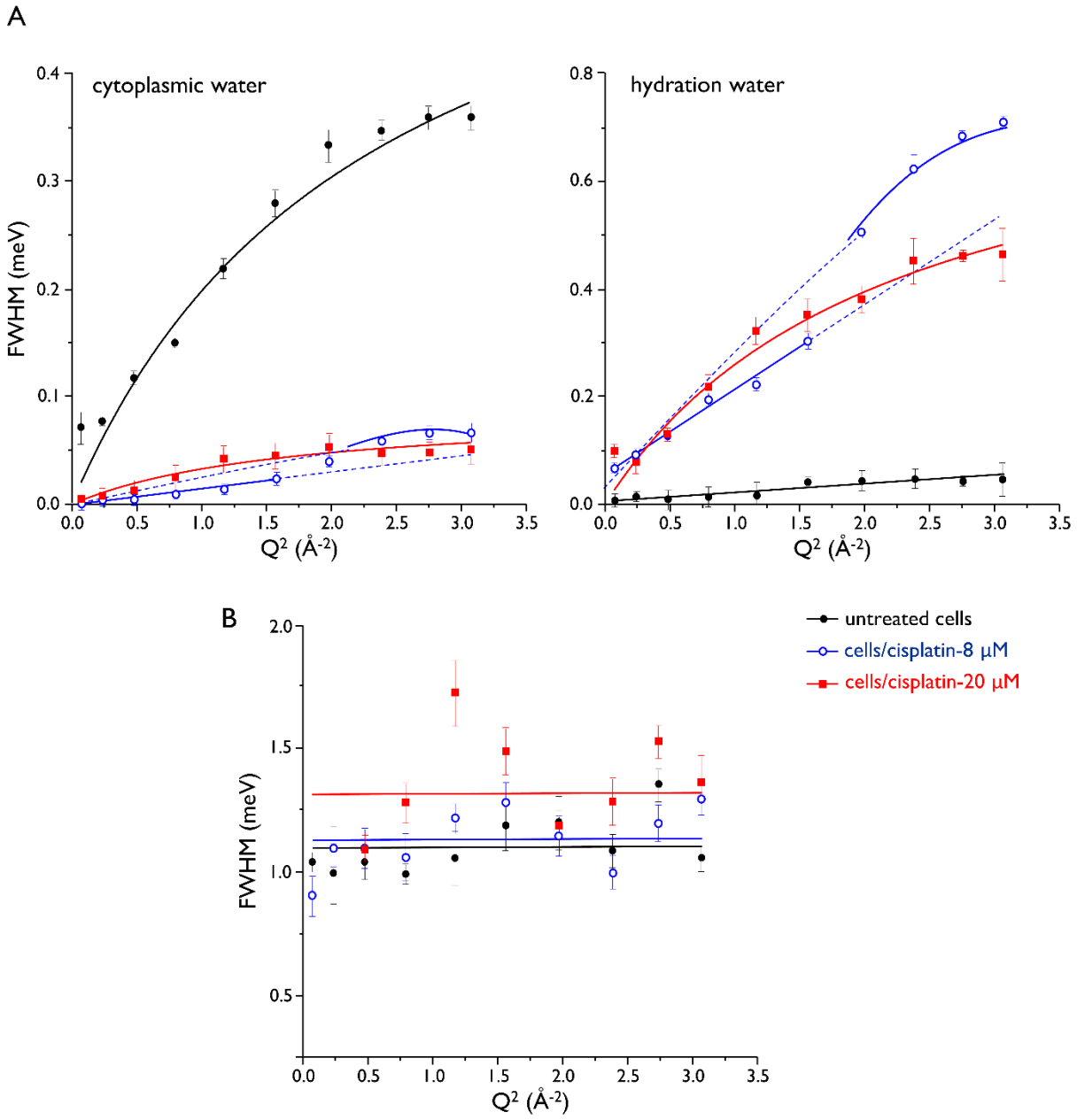

Figure 53 – Variation of the full widths at half-maximum (FWHM) with Q^2 for untreated and cisplatin-treated (8 and 20 μM) MDA-MB-231 cells in deuterated saline medium (washed), at 298 K: (A) Lorentzian functions representing the translational motions of intracellular water – cytoplasmic and hydration water. (B) Lorentzian function representing the internal localised motions within the cell.

Each of the motions taking place within the MDA-MB-231 cells may then be approximated by a different model, which was shown to be affected by deuteration of the intracellular medium and, to a higher degree, by the presence of cisplatin. The plots represented in Figure 53 for the translational motions of intracellular water (both in the cytoplasm and in hydration shells) correspond to the most rational biochemical interpretation of the data, taking into account the knowledge available on the activation process and cytotoxic mechanism of cisplatin within the cell. Overall, cytoplasmic water displayed a higher degree of freedom than hydration water, as anticipated in view of the interactions taking place between the biomolecules and the water molecules in the corresponding hydration layers, that are tightly organised and allow only very restricted motions (Figure 51 and Figure 53). Regarding the translational motions of cytoplasmic water, a dynamical profile in accordance with a translational jump diffusion model was observed, with significantly restricted motions when going from untreated cells to PBS_{deut}-washed samples exposed to cisplatin at increasing dosages (8 and 20 μM, Figure 53 (A)). The hydration water, in turn, displayed a distinct dynamical pattern, going from a highly constrained Fickian diffusion in the drug-free cells (where hydration layers are intact) proceeding *via* a sequence of infinitely small steps (according to $\Gamma=DQ^2$), to a considerably less restricted purely translational jump behaviour for 20 μM-treated cells (where hydration shells are disordered, Figure 53 (A)). Apart from a probable direct drug effect, this variation in the hydration water confinement upon cisplatin exposure is proposed to be mainly due to the drug-prompted reorientation of the cellular biomolecules (*e.g.* proteins, DNA) causing a gradual disturbance of their native structure and a consequent disruption of their highly organised hydration layers, leading to an enhanced degree of freedom of the respective water molecules. This is hypothesised to be maximum when the cellular solutes adopt a random conformation triggered by the presence of the drug (at 8 μM), but undergoes a decrease upon further reorganisation of the biomolecules to a more ordered (although probably nonfunctional) structure in the extremely confined medium containing high cisplatin concentrations (20 μM). In fact, the conformational rearrangements of proteins and other cellular macromolecules were previously reported to be responsible for a dynamical heterogeneity within the corresponding hydration layers [350,351]. Overall, as anticipated, the anticancer drug was shown to have an impact on both the cytoplasmic medium and the

hydration water, which, in turn, influence each other. Actually, the drug impact on hydration water (mediated by the macromolecules´ rearrangement) is foreseen to spread to the surrounding water molecules in the cytoplasm, adding to the direct drug effect, and cisplatin´s impact on the cytosol will gradually extend to the neighbouring hydration layers.

Particularly interesting is the intermediate behaviour detected for both cytoplasmic and hydration water in the samples exposed to the lowest drug dosage (8 μM): the experimental data is fitted to an unrestricted Fickian diffusion at low Q, and to a jump reorientation mechanism in the high Q region (beyond Q=1.25 $Å^{-1}$), each type of water population within the intracellular environment appearing to display different dynamic regimes. This can be pictured as a transitional state of drug-induced disorganisation, in which neither the hydration nor the cytoplasmic water behave purely as such – the former is proposed to be partially detached from the macromolecules´ hydration shells mixing with the outside water in the cytosol, while the former starts to approach and become part of this more restricted environment around the cellular components. This dynamical change occurs for a distance of *ca.* 4 Å (that is within the boundaries of a biomolecule´s hydration shell) – beyond this limit, water molecules display a cytoplasmic behaviour; below, they behave as constrained hydration water.

Hence, upon a progressively higher degree of confinement to *ca.* 4 Å – from untreated non-washed to PBS_{deut}-washed untreated and PBS_{deut}-washed drug-containing cells – the dynamical profile of cytoplasmic water appears to be better adjusted by a translational jump model than by a simple Fickian diffusion. This jump reorientation or extended jump model (EJM) [280-282] was described to occur through a sequence of discrete large amplitude angular jumps involving an exchange of H-bond acceptors, as opposed to the Fickian-like continuous diffusive mechanism (either unrestricted or restricted) that proceeds *via* a sequence of infinitely small diffusive steps (according to $\Gamma=DQ^2$). In the translational jump model, the H-bond cleavage and the molecular reorientation take place concertedly and not successively as usually considered, and each time one of the approximately four H-bonds formed by a water molecule is exchanged, the molecule´s centre of mass undergoes a translational shift. This reorientation process is therefore dependent on the local environment of the water molecules, and is anticipated to be affected by the presence of an extrinsic entity (such as a

drug) in the intracellular medium. Moreover, when H-bonds are ruptured zones of higher density water are created (*i.e.* water density is locally higher than the bulk) which is expected to have an effect on the conformation (and therefore function) of neighbouring biomolecules.

The translational diffusion coefficients (D_T), translational jump times (τ_T) and correlation times for the localised motions of the cellular macromolecules (τ_L), at each drug concentration tested, were extracted from the dynamical model considered for each case. The values thus obtained clearly reflected the effect of cisplatin on the of the intracellular medium. For the cells in deuterated saline medium (washed samples), the diffusion coefficients obtained for cytoplasmic water were consistent with an enhanced rigidity, in a concentration-dependent way: D_T^{298}=1.04±0.05x10^{-5} *vs* 0.19±0.01 x10^{-5} cm^2s^{-1} and τ_T^{298}=1.00±0.10 *vs* 7.39±1.16 ps, for control and cisplatin/20 μM-treated cells, respectively. For water within hydration shells, in turn, a reverse effect was observed (as previously discussed): D_T^{298}=0.03±0.0004x10^{-5} *vs* 1.39±0.13 x10^{-5} cm^2s^{-1}, for control and cisplatin (20 μM)-exposed samples. Regarding the correlation times for the localised motions of the cellular constituents quite high values were measured, as expected in view of the large dimensions of the biomolecules and the crowded intracellular environment in which they move: τ_L^{298}=21.94±0.04, 21.43±0.04 and 18.12±0.07 ps for untreated and cisplatin-treated (8 and 20 μM), respectively. The τ_L decrease detected upon drug-exposure, mainly in the presence of the highest cisplatin concentration (20 μM), may be justified by the drug-induced structural disruption of the intracellular water that will ease these localised motions of the macromolecular solutes.

These dynamical parameters obtained for MDA-MB-231 cells were compared with previously reported values for *Escherichia coli* bacteria [189,205]: D_T^{298}=1.04±0.05x10^{-5} *vs* D_T^{301}=2.39±0.05x10^{-5} cm^2s^{-1} and τ_T^{298}=1.00±0.10 *vs* τ_T^{301}=1.54±0.08 ps, respectively for drug-free cancer cells and *E. coli*. Actually, while the results published for *E. coli* were not significantly different from those determined for pure water (D_T^{298}=2.3x10^{-5} cm^2s^{-1} [352]), evidencing an intracellular water diffusion process similar to bulk water, the same was not verified in the currently probed human breast adenocarcinoma cells for which a considerably restricted intracellular water dynamics was observed (under identical conditions). This may be justified by the fact that eukaryotic cells have an extremely crowded cellular environment (macromolecular concentrations as high as 400 $mg.mL^{-1}$ and distances among biomolecules of

ca. 1 nm) as opposed to bacteria, leading to a much higher degree of confinement of intracellular water, its dynamics being better adjusted by a jump diffusion model than by a simple Fickian diffusion. Furthermore, the translational diffusion coefficients presently obtained for cytoplasmic water in the breast cancer cells exposed to cisplatin are one order of magnitude lower than the value obtained by QENS for extreme halophiles (in which the high salt concentration leads to a significant reduced mobility of *ca.* 76% of intracellular water) [204] – $D_T^{298}=0.19\pm0.01\times10^{-5}$ (cisplatin-20 μM) *vs* $D_T^{285}=1.29\times10^{-5}$ cm^2s^{-1}, respectively.

4 Conclusions

4.1 General Conclusions

The present work aimed to investigate the effect of dinuclear Pt(II) and Pd(II) spermine complexes (with chlorides as leaving ligands) on the cellular response at the biochemical level, through analysis of the vibrational pattern of drug-treated and untreated cells. The multidisciplinary approach followed in this study, coupling biochemical assays for drug screening (both *in vitro* and *in vivo*) to spectroscopic techniques, aimed to link biological response to spectral signatures of cellular biochemistry and intracellular water dynamics, thus identifying spectral markers of drug activity.

The results presently gathered clearly evidenced that although both Pd_2Spm and Pt_2Spm displayed cytotoxicity against the triple negative MDA-MB-231 human breast carcinoma cells, the Pd-based complex was the most effective, combining promising anti-proliferative, anti-invasive and anti-angiogenic abilities, specifically for Pd_2Spm/DTX combinations (with a clear synergetic effect). In particular, a very **high anti-angiogenic and anti-invasive capacity** were induced by Pd_2Spm in sole administration, that were further enhanced by exposure to Pd_2Spm/DTX combination. This is suggested to occur through inhibition of endothelial cell proliferation and tubules formation, coupled to Pd_2Spm-prompted cell sensitisation. This proposed angiogenesis-targeting therapeutic strategy *via* concurrent exposure to Pd_2Spm and DTX may thus contribute to circumvent chemoresistance to cisplatin-like drugs in human low prognostic breast cancer, which is of the utmost relevance for future clinical applications of this polynuclear Pd(II) agent, both in primary and in adjuvant therapy.

The cutting-edge optical vibrational spectroscopy techniques used – Raman and SR-IR microspectroscopies – for the interrogation and measurement of the metabolic impact and cellular response to Pt_2Spm and Pd_2Spm (cisplatin being taken as a reference), allowed access to an accurate description of variations in cellular biochemistry, with molecular specificity, in the presence of each of the compounds under study, unveiling vibrational bands assigned to specific drug-elicited effects (spectral biomarkers) and to the cell´s response to the chemotherapeutic perturbation. In fact, drug exposure was found to trigger both a **direct biochemical effect**, *via* covalent drug binding to DNA, and a physiological response from

the cell as variations in the bands assigned to lipids and proteins were the combined outcome of direct drug interaction and the cellular reaction to the chemotherapeutic insult.

Multivariate analysis was of utmost importance in order to clearly distinguish between drug-treated and untreated cells. Additionally, it enabled to discriminate between groups of data and to correlate them with different chemotherapeutic conditions regarding concentration and type of drug – either Pt(II)- or Pd(II)-based, mononuclear or dinuclear.

Moreover, the intracellular water was under focus in this work starting with the assumption that in human cells the behaviour of cytoplasmic water (both structural and dynamical) determines not only the conformation and function of biomolecules (primarily through their hydration shells), but may also be tamed by the cellular constituents – the cellular macromolecules "dance" to the tune of intracellular water and *vice versa*, in a twofold, intertwined, process. Hence, any effect that a drug may exert on vital macromolecules (such as DNA or proteins) will also have a predictable **impact on intracellular water**, with consequences on cellular function, thus constituting a potential **secondary pharmacological target**. The reported combined inelastic and quasielastic neutron scattering spectroscopies allowed to establish the feasibility of these techniques to probe complex macromolecular systems such as human cells, with a view to gain a deeper insight into confined intracellular water and to monitor perturbations to its structural and dynamical behaviour (*e.g. via* interference with its native H-bonding network) due to the presence of external agents such as chemotherapeutic agents.

The results thus obtained revealed a clear picture of the intracellular water response to a drug, evidencing clear differences relative to non-treated cells and therefore disclosing a clear impact of cisplatin on the cytomatrix. Coupled to different structural properties, mainly reflected in the librational region of the INS spectra, this antitumour agent was found to affect the dynamic state of intracellular water, rendering it different from bulk water and also from the cellular medium in drug-free samples, this effect being concentration-dependent. Diffusion of intracellular water molecules is known to be restricted due to confinement within the crowded cytoplasmic environment coupled to strong interactions with biomolecules and membranes (structured water in hydration shells). In the presence of cisplatin, these effects were found to be enhanced due to the drug´s effect on DNA and subsequently on other

cellular constituents (*e.g.* proteins and membranes), disrupting their folded native conformation and thus increasing disorder and crowding in the cellular milieu with a significant impact on water properties. Intracellular water molecules with distinct structural and dynamical profiles – from the hydration shell of biomolecules (hydration water) and from the aqueous intracellular medium (cytoplasmic water) – could be discriminated by QENS. Both were found to be affected by the presence of the antitumour drug, in opposite ways: while the former showed a progressively restrained dynamics upon cisplatin exposure, the latter was prompted to a higher degree of freedom as the biomolecules´ native structure was disrupted by the antitumour agent and the corresponding hydration layers were destroyed. This marked change in the dynamical profile of hydration water in the presence of cisplatin is thus a consequence of the drug-triggered reorganisation of the intracellular macromolecules, which finally readjust into a more ordered (likely nonviable) conformation.

To this date, reduced mobility of cellular water on an atomic scale had never been detected in eukaryotic cells. To the best of the author´s knowledge this was the first study with neutron techniques involving live human cells. This is an innovative way of tackling a drug´s pharmacodynamics, searching for additional (and possibly ancillary) targets of drug action with a view to **improve chemotherapeutic efficiency** without increased deleterious side effects. The successful results already gathered pave the way for further work on a drug impact on intracellular water, for conventional as well as newly developed anticancer agents.

All the findings in the present work (Figure 54) are expected to contribute to the elucidation of potentially novel pathways of cytotoxicity for tailored Pt(II)- and Pd(II)-polyamine polynuclear compounds, leading to diverse and improved pharmacological properties coupled to minimal acquired resistance, and hopefully allowing to identify and predict the cellular response to chemotherapy.

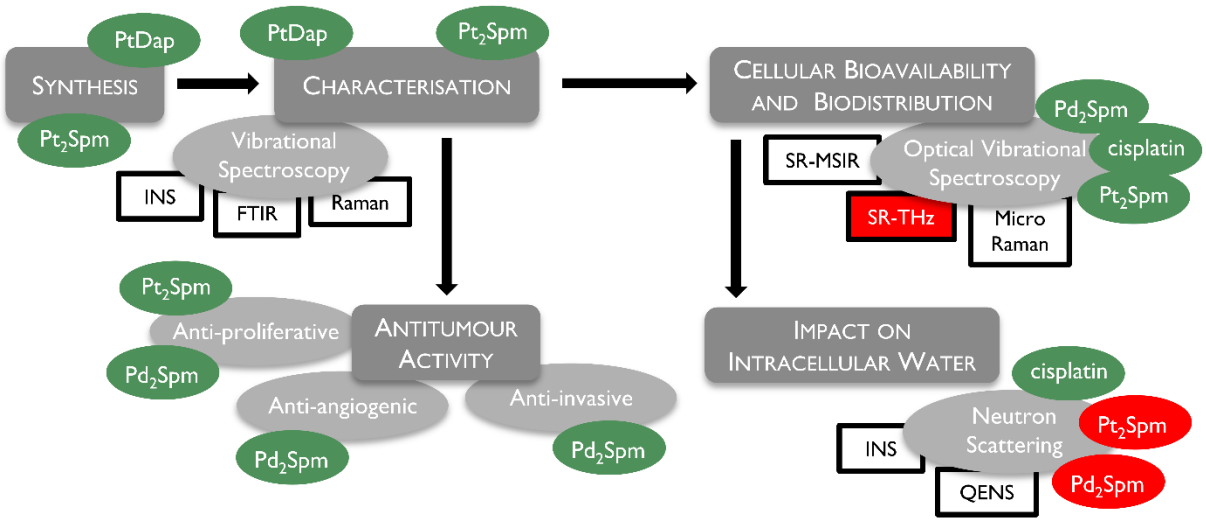

Figure 54 – Schematic representation of the present results (green) and future trends (red).

4.2 Futures Prospects

Future work should focus on the Pd_2Spm complex (the most promising of the tested metal-based agents). Further investigation through optical vibrational spectroscopy on its effect on the biochemical profile of cells and tissues should be performed, since information at the cellular and subcellular levels – *in vitro* bioavailability, biodistribution and metabolic impact – are pivotal in rational drug design. The correlation between vibrational microscopic chemical images and specific spectral changes induced by a particular compound should also be evaluated through single cell imaging, which will hopefully allow to attain an accurate description of cellular biochemistry in the presence of the pharmacological agent, as well as to monitor the cellular response to treatment regarding specific biomarkers of drug action.

Moreover, the full extent of Pd_2Spm influence on DNA should be probed, namely through synchrotron-based THz absorption spectroscopy. Actually, the drug has never been detected within a biological matrix such as a cell, and this can only be foreseen through this type of high resolution techniques, that will hopefully allow to clearly observe the low frequency vibrational modes characteristic of the complex (*e.g.* involving the metal centres).

As intracellular water may be envisaged as a secondary pharmacological target, it is of the utmost importance to pursue the experiments tackling intracellular water dynamical and structural behaviour, in the presence of the polynuclear complexes presented along this work, in order to better understand the drug's pharmacodynamics aiming at enhancing its

therapeutic activity. Additionally, whether this is a cell-specific effect or not may be clarified by monitoring the intracellular water in different cancer cell lines, subject to treatment with the same drug.

Overall, these future studies will build on the presently gathered data, and expectedly lead to a better understanding of the *in vivo* mechanism of action of antitumour agents used daily in the clinic, at a molecular level, providing valuable clues for the rational design of improved anticancer metal-based drugs (Figure 54).

5 References

1. Ferlay, J., Soerjomataram, I., Ervik, M., Dikshit, R., Eser, S., Mathers, C., Rebelo, M., Parkin, D.M., Forman, D., and Bray, F., *GLOBOCAN 2012 v1.0, Cancer Incidence and Mortality Worldwide: IARC CancerBase No. 11* [Internet]. Lyon, France: International Agency for Research on Cancer; 2013. Available from: http://globocan.iarc.fr, accessed on 14/05/2016.
2. Krawczyk, N., Banys, M., Hartkopf, A., Hagenbeck, C., Melcher, C., and Fehm, T., (**2013**). Circulating tumour cells in breast cancer. *Ecancermedicalscience*, **7**, 1.
3. Wheater, M.J., Johnson, P.W., and Blaydes, J.P., (**2010**). The Role of MNK Proteins and eIF4E Phosphorylation in Breast Cancer Cell Proliferation and Survival. *Cancer Biol Ther*, **10**(7), 728.
4. Weigelt, B., Peterse, J.L., and van 't Veer, L.J., (**2005**). Breast Cancer Metastasis: Markers and Models. *Nat Rev Cancer*, **5**(8), 591.
5. Cancer country profiles 2014, available from: http://www.who.int/cancer/country-profiles/prt_en.pdf?ua=1, accessed on 15/05/2016.
6. Pinder, S.E. and Ellis, I.O., (**2003**). The Diagnosis and Management of Pre-Invasive Breast Disease: Ductal Carcinoma *in situ* (DCIS) and Atypical Ductal Hyperplasia (ADH) -Current Definitions and Classification. *Breast Cancer Res*, **5**(5), 254.
7. Netter, F., *Atlas of Human Anatomy*. 6th ed. 2014: Elsevier.
8. Li, C.I., Uribe, D.J., and Daling, J.R., (**2005**). Clinical Characteristics of Different Histologic Types of Breast Cancer. *Br. J Cancer*, **93**(9), 1046.
9. Weigelt, B., Geyer, F.C., and Reis, J.S., (**2010**). Histological Types of Breast Cancer: How Special Are They? *Mol Oncol*, **4**(3), 192.
10. Polyak, K., (**2011**). Heterogeneity in Breast Cancer. *J Clin Invest*, **121**(10), 3786.
11. Bertos, N.R. and Park, M., (**2011**). Breast Cancer - One Term, Many Entities? *J Clin Invest*, **121**(10), 3789.
12. Kassam, F., Enright, K., Dent, R., Dranitsaris, G., Myers, J., Flynn, C., Fralick, M., Kumar, R., and Clemons, M., (**2009**). Survival Outcomes for Patients with Metastatic Triple-Negative Breast Cancer: Implications for Clinical Practice and Trial Design. *Clin Breast Cancer*, **9**(1), 29.
13. Lakhani, S.R., van de Vijver, M.J., Jacquemier, J., Anderson, T.J., Osin, P.P., McGuffog, L., and Easton, D.F., (**2002**). The Pathology of Familial Breast Cancer: Predictive Value of Immunohistochemical Markers Estrogen Receptor, Progesterone Receptor, HER-2, and p53 in Patients with Mutations in BRCA1 and BRCA2. *J Clin Oncol*, **20**(9), 2310.
14. Peshkin, B.N., Alabek, M.L., and Isaacs, C., (**2010**). BRCA1/2 Mutations and Triple Negative Breast Cancers. *Breast Disease*, **32**(1-2), 25.

15. Sikov, W.M., (**2015**). Assessing the Role of Platinum Agents in Aggressive Breast Cancers. *Curr Oncol Rep*, **17**(2), 3.
16. Kriege, M., Seynaeve, C., Meijers-Heijboer, H., Collee, J.M., Menke-Pluymers, M.B.E., Bartels, C.C.M., Tilanus-Linthorst, M.M.A., Blom, J., Huijskens, E., Jager, A., van den Ouweland, A., van Geel, B., Hooning, M.J., Brekelmans, C.T.M., and Klijn, J.G.M., (**2009**). Sensitivity to First-Line Chemotherapy for Metastatic Breast Cancer in BRCA1 and BRCA2 Mutation Carriers. *J Clin Oncol*, **27**(23), 3764.
17. Andre, M.D., Amaral, S., Mayer, A., and Miranda, A., (**2014**). Breast Cancer Patients Survival and Associated Factors: Reported Outcomes from the Southern Cancer Registry in Portugal. *Acta Medica Port*, **27**(3), 325.
18. Dent, R., Trudeau, M., Pritchard, K.I., Hanna, W.M., Kahn, H.K., Sawka, C.A., Lickley, L.A., Rawlinson, E., Sun, P., and Narod, S.A., (**2007**). Triple-negative Breast Cancer: Clinical Features and Patterns of Recurrence. *Clin Cancer Res*, **13**(15), 4429.
19. Bento, M.J., Goncalves, G., Aguiar, A., Castro, C., Veloso, V., and Rodrigues, V., (**2015**). Performance Indicators Evaluation of the Population-based Breast Cancer Screening Programme in Northern Portugal Using the European Guidelines. *Cancer Epidemiol*, **39**(5), 783.
20. Janni, W., Vogl, F.D., Wiedswang, G., Synnestvedt, M., Fehm, T., Juckstock, J., Borgen, E., Rack, B., Braun, S., Sommer, H., Solomayer, E., Pantel, K., Nesland, J., Friese, K., and Naume, B., (**2011**). Persistence of Disseminated Tumor Cells in the Bone Marrow of Breast Cancer Patients Predicts Increased Risk for Relapse - A European Pooled Analysis. *Clin Cancer Res*, **17**(9), 2967.
21. Wiedswang, G., Borgen, E., Karesen, R., Qvist, H., Janbu, J., Kvalheim, G., Nesland, J.M., and Naume, B., (**2004**). Isolated tumor cells in bone marrow three years after diagnosis in disease-free breast cancer patients predict unfavorable clinical outcome. *Clin Cancer Res*, **10**(16), 5342.
22. Longatto Filho, A., Lopes, J.M., and Schmitt, F.C., (**2010**). Angiogenesis and Breast Cancer. *J Oncol*, **2010**.
23. Adair, T.H. and Montani, J.P., *Chapter 1 - Overview of Angiogenesis.*, in *Angiogenesis*. 2010, Morgan & Claypool Life Sciences.
24. Schmidt, A., Brixius, K., and Bloch, W., (**2007**). Endothelial Precursor Cell Migration During Vasculogenesis. *Circ Res*, **101**(2), 125.
25. Fox, S.B., Generali, D.G., and Harris, A.L., (**2007**). Breast Tumour Angiogenesis. *Breast Cancer Res*, **9**(6), 216.
26. Ferrara, N. and Kerbel, R.S., (**2005**). Angiogenesis as a Therapeutic Target. *Nature*, **438**(7070), 967.

27. Castaneda-Gill, J.M. and Vishwanatha, J.K., (**2016**). Antiangiogenic Mechanisms and Factors in Breast Cancer Treatment. *J Carcinog*, **15**, 1.
28. Gey, G.O., Coffman, W.D., and Kubicek, M.T., (**1952**). Tissue Culture Studies of the Proliferative Capacity of Cervical Carcinoma and Normal Epithelium. *Cancer Res.*, **12**(4), 264.
29. Cailleau, R., Young, R., Olive, M., and Reeves, W.J., Jr., (**1974**). Breast Tumor Cell Lines from Pleural Effusions. *J Natl Cancer Inst*, **53**(3), 661.
30. Levenson, A.S. and Jordan, V.C., (**1997**). MCF-7: The First Hormone-Responsive Breast Cancer Cell Line. *Cancer Res.*, **57**(15), 3071.
31. Ethier, S.P., Mahacek, M.L., Gullick, W.J., Frank, T.S., and Weber, B.L., (**1993**). Differential Isolation of Normal Luminal Mammary Epithelial Cells and Breast Cancer Cells from Primary and Metastatic Sites Using Selective Media. *Cancer Res.*, **53**(3), 627.
32. Liu, M.C., Pitcher, B.N., Mardis, E.R., Davies, S.R., Friedman, P.N., Snider, J.E., Vickery, T.L., Reed, J.P., DeSchryver, K., Singh, B., Gradishar, W.J., Perez, E.A., Martino, S., Citron, M.L., Norton, L., Winer, E.P., Hudis, C.A., Carey, L.A., Bernard, P.S., Nielsen, T.O., Perou, C.M., Ellis, M.J., and Barry, W.T., (**2016**). PAM50 Gene Signatures and Breast Cancer Prognosis with Adjuvant Anthracycline- and Taxane-based Chemotherapy: Correlative Analysis of C9741 (Alliance). *NPJ Breast Cancer*, **2**, 15023.
33. Prat, A., Parker, J.S., Karginova, O., Fan, C., Livasy, C., Herschkowitz, J.I., He, X., and Perou, C.M., (**2010**). Phenotypic and Molecular Characterization of the Claudin-Low Intrinsic Subtype of Breast Cancer. *Breast Cancer Res*, **12**(5), R68.
34. Lehmann, B.D., Bauer, J.A., Chen, X., Sanders, M.E., Chakravarthy, A.B., Shyr, Y., and Pietenpol, J.A., (**2011**). Identification of Human Triple-Negative Breast Cancer Subtypes and Preclinical Models for Selection of Targeted Therapies. *J Clin Invest*, **121**(7), 2750.
35. Holliday, D.L. and Speirs, V., (**2011**). Choosing the Right Cell Line for Breast Cancer Research. *Breast Cancer Res*, **13**(4), 215.
36. Cimpean, A.M., Ribatti, D., and Raica, M., (**2008**). The Chick Embryo Chorioallantoic Membrane as a Model to Study Tumor Metastasis. *Angiogenesis*, **11**(4), 311.
37. Ribatti, D., (**2008**). Chick Embryo Chorioallantoic Membrane as a Useful Tool to Study Angiogenesis. *Int Rev Cel Mol Biol*, **270**, 181.
38. Deryugina, E.I. and Quigley, J.P., (**2008**). Chick Embryo Chorioallantoic Membrane Model Systems to Study and Visualize Human Tumor Cell Metastasis. *Histochem. Cell Biol.*, **130**(6), 1119.
39. Giannopoulou, E., Katsoris, P., Hatziapostolou, M., Kardamakis, D., Kotsaki, E., Polytarchou, C., Parthymou, A., Papaioannou, S., and Papadimitriou, E., (**2001**). X-rays Modulate Extracellular Matrix *in vivo*. *Int J Cancer*, **94**(5), 690.

40. Gabrielli, M.G. and Accili, D., (**2010**). The Chick Chorioallantoic Membrane: a Model of Molecular, Structural, and Functional Adaptation to Transepithelial Ion Transport and Barrier Function During Embryonic Development. *Journal of Biomedicine and Biotechnology*, **2010**, 940741.
41. Ribatti, D., (**2012**). Chicken Chorioallantoic Membrane Angiogenesis Model. *Methods Mol Biol*, **843**, 47.
42. DeFouw, D.O., Rizzo, V.J., Steinfeld, R., and Feinberg, R.N., (**1989**). Mapping of the Microcirculation in the Chick Chorioallantoic Membrane During Normal Angiogenesis. *Microvasc Res*, **38**(2), 136.
43. Ausprunk, D.H., Knighton, D.R., and Folkman, J., (**1974**). Differentiation of Vascular Endothelium in the Chick Chorioallantois: A Structural and Autoradiographic Study. *Dev Biol*, **38**(2), 237.
44. Guy, J.S., (**2015**). Isolation and Propagation of Coronaviruses in Embryonated Eggs. *Coronaviruses: Methods and Protocols*, **1282**, 63.
45. Tufan, A.C. and Satiroglu-Tufan, N.L., (**2005**). The Chick Embryo Chorioallantoic Membrane as a Model System for the Study of Tumor Angiogenesis, Invasion and Development of Anti-Angiogenic Agents. *Curr Cancer Drug Targets*, **5**(4), 249.
46. Fuchs, A. and Lindenbaum, E.S., (**1988**). The Two- and Three-Dimensional Structure of the Microcirculation of the Chick Chorioallantoic Membrane. *Acta Anat*, **131**(4), 271.
47. Richardson, M. and Singh, G., (**2003**). Observations on the Use of the Avian Chorioallantoic Membrane (CAM) Model in Investigations into Angiogenesis. *Curr Drug Targets Cardiovasc Haematol Disord*, **3**(2), 155.
48. Shumko, J.Z., Defouw, D.O., and Feinberg, R.N., (**1988**). Vascular Histodifferentiation in the Chick Chorioallantoic Membrane: A Morphometric Study. *Anat Rec*, **220**(2), 179.
49. Wagner-Amos, K. and Seymour, R.S., (**2002**). Effect of Regional Changes to Shell Conductance on Oxygen Consumption and Growth of Chicken Embryos. *Respir Physiol*, **129**(3), 385.
50. Tuan, R.S., (**1980**). Calcium Transport and Related Functions in the Chorioallantoic Membrane of Cultured Shell-Less Chick Embryos. *Dev Biol*, **74**(1), 196.
51. Tuan, R.S., (**1983**). Supplemented Eggshell Restores Calcium Transport in Chorioallantoic Membrane of Cultured Shell-Less Chick Embryos. *Development*, **74**(1), 119.
52. Stewart, M.E. and Terepka, A.R., (**1969**). Transport Functions of the Chick Chorio-Allantoic Membrane. *Exp Cell Res*, **58**(1), 93.
53. Saleuddin, A.S.M., Kyriakides, C.P.M., Peacock, A., and Simkiss, K., (**1976**). Physiological and Ultrastructural Aspects of Ion Movements Across the Chorioallantois. *Comp Biochem Physiol A-Physiol*, **54**(1), 7.

54. Li, M., Pathak, R.R., Lopez-Rivera, E., Friedman, S.L., Aguirre-Ghiso, J.A., and Sikora, A.G., (**2015**). The In Ovo Chick Chorioallantoic Membrane (CAM) Assay as an Efficient Xenograft Model of Hepatocellular Carcinoma. *J Vis Exp*, (104).
55. Ossowski, L., (**1988**). *In vivo* Invasion of Modified Chorioallantoic Membrane by Tumor Cells: The Role of Cell Surface-Bound Urokinase. *J Cell Biol*, **107**(6 Pt 1), 2437.
56. Lokman, N.A., Elder, A.S.F., Ricciardelli, C., and Oehler, M.K., (**2012**). Chick Chorioallantoic Membrane (CAM) Assay as an *in vivo* Model to Study the Effect of Newly Identified Molecules on Ovarian Cancer Invasion and Metastasis. *Int J Mol Sci*, **13**(8), 9959.
57. Sorlie, T., Perou, C.M., Tibshirani, R., Aas, T., Geisler, S., Johnsen, H., Hastie, T., Eisen, M.B., van de Rijn, M., Jeffrey, S.S., Thorsen, T., Quist, H., Matese, J.C., Brown, P.O., Botstein, D., Lonning, P.E., and Borresen-Dale, A.L., (**2001**). Gene Expression Patterns of Breast Carcinomas Distinguish Tumor Subclasses with Clinical Implications. *Proc Natl Acad Sci USA*, **98**(19), 10869.
58. Levrero, M., De Laurenzi, V., Costanzo, A., Gong, J., Wang, J.Y., and Melino, G., (**2000**). The p53/p63/p73 Family of Transcription Factors: Overlapping and Distinct Functions. *J Cell Sci*, **113 (Pt 10)**, 1661.
59. Leong, C.O., Vidnovic, N., DeYoung, M.P., Sgroi, D., and Ellisen, L.W., (**2007**). The p63/p73 Network Mediates Chemosensitivity to Cisplatin in a Biologically Defined Subset of Primary Breast Cancers. *J Clin Invest*, **117**(5), 1370.
60. Gong, J.G., Costanzo, A., Yang, H.Q., Melino, G., Kaelin, W.G., Jr., Levrero, M., and Wang, J.Y., (**1999**). The Tyrosine kinase c-Abl Regulates p73 in Apoptotic Response to Cisplatin-induced DNA Damage. *Nature*, **399**(6738), 806.
61. Zangen, R., Ratovitski, E., and Sidransky, D., (**2005**). ΔNp63α Levels Correlate with Clinical Tumor Response to Cisplatin. *Cell Cycle*, **4**(10), 1313.
62. Farmer, H., McCabe, N., Lord, C.J., Tutt, A.N.J., Johnson, D.A., Richardson, T.B., Santarosa, M., Dillon, K.J., Hickson, I., Knights, C., Martin, N.M.B., Jackson, S.P., Smith, G.C.M., and Ashworth, A., (**2005**). Targeting the DNA Repair Defect in BRCA Mutant Cells as a Therapeutic Strategy. *Nature*, **434**(7035), 917.
63. Graeser, M., McCarthy, A., Lord, C.J., Savage, K., Hills, M., Salter, J., Orr, N., Parton, M., Smith, I.E., Reis, J.S., Dowsett, M., Ashworth, A., and Turner, N.C., (**2010**). A Marker of Homologous Recombination Predicts Pathologic Complete Response to Neoadjuvant Chemotherapy in Primary Breast Cancer. *Clin Cancer Res*, **16**(24), 6159.
64. Rosenberg, B., Vancamp, L., and Krigas, T., (**1965**). Inhibition of Cell Division in Escherichia coli by Electrolysis Products from a Platinum Electrode. *Nature*, **205**, 698.
65. Rosenberg, B., VanCamp, L., Trosko, J.E., and Mansour, V.H., (**1969**). Platinum Compounds: A New Class of Potent Antitumour Agents. *Nature*, **222**(5191), 385.

66. Wheate, N.J., Walker, S., Craig, G.E., and Oun, R., (**2010**). The Status of Platinum Anticancer Drugs in the Clinic and in Clinical Trials. *Dalton Trans*, **39**(35), 8113.
67. Kelland, L., (**2007**). The Resurgence of Platinum-based Cancer Chemotherapy. *Nat Rev Cancer*, **7**(8), 573.
68. Farrell, N.P., (**2011**). Platinum Formulations as Anticancer Drugs Clinical and Pre-clinical Studies. *Curr Top Med Chem*, **11**(21), 2623.
69. Reedijk, J., (**2011**). Increased Understanding of Platinum Anticancer Chemistry. *Pure Appl Chem*, **83**(9), 1709.
70. Safaei, R., (**2006**). Role of Copper Transporters in the Uptake and Efflux of Platinum Containing Drugs. *Cancer Lett*, **234**(1), 34.
71. Marques, M.P.M., Gianolio, D., Cibin, G., Tomkinson, J., Parker, S.F., Valero, R., Lopes, R.P., and de Carvalho, L.A.E.B., (**2015**). A Molecular View of Cisplatin's Mode of Action: Interplay with DNA Bases and Acquired Resistance. *Phys Chem Chem Phys*, **17**(7), 5155.
72. Galluzzi, L., Senovilla, L., Vitale, I., Michels, J., Martins, I., Kepp, O., Castedo, M., and Kroemer, G., (**2012**). Molecular Mechanisms of Cisplatin Resistance. *Oncogene*, **31**(15), 1869.
73. Zhang, H.Y., Gou, S.H., Zhao, J., Chen, F.H., Xu, G., and Liu, X., (**2015**). Cytotoxicity Profile of Novel Sterically Hindered Platinum(II) Complexes with (1R,2R)-N-1,N-2-Dibutyl-1,2-Diaminocyclohexane. *Eur J Med Chem*, **96**, 187.
74. Yu, H.Y., Gou, S.H., Wang, Z.M., Chen, F.H., and Fang, L., (**2016**). Toward Overcoming Cisplatin Resistance *Via* Sterically Hindered Platinum(II) Complexes. *Eur J Med Chem*, **114**, 141.
75. Regan, M.M., O'Donnell, E.K., Kelly, W.K., Halabi, S., Berry, W., Urakami, S., Kikuno, N., and Oh, W.K., (**2010**). Efficacy of Carboplatin–Taxane Combinations in the Management of Castration-Resistant Prostate Cancer: A Pooled Analysis of Seven Prospective Clinical Trials. *Ann Oncol*, **21**(2), 312.
76. Hah, S.S., Stivers, K.M., White, R.W.D., and Henderson, P.T., (**2006**). Kinetics of Carboplatin-DNA Binding in Genomic DNA and Bladder Cancer Cells as Determined by Accelerator Mass Spectrometry. *Chem Res Toxicol*, **19**(5), 622.
77. Fricker, S.P., (**2007**). Metal Based Drugs: from Serendipity to Design. *Dalton Trans*, (43), 4903.
78. Alba, E., Chacon, J.I., Lluch, A., Anton, A., Estevez, L., Cirauqui, B., Carrasco, E., Calvo, L., Segui, M.A., Ribelles, N., Alvarez, R., Sanchez-Munoz, A., Sanchez, R., Garcia-Asenjo, J.A.L., Rodriguez-Martin, C., Escudero, M.J., and Albanell, J., (**2012**). A Randomized Phase II Trial of Platinum Salts in Basal-like Breast Cancer Patients in the Neoadjuvant Setting. Results from the GEICAM/2006-03, Multicenter Study. *Breast Cancer Res Treat*, **136**(2), 487.

79. Sharma, P., Stecklein, S.R., Kimler, B.F., Khan, Q.J., Connor, C.S., McGinness, M., Mammen, J., Wagner, J.L., Jensen, R.A., Godwin, A.K., and Fabian, C.J., (**2014**). Efficacy of Neoadjuvant Carboplatin/Docetaxel Chemotherapy in Sporadic and BRCA-Associated Triple-Negative Breast Cancer (TNBC). *J Clin Oncol*, **32**(15).
80. Derleth, C. and Mayer, I.A., (**2010**). Antiangiogenic Therapies in Early-stage Breast Cancer. *Clin Breast Cancer*, **10**(Supplement 1), E23.
81. Ghanbari, P., Mohseni, M., Tabasinezhad, M., Yousefi, B., Saei, A.A., Sharifi, S., Rashidi, M.R., and Samadi, N., (**2014**). Inhibition of Survivin Restores the Sensitivity of Breast Cancer Cells to Docetaxel and Vinblastine. *Appl Biochem Biotech*, **174**(2), 667.
82. Kidani, Y., Noji, M., and Tashiro, T., (**1980**). Antitumor Activity of Platinum(II) Complexes of 1,2-diamino-cyclohexane Isomers. *Gan*, **71**(5), 637.
83. Wang, Z.M., Wu, M., and Gou, S.H., (**2016**). Toward a Better Understanding of the Oxaliplatin Mode of Action upon the Steric Hindrance of 1,2-Diaminocyclohexane and its Analogue. *J Inorg Biochem*, **157**, 1.
84. Raymond, E., Faivre, S., Chaney, S., Woynarowski, J., and Cvitkovic, E., (**2002**). Cellular and Molecular Pharmacology of Oxaliplatin. *Mol Cancer Ther*, **1**(3), 227.
85. Montagnani, F., Turrisi, G., Marinozzi, C., Aliberti, C., and Fiorentini, G., (**2011**). Effectiveness and Safety of Oxaliplatin Compared to Cisplatin for Advanced, Unresectable Gastric Cancer: a Systematic Review and Meta-analysis. *Gastric Cancer*, **14**(1), 50.
86. Florea, A.M. and Busselberg, D., (**2011**). Cisplatin as an Anti-tumor Drug: Cellular Mechanisms of Activity, Drug Resistance and Induced Side Effects. *Cancers*, **3**(1), 1351.
87. Tournigand, C., Andre, T., Achille, E., Lledo, G., Flesh, M., Mery-Mignard, D., Quinaux, E., Couteau, C., Buyse, M., Ganem, G., Landi, B., Colin, P., Louvet, C., and de Gramont, A., (**2004**). FOLFIRI Followed by FOLFOX6 or the Reverse Sequence in Advanced Colorectal Cancer: A Randomized GERCOR Study. *J Clin Oncol*, **22**(2), 229.
88. Noh, S.H., Park, S.R., Yang, H.K., Chung, H.C., Chung, I.J., Kim, S.W., Kim, H.H., Choi, J.H., Kim, H.K., Yu, W., Lee, J.I., Shin, D.B., Ji, J.F., Chen, J.S., Lim, Y., Ha, S., and Bang, Y.J., (**2014**). Adjuvant Capecitabine Plus Oxaliplatin for Gastric Cancer after D2 Gastrectomy (CLASSIC): 5-Year Follow-up of an Open-Label, Randomised Phase 3 Trial. *Lancet Oncol.*, **15**(12), 1389.
89. Droz, J.P., Muracciole, X., Mottet, N., Kaci, M.O., Vannetzel, J.M., Albin, N., Culine, S., Rodier, J.M., Misset, J.L., Mackenzie, S., Cvitkovic, E., and Benoit, G., (**2003**). Phase II Study of Oxaliplatin *versus* Oxaliplatin Combined with Infusional 5-Fluorouracil in Hormone Refractory Metastatic Prostate Cancer Patients. *Ann Oncol*, **14**(8), 1291.
90. Argyriou, A.A., Cavaletti, G., Antonacopoulou, A., Genazzani, A.A., Briani, C., Bruna, J., Terrazzino, S., Velasco, R., Alberti, P., Campagnolo, M., Lonardi, S., Cortinovis, D.,

Cazzaniga, M., Santos, C., Psaromyalou, A., Angelopoulou, A., and Kalofonos, H.P., (**2013**). Voltage-Gated Sodium Channel Polymorphisms Play a Pivotal Role in the Development of Oxaliplatin-Induced Peripheral Neurotoxicity Results From a Prospective Multicenter Study. *Cancer*, **119**(19), 3570.

91. Avan, A., Postma, T.J., Ceresa, C., Avan, A., Cavaletti, G., Giovannetti, E., and Peters, G.J., (**2015**). Platinum-Induced Neurotoxicity and Preventive Strategies: Past, Present, and Future. *Oncologist*, **20**(4), 411.
92. Komeda, S., (**2011**). Unique Platinum-DNA Interactions May Lead to More Effective Platinum-based Antitumor Drugs. *Metallomics*, **3**(7), 650.
93. Hamana, K. and Matsuzaki, S., (**1992**). Polyamines as a chemotaxonomic marker in bacterial systematics. *Crit Rev Microbiol*, **18**(4), 261.
94. Jastrząb, R., Łomozik, L., and Tylkowski, B., (**2016**). Complexes of Biogenic Amines in their Role in Living Systems. *Physical Sciences Reviews*, **1**(6).
95. Pegg, A.E. and McCann, P.P., (**1982**). Polyamine metabolism and function. *Am J Physiol*, **243**(5), C212.
96. Thomas, T. and Thomas, T.J., (**2001**). Polyamines in cell growth and cell death: molecular mechanisms and therapeutic applications. *Cell Mol Life Sci*, **58**(2), 244.
97. Marra, M., Agostinelli, E., Tempera, G., Lombardi, A., Meo, G., Budillon, A., Abbruzzese, A., Giuberti, G., and Caraglia, M., (**2007**). Anticancer drugs and hyperthermia enhance cytotoxicity induced by polyamine enzymatic oxidation products. *Amino Acids*, **33**(2), 273.
98. Averill-Bates, D.A., Ke, Q., Tanel, A., Roy, J., Fortier, G., and Agostinelli, E., (**2008**). Mechanism of cell death induced by spermine and amine oxidase in mouse melanoma cells. *Int J Oncol*, **32**(1), 79.
99. Moinard, C., Cynober, L., and de Bandt, J.P., (**2005**). Polyamines: metabolism and implications in human diseases. *Clin Nutr*, **24**(2), 184.
100. Marques, M.P.M., (**2013**). Platinum and Palladium Polyamine Complexes as Anticancer Agents: The Structural Factor. *ISRN Spectrosc.*, **2013**, 29.
101. Matos, C.S., de Carvalho, A.L.M.B., Lopes, R.P., and Marques, M.P.M., (**2012**). New Strategies Against Prostate Cancer - Pt(II)-Based Chemotherapy. *Curr Med Chem*, **19**(27), 4678.
102. Silva, T.M., Andersson, S., Sukumaran, S.K., Marques, M.P., Persson, L., and Oredsson, S., (**2013**). Norspermidine and Novel Pd(II) and Pt(II) Polynuclear Complexes of Norspermidine as Potential Antineoplastic Agents Against Breast Cancer. *Plos One*, **8**(2).
103. Silva, T.M., Fiuza, S.M., Marques, M.P.M., Persson, L., and Oredsson, S., (**2014**). Increased Breast Cancer Cell Toxicity by Palladination of the Polyamine Analogue N-1,N-11-bis(ethyl)norspermine. *Amino Acids*, **46**(2), 339.

104. Fiuza, S.M., Holy, J., Batista de Carvalho, L.A.E., and Marques, M.P.M., (**2011**). Biologic Activity of a Dinuclear Pd(II)-spermine Complex Toward Human Breast Cancer. *Chem Biol Drug Des*, **77**(6), 477.

105. Alam, M.N. and Huq, F., (**2016**). Comprehensive Review on Tumour Active Palladium Compounds and Structure-Activity Relationships. *Coordin Chem Rev*, **316**, 36.

106. Cleare, M.J. and Hydes, P.C., *Antitumor Properties of Metal Complexes*, in *Metal Ions in Biological Systems*, Sigel, H., Editor. 1980, Marcel Dekker. p. 2.

107. Umapathy, P., (**1989**). The Chemical and Biochemical Consequences of the Binding of the Antitumour Drug Cisplatin and Other Platinum Group Metal Complexes to DNA. *Coordin Chem Rev*, **95**(2), 129.

108. Ruiz, J., Lorenzo, J., Vicente, C., Lopez, G., Lopez-De-Luzuriaga, J.M., Monge, M., Aviles, F.X., Bautista, D., Moreno, V., and Laguna, A., (**2008**). New Palladium(II) and Platinum(II) Complexes with 9-aminoacridine: Structures, Luminiscence, Theoretical Calculations, and Antitumor Activity. *Inorg. Chem.*, **47**(15), 6990.

109. Dorr, R.T., A Review of the Modulation of Cisplatin Toxicities by Chemoprotectants, in Platinum and Other Metal Coordination Compounds in Cancer Chemotherapy 2, Pinedo, H.M. and Schornagel, J.H., Editors. 1996, Springer US. p. 131.

110. Bunger, J., Stork, J., and Stalder, K., (**1996**). Cyto and Genotoxic Effects of Coordination Complexes of Platinum, Palladium and Rhodium *in vitro*. *Int Arch Occup Environ Health*, **69**(1), 33.

111. Dilruba, S. and Kalayda, G.V., (**2016**). Platinum-based Drugs: Past, Present and Future. *Cancer Chemother Pharmacol*, **77**(6), 1103.

112. Han, X.P., Sun, J., Wang, Y.J., and He, Z.G., (**2015**). Recent Advances in Platinum (IV) Complex-Based Delivery Systems to Improve Platinum (II) Anticancer Therapy. *Med Res Rev*, **35**(6), 1268.

113. Zalba, S. and Garrido, M.J., (**2013**). Liposomes, a Promising Strategy for Clinical Application of Platinum Derivatives. *Expert Opin Drug Deliv*, **10**(6), 829.

114. Boulikas, T., (**2004**). Low Toxicity and Anticancer Activity of a Novel Liposomal Cisplatin (Lipoplatin) in Mouse Xenografts. *Oncol. Rep.*, **12**(1), 3.

115. Devarajan, P., Tarabishi, R., Mishra, J., Ma, Q., Kourvetaris, A., Vougiouka, M., and Boulikas, T., (**2004**). Low Renal Toxicity of Lipoplatin Compared to Cisplatin in Animals. *Anticancer Res*, **24**(4), 2193.

116. Wong, D.Y.Q., Yeo, C.H.F., and Ang, W.H., (**2014**). Immuno-Chemotherapeutic Platinum(IV) Prodrugs of Cisplatin as Multimodal Anticancer Agents. *Angew Chem Int Edit*, **53**(26), 6752.

117. Teixeira-Dias, J.J.C., *Especroscopia Molecular: Fundamentos, Métodos e Aplicações*. 1986, Lisboa: Fundação Calouste Gulbenkian.

118. Schrader, B., Infrared and Raman Spectroscopy - Methods and Applications, ed. Inc, V.p. 1995, New York.

119. Hollas, J.M., *Modern Spectroscopy*. 1996: John Wiley & Sons. 416.

120. Abney, W. and Festing, E.R., (**1881**). On the Influence of the Atomic Grouping in the Molecules of Organic Bodies on Their Absorption in the InfraRed Region of the Spectrum. *Philos Trans R Soc Lond*, **172**, 887.

121. Peter Griffiths, J.A.D.H., *Fourier Transform Infrared Spectrometry*. 1986: Wiley-Interscience. 672.

122. Miller, L.M. and Smith, R.J., (**2005**). Synchrotrons *versus* Globars, Point-Detectors *versus* Focal Plane Arrays: Selecting the Best Source and Detector for Specific Infrared Microspectroscopy and Imaging Applications. *Vib. Spectrosc.*, **38**(1-2), 237.

123. Bassan, P., Weida, M.J., Rowlette, J., and Gardner, P., (**2014**). Large Scale Infrared Imaging of Tissue Micro Arrays (TMAs) Using a Tunable Quantum Cascade Laser (QCL) Based Microscope. *Analyst*, **139**(16), 3856.

124. Pilling, M. and Gardner, P., (**2016**). Fundamental Developments in Infrared Spectroscopic Imaging for Biomedical Applications. *Chem Soc Rev*, **45**(7), 1935.

125. Quaroni, L., Zlateva, T., Sarafimov, B., Kreuzer, H.W., Wehbe, K., Hegg, E.L., and Cinque, G., (**2014**). Synchrotron Based Infrared Imaging and Spectroscopy *Via* Focal Plane Array on Live Fibroblasts in D_2O Enriched Medium. *Biophys Chem*, **189**, 40.

126. Ash, P.A., Reeve, H.A., Quinson, J., Hidalgo, R., Zhu, T., McPherson, I.J., Chung, M.W., Healy, A.J., Nayak, S., Lonsdale, T.H., Wehbe, K., Kelley, C.S., Frogley, M.D., Cinque, G., and Vincent, K.A., (**2016**). Synchrotron-Based Infrared Microanalysis of Biological Redox Processes under Electrochemical Control. *Anal Chem*, **88**(13), 6666.

127. Donaldson, P.M., Kelley, C.S., Frogley, M.D., Filik, J., Wehbe, K., and Cinque, G., (**2016**). Broadband Near-Field Infrared Spectromicroscopy Using Photothermal Probes and Synchrotron Radiation. *Opt Express*, **24**(3), 1852.

128. Stevenso.Jr, Ellis, H., and Bartlett, R., (**1973**). Synchrotron Radiation as an Infrared Source. *Appl Optics*, **12**(12), 2884.

129. Meyer, P. and Lagarde, P., (**1976**). Synchrotron Radiation in Infrared. *J Phys*, **37**(12), 1387.

130. Yarwood, J., Shuttleworth, T., Hasted, J.B., and Nanba, T., (**1984**). A New Radiation Source for the Infrared Region. *Nature*, **312**(5996), 742.

131. Thoonen, G., Nys, B., Vander Haeghen, Y., De Roy, G., and Scheunders, P., (**2016**). Automatic Forensic Analysis of Automotive Paints Using Optical Microscopy. *Forensic Sci Int*, **259**, 210.

132. Nabers, A., Ollesch, J., Schartner, J., Kotting, C., Genius, J., Haussmann, U., Klafki, H., Wiltfang, J., and Gerwert, K., (**2016**). An Infrared Sensor Analysing Label-Free the Secondary Structure of the Abeta Peptide in Presence of Complex Fluids. *J Biophotonics*, **9**(3), 224.

133. Ostrowska, K.M., Garcia, A., Meade, A.D., Malkin, A., Okewumi, I., O'Leary, J.J., Martin, C., Byrne, H.J., and Lyng, F.M., (**2011**). Correlation of p16(INK4A) Expression and HPV Copy Number with Cellular FTIR Spectroscopic Signatures of Cervical Cancer Cells. *Analyst*, **136**(7), 1365.

134. Jimenez-Hernandez, M., Brown, M.D., Hughes, C., Clarke, N.W., and Gardner, P., (**2015**). Characterising Cytotoxic Agent Action as a Function of the Cell Cycle Using Fourier Transform Infrared Microspectroscopy. *Analyst*, **140**(13), 4453.

135. Diem, M., Ergin, A., Remiszewski, S., Mu, X., Akalin, A., and Raz, D., (**2016**). Infrared Micro-spectroscopy of Human Tissue: Principles and Future Promises. *Farad Discuss*, **187**(0), 9.

136. Marques, M.P.M., Goncalves, D., Amarante, A.I.C., Makhoul, C.I., Parker, S., and Batista de Carvalho, L.A.E., (**2016**). Osteometrics in Burned Human Skeletal Remains by Neutron and Optical Vibrational Spectroscopy. *Rsc Adv*.

137. Pilling, M.J., Henderson, A., Bird, B., Brown, M.D., Clarke, N.W., and Gardner, P., (**2016**). High-Throughput Quantum Cascade Laser (QCL) Spectral Histopathology: A Practical Approach Towards Clinical Translation. *Farad Discuss*, **187**, 135.

138. Dumas, P., Sockalingum, G.D., and Sule-Suso, J., (**2007**). Adding Synchrotron Radiation to Infrared Microspectroscopy: What's New in Biomedical Applications? *Trends Biotechnol*, **25**(1), 40.

139. Baker, M.J., Trevisan, J., Bassan, P., Bhargava, R., Butler, H.J., Dorling, K.M., Fielden, P.R., Fogarty, S.W., Fullwood, N.J., Heys, K.A., Hughes, C., Lasch, P., Martin-Hirsch, P.L., Obinaju, B., Sockalingum, G.D., Sule-Suso, J., Strong, R.J., Walsh, M.J., Wood, B.R., Gardner, P., and Martin, F.L., (**2014**). Using Fourier Transform IR Spectroscopy to Analyze Biological Materials. *Nat Protoc*, **9**(8), 1771.

140. Quaroni, L., Zlateva, T., Wehbe, K., and Cinque, G., (**2016**). Infrared Imaging of Small Molecules in Living Cells: from *in vitro* Metabolic Analysis to Cytopathology. *Farad Discuss*, **187**(0), 259.

141. Whelan, D.R., Hiscox, T.J., Rood, J.I., Bambery, K.R., McNaughton, D., and Wood, B.R., (**2014**). Detection of an *en masse* and Reversible B- to A-DNA Conformational Transition in Prokaryotes in Response to Desiccation. *J R Soc Interface*, **11**(97).

142. Wehbe, K., Forfar, I., Eimer, S., and Cinque, G., (**2015**). Discrimination Between Two Different Grades of Human Glioma Based on Blood Vessel Infrared Spectral Imaging. *Anal Bioanal Chem*, **407**(24), 7295.

143. Salvadó, N., Butí, S., Cotte, M., Cinque, G., and Pradell, T., (**2013**). Shades of Green in 15th Century Paintings: Combined Microanalysis of the Materials Using Synchrotron Radiation XRD, FTIR and XRF. *Applied Physics A*, **111**(1), 47.

144. Diamond Light Source, available from: http://www.diamond.ac.uk, accessed on 18/09/2015.

145. Cinque, G., Frogley, M., Wehbe, K., Filik, J., and Pijanka, J., (**2011**). Multimode InfraRed Imaging and Microspectroscopy (MIRIAM) Beamline at Diamond. *Synchrotron Radiation News*, **24**(5), 24.

146. Raman, C.V. and Krishnan, K.S., (**1928**). A New Type of Secondary Radiation. *Nature*, **121**(3048), 201.

147. Raman, C.V. and Krishnan, K.S., (**1929**). The Production of New Radiations by Light Scattering. Part I. *Proc R Soc London Ser A-Math Phys Eng Sci*, **122**(789), 23.

148. Long, D.A., *Survey of Light-Scattering Phenomena*, in *The Raman Effect*. 2002, John Wiley & Sons, Ltd. p. 3.

149. Rayleigh, J.W.S., *Scientific Papers*. 1964, New York: Dover Publications.

150. Wood, R.W., (**1928**). Wave-length Shifts in Scattered Light. *Nature*, **122**(3071), 349.

151. General survey of vibrational spectroscopy, in Infrared and Raman Spectroscopy: Methods and Applications, Schrader, B., Editor. 1995, Wiley-VCH Verlag GmbH. p. 7.

152. Baia, M., Astilean, S., and Iliescu, T., Fundamentals of Infrared and Raman Spectroscopy, SERS, and Theoretical Simulations, in Raman and SERS Investigations of Pharmaceuticals. 2008, Springer Berlin Heidelberg. p. 9.

153. Nawaz, H., Garcia, A., Meade, A.D., Lyng, F.M., and Byrne, H.J., (**2013**). Raman Micro Spectroscopy Study of the Interaction of Vincristine with A549 Cells Supported by Expression Analysis of bcl-2 Protein. *Analyst*, **138**(20), 6177.

154. Kong, K., Zaabar, F., Rakha, E., Ellis, I., Koloydenko, A., and Notingher, I., (**2014**). Towards Intra-operative Diagnosis of Tumours During Breast Conserving Surgery by Selective-sampling Raman Micro-spectroscopy. *Phys Med Biol*, **59**(20), 6141.

155. Krafft, C., S., D., Latka, I., Dietzek, B., and Popp, J., (**2012**). Diagnosis and Screening of Cancer Tissues by Fiber-optic Probe Raman Spectroscopy. *Biomedical Spectroscopy and Imaging*, **1**(1), 39.

156. Dieckmann, R., Hammerl, J.A., Hahmann, H., Wicke, A., Kleta, S., Dabrowski, P.W., Nitsche, A., Stammler, M., Al Dahouk, S., and Lasch, P., (**2016**). Rapid Characterisation of

Klebsiella Oxytoca Isolates from Contaminated Liquid Hand Soap Using Mass Spectrometry, FTIR and Raman Spectroscopy. *Farad Discuss*, **187**(0), 353.

157. Pahlow, S., Meisel, S., Cialla-May, D., Weber, K., Rosch, P., and Popp, J., (**2015**). Isolation and Identification of Bacteria by Means of Raman Spectroscopy. *Adv Drug Deliver Rev*, **89**, 105.

158. Lasch, P. and Naumann, D., Infrared Spectroscopy in Microbiology, in Encyclopedia of Analytical Chemistry. 2006, John Wiley & Sons, Ltd.

159. Farhane, Z., Bonnier, F., Casey, A., and Byrne, H.J., (**2015**). Raman Micro Spectroscopy for *in vitro* Drug Screening: Subcellular Localisation and Interactions of Doxorubicin. *Analyst*, **140**(12), 4212.

160. Farhane, Z., Bonnier, F., Casey, A., Maguire, A., O'Neill, L., and Byrne, H.J., (**2015**). Cellular Discrimination Using *in vitro* Raman Micro Spectroscopy: the Role of the Nucleolus. *Analyst*, **140**(17), 5908.

161. Verrier, S., Zoladek, A., and Notingher, I., *Raman Micro-Spectroscopy as a Non-invasive Cell Viability Test*, in *Methods Mol Biol*, Stoddart, M.J., Editor. 2011, Humana Press. p. 179.

162. Notingher, I., Non-Invasive Characterisation of Living Cells and Tissue Engineering Scaffolds by Raman Micro-Spectroscopy, in Woodhead Publ Mater, Boccaccini, A.R. and Gough, J.E., Editors. 2007, Woodhead Publishing Ltd. p. 248.

163. Smith, R., Wright, K.L., and Ashton, L., (**2016**). Raman Spectroscopy: an Evolving Technique for Live Cell Studies. *Analyst*, **141**(12), 3590.

164. Kann, B., Offerhaus, H.L., Windbergs, M., and Otto, C., (**2015**). Raman Microscopy for Cellular Investigations - From Single Cell Imaging to Drug Carrier Uptake Visualization. *Adv Drug Deliver Rev*, **89**, 71.

165. Kong, K., Rowlands, C.J., Varma, S., Perkins, W., Leach, I.H., Koloydenko, A.A., Williams, H.C., and Notingher, I., (**2013**). Diagnosis of Tumors During Tissue-Conserving Surgery with Integrated Autofluorescence and Raman Scattering Microscopy. *Proc Natl Acad Sci USA*, **110**(38), 15189.

166. Kong, K., Kendall, C., Stone, N., and Notingher, I., (**2015**). Raman Spectroscopy for Medical Diagnostics - From *in-vitro* Biofluid Assays to *in-vivo* Cancer Detection. *Adv Drug Deliver Rev*, **89**, 121.

167. Ramos, I.R., Meade, A.D., Ibrahim, O., Byrne, H.J., McMenamin, M., McKenna, M., Malkin, A., and Lyng, F.M., (**2016**). Raman Spectroscopy for Cytopathology of Exfoliated Cervical Cells. *Farad Discuss*, **187**(0), 187.

168. Wang, J., Lin, K., Zheng, W., Ho, K.Y., Teh, M., Yeoh, K.G., and Huang, Z., (**2016**). Fiber-Optic Raman Spectroscopy for *in vivo* Diagnosis of Gastric Dysplasia. *Farad Discuss*, **187**(0), 377.

169. Isabelle, M., Dorney, J., Lewis, A., Lloyd, G.R., Old, O., Shepherd, N., Rodriguez-Justo, M., Barr, H., Lau, K., Bell, I., Ohrel, S., Thomas, G., Stone, N., and Kendall, C., (**2016**). Multi-centre Raman Spectral Mapping of Oesophageal Cancer Tissues: a Study to Assess System Transferability. *Farad Discuss*, **187**(0), 87.

170. Rutherford, E., (**2012**). The Scattering of α and β Particles by Matter and the Structure of the Atom. *Philos Mag*, **92**(4), 379.

171. Thomson, J.J., (**1897**). XL. Cathode Rays. *Philos Mag*, **44**(269), 293.

172. Bohr, N., (**1913**). I. On the Constitution of Atoms and Molecules. *Philos Mag*, **26**(151), 1.

173. Bohr, N., (**1913**). XXXVII. On the Constitution of Atoms and Molecules. *Philos Mag*, **26**(153), 476.

174. Bohr, N., (**1913**). LXXIII. On the Constitution of Atoms and Molecules. *Philos Mag*, **26**(155), 857.

175. Nakamura, K., Hagiwara, K., Hikasa, K., Murayama, H., Tanabashi, M., Watari, T., Amsler, C., Antonelli, M., Asner, D.M., Baer, H., Band, H.R., Barnett, R.M., Basaglia, T., Bergren, E., Beringer, J., Bernardi, G., Bertl, W., Bichsel, H., Biebel, O., Blucher, E., Blusk, S., Cahn, R.N., Carena, M., Ceccucci, A., Chakraborty, D., Chen, M.C., Chivukula, R.S., Cowan, G., Dahl, O., D'Ambrosio, G., Damour, T., de Florian, D., de Gouvea, A., DeGrand, T., Dissertori, G., Dobrescu, B., Doser, M., Drees, M., Edwards, D.A., Eidelman, S., Erler, J., Ezhela, V.V., Fetscher, W., Fields, B.D., Foster, B., Gaisser, T.K., Garren, L., Gerber, H.J., Gerbier, G., Gherghetta, T., Giudice, C.F., Golwala, S., Goodman, M., Grab, C., Gritsan, A.V., Grivaz, J.F., Groom, D.E., Grunewald, M., Gurtu, A., Gutsche, T., Haber, H.E., Hagmann, C., Hayes, K.G., Heffner, M., Heltsley, B., Hernandez-Rey, J.J., Hocker, A., Holder, J., Huston, J., Jackson, J.D., Johnson, K.F., Junk, T., Karle, A., Karlen, D., Kayser, B., Kirkby, D., Klein, S.R., Kolda, C., Kowalewski, R.V., Krusche, B., Kuyanov, Y.V., Kwon, Y., Lahav, O., Langacker, P., Liddle, A., Ligeti, Z., Lin, C.J., Liss, T.M., Littenberg, L., Lugovsky, K.S., Lugovsky, S.B., Lys, J., Mahlke, H., Mannel, T., Manohar, A.V., Marciano, W.J., Martin, A.D., Masoni, A., Milstead, D., Miquel, R., Monig, K., Narain, M., Nason, P., Navas, S., Nevski, P., Nir, Y., Olive, K.A., Pape, L., Patrignani, C., Peacock, J.A., Petcov, S.T., Piepke, A., Punzi, G., Quadt, A., Raby, S., Raffelt, G., Ratcliff, B.N., Richardson, P., Roesler, S., Rolli, S., Romaniouk, A., Rosenberg, L.J., Rosner, J.L., Sachrajda, C.T., Sakai, Y., Salam, G.P., Sarkar, S., Sauli, F., Schneider, O., Scholberg, K., Scott, D., Seligman, W.G., Shaevitz, M.H., Silari, M., Sjostrand, T., Smith, J.G., Smoot, G.F., Spanier, S., Spieler, H., Stahl, A., Stanev, T., Stone, S.L., Sumiyoshi, T., Syphers, M.J., Terning, J., Titov, M., Tkachenko, N.P., Tornqvist, N.A., Tovey, D., Trippe, T.G., Valencia, G., van Bibber, K., Venanzoni, G., Vincter, M.G., Vogel, P., Vogt, A., Walkowiak, W., Walter, C.W., Ward, D.R., Webber, B.R., Weiglein, G., Weinberg, E.J., Wells, J.D., Wheeler, A., Wiencke, L.R.,

Wohl, C.G., Wolfenstein, L., Womersley, J., Woody, C.L., Workman, R.L., Yamamoto, A., Yao, W.M., Zenin, O.V., Zhang, J., Zhu, R.Y., Zyla, P.A., Harper, G., Lugovsky, V.S. and Schaffner, P., (**2010**). Review of Particle Physics. *J Phys G-Nucl Part Phys*, **37**(7a), 1.

176. Colella, R., Overhauser, A.W., and Werner, S.A., (**1975**). Design of a Neutron Interferometer for Observing Gravitationally Induced Quantum Interference. *Acta Crystallogr Sect A*, **31**, S253.
177. ISIS - STFC, available from: http://www.isis.stfc.ac.uk, accessed on 21/01/2016.
178. Mitchell, P.C.H., Parker, S.F., Ramirez-Cuesta, A.J., and Tomkinson, J., *Vibrational Spectroscopy with Neutrons - Applications in Chemistry, Biology, Materials Science and Catalysis*. Neutron Techniques and Applications. 2005, Hackensack, NJ: Worls Scientific. 668.
179. Karlsson, M., (**2015**). Proton Dynamics in Oxides: Insight into the Mechanics of Proton Conduction from Quasielastic Neutron Scattering. *Phys Chem Chem Phys*, **17**(1), 26.
180. Fitter, J.G., Thomas; Katsaras, John, *Neutron Scattering in Biology. Techniques and Applications*. 2006: Springer.
181. Marquardt, D., Alsop, R., Rheinstädter, M., and Harroun, T., (**2015**). Neutron Scattering at the Intersection of Heart Health Science and Biophysics. *Journal of Cardiovascular Development and Disease*, **2**(2), 125.
182. Beall, P.T., Hazlewood, C.F., and Rao, P.N., (**1976**). Nuclear Magnetic-Resonance Patterns of Intracellular Water as a Function of Hela-Cell Cycle. *Science*, **192**(4242), 904.
183. Pfeuffer, J., Flogel, U., and Leibfritz, D., (**1998**). Monitoring of Cell Volume and Water Exchange Time in Perfused Cells by Diffusion-Weighted H-1 NMR Spectroscopy. *NMR Biomed*, **11**(1), 11.
184. Yamada, T., (**2001**). 1H-NMR Studies of the Intracellular Water of Skeletal Muscle Fibers under Various Physiological Conditions. *Cell Mol Biol*, **47**(5), 925.
185. Smouha, E. and Neeman, M., (**2001**). Compartmentation of Intracellular Water in Multicellular Tumor Spheroids: Diffusion and Relaxation NMR. *Magn Reson Med*, **46**(1), 68.
186. Hortelano, S., Garcia-Martin, M.L., Cerdan, S., Castrillo, A., Alvarez, A.M., and Bosca, L., (**2001**). Intracellular Water Motion Decreases in Apoptotic Macrophages After Caspase Activation. *Cell Death Differ*, **8**(10), 1022.
187. Zhao, L., Kroenke, C.D., Song, J., Piwnica-Worms, D., Ackerman, J.J.H., and Neil, J.J., (**2008**). Intracellular Water-Specific MR of Microbead-Adherent Cells: The HeLa Cell Intracellular Water Exchange Lifetime. *NMR Biomed*, **21**(2), 159.
188. Aslund, I. and Topgaard, D., (**2009**). Determination of the Self-diffusion Coefficient of Intracellular Water Using PGSE NMR with Variable Gradient Pulse Length. *J Magn Reson*, **201**(2), 250.

189. Jasnin, M., Stadler, A., Tehei, M., and Zaccai, G., (**2010**). Specific Cellular Water Dynamics Observed *in vivo* by Neutron Scattering and NMR. *Phys Chem Chem Phys*, **12**(35), 10154.

190. Springer, C.S., Li, X., Tudorica, L.A., Oh, K.Y., Roy, N., Chui, S.Y.C., Naik, A.M., Holtorf, M.L., Afzal, A., Rooney, W.D., and Huang, W., (**2014**). Intratumor Mapping of Intracellular Water Lifetime: Metabolic Images of Breast Cancer? *NMR Biomed*, **27**(7), 760.

191. Potma, E.O., de Boeij, W.P., van Haastert, P.J.M., and Wiersma, D.A., (**2001**). Real-Time Visualization of Intracellular Hydrodynamics in Single Living Cells. *Proc Natl Acad Sci USA*, **98**(4), 1577.

192. Potma, E.O., de Boeij, W.P., and Wiersma, D.A., (**2001**). Femtosecond Dynamics of iIntracellular Water Probed with Nonlinear Optical Kerr Effect Microspectroscopy. *Biophys J*, **80**(6), 3019.

193. Born, B., Kim, S.J., Ebbinghaus, S., Gruebele, M., and Havenith, M., (**2009**). The Terahertz Dance of Water with the Proteins: the Effect of Protein Flexibility on the Dynamical Hydration Shell of Ubiquitin. *Farad Discuss*, **141**, 161.

194. Doster, W., Cusack, S., and Petry, W., (**1989**). Dynamical Transition of Myoglobin Revealed by Inelastic Neutron Scattering. *Nature*, **337**(6209), 754.

195. Dellerue, S. and Bellissent-Funel, M.C., (**2000**). Relaxational Dynamics of Water Molecules at Protein Surface. *Chem Phys*, **258**(2-3), 315.

196. Russo, D., Baglioni, P., Peroni, E., and Teixeira, J., (**2003**). Hydration Water Dynamics of a Completely Hydrophobic Oligopeptide. *Chem Phys*, **292**(2-3), 235.

197. Lechner, R.E., Fitter, J., Dencher, N.A., and Hauss, T., (**2006**). Low-Energy Dynamics and Biological Function. *Physica B*, **385-86**, 835.

198. GoupilLamy, A.V., Smith, J.C., Yunoki, J., Parker, S.F., and Kataoka, M., (**1997**). High-resolution Vibrational Inelastic Neutron Scattering: A New Spectroscopic Tool for Globular Proteins. *J Am Chem Soc*, **119**(39), 9268.

199. Beta, I.A., Kolesnikov, A.I., Michalarias, I., Wu, G.L., Ford, R.C., and Li, J.C., (**2003**). Incoherent Inelastic Neutron-scattering Studies of the Structure of Water Associated with DNA and Gelatin. *Can J Phys*, **81**(1-2), 367.

200. Beta, I.A., Michalarias, I., Ford, R.C., Li, J.C., and Bellissent-Funel, M.C., (**2003**). Quasi-elastic Neutron Scattering Study of Hydrated DNA. *Chem Phys*, **292**(2-3), 451.

201. Trantham, E.C., Rorschach, H.E., Clegg, J.S., Hazlewood, C.F., Nicklow, R.M., and Wakabayashi, N., (**1984**). Diffusive Properties of Water in Artemia Cysts as Determined from Quasi-Elastic Neutron-Scattering Spectra. *Biophys J*, **45**(5), 927.

202. Ford, R.C., Ruffle, S.V., Ramirez-Cuesta, A.J., Michalarias, I., Beta, I., Miller, A., and Li, J.C., (**2004**). Inelastic Incoherent neutron Scattering Measurements of Intact Cells and Tissues and Detection of Interfacial Water. *J Am Chem Soc*, **126**(14), 4682.

203. Stadler, A.M., Embs, J.P., Digel, I., Artmann, G.M., Unruh, T., Buldt, G., and Zaccai, G., (**2008**). Cytoplasmic Water and Hydration Layer Dynamics in Human Red Blood Cells. *J Am Chem Soc*, **130**(50), 16852.

204. Tehei, M., Franzetti, B., Wood, K., Gabel, F., Fabiani, E., Jasnin, M., Zamponi, M., Oesterhelt, D., Zaccai, G., Ginzburg, M., and Ginzburg, B.Z., (**2007**). Neutron Scattering Reveals Extremely Slow Cell Water in a Dead Sea Organism. *Proc Natl Acad Sci USA*, **104**(3), 766.

205. Jasnin, M., Moulin, M., Haertlein, M., Zaccai, G., and Tehei, M., (**2008**). Down to Atomic-scale Intracellular Water Dynamics. *EMBO Rep*, **9**(6), 543.

206. Pieper, J., Charalambopoulou, G., Steriotis, T., Vasenkov, S., Desmedt, A., and Lechner, R.E., (**2003**). Water Diffusion in Fully Hydrated Porcine Stratum Corneum. *Chem Phys*, **292**(2-3), 465.

207. Pal, S., Balasubramanian, S., and Bagchi, B., (**2003**). Dynamics of Bound and Free Water in an Aqueous Micellar Solution: Analysis of the Lifetime and Vibrational Frequencies of Hydrogen Bonds at a Complex Interface. *Phys Rev E*, **67**(6).

208. Qvist, J., Persson, E., Mattea, C., and Halle, B., (**2009**). Time Scales of Water Dynamics at Biological Interfaces: Peptides, Proteins and Cells. *Farad Discuss*, **141**, 131.

209. Tobias, D.J., Sengupta, N., and Tarek, N., (**2009**). Hydration Dynamics of Purple Membranes. *Farad Discuss*, **141**, 99.

210. ISIS - STFC - TOSCA, available from: http://www.isis.stfc.ac.uk/instruments/tosca, accessed on 21/01/2016..

211. Lechner, R.E. and Longeville, S., *Quasielastic Neutron Scattering in Biology, Part II: Applications*, in *Neutron Scattering in Biology: Techniques and Applications*, Fitter, J., Gutberlet, T., and Katsaras, J., Editors. 2006, Springer. p. 355.

212. Frolich, A., Gabel, F., Jasnin, M., Lehnert, U., Oesterhelt, D., Stadler, A.M., Tehei, M., Weik, M., Wood, K., and Zaccai, G., (**2009**). From Shell to Cell: Neutron Scattering Studies of Biological Water Dynamics and Coupling to Activity. *Farad Discuss*, **141**, 117.

213. ISIS - STFC - OSIRIS, available from: http://www.isis.stfc.ac.uk/instruments/osiris, accessed on 21/01/2016.

214. Skehan, P., Storeng, R., Scudiero, D., Monks, A., Mcmahon, J., Vistica, D., Warren, J.T., Bokesch, H., Kenney, S., and Boyd, M.R., (**1990**). New Colorimetric Cytotoxicity Assay for Anticancer-Drug Screening. *J Natl Cancer Inst*, **82**(13), 1107.

215. Keepers, Y.P., Pizao, P.E., Peters, G.J., Vanarkotte, J., Winograd, B., and Pinedo, H.M., (**1991**). Comparison of the Sulforhodamine-B Protein and Tetrazolium (Mtt) Assays for Invitro Chemosensitivity Testing. *Eur J Cancer*, **27**(7), 897.

216. Lazic, M.J., Andelkovic, K.K., Sladic, D.M., Tesic, Z.L., and Radulovic, S.S., (**2005**). The evaluation of cytotoxic activity of planar pentadentate ligand 2 ',2 '"-(2,6-pyridindiyldiethylidyne) dioxamohydrazide dihydrate (H(2)Lx2H(2)O) and its metal coordination complexes; Pitfalls in the use of the MTT-assay. *J Exp Clin Canc Res*, **24**(1), 63.

217. Perez, R.P., Godwin, A.K., Handel, L.M., and Hamilton, T.C., (**1993**). A Comparison of Clonogenic, Microtetrazolium and Sulforhodamine-B Assays for Determination of Cisplatin Cytotoxicity in Human Ovarian-Carcinoma Cell-Lines. *Eur J Cancer*, **29a**(3), 395.

218. Folkman, J., *Tumor Angiogenesis: from Bench to Bedside*, in *Tumor Angiogenesis: Basic Mechanisms and Cancer Therapy*, Marmé, D. and Fusenig, N., Editors. 2008, Springer Berlin Heidelberg. p. 3.

219. Folkman , J., (**1971**). Tumor Angiogenesis: Therapeutic Implications. *New Engl J Med*, **285**(21), 1182.

220. Mandriota, S.J. and Pepper, M.S., (**1997**). Vascular Endothelial Growth Factor-Induced *in vitro* Angiogenesis and Plasminogen Activator Expression are Dependent on Endogenous Basic Fibroblast Growth Factor. *J Cell Sci*, **110 (Pt 18)**, 2293.

221. Kurebayashi, J., Otsuki, T., Kunisue, H., Mikami, Y., Tanaka, K., Yamamoto, S., and Sonoo, H., (**1999**). Expression of Vascular Endothelial Growth Factor (VEGF) Family Members in Breast Cancer. *Jpn J Cancer Res*, **90**(9), 977.

222. Lohela, M., Bry, M., Tammela, T., and Alitalo, K., (**2009**). VEGFs and Receptors Involved in Angiogenesis *versus* Lymphangiogenesis. *Curr Opin Cell Biol*, **21**(2), 154.

223. Salven, P., Lymboussaki, A., Heikkila, P., Jaaskela-Saari, H., Enholm, B., Aase, K., von Euler, G., Eriksson, U., Alitalo, K., and Joensuu, H., (**1998**). Vascular Endothelial Growth Factors VEGF-B and VEGF-C Are Expressed in Human Tumors. *Am J Pathol*, **153**(1), 103.

224. De Jong, J.S., Van Diest, P.J., Van der Valk, P., and Baak, J.P.A., (**1998**). Expression of Growth Factors, Growth-inhibiting Factors, and their Receptors in Invasive Breast Cancer. II: Correlations with Proliferation and Angiogenesis. *J Pathol*, **184**(1), 53.

225. Caine, G.J., Stonelake, P.S., Lip, G.Y.H., and Blann, A.D., (**2007**). Changes in Plasma Vascular Endothelial Growth Factor, Angiopoietins, and their Receptors Following Surgery for Breast Cancer. *Cancer Lett*, **248**(1), 131.

226. Oldenhuis, C.N.A.M., Oosting, S.F., Gietema, J.A., and de Vries, E.G.E., (**2008**). Prognostic *versus* Predictive Value of Biomarkers in Oncology. *Eur J Cancer*, **44**(7), 946.

227. Lawicki, S., Zajkowska, M., Glazewska, E.K., Bedkowska, G.E., and Szmitkowski, M., (**2016**). Plasma Levels and Diagnostic Utility of VEGF, MMP-9, and TIMP-1 in the Diagnosis of Patients with Breast Cancer. *OncoTargets Ther*, **9**, 911.

228. Gasparini, G., (**2000**). Prognostic Value of Vascular Endothelial Growth Factor in Breast Cancer. *Oncologist*, **5 Suppl 1**, 37.

229. Medical Art-Work, available from: http://medicalart-work.co.uk, acessed on 06/04/2016.

230. Mierke, C.T., (**2008**). Role of the Endothelium During Tumor Cell Metastasis: Is the Endothelium a Barrier or a Promoter for Cell Invasion and Metastasis? *Journal of Biophysics*, **2008**, 183516.

231. Tran, T.-A., Gillet, L., Roger, S., Besson, P., White, E., and Le Guennec, J.-Y., (**2009**). Non-Anti-Mitotic Concentrations of Taxol Reduce Breast Cancer Cell Invasiveness. *Biochem Biophys Res Commun*, **379**(2), 304.

232. Belov, L., Zhou, J., and Christopherson, R.I., (**2011**). Cell Surface Markers in Colorectal Cancer Prognosis. *Int J Mol Sci*, **12**(1), 78.

233. Moss, N.M., Wu, Y.I., Liu, Y., Munshi, H.G., and Stack, M.S., (**2009**). Modulation of the Membrane Type 1 Matrix Metalloproteinase Cytoplasmic Tail Enhances Tumor Cell Invasion and Proliferation in Three-Dimensional Collagen Matrices. *J Biol Chem*, **284**(30), 19791.

234. Chu, Y.W., Runyan, R.B., Oshima, R.G., and Hendrix, M.J., (**1993**). Expression of Complete Keratin Filaments in Mouse L Cells Augments Cell Migration and Invasion. *Proc Natl Acad Sci USA*, **90**(9), 4261.

235. Chen, H.C., (**2005**). Boyden Chamber Assay. *Methods Mol Biol*, **294**, 15.

236. Kramer, N., Walzl, A., Unger, C., Rosner, M., Krupitza, G., Hengstschläger, M., and Dolznig, H., (**2013**). *In vitro* Cell Migration and Invasion Assays. *Mutat Res-Rev Mutat Res*, **752**(1), 10.

237. Marques, M.P.M., Girao, T., De Lima, M.C.P., Gameiro, A., Pereira, E., and Garcia, P., (**2002**). Cytotoxic Effects of Metal Complexes of Biogenic Polyamines. I. Platinum(II) Spermidine Compounds: Prediction of their Antitumour Activity. *Biochim Biophys Acta-Mol Cell*, **1589**(1), 63.

238. Teixeira, L.J., Seabra, M., Reis, E., da Cruz, M.T.G., de Lima, M.C.P., Pereira, E., Miranda, M.A., and Marques, M.P.M., (**2004**). Cytotoxic Activity of Metal Complexes of Biogenic Polyamines: Polynuclear Platinum(II) Chelates. *J Med Chem*, **47**(11), 2917.

239. Soares, A.S., Fiuza, S.M., Goncalves, M.J., de Carvalho, L.A.E.B., Paula, M., Marques, M.P.M., and Urbano, A.M., (**2007**). Effect of the Metal Center on the Antitumor Activity of the Analogous Dinuclear Spermine Chelates $(PdCl_2)_{(2)}$(spermine) and$(PtCl_2)_{(2)}$(spermine). *Lett. Drug Des. Discov.*, **4**(7), 460.

240. Tummala, R., Diegelman, P., Fiuza, S.M., De Carvalho, L.A.E.B., Marques, M.P.M., Kramer, D.L., Clark, K., Vujcic, S., Porter, C.W., and Pendyala, L., (**2010**). Characterization of Pt-,

Pd-Spermine Complexes for their Effect on Polyamine Pathway and Cisplatin Resistance in A2780 Ovarian Carcinoma Cells. *Oncol. Rep.*, **24**(1), 15.

241. Corduneanu, O., Chiorcea-Paquim, A.M., Fiuza, S.M., Marques, M.P.M., and Oliveira-Brett, A.M., (**2010**). Polynuclear Palladium Complexes with Biogenic Polyamines: AFM and Voltammetric Characterization. *Bioelectrochemistry*, **78**(2), 97.
242. Corduneanu, O., Chiorcea-Paquim, A.M., Diculescu, V., Fiuza, S.M., Marques, M.P.M., and Oliveira-Brett, A.M., (**2010**). DNA Interaction with Palladium Chelates of Biogenic Polyamines Using Atomic Force Microscopy and Voltammetric Characterization. *Anal Chem*, **82**(4), 1245.
243. Lamego, I., Duarte, I.F., Marques, M.P.M., and Gil, A.M., (**2014**). Metabolic Markers of MG-63 Osteosarcoma Cell Line Response to Doxorubicin and Methotrexate Treatment: Comparison to Cisplatin. *J Proteome Res*, **13**(12), 6033.
244. MIRIAM - B22 - Diamond Light Source, available from: http://www.diamond.ac.uk/Beamlines/Soft-Condensed-Matter/B22.html, accessed on 12/04/2016.
245. Ramirez-Cuesta, A.J., (**2004**). aCLIMAX 4.0.1, The New Version of the Software for Analyzing and Interpreting INS spectra. *Comput Phys Commun*, **157**(3), 226.
246. Carpentier, G., Martinelli, M., Courty, J., and Cascone, I. *Angiogenesis Analyzer for ImageJ. 4th ImageJ*. in *User and Developer Conference proceedings*. 2012. Mondorf-les-Bains, Luxembourg.
247. Azuah, R.T., Kneller, L.R., Qiu, Y.M., Tregenna-Piggott, P.L.W., Brown, C.M., Copley, J.R.D., and Dimeo, R.M., (**2009**). DAVE: A Comprehensive Software Suite for the Reduction, Visualization, and Analysis of Low Energy Neutron Spectroscopic Data. *J Res Natl Inst Stand Technol*, **114**(6), 341.
248. Martens, H., Nielsen, J.P., and Engelsen, S.B., (**2003**). Light Scattering and Light Absorbance Separated by Extended Multiplicative Signal Correction. Application to Near-Infrared Transmission Analysis of Powder Mixtures. *Anal Chem*, **75**(3), 394.
249. Schindelin, J., Arganda-Carreras, I., Frise, E., Kaynig, V., Longair, M., Pietzsch, T., Preibisch, S., Rueden, C., Saalfeld, S., Schmid, B., Tinevez, J.-Y., White, D.J., Hartenstein, V., Eliceiri, K., Tomancak, P., and Cardona, A., (**2012**). Fiji: An Open-Source Platform for Biological-Image Analysis. *Nat Methods*, **9**(7), 676.
250. Arnold, O., Bilheux, J.C., Borreguero, J.M., Buts, A., Campbell, S.I., Chapon, L., Doucet, M., Draper, N., Leal, R.F., Gigg, M.A., Lynch, V.E., Markyardsen, A., Mikkelson, D.J., Mikkelson, R.L., Miller, R., Palmen, K., Parker, P., Passos, G., Perring, T.G., Peterson, P.F., Ren, S., Reuter, M.A., Savici, A.T., Taylor, J.W., Taylor, R.J., Tolchenoy, R., Zhou, W., and Zikoysky, J., (**2014**). Mantid-Data Analysis and Visualization Package for Neutron

Scattering and μSR Experiments. *Nucl Instrum Methods Phys Res Sect A-Accel Spectrom Dect Assoc Equip*, **764**, 156.

251. Roulet, R. and Ernst, R., (**1971**). Substitution Reactions in Tetrachloropalladate(Ii) Ion with Diamines .1. Ethylenediamine. *Helv Chim Acta*, **54**(8), 2357.
252. Codina, G., Caubet, A., Lopez, C., Moreno, V., and Molins, E., (**1999**). Palladium(II) and Platinum(II) Polyamine Complexes: X-Ray Crystal Structures of (*SP*-4-2)-Chloro{*N*-[(3-amino-κ*N*)propyl]propane-1,3-diamine-κ*N*,κ*N*′}palladium(1+) Tetrachloropalladate (2–) (2 : 1) and (*R,S*)-Tetrachloro[μ -(spermine)]dipalladium(II) (={ μ -{*N*,*N*′-Bis[(3-amino- κ *N*)propyl]butane-1,4-diamine- κ*N*: κ*N*′}}tetrachlorodipalladium). *Helv Chim Acta*, **82**(7), 1025.
253. Fiuza, S.M., Amado, A.M., Parker, S.F., Marques, M.P.M., and Batista de Carvalho, L.A.E., (**2015**). Conformational Insights and Vibrational Study of a Promising Anticancer Agent: the Role of the Ligand in Pd(II)-amine Complexes. *New J Chem*, **39**(8), 6274.
254. ECACC available from: http://bit.ly/1OgAjDi, accessed on 18/09/2015.
255. Strober, W., (**2001**). Trypan Blue Exclusion Test of Cell Viability. *Curr Protoc Immunol*, **Appendix 3**, Appendix 3B.
256. Papazisis, K.T., Geromichalos, G.D., Dimitriadis, K.A., and Kortsaris, A.H., (**1997**). Optimization of the Sulforhodamine B Colorimetric Assay. *J Immunol Methods*, **208**(2), 151.
257. Lazic, M.J., Andelkovic, K.K., Sladic, D.M., Tesic, Z.L., and Radulovic, S.S., (**2005**). The Evaluation of Cytotoxic Activity of Planar Pentadentate Ligand 2',2'''-(2,6-pyridindiyldiethylidyne) Dioxamohydrazide Dihydrate (H(2)Lx2H(2)O) and its Metal Coordination Complexes; Pitfalls in the Use of the MTT-Assay. *J Exp Clin Canc Res*, **24**(1), 63.
258. Albini, A. and Benelli, R., (**2007**). The Chemoinvasion Assay: A Method to Assess Tumor and Endothelial Cell Invasion and its Modulation. *Nat Protoc*, **2**(3), 504.
259. Rahn, H., Paganelli, C.V., and Ar, A., (**1974**). The Avian Egg: Air-Cell Gas Tension, Metabolism and Incubation Time. *Respir Physiol*, **22**(3), 297.
260. Wen, W., Lu, J.M., Zhang, K.Q., and Chen, S., (**2008**). Grape Seed Extract Inhibits Angiogenesis *Via* Suppression of the Vascular Endothelial Growth Factor Receptor Signaling Pathway. *Cancer Prev Res*, **1**(7), 554.
261. Frisch, M.J., Trucks, G.W., Schlegel, H.B., G. E. Scuseria, Robb, M.A., Cheeseman, J.R., J. A. Montgomery, J., Vreven, T., Kudin, K.N., Burant, J.C., Millam, J.M., Iyengar, S.S., Tomasi, J., Barone, V., Mennucci, B., Cossi, M., Scalmani, G., N. Rega, Petersson, G.A., Nakatsuji, H., Hada, M., Ehara, M., K. Toyota, Fukuda, R., Hasegawa, J., Ishida, M., Nakajima, T., Honda, Y., Kitao, O., Nakai, H., Klene, M., Li, X., Knox, J.E., Hratchian, H.P., Cross, J.B.,

Bakken, V., Adamo, C., Jaramillo, J., R. Gomperts, Stratmann, R.E., Yazyev, O., Austin, A.J., Cammi, R., C. Pomelli, Ochterski, J., Ayala, P.Y., Morokuma, K., Voth, G.A., P. Salvador, Dannenberg, J.J., Zakrzewski, V.G., Dapprich, S., Daniels, A.D., Strain, M.C., Farkas, O., Malick, D.K., A. D. Rabuck, Raghavachari, K., Foresman, J.B., Ortiz, J.V., Q. Cui, Baboul, A.G., Clifford, S., Cioslowski, J., Stefanov, B.B., G. Liu, Liashenko, A., Piskorz, P., Komaromi, I., Martin, R.L., Fox, D.J., Keith, T., Al-Laham, M.A., Peng, C.Y., A. Nanayakkara, Challacombe, M., Gill, P.M.W., Johnson, B.G., Chen, W., Wong, M.W., Gonzalez, C., and Pople, J.A., *GAUSSIAN 03 (Revision D.01)*. 2004, Gaussian, Inc: Wallingford, CT.

262. Fiuza, S.M., Amado, A.M., Marques, M.P., and Batista de Carvalho, L.A.E., (**2008**). Use of Effective Core Potential Calculations for the Conformational and Vibrational Study of Platinum(II) Anticancer Drugs. *cis*-Diamminedichloroplatinum(II) as a Case Study. *J Phys Chem A*, **112**(14), 3253.
263. Amado, A.M., Fiuza, S.M., Marques, M.P., and Batista de Carvalho, L.A.E., (**2007**). Conformational and Vibrational Study of Platinum(II) Anticancer Drugs: *cis*-diamminedichloro-platinum(II) as a Case Study. *J Chem Phys*, **127**(18), 185104.
264. Adamo, C. and Barone, V., (**1998**). Exchange Functionals With Improved Long-Range Behavior and Adiabatic Connection Methods Without Adjustable Parameters: The mPW and mPW1PW Models. *J Chem Phys*, **108**(2), 664.
265. Perdew, J.P., Burke, K., and Wang, Y., (**1996**). Generalized Gradient Approximation for the Exchange-Correlation Hole of a Many-Electron System. *Phys Rev B*, **54**(23), 16533.
266. Harihara.Pc and Pople, J.A., (**1973**). Influence of Polarization Functions on Molecular-Orbital Hydrogenation Energies. *Theor Chim Acta*, **28**(3), 213.
267. Hay, P.J. and Wadt, W.R., (**1985**). Abinitio Effective Core Potentials for Molecular Calculations - Potentials for the Transition-Metal Atoms Sc to Hg. *J Chem Phys*, **82**(1), 270.
268. Peng, C., Ayala, P.Y., Schlegel, H.B., and Frisch, M.J., (**1996**). Using Redundant Internal Coordinates to Optimize Equilibrium Geometries and Transition States. *J Comput Chem*, **17**(1), 49.
269. Zoladek, A., Pascut, F.C., Patel, P., and Notingher, I., (**2011**). Non-Invasive Time-Course Imaging of Apoptotic Cells by Confocal Raman Micro-Spectroscopy. *J Raman Spectrosc*, **42**(3), 251.
270. Wehbe, K., Filik, J., Frogley, M.D., and Cinque, G., (**2013**). The Effect of Optical Substrates on Micro-FTIR Analysis of Single Mammalian Cells. *Anal Bioanal Chem*, **405**(4), 1311.
271. VIBIMA, available from: http://www.uc.pt/en/iii/infrastructures/vibima, accessed on 18/09/2015.

272. Parker, S.F., Carlile, C.J., Pike, T., Tomkinson, J., Newport, R.J., Andreani, C., Ricci, F.P., Sacchetti, F., and Zoppi, M., (**1997**). TOSCA: A World Class Inelastic Neutron Spectrometer. *Physica B*, **241**, 154.

273. Telling, M.T.F. and Andersen, K.H., (**2005**). Spectroscopic Characteristics of the OSIRIS Near-Backscattering Crystal Analyser Spectrometer on the ISIS Pulsed Neutron Source. *Phys Chem Chem Phys*, **7**(6), 1255.

274. Demmel, F., McPhail, D., Crawford, J., Maxwell, D., Pokhilchuk, K., Garcia-Sakai, V., Mukhopadyay, S., Telling, M.T.F., Bermejo, F.J., Skipper, N.T., and Fernandez-Alonso, F., (**2015**). Opening the Terahertz Window on the OSIRIS Spectrometer. *Epj Web Conf*, **83**.

275. Sebaugh, J.L., (**2011**). Guidelines for Accurate EC50/IC50 Estimation. *Pharm Stat*, **10**(2), 128.

276. Tallarida, R.J., (**2012**). Revisiting the Isobole and Related Quantitative Methods for Assessing Drug Synergism. *J Pharmacol Exp Ther*, **342**(1), 2.

277. Bassan, P., Kohler, A., Martens, H., Lee, J., Byrne, H.J., Dumas, P., Gazi, E., Brown, M., Clarke, N., and Gardner, P., (**2010**). Resonant Mie Scattering (RMieS) Correction of Infrared Spectra from Highly Scattering Biological Samples. *Analyst*, **135**(2), 268.

278. Bassan, P., Sachdeva, A., Kohler, A., Hughes, C., Henderson, A., Boyle, J., Shanks, J.H., Brown, M., Clarke, N.W., and Gardner, P., (**2012**). FTIR Microscopy of Biological Cells and Tissue: Data Analysis Using Resonant Mie scattering (RMieS) EMSC Algorithm. *Analyst*, **137**(6), 1370.

279. Ullo, J.J., (**1987**). Molecular-Dynamics Study of Translational Motions in Water as Probed Through Quasi-Elastic Neutron-Scattering. *Phys Rev A*, **36**(2), 816.

280. Laage, D. and Hynes, J.T., (**2006**). A Molecular Jump Mechanism of Water Reorientation. *Science*, **311**(5762), 832.

281. Laage, D. and Hynes, J.T., (**2008**). On the Molecular Mechanism of Water Reorientation. *J Phys Chem B*, **112**(45), 14230.

282. Laage, D., (**2009**). Reinterpretation of the Liquid Water Quasi-elastic Neutron Scattering Spectra Based on a Nondiffusive Jump Reorientation Mechanism. *J Phys Chem B*, **113**(9), 2684.

283. Merrick, J.P., Moran, D., and Radom, L., (**2007**). An Evaluation of Harmonic Vibrational Frequency Scale Factors. *J Phys Chem A*, **111**(45), 11683.

284. Batista de Carvalho, L.A.E., Marques, M.P.M., Martin, C., Parker, S.F., and Tomkinson, J., (**2011**). Inelastic Neutron Scattering Study of Pt-II Complexes Displaying Anticancer Properties. *Chemphyschem*, **12**(7), 1334.

285. Mendes, S.R.O., Estudo Conformacional de $H_2N(CH_2)_nNH_2$ (n=3,4), in Department of Chemistry. 2010, University of Coimbra: Coimbra.

286. Marques, M.P.M., Batista de Carvalho, L.A.E., and Tomkinson, J., (**2002**). Study of Biogenic and α , ω -Polyamines by Combined Inelastic Neutron Scattering and Raman Spectroscopies and by *Ab Initio* Molecular Orbital Calculations. *J Phys Chem A*, **106**(11), 2473.

287. Tomkinson, J., Parker, S.F., Braden, D.A., and Hudson, B.S., (**2002**). Inelastic Neutron Scattering Spectra of the Transverse Acoustic Modes of the Normal Alkanes. *Phys Chem Chem Phys*, **4**(5), 716.

288. Batista de Carvalho, L.A.E., Marques, M.P.M., and Tomkinson, J., (**2006**). Transverse Acoustic Modes of Biogenic and α,ω-Polyamines: A Study by Inelastic Neutron Scattering and Raman Spectroscopies Coupled to DFT Calculations. *J Phys Chem A*, **110**(47), 12947.

289. Batista de Carvalho, A.L.M., Fiuza, S.M., Tomkinson, J., Batista de Carvalho, L.A.E., and Marques, M.P.M., (**2012**). Pt(II) Complexes with Linear Diamines-Part I: Vibrational Study of Pt-Diaminopropane. *Spectrosc-Int J*, **27**(5-6), 403.

290. Reck, M., Mellemgaard, A., von Pawel, J., Gottfried, M., Bondarenko, I., Cheng, Y., Zarogoulidis, K., Luft, A., Bennouna, J., Barrueco, J., Aboshady, H., Hocke, J., Kaiser, R., and Douillard, J.Y., (2015). Anti-Angiogenic-Apecific Adverse Events in Patients with Non-Small Cell Lung Cancer Treated with Nintedanib and Docetaxel. Lung Cancer, 90(2), 267.

291. Grant, D.S., Williams, T.L., Zahaczewsky, M., and Dicker, A.P., (2003). Comparison of Antiangiogenic Activities Using Paclitaxel (Taxol) and Docetaxel (Taxotere). Int J Cancer, 104(1), 121.

292. Vacca, A., Ribatti, D., Iurlaro, M., Merchionne, F., Nico, B., Ria, R., and Dammacco, F., (**2002**). Docetaxel *versus* Paclitaxel for Antiangiogenesis. *J Hematother Stem Cell Res*, **11**(1), 103.

293. Crown, J., O'Leary, M., and Ooi, W.S., (**2004**). Docetaxel and Paclitaxel in the Treatment of Breast Cancer: a Review of Clinical Experience. *Oncologist*, **9**(Suppl 2), 24.

294. Nicolini, A., Giardino, R., Carpi, A., Ferrari, P., Anselmi, L., Colosimo, S., Conte, M., Fini, M., Giavaresi, G., Berti, P., and Miccoli, P., (**2006**). Metastatic Breast Cancer: An Updating. *Biomed Pharmacother*, **60**(9), 548.

295. Lu, J., Zhang, K., Nam, S., Anderson, R.A., Jove, R., and Wen, W., (**2010**). Novel angiogenesis inhibitory activity in cinnamon extract blocks VEGFR2 kinase and downstream signaling. *Carcinogenesis*, **31**(3), 481.

296. Carmeliet, P. and Jain, R.K., (**2011**). Molecular Mechanisms and Clinical Applications of Angiogenesis. *Nature*, **473**(7347), 298.

297. Gacche, R.N. and Meshram, R.J., (**2014**). Angiogenic Factors as Potential Drug Target: Efficacy and Limitations of Anti-angiogenic Therapy. *Biochim Biophys Acta-Rev Cancer*, **1846**(1), 161.

298. Batista de Carvalho, A.L.M., Pilling, M., Gardner, P., Doherty, J., Cinque, G., Wehbe, K., Kelley, C., Batista de Carvalho, L.A.E., and Marques, M.P.M., (**2016**). Chemotherapeutic response to cisplatin-like drugs in human breast cancer cells probed by vibrational microspectroscopy. *Farad Discuss*.

299. Bayless, K.J. and Johnson, G.A., (**2011**). Role of the Cytoskeleton in Formation and Maintenance of Angiogenic Sprouts. *J Vasc Res*, **48**(5), 369.

300. Zamora, A., Perez, S.A., Rodriguez, V., Janiak, C., Yellol, G.S., and Ruiz, J., (**2015**). Dual Antitumor and antiangiogenic Activity of Organoplatinum(II) Complexes. *J Med Chem*, **58**(3), 1320.

301. Fan, Y., Xu, B.H., Yuan, P., Ma, F., Wang, J.Y., Ding, X.Y., Zhang, P., Li, Q., and Cai, R.G., (**2013**). Docetaxel-cisplatin might be Superior to Docetaxel-capecitabine in the First-line Treatment of Metastatic Triple-negative Breast Cancer. *Ann Oncol*, **24**(5), 1219.

302. Tai, C.J., Chen, C.S., Hung, C.S., Kuo, L.J., Wei, P.L., Chiou, J.F., Hsu, C.H., Chiou, H.Y., and Wu, C.H., (**2012**). Bevacizumab Plus Docetaxel and Cisplatin for Metastatic Breast Cancer: A Pilot Phase II Study. *Anticancer Res*, **32**(12), 5501.

303. Nielsen, D.L., Andersson, M., Andersen, J.L., and Kamby, C., (**2010**). Antiangiogenic Therapy for Beast Cancer. *Breast Cancer Res*, **12**(5), 209.

304. Hu, G., Ryan, S., Zhu, Y., Reed, E., Li, X., Wang, G., and Li, Q.Q., (**2003**). Vascular Endothelial Growth Factor Modulates Cisplatin Sensitivity in Human Ovarian Carcinoma Cells. *Cancer Therapy*, **1**, 31.

305. Dasari, S. and Tchounwou, P.B., (**2014**). Cisplatin in Cancer Therapy: Molecular Mechanisms of Action. *Eur J Pharmacol*, **740**, 364.

306. Gazi, E., Dwyer, J., Lockyer, N.P., Miyan, J., Gardner, P., Hart, C., Brown, M., and Clarke, N.W., (**2005**). Fixation Protocols for Subcellular Imaging by Synchrotron-based Fourier Transform Infrared Microspectroscopy. *Biopolymers*, **77**(1), 18.

307. Mariani, M.M., Lampen, P., Popp, J., Wood, B.R., and Deckert, V., (**2009**). Impact of Fixation on *in vitro* Cell Culture Lines Monitored with Raman Spectroscopy. *Analyst*, **134**(6), 1154.

308. Meade, A.D., Clarke, C., Draux, F., Sockalingum, G.D., Manfait, M., Lyng, F.M., and Byrne, H.J., (**2010**). Studies of Chemical Fixation Effects in Human Cell Lines Using Raman Microspectroscopy. *Anal Bioanal Chem*, **396**(5), 1781.

309. Draux, F., Gobinet, C., Sule-Suso, J., Trussardi, A., Manfait, M., Jeannesson, P., and Sockalingum, G.D., (**2010**). Raman Spectral Imaging of Single Cancer Cells: Probing the Impact of Sample Fixation Methods. *Anal Bioanal Chem*, **397**(7), 2727.

310. Notingher, I., Verrier, S., Haque, S., Polak, J.M., and Hench, L.L., (**2003**). Spectroscopic Study of Human Lung Epithelial Cells (A549) in Culture: Living Cells *versus* Dead Cells. *Biopolymers*, **72**(4), 230.

311. Notingher, I., (**2007**). Raman Spectroscopy Cell-Based Biosensors. *Sensors-Basel*, **7**(8), 1343.

312. De Gelder, J., De Gussem, K., Vandenabeele, P., and Moens, L., (**2007**). Reference Database of Raman Spectra of Biological Molecules. *J Raman Spectrosc*, **38**(9), 1133.

313. Nawaz, H., Bonnier, F., Knief, P., Howe, O., Lyng, F.M., Meade, A.D., and Byrne, H.J., (**2010**). Evaluation of the Potential of Raman Microspectroscopy for Prediction of Chemotherapeutic Response to Cisplatin in Lung Adenocarcinoma. *Analyst*, **135**(12), 3070.

314. Nawaz, H., Bonnier, F., Meade, A.D., Lyng, F.M., and Byrne, H.J., (**2011**). Comparison of Subcellular Responses for the Evaluation and Prediction of the Chemotherapeutic Response to Cisplatin in Lung Adenocarcinoma Using Raman Spectroscopy. *Analyst*, **136**(12), 2450.

315. Vrana, O., Masek, V., Drazan, V., and Brabec, V., (**2007**). Raman Spectroscopy of DNA Modified by Intrastrand Cross-Links of Antitumor Cisplatin. *J Struct Biol*, **159**(1), 1.

316. Benevides, J.M. and Thomas, G.J., (**1983**). Characterization of DNA Structures by Raman-Spectroscopy - High-Salt and Low-Salt Forms of Double Helical Poly(Dg-Dc) in H2o and D2o Solutions and Application to B-DNA, Z-DNA and a-DNA. *Nucleic Acids Res*, **11**(16), 5747.

317. Fernandis, A.Z. and Wenk, M.R., (**2009**). Lipid-based Biomarkers for Cancer. *J Chromatogr B*, **877**(26), 2830.

318. Crozier, A., Jaganath, I.B., and Clifford, M.N., (**2009**). Dietary Phenolics: Chemistry, Bioavailability and Effects on Health. *Nat Prod Rep*, **26**(8), 1001.

319. Sak, K., (**2014**). Cytotoxicity of Dietary Flavonoids on Different Human Cancer Types. *Pharmacogn Rev*, **8**(16), 122.

320. Heleno, S.A., Martins, A., Queiroz, M.J.R.P., and Ferreira, I.C.F.R., (**2015**). Bioactivity of Phenolic Acids: Metabolites *versus* Parent Compounds: A Review. *Food Chem.*, **173**, 501.

321. Dias, M.M., Machado, N.F.L., and Marques, M.P.M., (**2011**). Dietary Chromones as Antioxidant Agents - the Structural Variable. *Food Funct*, **2**(10), 595.

322. Clegg, J.S., (**1984**). Intracellular Water and the Cytomatrix - Some Methods of Study and Current Views. *J Cell Biol*, **99**(1), S167.

323. Wiggins, P.M., (**1990**). Role of Water in Some Biological Processes. *Microbiol Rev*, **54**(4), 432.

324. Wiggins, P.M., (**2001**). High and Low Density Intracellular Water. *Cell Mol Biol*, **47**(5), 735.

325. Ruffle, S.V., Michalarias, I., Li, J.C., and Ford, R.C., (**2002**). Inelastic Incoherent Neutron Scattering Studies of Water Interacting with Biological Macromolecules. *J Am Chem Soc*, **124**(4), 565.

326. Le Bihan, D., (**2007**). The 'Wet Mind': Water and Functional Neuroimaging. *Phys Med Biol*, **52**(7), R57.

327. Wood, K., Plazanet, M., Gabel, F., Kessler, B., Oesterhel, D., Tobias, D.J., Zaccai, G., and Weik, M., (**2007**). Coupling of Protein and Hydration-Water Dynamics in Biological Membranes. *Proc Natl Acad Sci USA*, **104**(46), 18049.

328. Sokolov, A.P., Roh, J.H., Mamontov, E., and Sakai, V.G., (**2008**). Role of Hydration Water in Dynamics of Biological Macromolecules. *Chem Phys*, **345**(2-3), 212.

329. Mamontov, E. and Chu, X.Q., (**2012**). Water-Protein Dynamic Coupling and New Opportunities for Probing it at Low to Physiological Temperatures in Aqueous Solutions. *Phys Chem Chem Phys*, **14**(33), 11573.

330. Luby-Phelps, K., (**2013**). The Physical Chemistry of Cytoplasm and its Influence on Cell Function: An Update. *Mol Biol Cell*, **24**(17), 2593.

331. Ball, P., (**2008**). Water as an Active Constituent in Cell Biology. *Chem Rev*, **108**(1), 74.

332. Mentre, P., (**2001**). An Introduction to "Water in the Cell": Tamed Hydra? *Cell Mol Biol*, **47**(5), 709.

333. Fenimore, P.W., Frauenfelder, H., McMahon, B.H., and Parak, F.G., (**2002**). Slaving: Solvent Fluctuations Dominate Protein Dynamics and Functions. *Proc Natl Acad Sci USA*, **99**(25), 16047.

334. Fenimore, P.W., Frauenfelder, H., McMahon, B.H., and Young, R.D., (**2004**). Bulk-solvent and Hydration-shell Fluctuations, Similar to α- and β-fluctuations in Glasses, Control Protein Motions and Functions. *Proc Natl Acad Sci USA*, **101**(40), 14408.

335. Doster, W. and Settles, M., (**2005**). Protein-water Displacement Distributions. *BBA-Proteins Proteomics*, **1749**(2), 173.

336. Frauenfelder, H., Chen, G., Berendzen, J., Fenimore, P.W., Jansson, H., McMahon, B.H., Stroe, I.R., Swenson, J., and Young, R.D., (**2009**). A Unified Model of Protein Dynamics. *Proc Natl Acad Sci USA*, **106**(13), 5129.

337. Fulton, A.B., (**1982**). How Crowded Is the Cytoplasm. *Cell*, **30**(2), 345.

338. Porter, K.R., (**1984**). The Cytomatrix - a Short History of Its Study. *J Cell Biol*, **99**(1), S3.

339. Spitzer, J., (**2011**). From Water and Ions to Crowded Biomacromolecules: *in vivo* Structuring of a Prokaryotic Cell. *Microbiol Mol Biol Rev*, **75**(3), 491.

340. Tabaka, M., Kalwarczyk, T., Szymanski, J., Hou, S., and Holyst, R., (**2014**). The Effect of Macromolecular Crowding on Mobility of Biomolecules, Association Kinetics and Gene Expression in Living Cells. *Front Phys*, **2**.

341. Theillet, F.X., Binolfi, A., Frembgen-Kesner, T., Hingorani, K., Sarkar, M., Kyne, C., Li, C.G., Crowley, P.B., Gierasch, L., Pielak, G.J., Elcock, A.H., Gershenson, A., and Selenko, P., (**2014**). Physicochemical Properties of Cells and their Effects on Intrinsically Disordered Proteins (IDPs). *Chem Rev*, **114**(13), 6661.

342. Lenormand, G., Millet, E., Park, C.Y., Hardin, C.C., Butler, J.P., Moldovan, N.I., and Fredberg, J.J., (**2011**). Dynamics of the Cytoskeleton: How Much Does Water Matter? *Phys Rev E*, **83**(6).

343. Davidson, R.M., Lauritzen, A., and Seneff, S., (**2013**). Biological Water Dynamics and Entropy: A Biophysical Origin of Cancer and Other Diseases. *Entropy-Switz*, **15**(9), 3822.

344. Wang, D. and Lippard, S.J., (**2005**). Cellular Processing of Platinum Anticancer Drugs. *Nat Rev Drug Discov*, **4**(4), 307.

345. Batista de Carvalho, A.L.M., Pilling, M., Gardner, P., Doherty, J., Cinque, G., Wehbe, K., Kelley, C., Batista de Carvalho, L.A.E., and Marques, M.P.M., (**2016**). Chemotherapeutic Response to Cisplatin-like Drugs in Human Breast Cancer Cells Probed by Vibrational Microspectroscopy. *Farad Discuss*, **187**(0), 273.

346. Li, J.C., (**1996**). Inelastic Neutron Scattering Studies of Hydrogen Bonding in Ices. *J Chem Phys*, **105**(16), 6733.

347. Fukazawa, H. and Shinji, M., (**2000**). The Vibrational Spectra of Ice Ih and Polar Ice. *Physics of Ice Core Records*, 25.

348. Michalarias, I., Beta, I., Ford, R., Ruffle, S., and Li, J.C., (**2002**). Inelastic Neutron Scattering Studies of Water in DNA. *Appl Phys A-Mater Sci Process*, **74**, S1242.

349. Michalarias, I., Beta, I.A., Li, J.C., Ruffle, S., and Ford, R., (**2002**). The Interaction of Water with DNA - A Combined Inelastic Neutron Scattering and Infrared Spectroscopic Study. *J Mol Liq*, **101**(1-3), 19.

350. Ebbinghaus, S., Kim, S.J., Heyden, M., Yu, X., Heugen, U., Gruebele, M., Leitner, D.M., and Havenith, M., (**2007**). An Extended Dynamical Hydration Shell around Proteins. *Proc Natl Acad Sci USA*, **104**(52), 20749.

351. Fogarty, A.C. and Laage, D., (**2014**). Water Dynamics in Protein Hydration Shells: The Molecular Origins of the Dynamical Perturbation. *J Phys Chem B*, **118**(28), 7715.

352. Bellissent-Funel, M.C., Chen, S.H., and Zanotti, J.M., (**1995**). Single-particle Dynamics of Water-molecules in Confined Space. *Phys Rev E*, **51**(5), 4558.

Abbreviations

3D	three-dimensional
A	Adenine
ANG	Angiopoietin
ATP7	copper-transporting P-type adenosine triphosphate
BL	basal-like
BRCA	breast cancer associated
C	Cytosine
ca.	*circa* (around)
CAM	chorioallantoic membrane
CCD	charge-coupled device
CTR	copper transporter
Dap	1,3-diaminopropane
DFT	Density Functional Theory
dG	Deoxyguanine
DLaTGS	L-alanine doped triglycine sulphate
DLS	Diamond Light Source
DMEM-HG	Dulbeco's Modified Eagle Medium – High Glucose
DMSO	dimethyl sulfoxide
DNA	deoxyribonucleic acid
DTGS	deuterated triglycine sulphate
DTX	Docetaxel
ECACC	European Collection of Cell Cultures
ECM	extracellular matrix
E. coli	*Escherichia coli*
EDTA	ethylenediaminetetraacetic acid
e.g.	*exempli gratia* (for example)
EJM	extended jump model
EMSC	Extended Multiplicative Signal Correction
En	Ethylenediamine
ER	oestrogen receptor
EU	European Union

FBS	fetal bovine serum
FPA	focal plane array
FR	Fermi resonance
FTIR	fourier-transform infrared
FWHM	full width at half-maximum
G	Guanine
GSH	Glutathione
HER2	human epidermal growth factor 2
HMG	high mobility group
HWHM	half-width at half-maximum
Ic	cubic crystal variance form of ice
IC_{50}	half maximal inhibitory concentration
i.e.	*id est* (that is)
Ih	hexagonal crystal form of ice
IHC	Immunohistochemistry
IM	Immunomodulary
INS	inelastic neutron scattering
IR	Infrared
IRMS	infrared microspectroscopy
LAM	longitudinal acoustic mode
LANL2DZ	Los Alamos National Laboratory 2 Double-Zeta
LAR	luminal androgen receptor/luminal-like
laser	Light Amplification by Stimulated Emission of Radiation
LDA	low-density amorphous
LN_2	liquid nitrogen
M	Mesenchymal
MCT	mercury cadmium telluride
MIRIAM	Multimode InfraRed Imaging and Microspectroscopy
MMR	mismatch repair
mPW1PW	exchange functional and correlation functional proposed by Perdew and Wang

MRD	minimal residual disease
mRNA	messenger ribonucleic acid
MRP2	multidrug resistance-associated protein 2
MSL	mesenchymal-stem cell-like
MT	Metallothionein
NA	numerical aperture
Nd:YAG	neodymium-doped yttrium aluminium garnet crystal
NER	nucleotide excision repair
NMR	nuclear magnetic resonance
ORR	overall response rate
OS	overall survival
PA	Polyamines
PBS	phosphate buffered saline
PC	principal component
PCA	principal components analysis
Pen/Strep	penicillin-streptomycin
PET	polyethylene terephthalate
PFS	progression-free survival
Phe	Phenylalanine
PR	progesterone receptor
Put	Putrescine
QCL	quantum cascade lasers
QENS	quasielastic neutron scattering
QFM-UC	Unidade de I&D Química-Física Molecular
qPCR	quantitative protein chain reaction
RMieS	Resonant Mie Scattering
RNA	ribonucleic acid
S/N	signal-to-noise
SEM	standard error of the mean
SMC	smooth muscle cells
Spd	Spermidine

Spm	Spermine
SR	synchrotron radiation
SRB	suforhodamine B
STFC	Science and Technology Facilities Council
SU 5416	1,3-dihydro-3-[(3,5-dimethyl-1H-pyrrol-2-yl)methylene]-2H-indol-2-one
T	Thymine
TAM	transverse acoustic mode
TIE	tyrosine kinase endothelial
TNBC	triple negative breast cancer
Tris	tris(hydroxymethyl)aminomethane
Trp	Tryptophan
Tyr	Tyrosine
UK	United Kingdom
UNC	unclassified
UV	Ultraviolet
VEGF	vascular endothelial growth factor
VEGFR	vascular endothelial growth factor receptor
VIBIMA	Vibrational Bio-Imaging laboratory of the University of Coimbra
vs	*Versus*
ZPVE	zero point vibrational energy

Indexes

Table of Contents

Figure Index

Table Index